

2018

Physics-Based Approaches For Structural Health Monitoring And Nondestructive Evaluation With Ultrasonic Guided Waves

Md Yeasin Bhuiyan
University of South Carolina

Follow this and additional works at: <https://scholarcommons.sc.edu/etd>



Part of the [Mechanical Engineering Commons](#)

Recommended Citation

Bhuiyan, M. Y.(2018). *Physics-Based Approaches For Structural Health Monitoring And Nondestructive Evaluation With Ultrasonic Guided Waves*. (Doctoral dissertation). Retrieved from <https://scholarcommons.sc.edu/etd/4724>

This Open Access Dissertation is brought to you by Scholar Commons. It has been accepted for inclusion in Theses and Dissertations by an authorized administrator of Scholar Commons. For more information, please contact digres@mailbox.sc.edu.

PHYSICS-BASED APPROACHES FOR STRUCTURAL HEALTH MONITORING AND
NONDESTRUCTIVE EVALUATION WITH ULTRASONIC GUIDED WAVES

by

Md Yeasin Bhuiyan

Bachelor of Science

Bangladesh University of Engineering & Technology, 2011

Master of Science

Bangladesh University of Engineering & Technology, 2013

Master of Science

University of South Carolina, 2016

Submitted in Partial Fulfillment of the Requirements

For the Degree of Doctor of Philosophy in

Mechanical Engineering

College of Engineering and Computing

University of South Carolina

2018

Accepted by:

Victor Giurgiutiu, Major Professor

Sourav Banerjee, Committee Member

Lingyu Yu, Committee Member

Paul Ziehl, Committee Member

Bin Lin, Committee Member

Cheryl L. Addy, Vice Provost and Dean of the Graduate School

© Copyright by Md Yeasin Bhuiyan, 2018

All Rights Reserved.

DEDICATION

This work is dedicated to my beloved wife Rumpamoni, who has been a constant source of support and encouragement during the challenges of my life. This work is also dedicated to my parents, brothers, and sisters who have always loved me unconditionally and whose good examples have taught me to work hard for the things that I aspire to achieve.

ACKNOWLEDGMENTS

First and foremost, I would like to thank Almighty Allah for giving me the strength, knowledge, ability and opportunity to undertake this research study and to persevere and complete it satisfactorily.

I would like to express my sincere gratitude to my academic advisor, Prof. Victor Giurgiutiu (Dr. G), for your strong support, knowledgeable guidance, and giving me the opportunity to join the Laboratory of Active Materials and Smart Structures (LAMSS). It has been such a rewarding experience to be your student. Your passion for science and enlightening instructions helped me overcome many difficulties. This will remain as a lifetime encouragement in my future career. I must say about Dr. G and LAMSS that there are lot of pearls (of knowledge) spread out in this lab, it depends how much one can fill in his/her basket.

I would like to thank Dr. Sourav Banerjee, Dr. Lingyu Yu, Dr. Paul Ziehl, and Dr. Bin Lin for being my Doctoral Committee Members. I really appreciate your valuable guidance, collaboration, reading 300 page dissertation, and feedback. I would like to thank Dr. Bin Lin and Dr. Jingjing Bao for your help in experimental setup of my research. I would also thank you for providing me training in operating laser Doppler Vibrometer, teaching how to lead a project and participating numerous scientific discussions along the way. You were my instant source of information for everything I need in this lab. I would also like to thank Dr. Yangfen Shen and Dr. Banibrata Poddar for participating in conceptual discussions. When I first joined this lab, I step on to Dr. Shen's research and

you well guided me to navigate through the path you built during your PhD study. Dr. Poddar and I often had great discussions about our research. I also thank you for a collaborative research that we did even after you moved finishing your PhD.

Special thanks to my dear friend and colleague Dr. Erik Frankforter for reviewing my proposal dissertation, making comments and suggestions. I would like to thank my colleagues Dr. William Roth, Dr. Darun Barazanchy, Roshan Joseph, Mohammad Faisal Haider, Hanfei Mei, Asaad Migot, Anxo Martinez Dominguez, Robin James, Wenfeng Xiao, Stephen Howden for your friendship and accompany during this challenging journey.

I would like to thank undergraduate student researchers Matthew Droghini and Nathan Ezernack for helping me with the fatigue experiments and making test fixtures. I would also thank Malik Thompson, David Thompson for your friendship. I really had an amazing time with all the LAMSS members.

I would like to thank Tighe's family of Columbia especially Elizabeth and Hagood for your close friendship in last five years. I would like to thank Laura, Dan, and your kids for warm-hearted friendship. Y'all made my stay in Columbia enjoyable and more engaging with the community. I hope our friendship lasts forever.

The following funding supports are thankfully acknowledged: Office of Naval Research #N00014-14-1-0655 and #N00014-17-1-2829, Dr. Ignacio Perez, Technical Representative; Air Force Office of Scientific Research #FA9550-11-1-0133, Dr. David Stargel, Program Manager; National Aeronautics and Space Administration; Office of the Vice President for Research, University of South Carolina.

ABSTRACT

The engineering infrastructures have a growing demand for damage monitoring systems to avoid any potential risk of failure. Proper damage monitoring solutions are of a great interest to this growing demand. The structural health monitoring (SHM) and nondestructive evaluation (NDE) offer appropriate online and offline damage monitoring solutions for a variety of mechanical and civil infrastructures that includes unmanned aerial vehicles (UAV), spaceships, commercial aircraft, ground transportation, wind turbines, nuclear spent fuel storage tanks, bridges, naval ships, and submarines. The fundamentals of the ultrasonic SHM and NDE consist of multi-disciplinary fields. The dissertation addresses SHM and NDE using ultrasonic guided waves, with an emphasis on the development of an analytical solution for non-axisymmetric guided wave propagation, multiphysics simulation, and experimental study of acoustic emission from the structural fatigue damage.

An analytical solution for non-axisymmetric coupled guided wave propagation in plate-like structures was developed based on the equations of motion and elasticity relations. A general non-axisymmetric solution of guided wave propagation in plate is needed to analyze the guided wave-scatter from non-axisymmetric damage as encountered in practice. Under non-axisymmetric conditions, the problem is highly coupled and no potential based analytical solution has been reported in the literature so far. Helmholtz decomposition theorem was applied to the Navier-Lame equations that yielded a set of four coupled partial differential equations in four unknowns, the scalar potential Φ and the

three components of the vector potential H_r, H_θ, H_z . A fourth equation, the ‘gauge condition’ was then added to the decomposition. A particular interpretation of the gauge condition is proposed. Our proposed approach decouples the governing equations and reduced the number of unknowns from four to three thus allowing one to express the solution in an elegant straight-forward way. The Rayleigh-Lamb characteristic equations were recovered and a general normal-modes expression for the solution was obtained.

A hybrid global analytical and local finite element method was used to solve a practical aerospace rivet hole crack detection. The scatter cube of complex-valued wave damage interaction coefficients (WDICs) was developed to analyze any rivet hole of a multiple-rivet-hole lap joint system. It had been shown that not all parameters such as actuator-sensor locations, and frequencies were equally sensitive to the damage scatter. The optimum combination of parameters could better detect the crack in the rivet hole. The simulated time domain signals were produced for the optimum combination of parameters.

Multiphysics simulations for fatigue crack generated acoustic emission (AE) were performed and the results were validated by the experiments. A novel application of inexpensive piezoelectric wafer active sensors (PWAS) has been explored. It has been shown that PWAS transducers successfully captured the fatigue-crack generated acoustic emissions in the thin plate-like aerospace materials. PWAS performance was compared with existing commercial AE sensors. It was found that PWAS captured richer frequency content than the existing AE sensors. Various AE waveform signatures were found from the fatigue crack advancement during the fatigue load evolution. Some AE waveform signatures were found to be related to the fatigue-crack extension while some of them were related to the fatigue-crack fretting, rubbing, and clapping. This observation was confirmed

by synchronizing the fatigue loading with AE measurement by the same AE instrument. The in-situ microscopic measurement was performed during fatigue loading in MTS which provided the insights of the AE waveform evolution. It was hypothesized that the crack length estimation could be related the AE waveform signatures. FEM simulations and experiments were conducted using laser Doppler vibrometer (LDV) to verify our hypothesis.

Two case studies are discussed showing the implementation of SHM and NDE approach in practical applications: (1) horizontal crack detection, size, and shape estimation in stiffened structures, (2) impact damage detection in manufactured aerospace composite structures.

The dissertation finishes with conclusions, major contributions, and suggestions for future work.

TABLE OF CONTENTS

DEDICATION	iii
ACKNOWLEDGMENTS	iv
ABSTRACT	vi
LIST OF FIGURES	xiii
LIST OF TABLES	xxi
CHAPTER 1 INTRODUCTION	1
1.1 MOTIVATION	2
1.2 RESEARCH GOAL, SCOPE, AND OBJECTIVES	5
1.3 ORGANIZATION OF THE DISSERTATION	7
CHAPTER 2 FUNDAMENTALS OF GUIDED WAVES AND SENSORS FOR STRUCTURAL HEALTH MONITORING.....	9
2.1 STRUCTURAL HEALTH MONITORING USING GUIDED WAVES.....	10
2.2 GENERAL THEORY OF ELASTIC WAVES	14
2.3 GUIDED WAVES	16
2.4 PIEZOELECTRIC WAFER ACTIVE SENSORS	26
2.5 ACOUSTIC EMISSION SENSORS AND THEIR FREQUENCY RESPONSES	30
2.6 AE SENSOR CONSTRUCTION AND SENSING MECHANISM	34
CHAPTER 3 USING THE GAUGE CONDITION TO SIMPLIFY THE ELASTODYNAMIC ANALYSIS OF GUIDED WAVE PROPAGATION.....	37
3.1 STATE OF THE ART	37
3.2 INTRODUCTION.....	38

3.3	GOVERNING EQUATIONS AND ORIGIN OF GAUGE CONDITION IN ELASTODYNAMICS	42
3.4	DIFFERENT FORMS OF GAUGE CONDITION IN ELECTRODYNAMICS	45
3.5	APPLICATION OF GAUGE CONDITION TO STRAIGHT CRESTED GUIDED WAVES IN A PLATE	46
3.6	APPLICATION OF GAUGE CONDITION TO CIRCULAR CRESTED GUIDED WAVES IN A PLATE	53
3.7	CONCLUSION	58
CHAPTER 4 A HELMHOLTZ POTENTIAL BASED SOLUTION TO THE NON-AXISYMMETRIC COUPLED GUIDED WAVE PROPAGATION IN A PLATE		60
4.1	INTRODUCTION.....	61
4.2	DESCRIPTION OF THE NON-AXISYMMETRIC GUIDED WAVE PROBLEM IN CYLINDRICAL COORDINATES	63
4.3	A JUDICIOUS FORM OF THE GAUGE CONDITION	69
4.4	SIMPLIFICATION OF THE NON-AXISYMMETRIC PROBLEM USING THE GAUGE CONDITION	71
4.5	SOLUTION OF THE NON-AXISYMMETRIC GUIDED WAVE PROBLEM IN CYLINDRICAL COORDINATES	76
4.6	GENERAL HELMHOLTZ SOLUTION FOR NON-AXISYMMETRIC GUIDED WAVES IN CYLINDRICAL COORDINATES	90
4.7	SUMMARY AND CONCLUSION.....	96
CHAPTER 5 ANALYTICAL-FEM SIMULATION FOR ENHANCED DAMAGE DETECTION FOR AEROSPACE RIVET HOLE		98
5.1	INTRODUCTION.....	99
5.2	DESCRIPTION OF THE SHM OF MULTIPLE-RIVET-HOLE LAP JOINT.....	101
5.3	OVERVIEW OF COMBINED ANALYTICAL AND FEM APPROACH.....	103
5.4	DESCRIPTION OF THE ANALYTICAL MODEL	104

5.5	EFFECT OF LOCAL DAMAGE THROUGH THE INSERTION OF SCATTER CUBE OF WDIC	108
5.6	DESCRIPTION OF THE FEM MODELING	112
5.7	DISCUSSION OF THE SIMULATION RESULTS	119
5.8	SIMULATED TIME DOMAIN SIGNALS	127
5.9	CONCLUSIONS	134
CHAPTER 6 MULTIPHYSICS FEM SIMULATIONS FOR FATIGUE-CRACK GENERATED ACOUSTIC EMISSIONS VALIDATED BY EXPERIMENTS		136
6.1	STATE OF THE ART	136
6.2	SCOPE OF THE CHAPTER	138
6.3	DESCRIPTION OF 3D MULTIPHYSICS FEM SIMULATION.....	139
6.4	MULTIPHYSICS FEM SIMULATION RESULTS	145
6.5	VALIDATION OF MULTIPHYSICS SIMULATION RESULTS WITH EXPERIMENTAL MEASUREMENTS.....	148
6.6	EFFECT OF RISE TIME ON THE SIMULATED AE SIGNALS	153
6.7	EFFECT OF DIPOLE ORIENTATION IN THE SIMULATED AE SIGNALS	154
6.8	CONCLUSION.....	155
CHAPTER 7 PHYSICS OF MATERIALS BASED ANALYSIS OF AE SIGNALS FROM IN-SITU AE-FATIGUE EXPERIMENTS		156
7.1	INTRODUCTION AND STATE OF THE ART	157
7.2	SCOPE OF THE CURRENT RESEARCH.....	159
7.3	SENSOR EFFECT ON THE AE WAVEFORMS.....	159
7.4	VARIOUS AE WAVEFORM GROUPS WITH FATIGUE LOAD EVOLUTION	178
7.5	SOURCE LOCALIZATION OF THE AE SIGNAL GROUPS.....	197
7.6	DISTINGUISHING CRACK GROWTH AND CRACK-RUBBING/FRETTING AE SIGNALS	203

7.7	CONCLUSION.....	204
CHAPTER 8 CAN WE HEAR CRACK LENGTH FROM ACOUSTIC WAVEFORMS?		
		206
8.1	INTRODUCTION AND STATE OF THE ART	206
8.2	3D FEM SIMULATION OF AE WAVEFORM GENERATION AND CRACK RESONANCE	207
8.3	EXPERIMENTAL VERIFICATION OF CRACK RESONANCES	211
8.4	SUMMARY AND FINDINGS	213
CHAPTER 9 TWO CASE STUDIES.....		
		214
9.1	CASE STUDIES #1: ACTIVE SHM FOR HORIZONTAL CRACK DETECTION, SIZE, AND SHAPE ESTIMATION IN STIFFENED STRUCTURES	214
9.2	CASE STUDIES #2: SHM AND NDE OF A MANUFACTURED COMPOSITE PLATE.	226
CHAPTER 10 CONCLUSIONS AND FUTURE WORK.....		
		242
10.1	RESEARCH CONCLUSIONS	244
10.2	MAJOR CONTRIBUTIONS.....	249
10.3	RECOMMENDATION FOR FUTURE WORK.....	252
REFERENCES		
		255

LIST OF FIGURES

Figure 2.1 Schematic representation of a generic SHM system, consisting of active sensors, data concentrators, wireless communication, and SHM central unit [10].	11
Figure 2.2 Pitch-catch active sensing: (a) baseline response; (b) response with damage; (c) scattered response [12].	12
Figure 2.3 (a) Phased array imaging using EUSR [13], (b) sparse array imaging using time-reversal method [15].	13
Figure 2.4 (a) Electro-mechanical coupling between the PZT active sensor and the structure [16], (b) EMIS spectrum [17].	14
Figure 2.5 Coordinate definition and particle motion of SH plate waves [21].	17
Figure 2.6 (a) SH plate wave-speed dispersion curves, (b) symmetric mode shapes, (c) antisymmetric mode shapes [21].	18
Figure 2.7 Particle motion of Lamb wave modes: (a) symmetric mode and (b) antisymmetric mode [21].	19
Figure 2.8 (a) Wave speed dispersion curve; (b) wavenumber dispersion curve [11]	20
Figure 2.9 Modeshapes of S0 and A0 Lamb waves in a 2-mm thick aluminum plate [11].	22
Figure 2.10 (a) Cylindrical coordinate for problem derivation [21]; (b) circular crested wave pattern.	23
Figure 2.11 Hankel function of order zero ($H_0^{(1)}(R)$) and order one ($H_1^{(1)}(R)$).	25
Figure 2.12 (a) Piezoelectric wafer active sensors (PWAS), (b) PWAS measures in-plane and out-of-plane wave motion through in-plane strain sensing.	27
Figure 2.13 Schematic of PWAS application modes [21].	28
Figure 2.14 Lamb wave generation using PWAS transducers [21].	29

Figure 2.15 (a) Strain Lamb wave tuning results from analytical solution (1.6-mm aluminum plate), (b) Experimental results from PWAS response [25].	30
Figure 2.16 R15I-AST, R15 α , R15, and WS α AE sensors from Physical Acoustics Corporation (PAC) Mistras; PWAS that has been customized in our lab.	31
Figure 2.17 Nano-30, PICO, S9225 and R15 AE sensors from Physical Acoustics Corporation (PAC) Mistras; PWAS that has been customized in our lab.	31
Figure 2.18 Frequency response curves of R15I-AST, WS α , and R15 α (obtained from PAC-Mistras).	33
Figure 2.19 Frequency response curves of Nano-30, PICO, and S9225 (obtained from PAC-Mistras).	34
Figure 2.20 Cross-section of a typical commercial AE sensor. It measures out-of-plane wave motion.	35
Figure 3.1 Problem definition and displacement components in Cartesian coordinate system.	40
Figure 3.2 Problem definition in cylindrical coordinate system.	53
Figure 4.1 Non-axisymmetric guided wave propagation in a plate	64
Figure 4.2 Traction on a differential element of a plate in cylindrical coordinates	66
Figure 5.1 Illustration of the multiple-rivet-hole lap joint.	102
Figure 5.2 Overview of the combined analytical and FEM approach [11]	104
Figure 5.3 Illustration of local finite element method (FEM) modeling (a) Pristine model, (b) Local damage model with NRB, (c) 3D view of damage model (d) Stress modeshapes (e) FE loading in the thickness direction	113
Figure 5.4 Comparison between analytical and FEM results (a) $WDIC_{LW_LW}$ (b) $WDIC_{LW_SH}$ in polar coordinates (pristine plate).	115
Figure 5.5 Crack modeling schematic. Two nodes along two crack-faces remained unmerged.	116
Figure 5.6 Dispersion curves for (a) Lamb wave and (b) SH wave for 1.6 mm thick aluminum plate.	117
Figure 5.7 S0 and A0 Lamb mode wavelength variation with frequencies for 1.6 mm thick aluminum plate.	117

Figure 5.8 Die-out distance required for the non-propagating A1 mode.....	118
Figure 5.9 Alteration of WDIC profiles of scattered Lamb and SH wave with different damage conditions	120
Figure 5.10 Subtracted WDIC profiles of scattered Lamb and SH wave to account the damage effect only	121
Figure 5.11 Frequency domain variation of $WDIC_{S0_S0}$ at different azimuthal positions ($\theta = 9^\circ$).....	123
Figure 5.12 Frequency domain variation of $WDIC_{S0_S0}$ for multiple incident directions.....	123
Figure 5.13 Frequency domain variation of $WDIC_{A0_A0}$ for multiple incident directions.....	124
Figure 5.14 Azimuthal variation of (a) $WDIC_{S0_S0}$ (b) $WDIC_{A0_A0}$ at different frequencies	125
Figure 5.15 $WDIC_{S0_S0}$ for various incident angles at most sensitive frequencies	127
Figure 5.16 (a) The baseline reference signal for the hole. (b) The signal due to Hole + Crack (c) Subtracted signal due to the crack only ($f = 538$ kHz, $\theta = 0^\circ$)	128
Figure 5.17 A simplified case of the multiple-rivet-hole problem	129
Figure 5.18 Sensing signals for different sets of frequency-location ($\theta = 9^\circ$).....	131
Figure 5.19 Sensing signals for different sets of frequency-location ($\theta = 18^\circ$).....	132
Figure 5.20 Sensing signals for different sets of frequency-location ($\theta = 27^\circ$).....	133
Figure 6.1 The meshed FEM model with in-plane dipole excitation: (a) overall view (obtained directly from ANSYS); (b) zoomed in view of crack tip area showing dipole loading; (c) side view showing the thickness-wise assignment of dipole components ..	141
Figure 6.2 The dipole loading used for simulating the AE event at the crack tip. (a) A typical half-cosine bell step function and its frequency response (rise time = 1.5 μ s), (b) the half-cosine bell step-up from 0 to 1 in the amplitude scale.	144
Figure 6.3 The animation snapshots of the acoustic wave propagation at different time of simulation.	146

Figure 6.4 Multiphysics simulated AE signals from the two PWAS transducers: (a) near-field PWAS 1 (b) far-field PWAS 2. 147

Figure 6.5 (a) Schematic diagram of the specimen with fatigue crack and a PWAS transducer bonded at 5-mm and 25-mm from the crack (b) Actual specimen with two PWAS transducers bonded at 5-mm and 25-mm from the crack. 149

Figure 6.6 (a) Actual test coupon in the MTS grip without any AE instrumentation for the initial 20-mm crack (b) Instrumented Test coupon in the MTS grip for capturing fatigue-crack related AE signals..... 149

Figure 6.7 Experimentally measured AE signals by the two PWAS transducers: (a) near-field PWAS (b) far-field PWAS. 151

Figure 6.8 Effect of rise time on the simulated AE signals. 153

Figure 6.9 The meshed FEM model with in-plane dipole excitation: (a) overall view; (b) top view zoomed into crack tip area showing dipole loading; (c) side view showing the thickness-wise assignment of dipole components, (d) simulated AE signals..... 154

Figure 7.1 Test specimen on the MTS machine for initial 20-mm fatigue crack generation 161

Figure 7.2 Schematic diagram of the experimental setup with two PWAS and two S9225 AE sensors. 163

Figure 7.3 (a) Experimented test coupon on MTS load frame subjected to fatigue loading, (b) S9225 AE sensors were bonded to one side of the plate and (c) PWAS transducers were bonded to the other side of the plate. 165

Figure 7.4 AE hits captured by (a) PWAS transducer and (b) S9225 AE sensors, both of them showing the similar trend..... 166

Figure 7.5 “Group A” AE waveform and its frequency spectrum captured by (a) PWAS transducer and (b) S9225 AE sensor at the same time..... 167

Figure 7.6 “Transition” AE waveform and its frequency spectrum captured up by (a) PWAS transducer and (b) S9225 AE sensor at the same time. 168

Figure 7.7 “Group B” AE waveform and its frequency spectrum captured by (a) PWAS transducer and (b) S9225 AE sensor at the same time..... 169

Figure 7.8 (a) Sensing AE signal by the S9225, (b) the frequency response plot of S9225 (from the manufacturer); (b) shows is a weak response in the frequency range of 170-300 kHz and the S9225 also sense a weak signal in this range 170

Figure 7.9 (a) Schematic diagram of the experimental setup with PWAS and PICO AE sensors. (b) A zoomed-in view of the PWAS and PICO with respect to the fatigue crack. For scale, please note, the hole has 1-mm diameter. 171

Figure 7.10 The AE hits captured by the PWAS and PICO AE sensors. Both of them are showing a similar trend in the AE-hit plots. 172

Figure 7.11 PWAS and PICO AE hits synchronized with the fatigue loading cycle. 174

Figure 7.12 The comparison between PWAS and PICO AE waveforms and their frequency spectra for the same AE event at approx. 360.36 s (marked by “1” on Figure 7.11). 175

Figure 7.13 The comparison between PWAS and PICO AE waveforms and their frequency spectra for the same AE event at approx. 378.79 s (marked by “2” on Figure 7.11). 176

Figure 7.14 The comparison between (a) PWAS and (b) PICO AE waveforms and their frequency spectra for the same AE event at approx. 400.36 s (marked by “3” on Figure 7.11). 177

Figure 7.15 (a) A typical AE waveform and its frequency spectrum captured by the PICO AE sensor, (b) frequency response curve of PICO (obtained from the manufacturer)... 178

Figure 7.16 Schematic diagram of the fatigue test plate-specimen with a PWAS transducer, 5-mm from the crack..... 179

Figure 7.17 The actual fatigue test specimen mounted in the MTS grips with an in-situ microscope 180

Figure 7.18 The fatigue test specimen mounted in the MTS grips and a high-resolution video camera with an extension tube to measure fatigue crack growth. 181

Figure 7.19 AE hits captured by the PWAS transducer are plotted in synchronization with the cyclic fatigue loading. 182

Figure 7.20 (a) Group A, B AE hits are plotted in sync with the cyclic fatigue loading. They happened at every cycle but at different load levels; group A happened at 84% of maximum load level while group B happened at 78% of maximum load level. (b),(c) The waveforms and frequency spectra of group A, B, respectively; the major frequency peaks of each group are marked by dotted ellipses..... 184

Figure 7.21 Load level determination of group A and group B AE hit. 185

Figure 7.22 Similarity between the AE events happened at two different times (~350 s, ~800 s) in a particular group. For illustration purpose, only two groups (A, B) are presented here. The time-domain and the frequency spectrum of each signal are plotted. 186

Figure 7.23 (a) Group C AE hits are plotted in sync with the cyclic fatigue loading; the hit amplitude varied over the fatigue cycles, they happened at every cycle approx. 81% of maximum load; (b) the time domain signal and frequency spectrum of a representative group C waveform. 187

Figure 7.24 (a) Group D AE hits are plotted in sync with the cyclic fatigue loading; they happened at approx. 78% of maximum load, they appeared in the beginning and disappeared after approx. 300 s; (b) the raw time domain signal of group D; (c) denoised waveform of (b); (d) frequency spectrum of the denoised group D waveform. 189

Figure 7.25 (a) Clustered Group E AE hits in sync with the cyclic fatigue loading (b) the time domain signal and frequency spectrum of a representative group E waveform. 190

Figure 7.26 Similarity in the frequency spectra of clustered (Group E) waveforms 191

Figure 7.27 The view of the zigzags and the faying surfaces of the fatigue crack. The image was captured at maximum load level; two different locations along the fatigue crack length are shown here; the light was shining behind the crack..... 193

Figure 7.28 Schematic representation of the faying surfaces of the fatigue crack 193

Figure 7.29 (a) Group F AE hits are plotted in sync with the cyclic fatigue loading; they happened at every cycle and at approx. 57% of maximum load, they appeared after approx. 250s and then continued; (b) the time domain denoised signal and frequency spectrum of a representative group F waveform..... 194

Figure 7.30 (a) Group G AE hits appeared sporadically over the cycles at approx. 78-81% of maximum load; (b) the denoised time domain signal and the frequency spectrum of a representative group G waveform..... 195

Figure 7.31 (a) Group H AE hits are plotted in sync with the cyclic fatigue loading; they appeared at relatively lower load level (23% of max. load); (b) the denoised time domain signal and the frequency spectrum of a representative group H waveform..... 196

Figure 7.32 (a) Schematic diagram for the source localization of the AE signals; two PWAS transducers and two PICO AE sensors were bonded symmetrically about the fatigue crack and at same distances (5-mm, 25-mm) from the crack; (b) actual fatigue test specimen mounted on the MTS grip showing the positions of the four sensors. 198

Figure 7.33 Relative position of the near-field PWAS and PICO sensors. The centers of the two sensors were at an equal distance, 5-mm from the crack..... 199

Figure 7.34 Four possible hypotheses on the sequence-of-arrival of the AE signals. 200

Figure 7.35 Group B AE signals captured by the four sensors: (a) near-field PICO, (b) near-field PWAS, (c) far-field PICO, (d) far-field PWAS..... 200

Figure 7.36 The four AE-hit plots of Figure 7.35 are overlapped together in a common timeline and zoomed-in a particular portion around 240 s. A particular AE event occurred around 240 s was captured by the four sensors. The actual time of arrival is stamped by these AE hits. 201

Figure 8.1 3-D FEM model for harmonic analysis (a) top view (b) front view (c) dipole loading at the crack tip (d) line load along the thickness..... 208

Figure 8.2 Animation snapshots of transient FEM simulation as the time progress (a) $t = 1.5 \mu s$, (b) $t = 3 \mu s$, (c) $t = 3.9 \mu s$, (d) $t = 4.8 \mu s$ 209

Figure 8.3 FEM simulation results for (a) the crack resonance captured at the mouth of the crack in harmonic analysis, (b) comparison between FFT of AE waveform of the hole and hole+10 mm crack (sensing at 20 mm away from the hole) in transient analysis [153]. 210

Figure 8.4 Laser Doppler Vibrometer (LDV) experimental setup 211

Figure 8.5 LDV experimental results (out-of-plane velocity) measured at 20 mm away from the slit. The resonance frequencies are labeled in the frequency spectrum [154]. 212

Figure 9.1 Geometric dimension of the plate with stiffener used for manufacturing..... 216

Figure 9.2 Test plan for the ultrasonic inspection of the plate to detect crack in the stiffener using non-contact laser measurement. 218

Figure 9.3 (a) Experimental setup for scanning using laser Doppler vibrometer (LDV), (b) The test specimen with a laser beam at the center of the scanning area. 219

Figure 9.4 LDV scanning results for comparison of the wavefield due to the pristine and cracked stiffener. In both cases, S_0 Lamb waves are incident waves. The wavefields are captured at the same time of 74- μs . (a) The wavefield due to the pristine stiffener: reflected and transmitted waves are straight-crested waves, (b) the wavefield due to the cracked stiffener: reflected and transmitted waves are no more straight-crested waves; trapped wavemodes are generated within the half-penny-shaped crack; the effect of crack is carried by the propagating waves in the plate..... 221

Figure 9.5 Transmitted waveform comparison between pristine and cracked stiffener due to A_0 incident Lamb wavemode. The waveforms are captured at three different locations on the transmission side as marked by 1, 2, 3 in Figure 9.2. The points 1, 2, 3 are located at 4.2, 4.6, 4.8 inches from the stiffener. Due to the presence of a horizontally oriented crack, more transmission of A_0 mode is observed. 223

Figure 9.6 Transmitted waveform comparison between pristine and cracked stiffener due to S_0 incident Lamb wavemode. The waveforms are captured at three different locations on the transmission side as marked by 1, 2, 3 in Figure 9.2. The points 1, 2, 3 are located

at 4.2, 4.6, 4.8 inches from the stiffener. Due to the presence of horizontally oriented crack, less mode-conversion of the S0 model is observed. 224

Figure 9.7 Cutting and laying up the PPS prepreg fabrics..... 227

Figure 9.8 Composite layers are placed in the hot-press to apply heat and pressure 228

Figure 9.9 Cure cycle for the PPS prepreg 229

Figure 9.10 Final composite plate after cutting the extra resin flow around the plate ... 229

Figure 9.11 NDI experimental setup for damage inspection of the composite plate using phased array based Rollerform from Olympus and Omniscan..... 231

Figure 9.12 The phased array wheel probe element [155]..... 232

Figure 9.13 NDI inspection area and the division scheme for ultrasonic scanning..... 233

Figure 9.14 NDI 3D scanning results of the manufactured composite plate 234

Figure 9.15 SHM scheme for impact detection and localization on the manufactured composite plate 236

Figure 9.16 PWAS recorded acoustic signals due to impact at location #1 237

Figure 9.17 PWAS recorded acoustic signals due to impact at location #3 238

Figure 9.18 Wavelet transform of the PWAS recorded signals to determine time of flight (TOF) (for location #3) 238

Figure 9.19 Experimentally measured impact location and actual impact location on the manufactured composite plate 240

LIST OF TABLES

Table 2.1 Dimensions and masses of the sensors	32
Table 4-1: The constants A, B, C, D, E, F for symmetric and antisymmetric modes.....	91
Table 7.1 Summary statistics of the 427 AE hits over the 50 fatigue cycles with 300- μm crack growth.....	197
Table 7.2 Source localizations for the different groups of AE signals	202
Table 9.1 Experimental measurement vs. actual location of the impact	240

CHAPTER 1

INTRODUCTION

This chapter serves as the introduction to the entire dissertation by addressing the motivation and importance of conducting the research, discussing research goal, scope, and objectives, and introducing the organization of the dissertation.

Structural Health Monitoring (SHM) is a multi-disciplinary field, which requires a strong background in elasticity, structural mechanics, fracture mechanics, and material science as well as proficiency in electrical signal analysis, sensors, and data acquisition. This involves similar approaches taken by nondestructive evaluation (NDE), only that SHM takes it one step further: SHM attempts to develop (a) damage detection sensors that can be permanently installed on the structure and (b) monitoring methods that can provide on-demand structural health bulletins. SHM aims at detecting, localizing and characterizing structural damage and provide diagnosis and prognosis of structural health status in real-time or on-demand, as required. With the advancement of SHM and NDE technology, the industry can significantly reduce the maintenance cost, shorten the machine service downtime, and improve the safety and reliability of engineering structures. SHM has shown great potential in both the health management of aging structures and the development of novel self-sensing smart and intelligent structures. Although the concept of SHM originated in the application to aerospace structures, later it has been also useful for civil infrastructures.

1.1 MOTIVATION

The true motivation for this research comes from ensuring the safety of the public by designing efficient, low-cost and safer engineering infrastructure. In the U.S., more than 2.5 million people travel every day through airlines [1]. The structural safety is a major concern to ensure proper operations of the airline flights. The structural safety has been drastically increased over the past decades because of continuous research and development. In last five years, there were only 0.1 fatal accidents per millions of flights in the U.S. whereas this number was five times higher twenty years ago [2]. Structural health monitoring (SHM) and nondestructive evaluation (NDE) have contributed to this achievement by ensuring the structural safety and reliability.

Every four years, the American Society of Civil Engineers issues a report grading current infrastructure conditions and needs in the United States. According to the 2017 infrastructure report card, the U.S. barely passed with a score of C+, which was identical to its 2013 score [3]. This shows that research furthering the safety of infrastructures is needed and that the early detection of failures is considerably important to American infrastructure. This report shows that 9.1% (56,007) bridges of total 614,387 bridges are structurally deficient and most of them are 50 years or older. More than 180 million trips take place across the structurally deficient bridges each day. In terms of infrastructure, data from the Congressional Budget Office (CBO) shows that the U.S. total infrastructure costs amounted to \$416 billion in 2014 [4]. SHM and NDE can significantly contribute to our infrastructure by developing low-cost and efficient damage monitoring solutions for these aging structures.

Proper damage monitoring solutions for a variety of structures including but not limited to unmanned aerial vehicles (UAV), rockets, space shuttles, commercial aircraft, ground transportation, nuclear spent-fuel storage casks, bridges, naval ships, submarines are a growing demand. For example, SHM contributes to high altitude long endurance (HALE) UAV development of “Digital Twin” of Air Force research with a 20 years vision from now [5]. The U.S. Naval research is focusing on integrated system health management for navy ships as a part of continuous development from USS North Carolina to USS Gerald R. Ford Navy aircraft carrier [6]. A comprehensive motivation came from a keynote speech by National Aeronautics and Space Administration (NASA) scientists at Stanford University that explained SHM applications for NASA future aerospace vehicles [7]. This speech emphasized the need for ultrasonic guided wave based SHM.

The development of a physics-based modeling approach for the SHM and NDE has always been an interest to the community. The underlying theories of the SHM and NDE technology are based on the fundamental laws of physics. Effective design of SHM and NDE systems requires a solid analytical understanding of the structures, guided wave propagation, and sensors. The equations of motion and the elasticity relations govern the guided waves and are most important for developing the analytical solutions for guided wave problems. The analytical methods are very lucrative because they provide a very fast solution as compared to the computationally expensive finite element method (FEM) and spectral element methods.

In 1917, Prof. Horace Lamb mathematically developed an analytical solution for the guided waves propagating in an elastic plate [8]. Named after its discoverer, Lamb waves refer to elastic perturbations propagating in elastic plates (or layers) with free

boundaries. However, plane strain assumptions were made on the Lamb discoveries. Later, the analytical solutions for axisymmetric wave propagation were developed [9]. However, the presence of any damage in the thin-walled structure is no more axisymmetric. The detection of damage in the structure, which is the main objective of SHM and NDE, needs an analytical solution for non-axisymmetric guided wave propagation. Thus, it is of great importance to develop an accurate, efficient, and versatile analytical solution for non-axisymmetric guided wave propagation.

In practical engineering applications, the SHM can be performed into two main ways: (1) active SHM where a combination of transmitter and receiver sensors are used, and (2) passive SHM where only receiver sensors are used. Depending on the application, one way can be more suitable than the other. In some cases, a combination of active and passive SHM can be employed. In general, the passive SHM and NDE designs require less number of sensors and circuits than the active designs. The passive SHM and NDE mostly use acoustic emission (AE) technology. Acoustic emissions happen from any state change in the materials during any damage progression. Conventional AE techniques rely on the statistical hit-based approaches and sometimes provide a false indication of the criticality of the damage in the structure. A physics-based approach for AE analysis is demanded by the research community to overcome the shortcomings of the conventional approach.

In addition, the current AE practice also does not possess an early warning capability. Such early warning capability, if existed, would greatly assist the effective management of structural fatigue in coordination with mission profile allocation and maintenance schedule. The physics-of-materials based approach considers all possible simultaneous physical events including the source of AE events, AE wave propagation

mechanism, interaction with structural discontinuity, physical microscopic changes in materials, and sensor characteristics. The physics-based AE approach may provide more deterministic and accurate indication of the progressive damage, hence offers a better diagnosis and prognosis. The experimental studies along with the multiphysics computational models may assist this process.

The developed algorithms for enhanced SHM and NDE system are often required to be demonstrated in some practical applications. The theoretical analyses, FEM simulations, and experimental analyses should be combined together to demonstrate such applications. Hence, the demonstration of some case studies is always important for the fundamental scientific research.

1.2 RESEARCH GOAL, SCOPE, AND OBJECTIVES

The research goal of the Ph.D. work presented in this dissertation is to develop analytical, FEM, and experimental tools based on the physics of materials for accurate, efficient, and versatile damage monitoring solutions to be used with SHM and NDE ultrasonic guided wave systems. The scope of this research covers developing the analytical solutions, multiphysics FEM simulations, hybrid analytical–FEM methods, and AE-fatigue experiments to support the physics of material based approaches. It also discusses some practical applications by demonstrating some case studies, for example, horizontal-crack monitoring of stiffened structures and impact damage (i.e. bird strike) monitoring for aerospace composite structures. The objectives of the work presented in this dissertation are as follows:

1. To develop an analytical solution for the non-axisymmetric coupled guided wave propagation.

2. To use the fundamental laws of physics to describe the vector fields in terms of Helmholtz potentials and obtain a relation among the potentials.
3. To find the suitable elastodynamic gauge conditions for different wave propagation problems such as straight crested guided waves, circular crested guided waves, non-axisymmetric guided waves.
4. To develop a scatter cube of wave damage interaction coefficients for an active SHM system of a practical problem such as multiple rivet holes in an aerospace lap joint.
5. To use an efficient and versatile hybrid global analytical and local FEM framework to obtain the simulated signals for enhanced damage detection of cracks in rivet holes.
6. To conduct multiphysics FE simulations for fatigue-crack generated acoustic emissions.
7. To conduct in-situ AE-fatigue experiments under different conditions to collect the AE signals by using different types of sensors.
8. To perform experimental AE signal analysis and develop new signal processing methods.
9. To interpret the experimental AE signals and correlate with the fatigue crack growth mechanisms.
10. To develop a comprehensive waveform-based method for analyzing the AE signals and study the AE sensor effect on the AE waveforms.
11. To analyze the AE waveform signatures and correlate them with the fatigue load evolutions and estimation of the crack length.

1.3 ORGANIZATION OF THE DISSERTATION

To achieve the objectives set forth in the preceding section, the dissertation is organized into nine chapters. The focus and contents of each chapter are introduced in Chapter 1.

In Chapter 2, the fundamentals of guided waves, physics-based concepts of SHM and NDE, and different types of sensors, guided wave theory are briefly reviewed. Guided wave application to SHM is discussed, the sensing mechanism of piezoelectric wafer active sensors (PWAS) and AE sensors are discussed.

In Chapter 3, the elastodynamic gauge condition is analytically derived from the equations of motion and the potential representation of the vector quantities. A novel concept of the gauge condition is proposed. This illustrates the application of the gauge condition to some classical problems.

In Chapter 4, our concept of the gauge condition is applied to a complicated challenging problem which is the coupled non-axisymmetric guided wave propagation in a plate. This illustrates how efficiently the gauge condition makes it possible to analytically solve the complicated non-axisymmetric problem. The development of the Helmholtz potential based analytical solution for the non-axisymmetric guided wave propagation in a plate is presented.

In Chapter 5, the application of the hybrid global analytical and local FEM method for enhanced damage detection in an aerospace rivet hole is illustrated. An aerospace lap joint with multiple rivet holes is considered. The development of a scatter cube of wave damage interaction coefficient (WDIC) for the rivet hole with butterfly cracks is discussed.

Efficient damage detection using the optimum sensor locations and frequencies is demonstrated.

In Chapter 6, the multiphysics FEM simulations of a predictive design for a passive SHM system are described. For the multiphysics simulations, the practical problem of the detection a fatigue-crack generated acoustic emission is considered. The validation of the simulated results with experiments is illustrated.

In Chapter 7, the physics-of-materials based analysis of acoustic emissions from in-situ AE-fatigue experiments is discussed. Multiphysics FEM simulations to interpret the fatigue-crack generated AE signals are discussed. Distinguishing the crack growth related AE signals from the non-crack growth related AE signals is discussed. The difference between AE hit-based and AE waveform-based analyses is presented. The AE sensor effect, various AE signal group identification, their relation to cyclic fatigue load evolution, and AE source localization are discussed.

In Chapter 8, the possibility of crack length estimation from the fatigue crack-related AE waveforms is discussed.

In Chapter 9, two case studies are presented: (1) NDE/SHM system for a manufactured composite plate and (2) horizontal-crack detection, size, and shape estimation in stiffened structures.

The dissertation finishes in Chapter 10 with conclusions, major contributions, and future work.

CHAPTER 2

FUNDAMENTALS OF GUIDED WAVES AND SENSORS FOR STRUCTURAL HEALTH MONITORING

Structural health monitoring methods based on elastic wave propagation are very diverse and constitute a vast area of study. In order to use ultrasonic elastic waves in nondestructive evaluation (NDE) and structural health monitoring (SHM), different types of waves must be studied to understand the underlying physical phenomena. This chapter deals with fundamentals of elastic waves and then an important class of elastic waves (*guided waves*) that have widespread applications in SHM. Guided waves are especially important for SHM because they can travel at large distances in structures. Thus, they enable the SHM of large areas from a single location. In addition, guided waves have the important property that they remain confined inside the walls of a thin-wall structure. Furthermore, guided waves can also travel inside curved walls. These properties make them well suited for the ultrasonic inspection of aircraft, missiles, pressure vessels, oil tanks, pipelines, etc. This study will also serve as the theoretical prerequisite for the complicated analysis of guided wave interaction modeling and simulation. This chapter also introduces a fundamental study of the guided-wave transducers including their working principle, their coupling with guided waves, and their operation modes.

2.1 STRUCTURAL HEALTH MONITORING USING GUIDED WAVES

Structural Health Monitoring (SHM) is an area of growing multi-disciplinary field with wide applications. This technology evolves from the conventional nondestructive evaluation (NDE) and condition based maintenance (CBM), where the damage detection and evaluation are done in schedule based or condition-based manners. In contrast with NDE and CBM, SHM aims at developing real-time or on-demand damage detection and characterization systems for evaluation of structural health status. Within the scope of SHM, guided wave techniques are preferred for their capability of interrogating large areas of structure from a single location. In this section, fundamental SHM concepts are introduced, prevalent guided wave techniques are covered, and key points in a guided wave based SHM are discussed.

2.1.1 STRUCTURAL HEALTH MONITORING CONCEPTS

General sensing technology can be cast into two methodological categories: (1) active sensing and (2) passive sensing. Active sensing procedure has three main advantages for SHM applications: (1) it allows the real-time and on-demand inspection of the structures; (2) the excitation can be optimized for the most sensitive and effective response for damage detection; (3) the active sensing procedure is repeatable, which allows the comparison between two independent interrogations (a baseline data and a current status data). Passive sensing systems only passively record events which happened during the actual time of the event. By analyzing the recorded signal, diagnosis can be made on the health status of the structure. Examples of passive sensing SHM can be found in the acoustic emission (AE) monitoring and impact detection, where passive sensors are triggered by crack advancing or impact events. By analyzing the AE or impact signal,

location of the AE or impact source can be identified. By analyzing the AE data, diagnosis and prognosis can be made. The passive sensing may be advantageous in certain applications.

A schematic representation of a generic SHM system is shown in Figure 2.1. The active sensors clusters are implemented in the critical areas of high monitoring interest, such as airplane wings, engine turbines, fuselage, and fuel tank. Permanently bonded on the host structures, the sensors can actively interrogate large areas from local cluster zones in a real-time or on-demand manner, sending the sensing data to the data concentrators. These data concentrators will transmit the data to the SHM processing unit, where the data will be processed and diagnosis will be made.

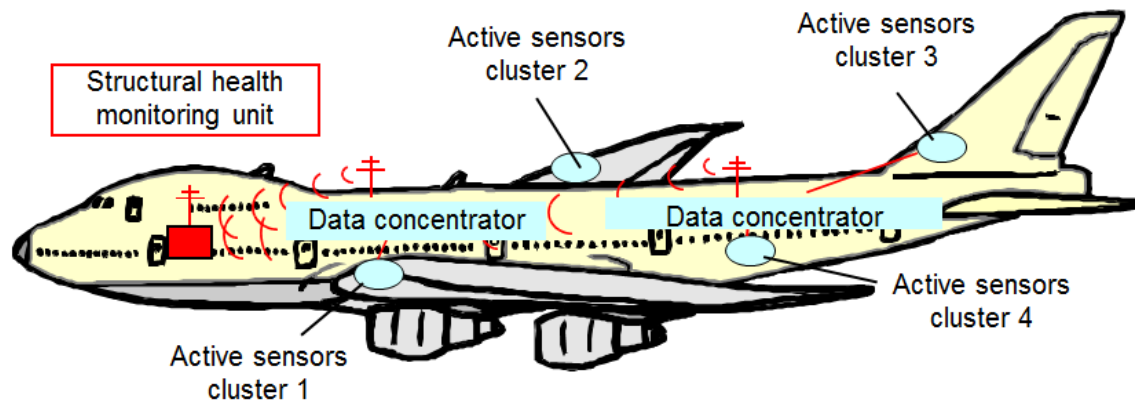


Figure 2.1 Schematic representation of a generic SHM system, consisting of active sensors, data concentrators, wireless communication, and SHM central unit [10].

2.1.2 GUIDED WAVE TECHNIQUES

The guided wave techniques include pitch-catch, pulse-echo, electro-mechanical impedance spectroscopy (EMIS), phased array, and sparse array time-reversal imaging method. There are also some nonlinear techniques that deal with the higher harmonic generation, subharmonic generation, and mixed frequency response [11].

The pitch-catch active sensing method in SHM is shown in Figure 2.2. One transducer (sensor 1) acts as the transmitter and radiates the guided waves, and another transducer acts as the receiver and picks up the sensing signal. In the pristine case (baseline), the interrogating waves are generated by the transmitter, propagate along the structure, and are picked up by the receiver. In the damaged case, the interrogating waves generated by the transmitter, propagate along the structure, interact with the damage, carry the damage information with them, and are finally picked up by the receiver. The subtraction between these two states reveals the damage scattering response, which may indicate the presence and severity of the damage.

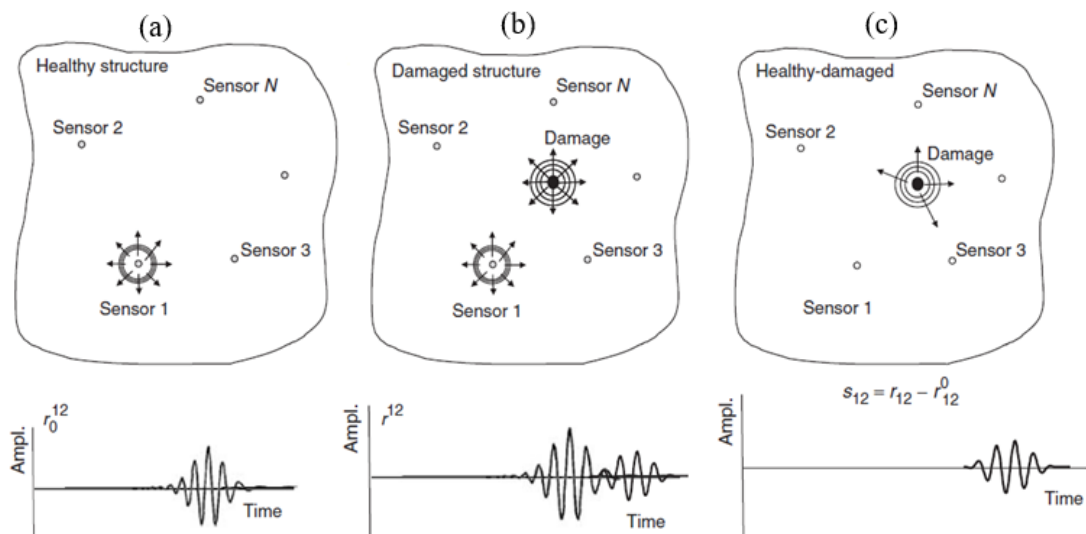


Figure 2.2 Pitch-catch active sensing: (a) baseline response; (b) response with damage; (c) scattered response [12]

Several sensors may work together in a systematically designed manner forming a sensor network and achieve more complicated diagnostic approaches. Advanced damage imaging techniques have been developed using a phased array and sparse array. Giurgiutiu and Bao [13] investigated the embedded-ultrasonics structural radar (EUSR) for in situ

monitoring of thin-wall structures. Figure 2.3a shows the 1-D phased array EUSR and its imaging result for a crack. Yu and Giurgiutiu [14] further extended the EUSR principle to 2-D phased array using 64 sensors. Wang et al. [15] proposed the synthetic time-reversal imaging method for structural health monitoring. Figure 2.3b shows the sparse array with four sensors and its imaging result using a time-reversal method.

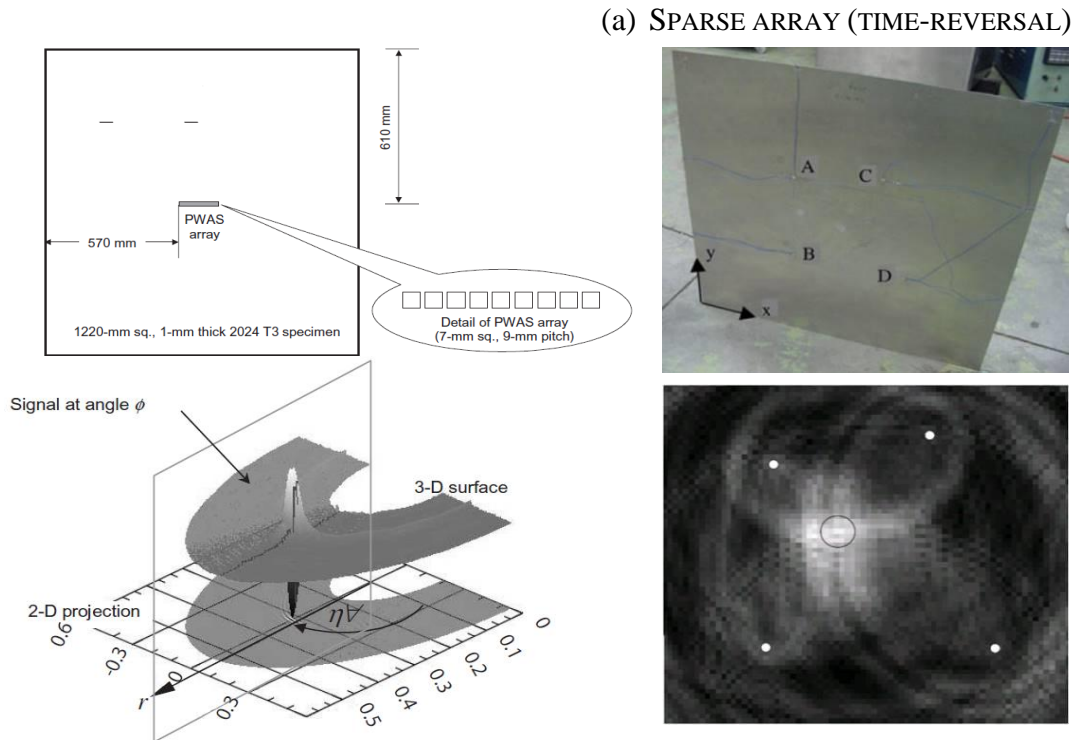


Figure 2.3 (a) Phased array imaging using EUSR [13], (b) sparse array imaging using time-reversal method [15].

In addition to traveling wave techniques, standing guided wave SHM techniques such as EMIS can also be used. The continuous harmonic excitation of a transducer will excite the structure with guided waves, which will be reflected by structural boundaries and damage, forming standing waves between the wave source and the reflectors. This

standing wave formation will result in local mechanical resonance, which will be shown in the electrical response through the electromechanical coupling.

Figure 2.4a shows the electromechanical coupling between the transducer and the structure. Figure 2.4b is a typical EMIS spectrum, showing that the damaged case spectrum deviates from the pristine case.

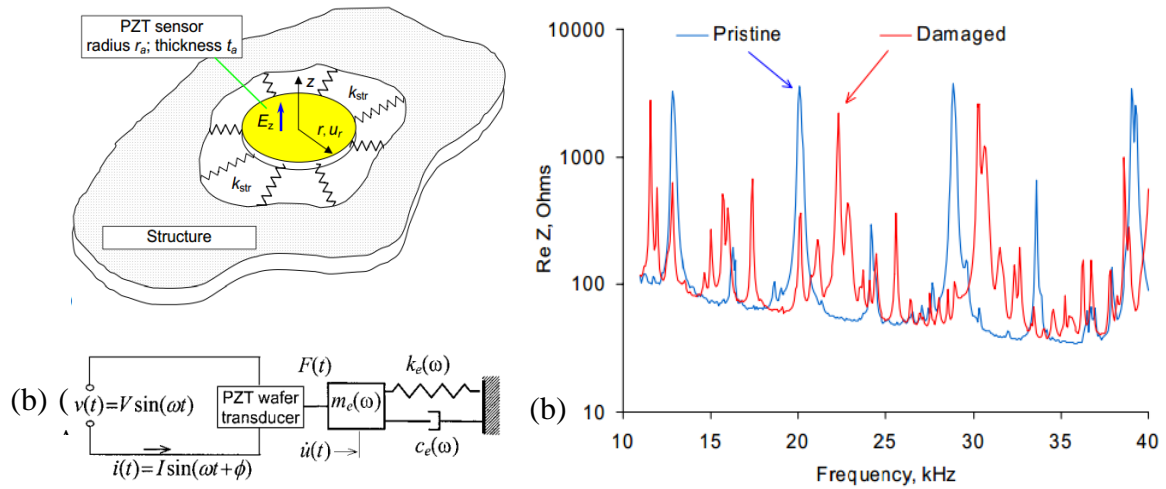


Figure 2.4 (a) Electro-mechanical coupling between the PZT active sensor and the structure [16], (b) EMIS spectrum [17].

2.2 GENERAL THEORY OF ELASTIC WAVES

The fundamentals of guided elastic waves are tied with the elastodynamic relations. The backbone of classical elastodynamics is the equations of motion which can be represented as the Navier-Lame equations for homogeneous linearly isotropic elastic solids [18], i.e.,

$$(\lambda + \mu)\vec{\nabla}(\vec{\nabla} \cdot \vec{u}) + \mu\nabla^2 \vec{u} = \rho\ddot{\vec{u}} \quad (2.1)$$

where \vec{u} is the displacement vector, ρ is the density, λ and μ are the Lamé constants.

2.2.3 WAVE EQUATIONS FOR POTENTIALS

To construct the solutions of Navier-Lame equations, the displacement fields can be considered as the superposition of the gradient of a scalar potential Φ and the curl of the

vector potential \vec{H} . Use the Helmholtz theorem (mentioned originally in ref. [19] and then in its translated version [20]) to write

$$\vec{u} = \text{grad}\Phi + \text{curl}\vec{H} = \vec{\nabla}\Phi + \vec{\nabla} \times \vec{H} \quad (2.2)$$

Substituting Eq. (2.2) into Eq. (2.1) one obtains

$$(\lambda + 2\mu)\nabla^2\Phi - \rho\ddot{\Phi} = 0 \quad (2.3)$$

$$\mu\nabla^2\vec{H} - \rho\ddot{\vec{H}} = 0 \quad (2.4)$$

Assuming harmonic time variation with circular frequency ω and defining

$c_p = \sqrt{(\lambda + 2\mu)/\rho}$, $c_s = \sqrt{\mu/\rho}$, Eq. (2.3) and (2.4) become

$$\nabla^2\Phi + \frac{\omega^2}{c_p^2}\Phi = 0 \quad (\text{scalar wave equation}) \quad (2.5)$$

$$\nabla^2\vec{H} + \frac{\omega^2}{c_s^2}\vec{H} = 0 \quad (\text{vector wave equation}) \quad (2.6)$$

Eq. (2.5) indicates that the scalar potential Φ propagates with the pressure wavespeed c_p , whereas Eq. (2.6) indicates that the vector potential \vec{H} propagates with the shear wavespeed c_s . It can be shown that the pressure waves are irrotational waves i.e., have zero rotation, whereas the shear waves are equivolume waves, i.e., they have zero dilatation and are known as distortional waves [18]. From now on, we call the scalar potential Φ as pressure potential and the vector potential \vec{H} as shear potential.

The pressure waves are also known as *P waves* and shear waves can be divided into *SV waves* and *SH waves* depending on the polarization of the displacement. SV waves have vertically polarized displacement whereas SH waves have horizontally polarized displacement.

2.3 GUIDED WAVES

Under certain assumptions and boundary conditions, the general elastic waves turn into guided waves. Ultrasonic guided waves are sensitive to changes in the propagating medium, such as plastic zone, fatigue zone, cracks, delamination, disbonds, discontinuity. This sensitivity exists for both surface damage and cross thickness/interior damage because guided waves have various mode shapes throughout the cross-section of the waveguides.

The assumption of straight crested wave or axisymmetric circular crested waves make the elastic wave problem to be split into two separate cases, (1) SH waves; and (2) P+SV waves. The P+SV waves in a plate give rise to the Lamb waves through multiple reflections on the plate's lower and upper surfaces and through constructive and destructive interference. The Lamb waves consist of a pattern of standing waves in the thickness direction also known as Lamb wave modes.

2.3.1 SHEAR HORIZONTAL PLATE WAVES

Shear horizontal (SH) plate waves have a shear-type particle motion contained in the horizontal plane. Figure 2.5 shows the coordinate definition and particle motion of SH plate waves. According to the coordinate definition, an SH wave has the particle motion along the z axis, whereas the wave propagation takes place along the x axis. The particle motion has only the u_z component.

The phase velocity dispersion curve of the SH plate wave can be calculated as

$$c(\omega) = \frac{c_s}{\sqrt{1 - (\eta d)^2 \left(\frac{c_s}{\omega d}\right)^2}} \quad (2.7)$$

where η is given in Eq. (2.8) and d is the half plate thickness.

$$\eta^2 = \frac{\omega^2}{c_S^2} - \frac{\omega^2}{c^2} \quad (2.8)$$

By substituting the appropriate eigenvalue, one may obtain an analytical expression for the wave-speed dispersion curve of each SH wave mode. For detailed expressions, the readers are referred to ref. [21].

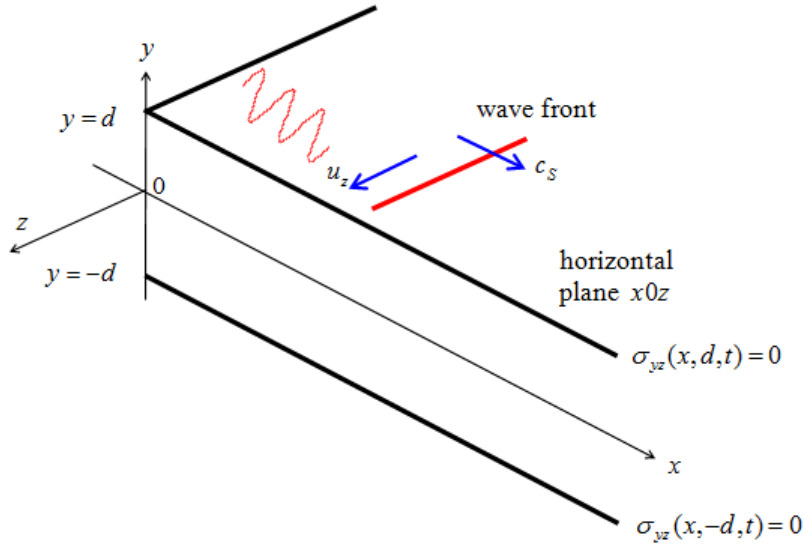


Figure 2.5 Coordinate definition and particle motion of SH plate waves [21].

Figure 2.6 shows the wave-speed dispersion curve of SH plate waves and the mode shapes. It can be noticed that the fundamental symmetric mode (S0) wave is non-dispersive and always exists starting from low frequency-thickness product values. This nice property makes it a good candidate for the interrogating waves in SHM systems. Recently, considerable research has been carried out on the transmission and reception of SH plate wave for SHM [22] [23]. Higher wave modes only appear beyond the corresponding cut-off frequencies, showing dispersive characteristics, i.e., their phase velocity changes with frequency. For dispersive waves, group velocity is usually used to evaluate the propagation of wave packets. The definition of group velocity is given in Eq. (2.9).

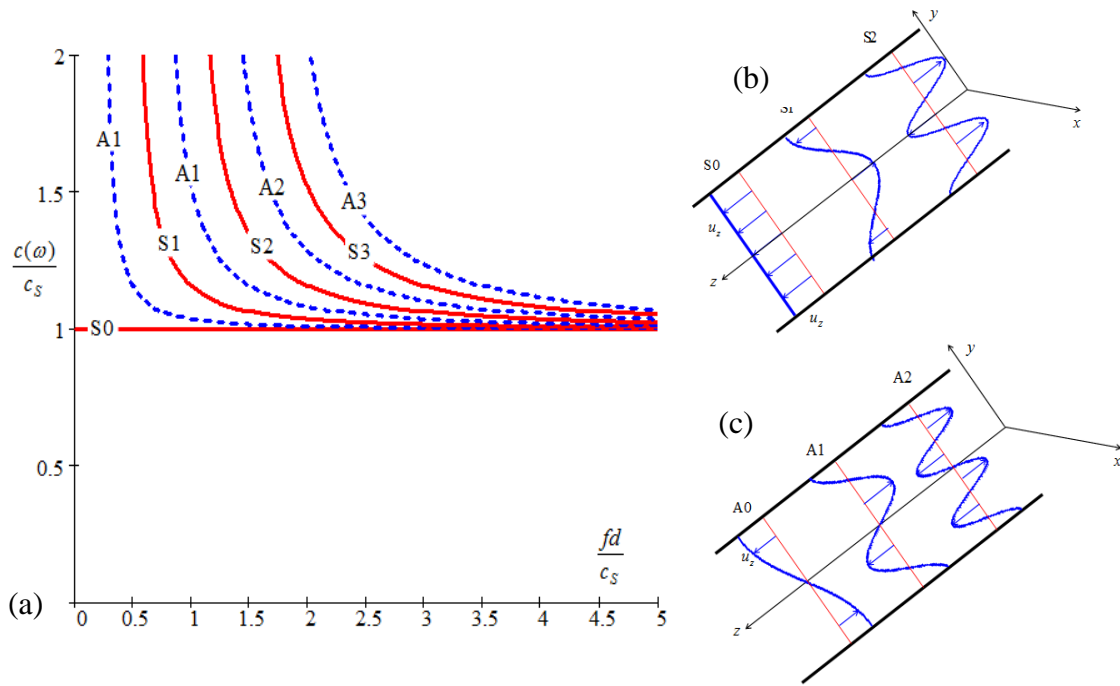


Figure 2.6 (a) SH plate wave-speed dispersion curves, (b) symmetric mode shapes, (c) antisymmetric mode shapes [21].

$$c_g = \frac{d\omega}{d\xi} \tag{2.9}$$

2.3.2 STRAIGHT CRESTED LAMB WAVES

Lamb waves are a type of ultrasonic waves that are guided between two parallel free surfaces, such as the upper and lower surfaces of a plate. Lamb waves can exist in two basic types, symmetric and antisymmetric. Figure 2.7 shows the particle motion of symmetric and antisymmetric Lamb waves. The Lamb wave motion has asymptotic behavior at low frequency and high frequency. At low frequency, the symmetric mode resembles axial waves, while the antisymmetric mode resembles flexural waves. At high frequency, both symmetric and antisymmetric wave approaches Rayleigh waves, because the particle motion is strong at the surfaces and decays rapidly across the thickness. The axial wave and flexural wave, by their nature, are only low-frequency approximations of

Lamb waves. The plate structure cannot sustain pure axial and flexural motion at large frequency-thickness product values.

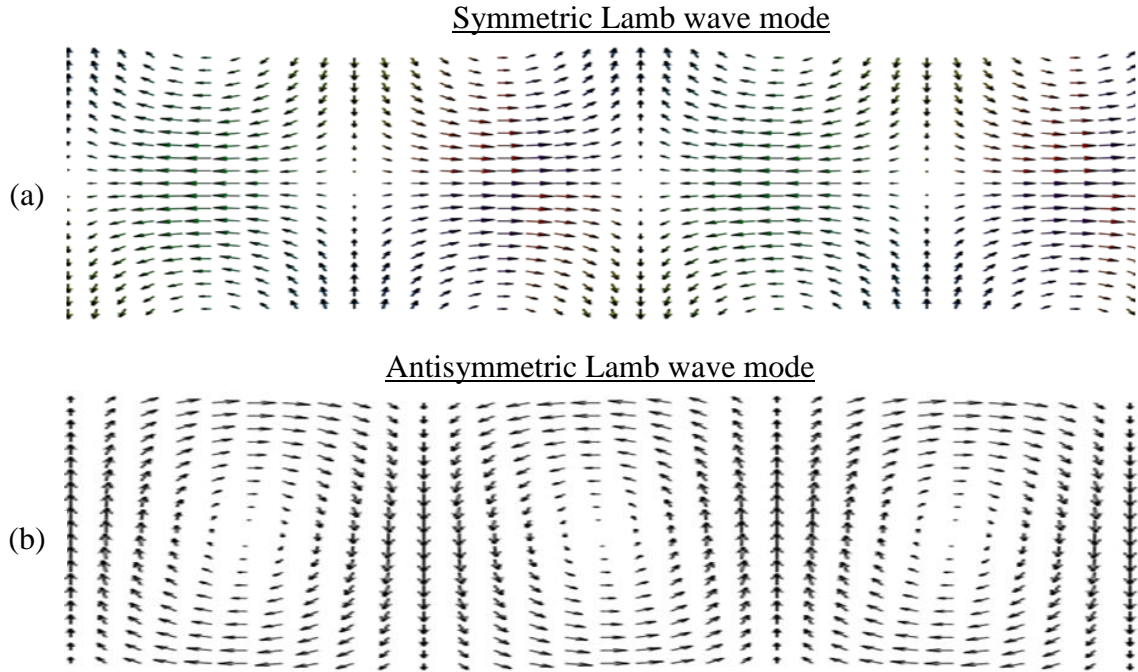


Figure 2.7 Particle motion of Lamb wave modes: (a) symmetric mode and (b) antisymmetric mode [21].

The straight crested Lamb wave equations are derived under z -invariant assumptions using pressure wave and shear vertical wave (P+SV) waves in a plate. Through multiple reflections on the plate's lower and upper surfaces, and through constructive and destructive interference, the pressure waves and shear vertical waves give rise to the Lamb-waves, which consist of a pattern of standing waves in the thickness y -direction (Lamb-wave modes) behaving like traveling waves in the x -direction. For a detailed derivation of Lamb wave equations, readers are referred to ref. [18] [21] [8]. The Rayleigh-Lamb equation has been obtained as characteristic equation of the wavenumbers, i.e.,

$$\frac{\tan \eta_s d}{\tan \eta_p d} = \left[\frac{-4\eta_p \eta_s \xi^2}{(\xi^2 - \eta_s^2)^2} \right]^{\pm 1} \quad (2.10)$$

where +1 exponent corresponds to symmetric Lamb wave modes and -1 exponent corresponds to antisymmetric Lamb wave modes, d is the half plate thickness, ξ is the frequency dependent wavenumber, η_p and η_s are given in Eq. (2.11), λ and μ are Lamé's constants of the material, and ρ is the material density.

$$\eta_p^2 = \frac{\omega^2}{c_p^2} - \xi^2; \quad \eta_s^2 = \frac{\omega^2}{c_s^2} - \xi^2; \quad c_p = \sqrt{\frac{\lambda + 2\mu}{\rho}}; \quad c_s = \sqrt{\frac{\mu}{\rho}}; \quad (2.11)$$

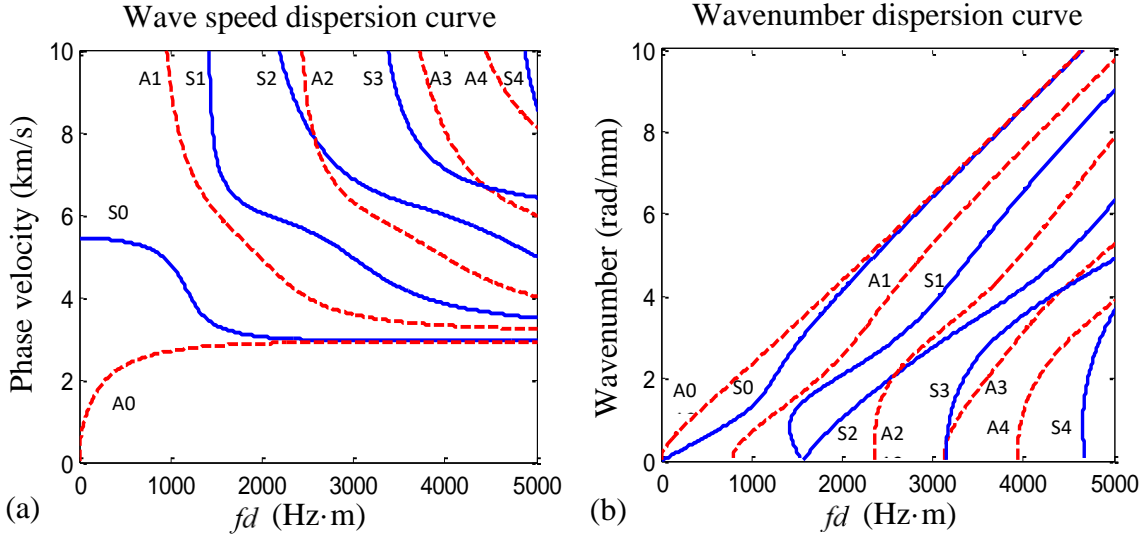


Figure 2.8 (a) Wave speed dispersion curve; (b) wavenumber dispersion curve [11]

Figure 2.8 shows the dispersion curves of aluminum plates calculated from the Rayleigh-Lamb equations. It can be noticed at least two wave modes (the fundamental symmetric mode: S0; the fundamental antisymmetric mode: A0) exist simultaneously. Beyond the corresponding cut-off frequencies, higher Lamb modes will participate in the propagation. At small frequency-thickness product values, the S0 mode is less dispersive

than A0 mode, and all the Lamb wave modes converge to non-dispersive Rayleigh waves at large frequency-thickness product values. The dispersive and multi-mode nature of Lamb waves add complexity in both Lamb wave propagation modeling and SHM application.

In their multi-modal and dispersive nature, Lamb waves also have complicated frequency-dependent mode shapes associated with particle motion across the plate thickness. Even for certain Lamb modes, the mode shape changes under different frequencies. The displacement mode shapes can be calculated using Eq. (2.12) and Eq. (2.13) [21].

For symmetric Lamb modes:

$$\begin{aligned} u_x^S(x, y, t) &= iC^S \left[-2\xi^2 \eta_S \cos \eta_S d \cos \eta_P y + \eta_S (\xi^2 - \eta_S^2) \cos \eta_P d \cos \eta_S y \right] e^{i(\xi x - \omega t)} \\ u_y^S(x, y, t) &= C^S \left[2\xi \eta_P \eta_S \cos \eta_S d \sin \eta_P y + \xi (\xi^2 - \eta_S^2) \cos \eta_P d \sin \eta_S y \right] e^{i(\xi x - \omega t)} \end{aligned} \quad (2.12)$$

For antisymmetric Lamb modes:

$$\begin{aligned} u_x^A(x, y, t) &= iC^A \left[2\xi^2 \eta_S \sin \eta_S d \sin \eta_P y - \eta_S (\xi^2 - \eta_S^2) \sin \eta_P d \sin \eta_S y \right] e^{i(\xi x - \omega t)} \\ u_y^A(x, y, t) &= C^A \left[2\xi \eta_P \eta_S \sin \eta_S d \cos \eta_P y + \xi (\xi^2 - \eta_S^2) \sin \eta_P d \cos \eta_S y \right] e^{i(\xi x - \omega t)} \end{aligned} \quad (2.13)$$

where C^S and C^A determine the mode shape amplitudes; y is the location of interested point across the plate thickness; i is the imaginary number; x coordinate is along the propagation direction.

Figure 2.9 shows the mode shapes of fundamental S0 and A0 Lamb waves in a 2-mm aluminum plate under various frequencies. It can be observed that for certain Lamb mode, the mode shapes vary a lot with frequency. Within low-frequency range, the mode shapes show that S0 and A0 Lamb modes could be approximated by axial and flexural wave motion. However, within high frequency range, the mode shapes become more

complicated and deviate from the axial-flexural approximation. At even higher frequency, e.g. at 10 MHz, the particle motions are mainly near the top and bottom surfaces of the plate, while the particles in the middle of the plate undergo very small oscillation. This shows that at high-frequency range, Lamb modes converge to Rayleigh waves.

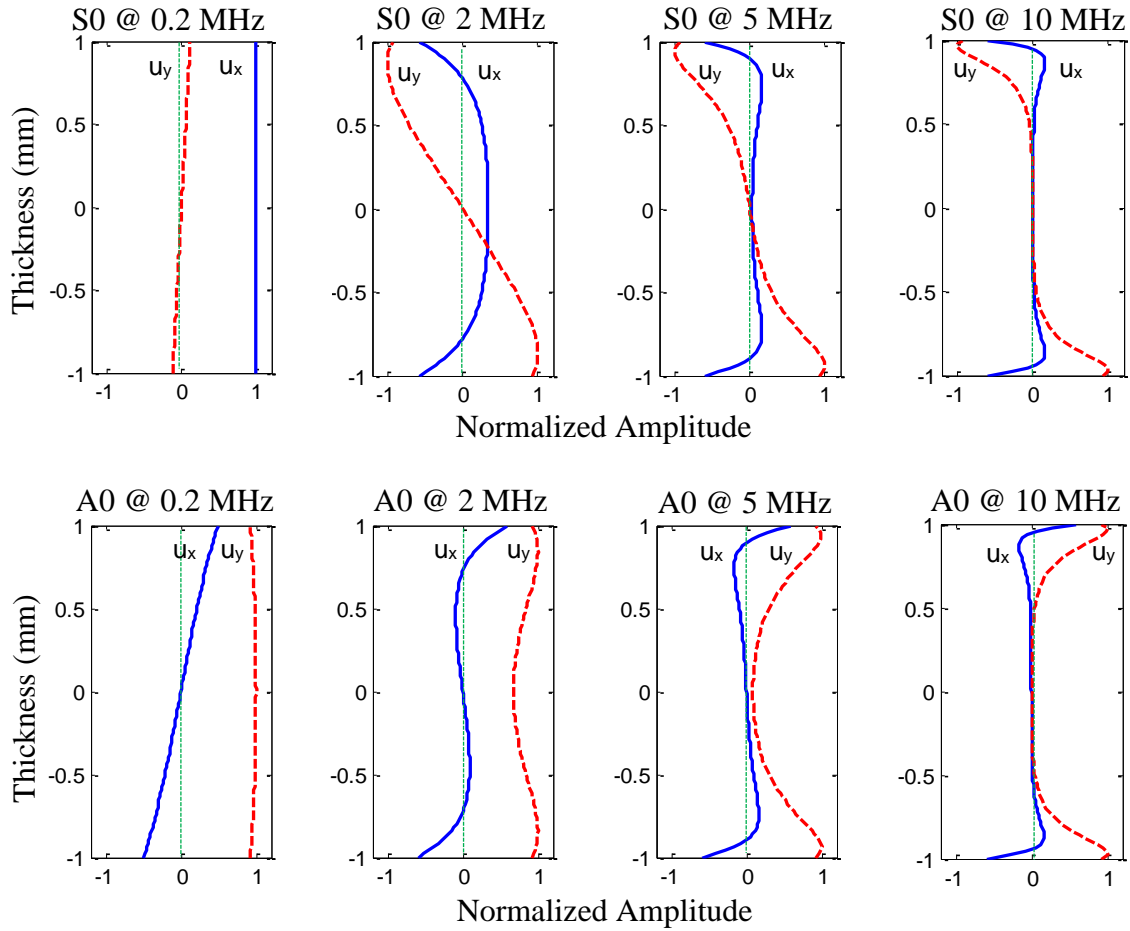


Figure 2.9 Modeshapes of S0 and A0 Lamb waves in a 2-mm thick aluminum plate [11]

2.3.3 CIRCULAR CRESTED LAMB WAVES

In their practical applications, the interrogating Lamb waves generated by a transmitter will propagate out in a circular crested wavefront instead of a straight crested wavefront, because the transmitter can be considered as a point source compared with the large inspection area. As the wave is propagating outward, this amount energy is distributed

over a larger and larger area. Thus, the amplitude of the interrogating wave is strong near the wave source and decays along the propagation direction. The circular crested Lamb wave solution can capture these effects due to outward propagation pattern.

A detailed and rigorous derivation of axisymmetric circular crested Lamb waves is well documented in [21]. The derivation of circular crested Lamb waves is found to be more appropriate in a cylindrical coordinate system shown in Figure 2.10a. The derivation arrives at the same Rayleigh-Lamb equation as Eq. (2.10), which means the circular crested Lamb waves propagate with the same wave speed as the straight crested Lamb waves.

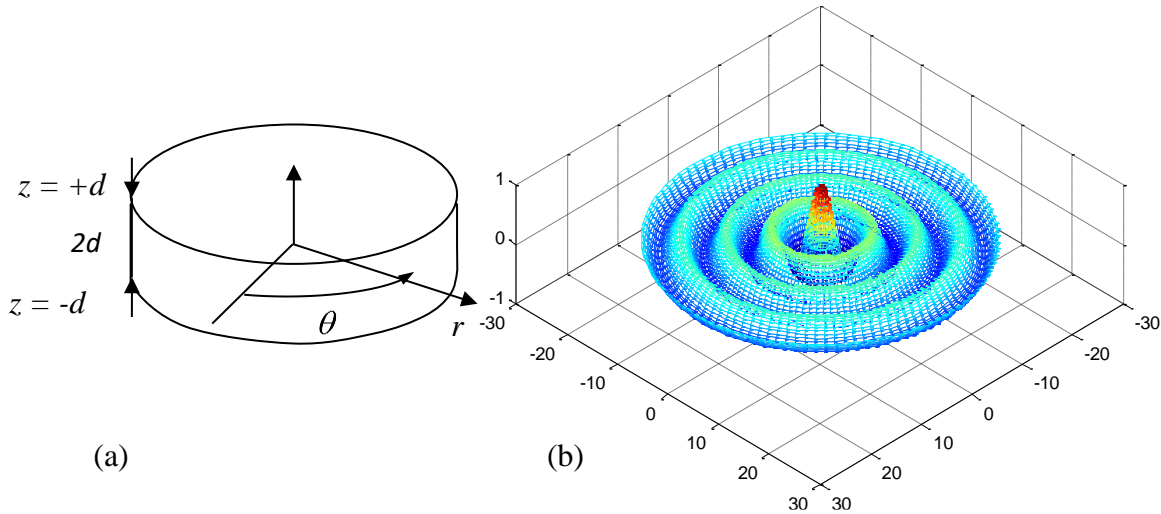


Figure 2.10 (a) Cylindrical coordinate for problem derivation [21]; (b) circular crested wave pattern.

The propagation pattern of circular Lamb waves admits the Bessel and Hankel function family solution. The Bessel functions J_0 and J_1 is appropriate for standing waves, and the Hankel functions $H_0^{(1)}$ and $H_1^{(1)}$ are appropriate for propagating waves. The Hankel functions of the first kind ($H_0^{(1)}$ and $H_1^{(1)}$) describe an outward propagating wavefield when $e^{-i\omega t}$ is chosen as the convention for harmonic time variation. The Hankel functions of the

second kind ($H_0^{(2)}$ and $H_1^{(2)}$) describe an outward propagating wavefield when $e^{i\omega t}$ is chosen as the convention. The mode shape solutions for the circular crested Lamb waves are given below for outward propagating wave fields.

Symmetric Lamb modes:

$$\begin{aligned} u_r^S(r, z, t) &= C^S \left[2\xi^2 \zeta_S \cos \zeta_S d \cos \zeta_P z - \zeta_S (\xi^2 - \zeta_S^2) \cos \zeta_P d \cos \zeta_S z \right] H_1^{(1)}(\xi r) e^{-i\omega t} \\ u_z^S(r, z, t) &= C^S \xi \left[2\zeta_P \zeta_S \cos \zeta_S d \sin \zeta_P z + (\xi^2 - \zeta_S^2) \cos \zeta_P d \sin \zeta_S z \right] H_0^{(1)}(\xi r) e^{-i\omega t} \end{aligned} \quad (2.14)$$

Antisymmetric Lamb modes:

$$\begin{aligned} u_r^A(r, z, t) &= -C^A \zeta_S \left[2\xi^2 \sin \zeta_S d \sin \zeta_P z - (\xi^2 - \zeta_S^2) \sin \zeta_P d \sin \zeta_S z \right] H_1^{(1)}(\xi r) e^{-i\omega t} \\ u_z^A(r, z, t) &= C^A \xi \left[2\zeta_P \zeta_S \sin \zeta_S d \cos \zeta_P z + (\xi^2 - \zeta_S^2) \sin \zeta_P d \cos \zeta_S z \right] H_0^{(1)}(\xi r) e^{-i\omega t} \end{aligned} \quad (2.15)$$

where C^S and C^A are the amplitude factor for symmetric mode and antisymmetric mode, and can be determined from the wave generation calculation. The constants ζ_P, ζ_S are defined as

$$\zeta_P^2 = \frac{\omega^2}{c_P^2} - \xi^2; \quad \zeta_S^2 = \frac{\omega^2}{c_S^2} - \xi^2 \quad (2.16)$$

It can be observed from Eq. (2.14) and Eq. (2.15) that the in-plane radial direction motion accepts as solution the Hankel function of the first kind and order one $H_1^{(1)}$, while the out-of-plane direction motion accepts as solution the Hankel function of the first kind and order zero $H_0^{(1)}$. Figure 2.10b shows a typical outward propagation wave pattern calculated using Hankel function $H_0^{(1)}$ describing an out-of-plane wave motion. It can be noticed that the wave amplitude at the wave source (coordinate center) is strong, and it decays as it propagates out. Figure 2.11 shows the plots of Hankel functions of order zero and order

one. It can be noticed that the amplitude is high near the origin of R , and beyond a certain distance, the amplitude becomes stable and changes more gradually.

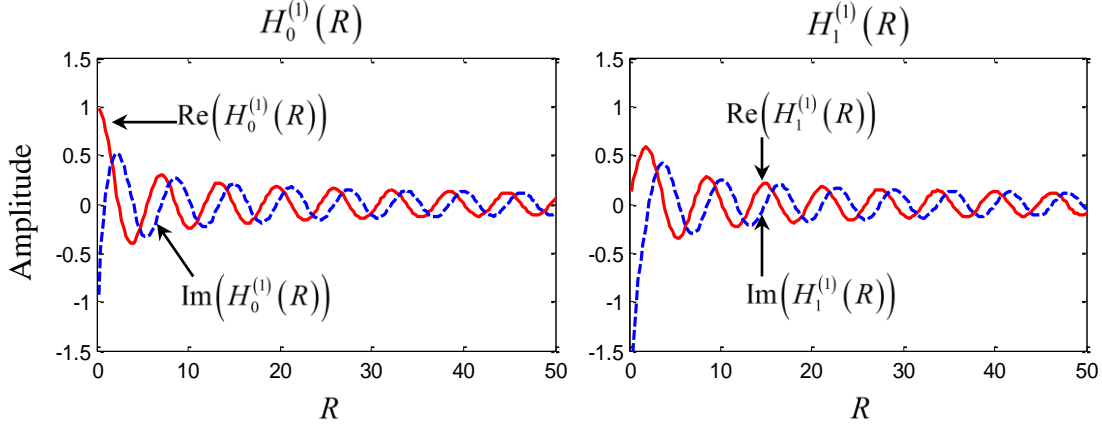


Figure 2.11 Hankel function of order zero, $H_0^{(1)}(R)$ and order one, $H_1^{(1)}(R)$.

Lamb wave field radiating from a point source takes the following solution [21][24]:

$$u_r = \sum_{n=1}^{\infty} a_n(z) H_1^{(1)}(\xi_n r) e^{-i\omega t} \quad (2.17)$$

where u_r is the radial displacement, $a_n(z)$ is the thickness dependent modeshape of wave mode number n , and $H_1^{(1)}$ is the first kind Hankel function of order one.

2.3.4 CIRCULAR CRESTED SH WAVES

Shear horizontal (SH) waves irradiating from a point source can be derived starting from the governing equation, i.e.,

$$\nabla^2 u_\theta - \frac{u_\theta}{r^2} = \frac{1}{c_s^2} \frac{\partial^2 u_\theta}{\partial t^2} \quad (2.18)$$

where u_θ is the tangential displacement, c_s is the shear wavespeed. In polar coordinate system and under axisymmetric assumption, Eq. (2.18) becomes

$$\frac{\partial^2 u_\theta}{\partial r^2} + \frac{1}{r} \frac{\partial u_\theta}{\partial r} - \frac{u_\theta}{r^2} = \frac{1}{c_s^2} \frac{\partial^2 u_\theta}{\partial t^2} \quad (2.19)$$

Assuming a harmonic wave field

$$u_\theta = U e^{-i\omega t}; \quad \frac{\partial^2 u_\theta}{\partial t^2} = -\omega^2 u_\theta \quad (2.20)$$

Substitution of Eq. (2.20) into Eq. (2.19) yields

$$\left(\xi^{SH} r\right)^2 \frac{\partial^2 u_\theta}{\partial \left(\xi^{SH} r\right)^2} + \left(\xi^{SH} r\right) \frac{\partial u_\theta}{\partial \left(\xi^{SH} r\right)} + \left(\left(\xi^{SH} r\right)^2 - 1\right) u_\theta = 0 \quad (2.21)$$

where $\xi^{SH} = \omega / c_s$ is the wavenumber of SH waves. Letting $x = \xi^{SH} r$, $y = u_\theta$, and $\nu = 1$,

Eq. (2.21) can be cast into the Bessel equation of order ν .

$$x^2 \frac{d^2 y}{dx^2} + x \frac{dy}{dx} + (x^2 - \nu^2) y = 0 \quad (2.22)$$

Eq. (2.21) can be immediately recognized as the Bessel equation of order one and accepts the following solution for outward propagating waves,

$$u_\theta = \sum_{n=1}^{\infty} b_n(z) H_1^{(1)}\left(\xi_n^{SH} r\right) e^{-i\omega t} \quad (2.23)$$

where $b_n(z)$ is the modeshape of the n^{th} SH mode, and $H_1^{(1)}$ is the first kind Hankel function of order one.

2.4 PIEZOELECTRIC WAFER ACTIVE SENSORS

Piezoelectric wafer active sensors (PWAS) are small, lightweight, inexpensive, and can be produced in different geometries. They are convenient enablers for generating and receiving guided waves. A PWAS mounted on the structure is shown in Figure 2.12.

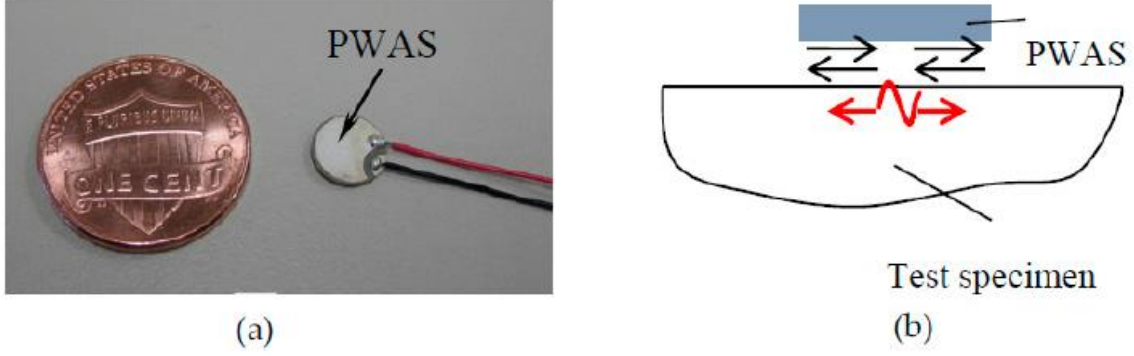


Figure 2.12 (a) Piezoelectric wafer active sensors (PWAS), (b) PWAS measures in-plane and out-of-plane wave motion through in-plane strain sensing.

PWAS transducers can be permanently bonded on host structures in large quantities and achieve real-time monitoring of the structural health status. They couple with the structure through in-plane motion and generate Lamb waves, which makes them suitable for inspection large areas of interest.

2.4.1 PWAS PRINCIPLES AND OPERATION MODES

PWAS transducers couple the electrical and mechanical effects (mechanical strain, S_{ij} , mechanical stress, T_{kl} , electrical field, E_k , and electrical displacement, D_j). The piezoelectric constitutive equations in tensor notations can be written as

$$\begin{aligned} S_{ij} &= s_{ijkl}^E T_{kl} + d_{kij} E_k \\ D_j &= d_{klj} T_{kl} + \varepsilon_{jk}^T E_k \end{aligned} \quad (2.24)$$

where s_{ijkl}^E is the mechanical compliance of the material measured at zero electric field ($E = 0$), ε_{jk}^T is the dielectric permittivity measured at zero mechanical stress ($T = 0$), and d_{klj} represents the piezoelectric coupling effect. PWAS utilize the d_{31} coupling between in-plane strains, S_1, S_2 and transverse electric field E_3 .

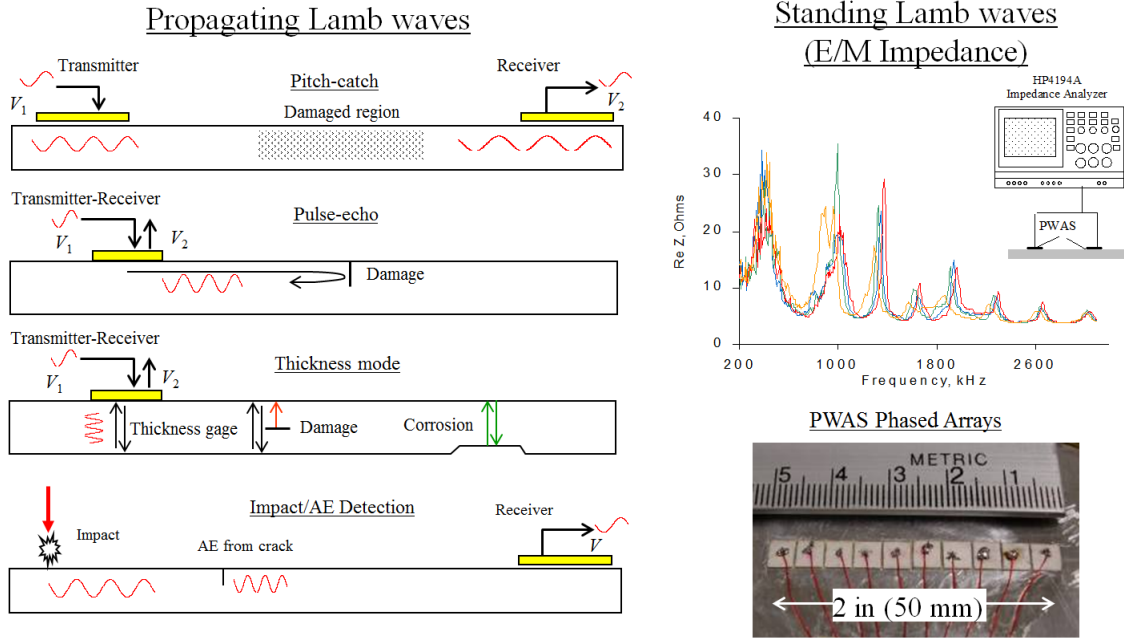


Figure 2.13 Schematic of PWAS application modes [21].

PWAS transducers can be used as both transmitters and receivers. Their modes of operation are shown Figure 2.13. PWAS can serve several purposes [21]: (a) high-bandwidth strain sensors; (b) high-bandwidth wave exciters and receivers; (c) resonators; (d) embedded modal sensors with the electromechanical (E/M) impedance method. By application types, PWAS transducers can be used for (i) active sensing of far-field damage using pulse-echo, pitch-catch, and phased-array methods, (ii) active sensing of near-field damage using high-frequency E/M impedance method and thickness gage mode, and (iii) passive sensing of damage-generating events through detection of low-velocity impacts and acoustic emission at the tip of advancing cracks (Figure 2.13). The main advantage of PWAS over conventional ultrasonic probes is in their lightweight, low profile, and low cost. In spite of their small size, PWAS are able to replicate many of the functions performed by conventional ultrasonic probes.

2.4.2 PWAS COUPLED GUIDED WAVES AND TUNING EFFECT

Figure 2.14 shows the coupling between PWAS and the host structure and illustrates how PWAS transducers generate Lamb waves. When an oscillatory electric voltage at ultrasonic frequencies is applied to PWAS, an oscillatory strain is induced in the transducer due to the piezoelectric effect. Since the structure constrains the motion of PWAS, the reacting force from the bonding layer will act as shear stress on the host structure and generate wave motion.

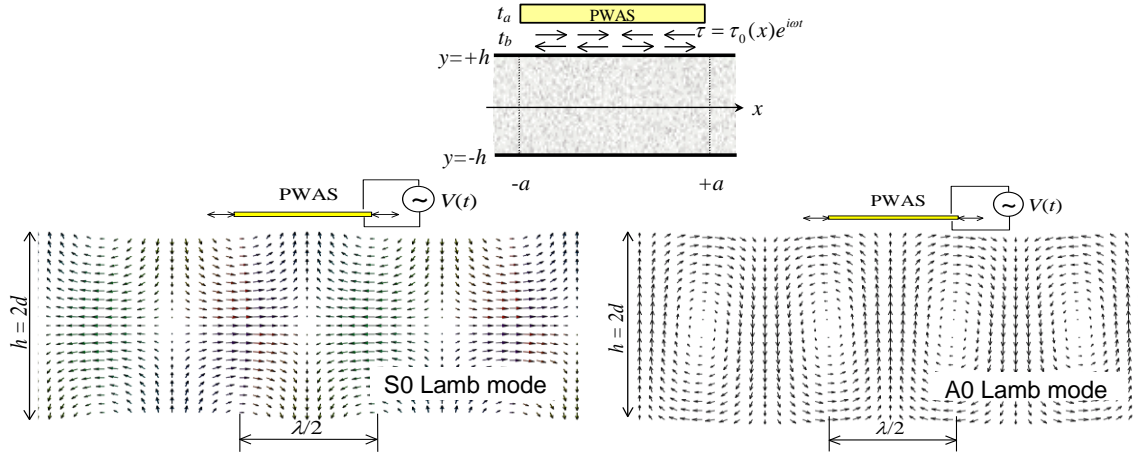


Figure 2.14 Lamb wave generation using PWAS transducers [21]

The Lamb wave amplitude excited by PWAS depends on the PWAS size, plate thickness, and excitation frequency. For a given PWAS and plate geometry, the amplitudes of Lamb modes change with frequency. It was found that tuning possibility exists for generating single Lamb mode with PWAS transducers. The tuning effect is important because it overcomes the multimode difficulty for Lamb wave applications. The analytical expression on tuning effect was first developed by Giurgiutiu [25] as

$$\varepsilon_x(x, t) = -i \frac{a\tau_0}{\mu} \left\{ \sum_{\xi^S} (\sin \xi^S a) \frac{N_S(\xi^S)}{D_S'(\xi^S)} e^{-i(\xi^S x - \omega t)} + \sum_{\xi^A} (\sin \xi^A a) \frac{N_A(\xi^A)}{D_A'(\xi^A)} e^{-i(\xi^A x - \omega t)} \right\} \quad (2.25)$$

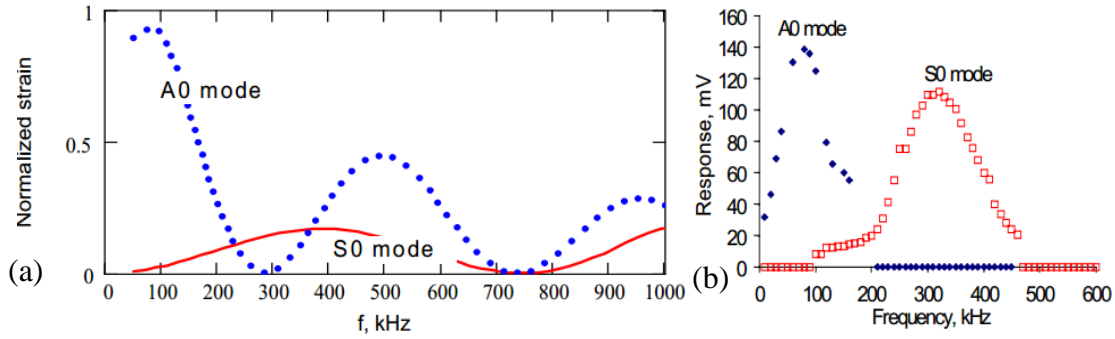


Figure 2.15 (a) Strain Lamb wave tuning results from analytical solution (1.6-mm aluminum plate), (b) Experimental results from PWAS response [25].

A typical tuning curve for 7 mm PWAS on a 1.6 mm thick aluminum plate is shown in Figure 2.15. It is apparent that the amplitudes of S0 and A0 Lamb modes excited by the PWAS transducer change with frequency. Around 300 kHz, A0 Lamb mode reaches the rejection point where no A0 mode Lamb wave will be excited. This is a sweet spot for generating only S0 wave mode for structural inspection.

2.5 ACOUSTIC EMISSION SENSORS AND THEIR FREQUENCY RESPONSES

The acoustic emission (AE) is a passive SHM technique. It is also used for structural integrity testing, diagnosis, and prognosis. For AE measurements, commercially available AE sensors exist. For example, R15I-AST, R15 α , R15, WS α , and conical AE sensors from Physical Acoustics Corporation (PAC) Mistras. The PWAS upon some customization may be used as AE sensor. The pictorial representation of these sensors is shown in Figure 2.16. A 7-mm diameter PWAS is shown in the picture for size comparison.



Figure 2.16 R15I-AST, R15 α , R15, and WS α AE sensors from Physical Acoustics Corporation (PAC) Mistras; PWAS that has been customized in our lab.

The miniature-sized AE sensors are also commercially available. A pictorial representation of miniature-sized AE sensors is shown in Figure 2.19. Three miniature AE sensors are nano-30, PICO, and S9225 from the PAC Mistras. A 7-mm diameter PWAS is also shown in the picture for size comparison.

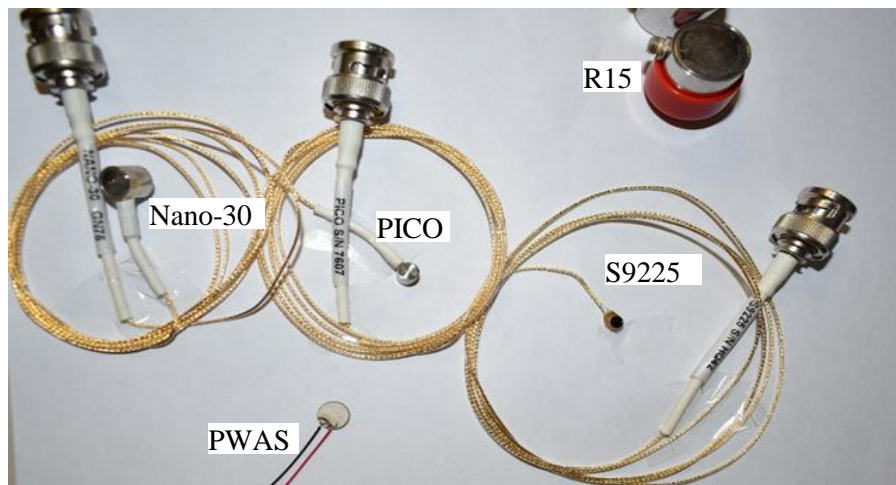


Figure 2.17 Nano-30, PICO, S9225 and R15 AE sensors from Physical Acoustics Corporation (PAC) Mistras; PWAS that has been customized in our lab.

Table 2.1 Dimensions and masses of the sensors

Sensor name	Dimension		Mass (g)
	Diameter (mm)	Height (mm)	
R15I-AST	28.5	31.7	68
R15 α	19	22.4	35
WS α	19	21.3	29
R15	17.5	16.8	20
Nano	8	7	3
PICO	4.75	4	0.5
S9225	3.5	2.4	0.3
PWAS	7	0.5	0.15

The dimension and masses of the sensors are given in Table 2.1. In this table, R15I-AST is bigger and heavyweight sensor and PWAS is the lightest sensor. Knowing the frequency response for any sensor is very important to determine the applicability of the sensor. The frequency response curves of R15I-AST, WS α , and R15 α are shown in Figure 2.18. These response curves were generated following ASTM 976 standards- “determining the reproducibility of acoustic emission sensor response”. The frequency response curves of miniature AE sensors (nano-30, PICO, and S9225) are shown in Figure 2.19. These response curves were obtained from the PAC Mistras.

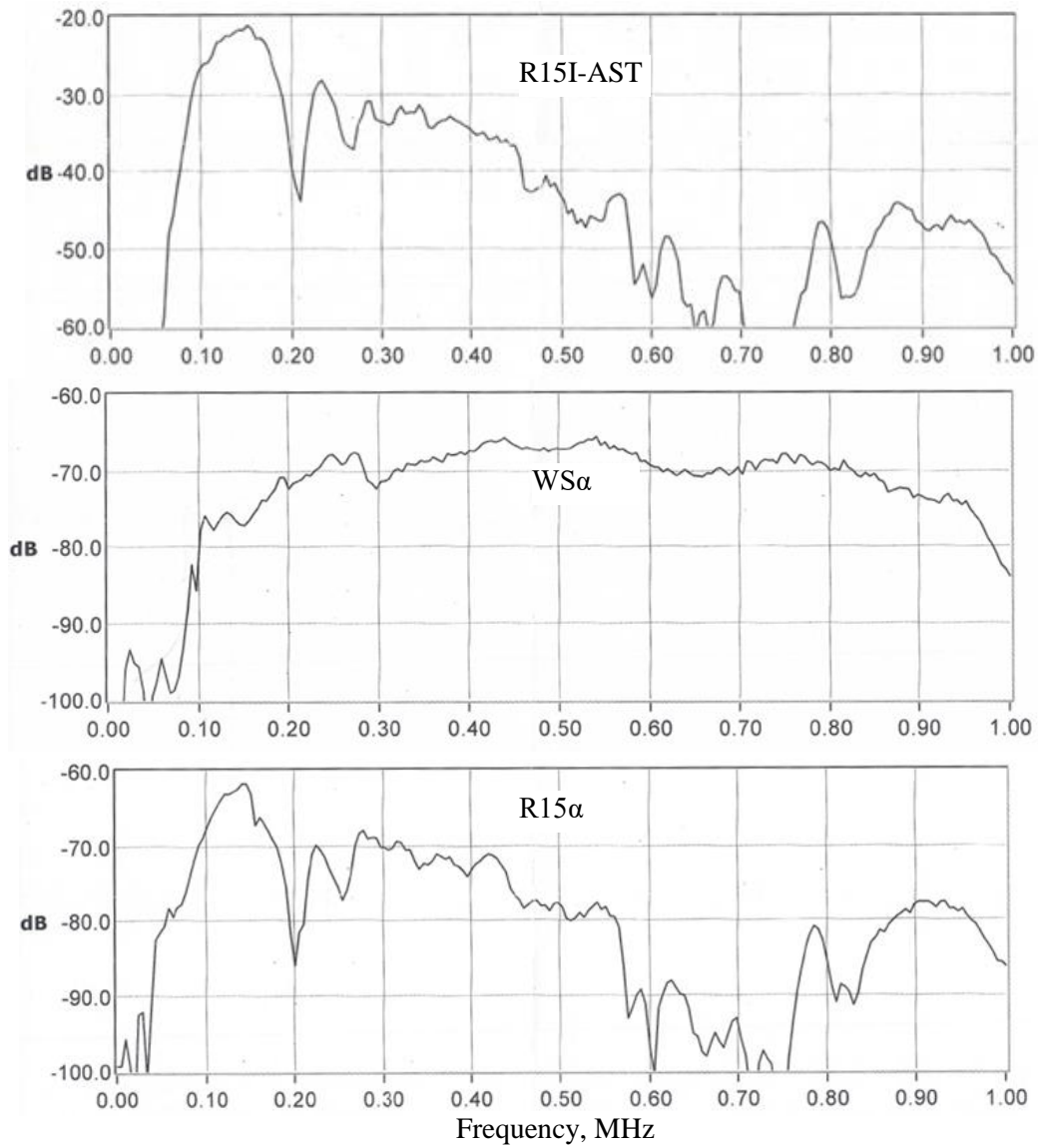


Figure 2.18 Frequency response curves of R15I-AST, WS α , and R15 α (obtained from PAC-Mistras).

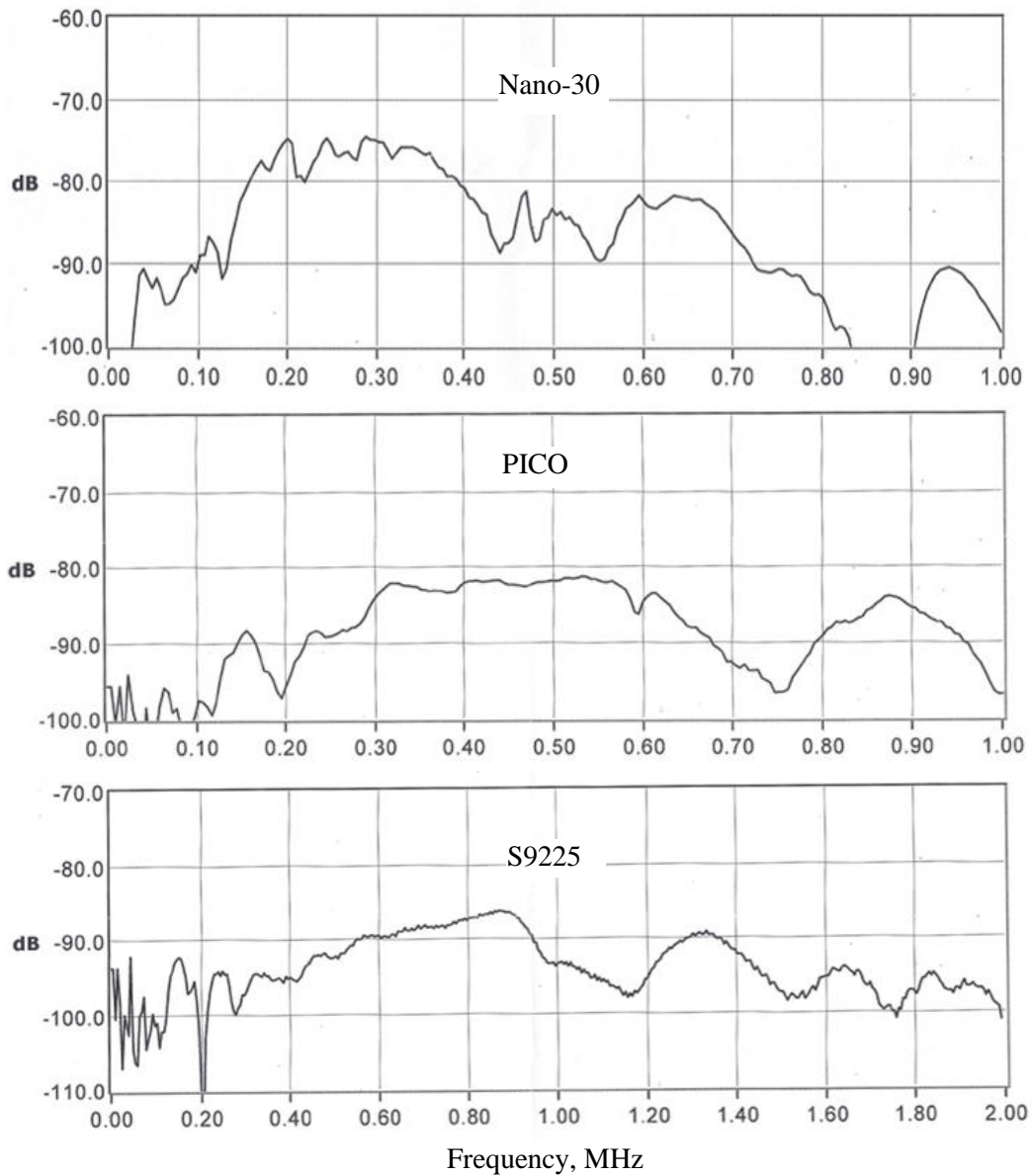


Figure 2.19 Frequency response curves of Nano-30, PICO, and S9225 (obtained from PAC-Mistras).

2.6 AE SENSOR CONSTRUCTION AND SENSING MECHANISM

The cross-section of a commercially available AE sensor is shown in Figure 2.20. It has several components inside a steel housing. It has a backing plate, PZT material, electrodes, and damping material inside the housing. The top electrode of PZT material is

connected to the center conductor of the connector and the bottom electrode is grounded to the housing.

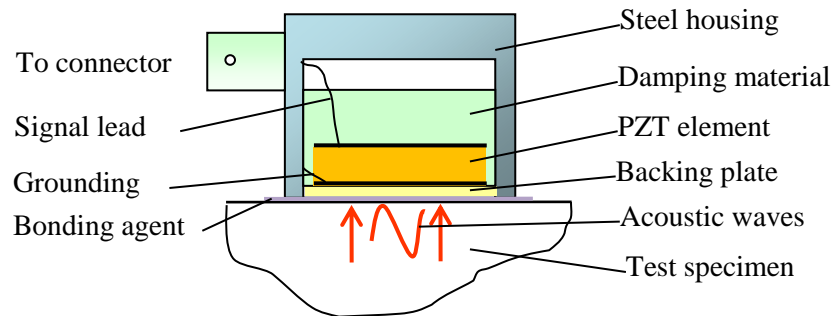


Figure 2.20 Cross-section of a typical commercial AE sensor. It measures out-of-plane wave motion.

In general, the AE sensors can be classified into “resonant” type and “wideband”. For example, R15I-AST, R15 α , and R15 are resonant type AE sensors and WS α , PICO, S9225 are wideband AE sensor. In both types, the sensing mechanism mainly depends on the piezoelectric effect of the PZT material. In resonant type AE sensor, when the AE waves strike the sensor surface, the PZT element oscillates at its resonant frequencies. The resonant frequency is, of course, modified by the associated damping material, backing plate and housing. Thus, proper calibration is necessary to find the exact resonant frequency. In other words, this type of sensor is mostly sensitive at the resonant frequency and not suitable for other frequencies. Thus, the resonance frequency is the decisive factor for which application these AE sensors can be used. These sensors are usually used if the frequency content itself is not of interest but only AE features such as amplitude, rise time, number of counts, arrival time or energy.

Wideband AE sensors respond uniformly to a very wide range of excitation frequencies. Wideband AE-sensors with a flat frequency response curve are usually desired

if the frequency of interest is unknown or if different frequencies in one signal need to be analyzed. However, in practice, it is difficult to achieve a sensor with flat frequency response. Finding the right sensor for a specific application has to consider factors such as frequency range, material, specimen thickness, nature of damage, and background noise. The correct frequency range for a certain application can be determined experimentally where possible.

CHAPTER 3

USING THE GAUGE CONDITION TO SIMPLIFY THE ELASTODYNAMIC ANALYSIS OF GUIDED WAVE PROPAGATION

In this chapter, the gauge condition in elastodynamics is explored to expose its potential capability of simplifying wave propagation problems in elastic medium. The inception of gauge condition in elastodynamics happens from the Navier-Lame equations upon application of Helmholtz theorem. In order to solve the elastic wave problems by potential function approach, the gauge condition provides the necessary conditions for the potential functions. The gauge condition may be considered as the superposition of the separate gauge conditions of Lamb waves and SH waves respectively, and thus, it may be resolved into corresponding gauges of Lamb waves and SH waves. The manipulation and proper choice of the gauge condition do not violate the classical solutions of elastic waves in plates; rather, it simplifies the problems [26]. The gauge condition allows one to obtain the analytical solution of complicated problems in a simplified manner.

3.1 STATE OF THE ART

Wave propagation in the elastic medium has a rich history. Pochhammer [27] in 1876 and Chree [28] in 1889 independently formulated the solution of the wave propagation in an isotropic infinitely long rod and the Pochhammer-Chree frequency equation was developed based on the exact theory of elasticity. The straight-crested guided-wave propagation in a plate (plane-strain condition) was considered in 1889 by Rayleigh

[29] and Lamb [30]. The resulting characteristic equation, the Rayleigh-Lamb equation [8], has the form

$$\frac{\tan \eta_p d}{\tan \eta_s d} = - \left[\frac{(\xi^2 - \eta_s^2)^2}{4\xi^2 \eta_p \eta_s} \right]^{\pm 1} \quad (3.1)$$

where ξ is the wavenumber, d is plate half-thickness, η_p and η_s are related to the pressure and shear wavenumbers, respectively. The solutions of Eq. (3.1) yield the propagating modes of these axial-flexural multi-modal guided waves.

The approach taken by Lamb [30] was to use the Helmholtz vector decomposition in terms of potentials. Since the problem was plane-strain, the axial-flexural multi-modal guided waves (now known as ‘Lamb waves’) were intrinsically decoupled from the multi-modal shear horizontal (SH) waves. Goodman [9] extended this approach to circular-crested Lamb waves (which, due to the implied axisymmetry, are also decoupled from the SH waves) and recovered the Rayleigh-Lamb equation (3.1).

Graff [18] (pp. 442-446) presented the simultaneously handling of the z-invariant Lamb and SH waves using all the four unknown potentials Φ, H_x, H_y, H_z . To obtain a solution, he used the gauge condition evaluated as an additional ‘boundary condition’ at the top and bottom faces of the plate. However, this work was limited to straight-crested plane-strain waves in which Lamb and SH waves were intrinsically decoupled.

3.2 INTRODUCTION

In elastodynamics, the equations of motion for homogeneous isotropic linearly elastic solids are represented by the Navier-Lame equations, in vector form,

$$(\lambda + \mu)\vec{\nabla}(\vec{\nabla} \cdot \vec{u}) + \mu\nabla^2 \vec{u} = \rho\ddot{\vec{u}} \quad (3.2)$$

where, \vec{u} is the displacement vector, ρ is the density, λ and μ are the Lamé constants. To construct the solutions of Navier-Lamé equations, the displacement fields can be considered as the superposition of the gradient of scalar potential Φ and the curl of the vector potential \vec{H} . Use the Helmholtz theorem (mentioned originally in ref. [19] and then in its translated version [20]) to write

$$\vec{u} = \text{grad}\Phi + \text{curl}\vec{H} = \vec{\nabla}\Phi + \vec{\nabla} \times \vec{H} \quad (3.3)$$

The potentials Φ and \vec{H} satisfy the wave equation, i.e.,

$$c_p^2 \nabla^2 \Phi = \ddot{\Phi}; \quad c_s^2 \nabla^2 \vec{H} = \ddot{\vec{H}} \quad (3.4)$$

where, c_p and c_s are the pressure and shear wavespeeds, respectively.

It can be noted from Eq.(3.3), in three dimensions, the three components of displacement are represented by four components of potentials Φ, H_x, H_y, H_z . Thus, an additional unknown exists. In order to ensure the uniqueness of the solution, Eq. (3.3) is complemented by the gauge condition [19], i.e.,

$$\vec{\nabla} \cdot \vec{H} = f(r, t) \quad (3.5)$$

The gauge condition is needed to mitigate the requirement of the additional unknown in the potential formulation. However, the formula given in Eq.(3.5) is not the only possible form of the gauge condition; in fact, a multitude of alternative forms exist [31] as used in elastodynamics [32] [18] (pg. 465), and electrodynamics [33] [34] [35].

3.2.1 GENERAL GUIDED WAVE SOLUTION IN TERMS OF POTENTIALS

Meeker and Meitzler [36] developed the general solution for y -invariant straight-crested guided waves (Figure 3.1) using the Helmholtz potentials

$$\Phi = (A \cos \alpha z + B \sin \alpha z) e^{i(\xi x - \omega t)} \quad (3.6)$$

$$H_x = (C \cos \beta z + D \sin \beta z)e^{i(\xi x - \omega t)} \quad (3.7)$$

$$H_y = (E \cos \beta z + F \sin \beta z)e^{i(\xi x - \omega t)} \quad (3.8)$$

$$H_z = (G \cos \beta z + H \sin \beta z)e^{i(\xi x - \omega t)} \quad (3.9)$$

and the gauge condition

$$\vec{\nabla} \cdot \vec{H} = \frac{\partial H_x}{\partial x} + \frac{\partial H_z}{\partial z} = 0 \quad (3.10)$$

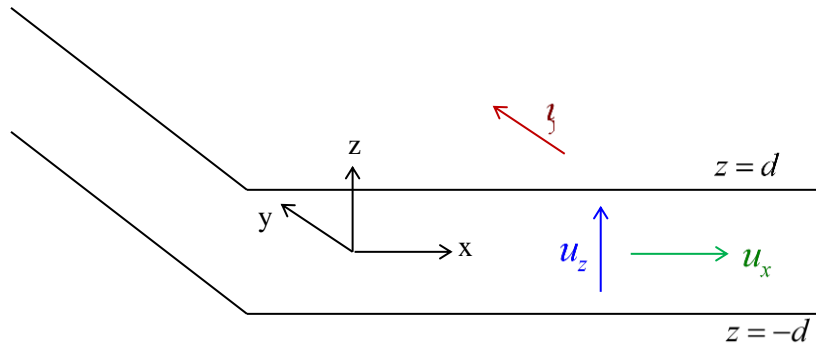


Figure 3.1 Problem definition and displacement components in Cartesian coordinate system

The constants A, B, C, D, E, F, G, H are eight unknowns to be determined from the six traction free boundary conditions on the top and bottom boundaries of the plate. Because the number of unknowns is greater than the number of conditions ($8 > 6$), the gauge condition Eq. (3.10) is used to produce two additional conditions. In ref. [36], this is done by evaluating the gauge condition at the top and bottom surfaces of the plate.

In order to produce the required additional equations, Graff [18] suggested to substitute the complex-valued H_x, H_z into equation Eq. (3.10) and to separate them into real and imaginary parts to produce four equations with four unknowns. However, the traction-free boundary condition equations were not separated into real and imaginary parts.

This complication may explain why the solution of SH waves is usually expressed in terms of displacement although the Lamb waves are elegantly solved using potentials functions [18] [8] [21]. Thus, the gauge condition seems to remain a redundant condition in these classical solutions.

3.2.2 GENERAL SOLUTION IN TERMS OF DISPLACEMENTS

Alternatively, Achenbach [37] [38] proposed a guided wave solution using an ingenious definition of the displacements that utilizes the solution of membrane wave equation, i.e.,

$$\begin{aligned}
 u_x^n &= \frac{1}{k_n} V^n(z) \frac{\partial \varphi}{\partial x}(x, y) \\
 u_y^n &= \frac{1}{k_n} V^n(z) \frac{\partial \varphi}{\partial y}(x, y) \quad (\text{Lamb wave}) \\
 u_z^n &= W^n(z) \varphi(x, y)
 \end{aligned} \tag{3.11}$$

$$\begin{aligned}
 u_x^n &= \frac{1}{l_n} U^n(z) \frac{\partial \psi}{\partial y}(x, y) \\
 u_y^n &= -\frac{1}{l_n} U^n(z) \frac{\partial \psi}{\partial x}(x, y) \quad (\text{SH wave}) \\
 u_z^n &= 0
 \end{aligned} \tag{3.12}$$

where, k and l are wavenumber-like quantities, n is the mode number and the functions φ , ψ satisfies the membrane wave equation. (The details can be found in ref. [37] [38])

However, this approach does not involve the wave equation since the displacement satisfies the Navier-Lame equation but not the wave equation.

3.2.3 THE SCOPE OF THIS CHAPTER

In this chapter, we propose a unified potential-based solution to the guided wave propagation that is simpler (and has fewer unknowns) than that of ref. [32] [18] [36]. We will show that it is possible to reduce the eight unknowns of Eqs. (3.6)-(3.9) to only six

unknowns by the proper utilization and manipulation of the gauge condition and thus, produce a much simpler solution of the guided wave propagation problem.

The origin of the gauge condition in elastodynamics is discussed in Section 3.3; it will be shown that the gauge condition can be chosen arbitrarily within certain limits. The different forms of the gauge condition in electrodynamics are discussed in Section 3.4. The proper choice and manipulation of the gauge condition of elastodynamics are discussed in Section 3.5; our manipulation on the gauge condition does not violate the fundamental elastodynamics assumptions. The use of the proposed method is demonstrated on two classical problems, i.e., the straight crested and the circular crested guided wave propagation in a uniform plate.

3.3 GOVERNING EQUATIONS AND ORIGIN OF GAUGE CONDITION IN ELASTODYNAMICS

3.3.1 GOVERNING EQUATIONS FOR HELMHOLTZ POTENTIALS

The backbone of classical elastodynamics is the Navier-Lame equations [18]. The origin of the gauge condition can be traced to the Navier-Lame equations as follows:

Substitute Eq. (3.3) into Eq. (3.2) to get

$$(\lambda + \mu)\vec{\nabla}\left\{\vec{\nabla}\cdot(\vec{\nabla}\Phi + \vec{\nabla}\times\vec{H})\right\} + \mu\nabla^2(\vec{\nabla}\Phi + \vec{\nabla}\times\vec{H}) = \rho(\vec{\nabla}\ddot{\Phi} + \vec{\nabla}\times\ddot{\vec{H}}) \quad (3.13)$$

Upon rearrangement,

$$(\lambda + 2\mu)\vec{\nabla}(\nabla^2\Phi) + \mu\vec{\nabla}\times(\nabla^2\vec{H}) + (\lambda + \mu)\vec{\nabla}\left\{\vec{\nabla}\cdot(\vec{\nabla}\times\vec{H})\right\} = \rho(\vec{\nabla}\ddot{\Phi} + \vec{\nabla}\times\ddot{\vec{H}}) \quad (3.14)$$

Applying the general vector property $\vec{\nabla}\cdot(\vec{\nabla}\times\vec{H}) = 0$ (divergence of any curl is zero), the third term drops out. Combining the similar potential functions, Eq. (3.14) can be written as

$$\vec{\nabla} \{(\lambda + 2\mu)\nabla^2\Phi - \rho\ddot{\Phi}\} + \vec{\nabla} \times (\mu\nabla^2\vec{H} - \rho\ddot{\vec{H}}) = 0 \quad (3.15)$$

Eq. (3.15) is separated into two independent wave equations

$$(\lambda + 2\mu)\nabla^2\Phi - \rho\ddot{\Phi} = 0 \quad (\text{scalar wave equation}) \quad (3.16)$$

$$\mu\nabla^2\vec{H} - \rho\ddot{\vec{H}} = 0 \quad (\text{vector wave equation}) \quad (3.17)$$

Assuming harmonic time variation with circular frequency ω and defining

$c_p = \sqrt{(\lambda + 2\mu)/\rho}$, $c_s = \sqrt{\mu/\rho}$, Eq. (3.16) and (3.17) become

$$\nabla^2\Phi + \frac{\omega^2}{c_p^2}\Phi = 0 \quad (3.18)$$

$$\nabla^2\vec{H} + \frac{\omega^2}{c_s^2}\vec{H} = 0 \quad (3.19)$$

Eq. (3.18) indicates that the scalar potential Φ propagates with the pressure wavespeed c_p , whereas Eq. (3.19) indicates that the vector potential \vec{H} propagates with the shear wavespeed c_s . It can be shown that the pressure waves are *irrotational waves* i.e., have zero rotation, whereas the shear waves are *equivolume waves*, i.e., they have zero dilatation and are known as *distortional waves* [18]. From now on, we call the scalar potential Φ as *pressure potential* and the vector potential \vec{H} as *shear potential*.

3.3.2 INCEPTION OF THE GAUGE CONDITION

Now let's take a look at the dropped out term in Eq. (3.14), i.e.,

$$(\lambda + \mu)\vec{\nabla} \{ \vec{\nabla} \cdot (\vec{\nabla} \times \vec{H}) \} = \vec{0} \quad (3.20)$$

Using the vector property $\vec{\nabla} \{ \vec{\nabla} \cdot (\vec{\nabla} \times \vec{H}) \} = \vec{\nabla} \times \{ \vec{\nabla} (\vec{\nabla} \cdot \vec{H}) \}$, Eq. (3.20) can be written as

$$(\lambda + \mu)\vec{\nabla} \times \{ \vec{\nabla} (\vec{\nabla} \cdot \vec{H}) \} = \vec{0} \quad (3.21)$$

But $(\lambda + \mu) \neq 0$, hence, Eq. (3.21) can be written as

$$\vec{\nabla} \times \{ \vec{\nabla} (\vec{\nabla} \cdot \vec{H}) \} = \vec{0} \quad (3.22)$$

Letting, $\vec{\nabla} \cdot \vec{H} = \Gamma$, a scalar quantity, Eq. (3.22) becomes

$$\vec{\nabla} \times \{ \vec{\nabla} \Gamma \} = \vec{0} \quad (3.23)$$

Eq. (3.23) represents the vector property that curl of any gradient field is zero. Thus, Γ can be chosen arbitrarily without affecting the generality of the solution; this is called *gauge invariance* conditions as described by Eq. (3.5). This is similar to the *gauge invariance* used in solving Maxwell's equations in electrodynamics through the potential approach (see Section 2.5 of Chapter 2 of ref. [31]). Owing to the uniqueness of the physical problem, any solution that satisfies the Navier-Lame equations be the unique solution to the problem, regardless of the value assumed by Γ . In general, Γ can be written as

$$\Gamma = \vec{\nabla} \cdot \vec{H} = f(\vec{r}, \omega) \quad (\text{gauge condition}) \quad (3.24)$$

The selection of the gauge depends on the nature of the problem. The simplest gauge condition may be selected as $\Gamma = \vec{\nabla} \cdot \vec{H} = 0$ which is similar to the Coulomb gauge [34] in electrodynamics. The physical quantities such as displacements and stresses do not depend on the choice of the gauge for a problem with unique solution. However, the proper choices of gauge make the problems easier to solve. As an example, Gazis used $\Gamma = F(\vec{r}, t)$ [32] in order to simplify the shear potentials when developing the solution of wave propagation in a hollow cylinder. To avoid any confusion on the gauge condition, we can quote from ref. [39] a statement on the gauge condition used in electrodynamics "As a rule, one should keep in mind that there are no 'right' or 'wrong' admissible gauge choices. Any

proper gauge will lead to the same values of gauge invariant quantities. But, depending on an actual problem, a certain gauge can be more appropriate than others.”

Therefore, the gauge condition may be used to simplify the problem. It is noted that the gauge condition does not depend on the pressure potential Φ ; rather, it depends only on the shear potential \vec{H} . The proper choice and manipulation of the gauge condition should simplify complicated wave problems.

3.4 DIFFERENT FORMS OF GAUGE CONDITION IN ELECTRODYNAMICS

Helmholtz theorem gained its popularity for simplifying the problems in numerous fields of physics: hydrodynamics, elastodynamics, electrodynamics, etc. In electrodynamics, Maxwell’s equations are solved using Helmholtz potential functions with a gauge condition that is not necessarily to be zero; rather, actual fields are invariant of the gauge condition. The choice of gauge is arbitrary and does not change the physical quantities, and the potential functions are adjusted according to the choice of gauge [33]. However, a certain gauge may be more appropriate than a random choice and may make the problem easier to solve analytically. Researchers in electrodynamics have taken advantage of this by utilizing various forms of the gauge condition to solve various problems in classical electrodynamics and quantum electrodynamics. Different choices of the gauge condition have already been used to solve different problems in electrodynamics. For example, the gauge invariance of classical field theory applied to electrodynamics allows one to consider the vector potential \vec{A} with various gauge conditions [34], i.e.,

$$\vec{\nabla} \cdot \vec{A} = 0 \quad (\text{Coulomb gauge}) \quad (3.25)$$

$$\partial_\mu A^\mu = 0 \quad (\text{Lorenz gauge with } \mu = 0, 1, 2, 3) \quad (3.26)$$

$$n_\mu A^\mu = 0 \quad (\text{Light cone gauge with } n^2 = 0) \quad (3.27)$$

$$x_\mu A^\mu = 0 \quad (\text{Fock-Schwinger gauge}) \quad (3.28)$$

$$A_0 = 0 \quad (\text{Hamiltonian or temporal gauge}) \quad (3.29)$$

where \vec{A} is the vector potential, n_μ is the time axis, ∂_μ is the four gradient, x_μ is the position four-vector. Each of the gauge condition mentioned here was used to solve particular types of electrodynamic problem and the appropriate choice of gauge simplified the calculations. However, in elastodynamics, very few variations of the gauge condition has been observed so far.

In this chapter, the proper choice and manipulation of the gauge condition will be demonstrated for two problems: (a) straight crested guided waves in a plate (Lamb waves and shear horizontal, SH waves) and (b) circular crested guided waves in a plate (Lamb waves and shear horizontal, SH waves). Both problems will be solved by a unified potential approach.

3.5 APPLICATION OF GAUGE CONDITION TO STRAIGHT CRESTED GUIDED WAVES IN A PLATE

The wave equations Eq. (3.18) and (3.19) can be expanded in Cartesian coordinates (Figure 3.1) as

$$\frac{\partial^2 \Phi}{\partial x^2} + \frac{\partial^2 \Phi}{\partial y^2} + \frac{\partial^2 \Phi}{\partial z^2} + \frac{\omega^2}{c_p^2} \Phi = 0 \quad (3.30)$$

$$\frac{\partial^2 H_x}{\partial x^2} + \frac{\partial^2 H_x}{\partial y^2} + \frac{\partial^2 H_x}{\partial z^2} + \frac{\omega^2}{c_s^2} H_x = 0 \quad (3.31)$$

$$\frac{\partial^2 H_y}{\partial x^2} + \frac{\partial^2 H_y}{\partial y^2} + \frac{\partial^2 H_y}{\partial z^2} + \frac{\omega^2}{c_s^2} H_y = 0 \quad (3.32)$$

$$\frac{\partial^2 H_z}{\partial x^2} + \frac{\partial^2 H_z}{\partial y^2} + \frac{\partial^2 H_z}{\partial z^2} + \frac{\omega^2}{c_s^2} H_z = 0 \quad (3.33)$$

The gauge condition takes the form

$$\Gamma = \frac{\partial H_x}{\partial x} + \frac{\partial H_y}{\partial y} + \frac{\partial H_z}{\partial z} = f(\vec{r}, \omega) \quad (3.34)$$

where $f(\vec{r}, \omega)$ may be chosen differently depending on the nature of the problem.

Expansion of Eq. (3.3) gives the displacement components in terms of pressure and shear potentials as

$$u_x = \frac{\partial \Phi}{\partial x} + \frac{\partial H_z}{\partial y} - \frac{\partial H_y}{\partial z} \quad (3.35)$$

$$u_y = \frac{\partial \Phi}{\partial y} + \frac{\partial H_x}{\partial z} - \frac{\partial H_z}{\partial x} \quad (3.36)$$

$$u_z = \frac{\partial \Phi}{\partial z} + \frac{\partial H_y}{\partial x} - \frac{\partial H_x}{\partial y} \quad (3.37)$$

3.5.3 MANIPULATION OF THE GAUGE CONDITION IN CARTESIAN COORDINATES

At first, we discuss the general case and then concentrate on the y -invariant case.

Examination of Eq. (3.35), (3.36), (3.37) yields the following observations:

u_x does not depend on shear potential H_x

u_y does not depend on shear potential H_y

u_z does not depend on shear potential H_z

u_x, u_y, u_z depend on pressure potential Φ

We notice that the pressure potential Φ contributes to all the displacement components. However, the shear waves may be divided into vertically polarized shear waves (SV waves) contained in the xz plane and horizontally polarized shear waves (SH waves) contained in the xy plane (Figure 3.1). SV and SH waves may depend on all three shear potentials if

coupling between them is expected in a physical problem. However, SV waves have u_z particle motion that does not depend on H_z whereas SH waves have u_y particle motion that does not depend on H_y . Since only two types of shear waves exist, it is apparent that SV waves must depend on H_y and SH waves must depend on H_z . Therefore, the wave equations Eqs. (3.32) and (3.33) may be associated with SV and SH waves, respectively.

$$\frac{\partial^2 H_y}{\partial x^2} + \frac{\partial^2 H_y}{\partial y^2} + \frac{\partial^2 H_y}{\partial z^2} + \frac{\omega^2}{c_s^2} H_y = 0 \quad (\text{SV waves}) \quad (3.38)$$

$$\frac{\partial^2 H_z}{\partial x^2} + \frac{\partial^2 H_z}{\partial y^2} + \frac{\partial^2 H_z}{\partial z^2} + \frac{\omega^2}{c_s^2} H_z = 0 \quad (\text{SH waves}) \quad (3.39)$$

The third potential H_x has contributions to both u_y and u_z particle motions as indicated by Eq. (3.36) and (3.37).

In straight crested guided wave propagation through plate-like structures, SH and SV waves may be treated separately; SV waves combine with pressure waves to form Lamb waves [18] whereas SH waves remain independent. Depending on the initial and boundary conditions, the Lamb waves and SH waves can either exist alone or coexist in the elastic body. The problem where only one of these waves exists is much easier to deal with. In a problem where both waves coexist, they can be treated separately and then superimpose on each other.

The gauge condition of Eq. (3.34) may be considered as a superposition of Lamb wave gauge (Γ_{LW}) and SH wave gauge (Γ_{SH}); hence, it can be resolved into two parts as follows

$$\Gamma = \Gamma_{LW} + \Gamma_{SH} = f(\vec{r}, \omega) \quad (\text{"Bhuiyan-Giurgiutiu" gauge condition}) \quad (3.40)$$

This partition of the gauge condition does not violate the classical solution; rather, it simplifies the problem. Considering that H_x is part of Lamb waves (eventually, H_x becomes zero for the y -invariant case), the gauge condition Eq. (3.34) may be written as

$$\frac{\partial H_x}{\partial x} + \frac{\partial H_y}{\partial y} = f_{LW}(\vec{r}, \omega) \quad (\text{Lamb wave gauge}) \quad (3.41)$$

$$\frac{\partial H_z}{\partial z} = f_{SH}(\vec{r}, \omega) \quad (\text{SH wave gauge}) \quad (3.42)$$

where $f(\vec{r}, \omega) = f_{LW}(\vec{r}, \omega) + f_{SH}(\vec{r}, \omega)$, with $f_{LW}(\vec{r}, \omega)$ and $f_{SH}(\vec{r}, \omega)$ being responsible for Lamb wave gauge and SH wave gauge, respectively.

For the y -invariant problem, we may choose the simplest gauge $f_{LW}(\vec{r}, \omega) = 0$.

Hence, Eq. (3.41) becomes

$$\frac{\partial H_x}{\partial x} + \frac{\partial H_y}{\partial y} = 0 \quad (3.43)$$

Since the problem is y -invariant, Eq. (3.43) yields

$$\frac{\partial H_x}{\partial x} = 0 \quad (3.44)$$

Integrating Eq. (3.44) gives

$$H_x = C \quad (3.45)$$

where C is a constant or a function of z . The simplest selection is $C = 0$. Thus, Eq. (3.45) becomes

$$H_x = 0 \quad (3.46)$$

We have thus seen that the application of gauge condition in this simple y -invariant problem has yielded the shear potential H_x to be zero. This illustrates how the

gauge condition has made the problem much simpler. Our result is similar to the solution of elastic waves in rods by Gazis [5] where one of the potentials was made zero using the gauge invariance property.

3.5.4 SOLUTION FOR y -INVARIANT STRAIGHT CRESTED LAMB + SH WAVES IN A PLATE

The application of the y -invariant condition, $\partial / \partial y \equiv 0$, and Eq. (3.46) into Eqs. (3.30)-(3.33) allows us to group the equations into Lamb waves and SH waves, i.e.,

Lamb waves:

$$\frac{\partial^2 \Phi}{\partial x^2} + \frac{\partial^2 \Phi}{\partial z^2} + \frac{\omega^2}{c_p^2} \Phi = 0 \quad (3.47)$$

$$\frac{\partial^2 H_y}{\partial x^2} + \frac{\partial^2 H_y}{\partial z^2} + \frac{\omega^2}{c_s^2} H_y = 0 \quad (3.48)$$

SH waves:

$$\frac{\partial^2 H_z}{\partial x^2} + \frac{\partial^2 H_z}{\partial z^2} + \frac{\omega^2}{c_s^2} H_z = 0 \quad (3.49)$$

The displacement equations Eqs. (3.35)-(3.37), can also be grouped, i.e.,

Lamb waves:

$$u_x = \frac{\partial \Phi}{\partial x} - \frac{\partial H_y}{\partial z} \quad (3.50)$$

$$u_z = \frac{\partial \Phi}{\partial z} + \frac{\partial H_y}{\partial x} \quad (3.51)$$

SH waves:

$$u_y = -\frac{\partial H_z}{\partial x} \quad (3.52)$$

Note that only three potentials Φ , H_y , H_z are involved in Eqs. (3.47)-(3.52), since $H_x = 0$ according to Eq. (3.46). The Lamb waves are represented by two potentials Φ , H_y , and the SH waves are represented by a single potential H_z .

The stress components can also be grouped as follows.

Lamb waves:

$$\sigma_{xx} = -\lambda \frac{\omega^2}{c_p^2} \Phi + 2\mu \left(\frac{\partial^2 \Phi}{\partial x^2} - \frac{\partial^2 H_y}{\partial x \partial y} \right) \quad (3.53)$$

$$\sigma_{yy} = -\lambda \frac{\omega^2}{c_p^2} \Phi \quad (3.54)$$

$$\sigma_{zz} = -\lambda \frac{\omega^2}{c_p^2} \Phi + 2\mu \left(\frac{\partial^2 \Phi}{\partial z^2} + \frac{\partial^2 H_y}{\partial x \partial z} \right) \quad (3.55)$$

$$\sigma_{zx} = \mu \left(2 \frac{\partial^2 \Phi}{\partial x \partial z} + \frac{\partial^2 H_y}{\partial x^2} - \frac{\partial^2 H_y}{\partial z^2} \right) \quad (3.56)$$

SH waves:

$$\sigma_{xy} = \mu \left(-\frac{\partial^2 H_z}{\partial x^2} \right) \quad (3.57)$$

$$\sigma_{yz} = \mu \left(-\frac{\partial^2 H_z}{\partial x \partial z} \right) \quad (3.58)$$

The solution for the Lamb waves is obtained by applying plate boundary conditions $\sigma_{zz} \big|_{z=\pm d} = 0$ and $\sigma_{zx} \big|_{z=\pm d} = 0$ that yield the Rayleigh-Lamb characteristic equation [21]. The Lamb wave solution is the classical solution [8] and will not be repeated here for the sake of brevity.

For SH waves, the governing equation Eq. (3.49) can be solved for the shear potential H_z by using the separation of variables as

$$H_z = (C_1 \sin \eta_s z + C_2 \cos \eta_s z) e^{i\xi x} \quad (3.59)$$

where C_1 , C_2 are constants, and ξ is the wavenumber in x direction, and

$$\eta_s^2 = \omega^2 / c_s^2 - \xi^2.$$

Substituting Eq. (3.59) into Eq. (3.52), (3.57), (3.58), the expressions of displacement and stress components become

$$u_z = -i\xi(C_1 \sin \eta_s z + C_2 \cos \eta_s z) e^{i\xi x} \quad (3.60)$$

$$\sigma_{xy} = \mu \xi^2 (C_1 \sin \eta_s z + C_2 \cos \eta_s z) e^{i\xi x} \quad (3.61)$$

$$\sigma_{yz} = -i\mu \eta_s \xi (C_1 \cos \eta_s z - C_2 \sin \eta_s z) e^{i\xi x} \quad (3.62)$$

The zero-traction boundary conditions apply at the top and bottom of the plate, i.e.,

$$\sigma_{yz} \Big|_{z=\pm d} = 0 \quad (3.63)$$

Substitution of Eq. (3.62) into boundary conditions Eq. (3.63) yields

$$C_1 \cos \eta_s d - C_2 \sin \eta_s d = 0 \quad (3.64)$$

$$C_1 \cos \eta_s d + C_2 \sin \eta_s d = 0 \quad (3.65)$$

Subtracting Eq. (3.64) from Eq. (3.65), the symmetric SH wave modes can be obtained and the characteristic equation corresponding to the symmetric modes becomes

$$\sin \eta_s d = 0 \quad (3.66)$$

Adding Eq. (3.64) and Eq. (3.65), the antisymmetric SH wave modes can be obtained and the characteristic equation corresponding to the antisymmetric modes becomes

$$\cos \eta_s d = 0 \quad (3.67)$$

The characteristic equations Eqs. (3.66) and (3.67) obtained through the potential approach are the same as the solution of SH waves in terms of u_y [21] and subsequently, the solutions for displacements and stresses should be the same.

3.6 APPLICATION OF GAUGE CONDITION TO CIRCULAR CRESTED GUIDED WAVES IN A PLATE

The governing equations in cylindrical coordinates (Figure 3.2) are much more involved than in Cartesian coordinates. We can simplify the governing equations using the axisymmetric assumption, $\partial/\partial\theta\equiv 0$. For the present analysis, we will consider the axisymmetric problem and will demonstrate that the proper choice and manipulation of the gauge condition yields much simpler formulations. Our solution will be compared with existing classical solutions [18] [21].

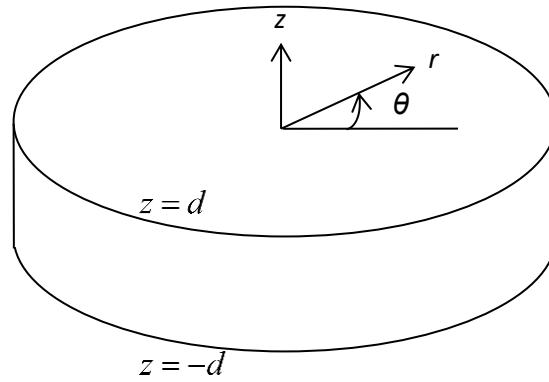


Figure 3.2 Problem definition in cylindrical coordinate system

3.6.5 AXISYMMETRIC CIRCULAR CRESTED GUIDED WAVES IN A PLATE

Under the axisymmetric assumption $\partial/\partial\theta\equiv 0$, the governing equations Eqs. (3.18), (3.19) can be written in cylindrical coordinates as

$$\frac{\partial^2 \Phi}{\partial r^2} + \frac{1}{r} \frac{\partial \Phi}{\partial r} + \frac{\partial^2 \Phi}{\partial z^2} + \frac{\omega^2}{c_p^2} \Phi = 0 \quad (3.68)$$

$$\frac{\partial^2 H_r}{\partial r^2} + \frac{1}{r} \frac{\partial H_r}{\partial r} + \frac{\partial^2 H_r}{\partial z^2} - \frac{1}{r^2} H_r + \frac{\omega^2}{c_s^2} H_r = 0 \quad (3.69)$$

$$\frac{\partial^2 H_\theta}{\partial r^2} + \frac{1}{r} \frac{\partial H_\theta}{\partial r} + \frac{\partial^2 H_\theta}{\partial z^2} - \frac{1}{r^2} H_\theta + \frac{\omega^2}{c_s^2} H_\theta = 0 \quad (3.70)$$

$$\frac{\partial^2 H_z}{\partial r^2} + \frac{1}{r} \frac{\partial H_z}{\partial r} + \frac{\partial^2 H_z}{\partial z^2} + \frac{\omega^2}{c_s^2} H_z = 0 \quad (3.71)$$

The gauge condition takes the form

$$\frac{\partial H_r}{\partial r} + \frac{1}{r} H_r + \frac{\partial H_z}{\partial z} = f(\vec{r}, \omega) \quad (3.72)$$

Displacements are expressed as

$$u_r = \frac{\partial \Phi}{\partial r} - \frac{\partial H_\theta}{\partial z} \quad (3.73)$$

$$u_\theta = \frac{\partial H_r}{\partial z} - \frac{\partial H_z}{\partial r} \quad (3.74)$$

$$u_z = \frac{\partial \Phi}{\partial z} + \frac{\partial H_\theta}{\partial r} + \frac{H_\theta}{r} \quad (3.75)$$

3.6.6 MANIPULATION OF THE GAUGE CONDITION IN CYLINDRICAL COORDINATES

We follow a similar analogy that has already been discussed in Section 3.5.3 to allocate the potential functions to the Lamb waves and the SH waves. In cylindrical coordinates, pressure waves must depend on Φ ; SV waves must depend on H_θ ; and SH waves must depend on H_z . The third shear potential, H_r , may have contributions to both SV and SH waves. However, when solving Eq. (3.69) and (3.70) by separation of variable methods, we notice that the shear potentials H_r and H_θ follow the same order (order 1) of Hankel function. On the other hand, the shear potential H_z has a different order (order 0) of Hankel function.

The pressure waves and SV waves group up to generate Lamb waves whereas SH waves remain independent. Separating the gauge condition Eq. (3.72) into Lamb waves and SH waves yields:

$$\frac{\partial H_r}{\partial r} + \frac{1}{r} H_r = f_{LW}(\vec{r}, \omega) \quad (\text{Lamb wave gauge}) \quad (3.76)$$

$$\frac{\partial H_z}{\partial z} = f_{SH}(\vec{r}, \omega) \quad (\text{SH wave gauge}) \quad (3.77)$$

where, $f(\vec{r}, \omega) = f_{LW}(\vec{r}, \omega) + f_{SH}(\vec{r}, \omega)$.

For the axisymmetric problem, we may choose the simplest gauge $f_{LW}(\vec{r}, \omega) = 0$.

Hence, Eq. (3.76) becomes

$$\frac{\partial H_r}{\partial r} + \frac{1}{r} H_r = 0 \quad (3.78)$$

Using the differential product rule, Eq. (3.78) yields

$$\frac{1}{r} \frac{\partial}{\partial r} (r H_r) = 0 \quad (3.79)$$

Integrating Eq. (3.79) gives

$$H_r = C_1 \quad (3.80)$$

where C_1 can be a constant or a function of z . The simplest selection may be $C_1 = 0$. Thus,

Eq. (3.80) becomes

$$H_r = 0 \quad (3.81)$$

This is similar to the y -invariant problem discussed for Cartesian coordinates in Section 3.5.3.

3.6.7 SOLUTION FOR AXISYMMETRIC CIRCULAR CRESTED LAMB + SH WAVES IN A PLATE

Upon manipulation of gauge condition we make $H_r = 0$ (Eq. (3.81)) and the governing equations Eqs. (3.68)-(3.71) can be grouped as follows.

Lamb waves:

$$\frac{\partial^2 \Phi}{\partial r^2} + \frac{1}{r} \frac{\partial \Phi}{\partial r} + \frac{\partial^2 \Phi}{\partial z^2} + \frac{\omega^2}{c_p^2} \Phi = 0 \quad (3.82)$$

$$\frac{\partial^2 H_\theta}{\partial r^2} + \frac{1}{r} \frac{\partial H_\theta}{\partial r} + \frac{\partial^2 H_\theta}{\partial z^2} - \frac{1}{r^2} H_\theta + \frac{\omega^2}{c_s^2} H_\theta = 0 \quad (3.83)$$

SH waves:

$$\frac{\partial^2 H_z}{\partial r^2} + \frac{1}{r} \frac{\partial H_z}{\partial r} + \frac{\partial^2 H_z}{\partial z^2} + \frac{\omega^2}{c_s^2} H_z = 0 \quad (3.84)$$

The displacement equations may also be grouped as follows.

Lamb waves:

$$u_r = \frac{\partial \Phi}{\partial r} - \frac{\partial H_\theta}{\partial z} \quad (3.85)$$

$$u_z = \frac{\partial \Phi}{\partial z} + \frac{\partial H_\theta}{\partial r} + \frac{H_\theta}{r} \quad (3.86)$$

SH waves:

$$u_\theta = -\frac{\partial H_z}{\partial r} \quad (3.87)$$

The stress components can also be grouped as follows.

Lamb waves:

$$\sigma_{rr} = -\lambda \frac{\omega^2}{c_p^2} \Phi + 2\mu \left(\frac{\partial^2 \Phi}{\partial r^2} - \frac{\partial^2 H_\theta}{\partial r \partial z} \right) \quad (3.88)$$

$$\sigma_{\theta\theta} = -\lambda \frac{\omega^2}{c_p^2} \Phi + 2\mu \left(\frac{1}{r} \frac{\partial \Phi}{\partial r} - \frac{1}{r} \frac{\partial H_\theta}{\partial z} \right) \quad (3.89)$$

$$\sigma_{zz} = -\lambda \frac{\omega^2}{c_p^2} \Phi + 2\mu \left(\frac{\partial^2 \Phi}{\partial z^2} + \frac{\partial^2 H_\theta}{\partial r \partial z} + \frac{1}{r} \frac{\partial H_\theta}{\partial z} \right) \quad (3.90)$$

$$\sigma_{rz} = \mu \left(2 \frac{\partial^2 \Phi}{\partial r \partial z} + \frac{\partial^2 H_\theta}{\partial r^2} - \frac{H_\theta}{r^2} + \frac{1}{r} \frac{\partial H_\theta}{\partial r} - \frac{\partial^2 H_\theta}{\partial z^2} \right) \quad (3.91)$$

SH waves:

$$\sigma_{r\theta} = -2\mu \left(\frac{\partial^2 H_z}{\partial r^2} - \frac{1}{r} \frac{\partial H_z}{\partial r} \right) \quad (3.92)$$

$$\sigma_{\theta z} = -\mu \frac{\partial^2 H_z}{\partial r \partial z} \quad (3.93)$$

The Lamb wave expressions for displacements and stresses are the same as for the classical solution [21]. The Rayleigh-Lamb equation is obtained from the plate boundary conditions; the complete Lamb wave solution will not be repeated here for the sake of brevity.

The SH wave solution in terms of potentials is discussed next. The governing equation Eq. (3.84) can be solved for shear potential H_z by using separation of variables, i.e.,

$$H_z = (A_1 \sin \eta_s z + A_2 \cos \eta_s z) H_0^1(\xi r) \quad (3.94)$$

where A_1, A_2 are constants, ξ is the wave number in the r direction, $\eta_s^2 = \omega^2 / c_s^2 - \xi^2$, and $H_0^1(\xi r)$ is the Hankel function of the first kind and order zero.

The traction free boundary conditions apply at the top and bottom of the plate i.e.

$$\sigma_{\theta z} \Big|_{z=\pm d} = 0 \quad (3.95)$$

Substituting Eq. (3.94) into Eq. (3.93) gives

$$\sigma_{\theta z} = -\mu\eta_s(A_1 \cos \eta_s z - A_2 \sin \eta_s z)(H_0^1(\xi r))' \quad (3.96)$$

Substitution of Eq. (3.96) into boundary conditions Eq. (3.95) yields

$$A_1 \cos \eta_s d - A_2 \sin \eta_s d = 0 \quad (3.97)$$

$$A_1 \cos \eta_s d + A_2 \sin \eta_s d = 0 \quad (3.98)$$

Subtraction and addition of Eq. (3.97) and (3.98), yields the symmetric and antisymmetric SH wave modes; the characteristic equations corresponding to the symmetric and antisymmetric modes are

$$\sin \eta_s d = 0 \quad (\text{symmetric}); \quad \cos \eta_s d = 0 \quad (\text{antisymmetric}) \quad (3.99)$$

The characteristic equations indicated by Eq. (3.99) are the same as the classical solutions of SH waves; subsequently, the solutions for displacements and stresses are also same. Hence, the potential approach has been shown to be easily implemented through the manipulation of the gauge condition.

3.7 CONCLUSION

The gauge condition originated in elastodynamics from the Navier-Lame equations upon application of Helmholtz theorem. The proper choice and manipulation of the gauge condition may simplify the problem and permits a straightforward analytical solution. The gauge condition provides the necessary conditions for the complete solution of the elastic waves in plates by the potential function approach. The gauge condition may be considered as the superposition of separate gauge conditions for Lamb waves and SH waves, respectively. Each gauge condition contains a different combination of the shear potential components. The gauge condition established a bridge between Lamb waves and SH waves. The gauge condition may decouple for the physical problems in which the Lamb and SH

waves are expected to decouple. The decoupling of the gauge condition does not violate the classical Lamb wave and SH wave solutions; rather, it simplifies the problem. The gauge condition plays a vital role in the separation of Lamb waves and SH waves; thus, it transforms a complicated problem into two simpler problems. In this chapter, the manipulation of the gauge condition has been illustrated on two well-known problems of guided waves in plates in which the Lamb waves and SH waves can be physically decoupled. The next challenge for this approach would be to address a coupled problem (Lamb waves + SH waves) such as the non-axisymmetric guided wave propagation in a plate; this problem will be discussed in the next chapter.

CHAPTER 4

A HELMHOLTZ POTENTIAL BASED SOLUTION TO THE NON-AXISYMMETRIC COUPLED GUIDED WAVE PROPAGATION IN A PLATE

This chapter presents a cylindrical-coordinates solution for the coupled non-axisymmetric plate guided-wave propagation using Helmholtz potentials and a particular interpretation of the gauge condition. The non-axisymmetric guided wave problem contains coupled Lamb and shear horizontal (SH) waves. A general non-axisymmetric solution of guided wave propagation in plate is needed to analyze the guided wave scattering from non-axisymmetric damage as encountered in practice. Application of the Helmholtz decomposition theorem to the Navier-Lame equations yields a set of four coupled partial differential equations in four unknowns, the scalar potential Φ and the three components of the vector potential H_r, H_θ, H_z . A fourth equation, the ‘gauge condition’ is then added to the decomposition. Under non-axisymmetric conditions, the problem is highly coupled and no Helmholtz-type solution has been published so far. We propose a Helmholtz-type solution in terms of potentials which is developed through a particular interpretation of the gauge condition. Our proposed approach decouples the governing equations and reduces the number of unknowns from four to three thus allowing one to express the solution in an elegant straight-forward way. The Rayleigh-Lamb characteristic equations are recovered and a general normal-modes expression for the solution is obtained.

4.1 INTRODUCTION

4.1.1 STATE OF THE ART

The state of the art for z-invariant and axisymmetric Lamb and SH wave was presented in Section 3.1 of previous Chapter 3. Here, we continue the discussion by addressing the non-axisymmetric case. A non-axisymmetric Helmholtz approach was developed by Gazis [40] [32] for the wave propagation in an infinitely long hollow cylinder. A particular form of the gauge condition was utilized. However, the case of guided wave propagation in a hollow cylinder is much simpler than that of non-axisymmetric guided wave propagation in a plate. Gazis' approach may serve as inspiration but cannot be applied directly.

The non-axisymmetric guided wave propagation in a plate due to the application of half-ring normal loads was studied by Scott and Miklowitz [41] using a special form of the vector potential \vec{H} and multi-integral transforms (Laplace, Fourier, and inverse Hankel transforms).

An integral representation of the non-axisymmetric wave displacement components to analyze the shear impact and oblique impact on plates was developed by Davids et al. [42] [43] through the use of trigonometric angular functions.

A comprehensive solution for the coupled non-axisymmetric guided-wave propagation in a plate was developed by Achenbach [38] [37] using an ingenious definition of the wave displacements based on the membrane solution combined with thickness-wise mode functions as discussed in Section 3.2.2 of Chapter 3. Subsequently, Achenbach's solutions have been extensively used to analyze guided-wave scattering from generic non-

axisymmetric damage [44] [45] [46]. However, this approach does not use the Helmholtz decomposition in which the contributing potentials satisfy the wave equation.

To our knowledge, no solution has yet been proposed for solving the coupled non-axisymmetric guided wave problem using the Helmholtz decomposition in cylindrical coordinates. Finding such a solution in which the contributing potentials explicitly satisfy the wave equation is the objective of this chapter.

4.1.2 WHY DOES ONE NEED THE HELMHOLTZ APPROACH FOR NON-AXISYMMETRIC GUIDE-WAVE SOLUTION?

Helmholtz, in his ground-breaking 1858 paper, proposed a vector-field decomposition theorem of wide-ranging utility [19] [20]. Helmholtz decomposition theorem is a mathematically robust approach that has been applied to many vector-field physics problems [31]. For elastodynamics, the Helmholtz decomposition theorem has the form

$$\vec{u} = \text{grad}\Phi + \text{curl}\vec{H} = \vec{\nabla}\Phi + \vec{\nabla} \times \vec{H} \quad (4.1)$$

where \vec{u} is a vector field, Φ is a dilatational scalar potential, and \vec{H} is an equivoluminal vector potential. The displacement field \vec{u} satisfies the Navier-Lame equations of motion [18], i.e.,

$$(\lambda + \mu)\vec{\nabla}(\vec{\nabla} \cdot \vec{u}) + \mu\nabla^2 \vec{u} = \rho\ddot{\vec{u}} \quad (4.2)$$

where ρ is the density, λ and μ are the Lamé constants. In cylindrical coordinates (Figure 4.1) $\vec{H} = H_r\vec{e}_r + H_\theta\vec{e}_\theta + H_z\vec{e}_z$. It can be noted from Eq. (4.1), that the three-component displacement vector \vec{u} is represented by four unknown potentials: the scalar potential Φ and the three components H_r, H_θ, H_z of the vector potential \vec{H} . To make the

decomposition unique [31], an additional equation is added in the form of the “gauge condition”.

We may identify the following reasons for using the Helmholtz approach to solve the non-axisymmetric guided-wave problem in cylindrical coordinates:

- a) The Helmholtz approach is one of the most robust mathematical approaches for solving vector-field physics problems [31].
- b) The Helmholtz approach has already been successfully used to solve many vector-field physics problems in electrodynamics, fluid mechanics, elastodynamics.
- c) The gauge condition of the Helmholtz approach can be cast in various forms in order to simplify the problems (e.g., Coulomb gauge, Lorenz gauge, Fock-Schwinger gauge, Hamiltonian gauge, etc.) [34]
- d) The Helmholtz approach had already been extensively used in elastodynamics (bulk-wave propagation, straight-crested guided-wave propagation in Cartesian coordinates, axisymmetric guided-wave propagation in cylindrical coordinates), but it has not yet been applied to the non-axisymmetric guided-wave propagation in cylindrical coordinates due to certain mathematical difficulties that are detailed later in this chapter. Why not attempt to solve this challenging problem and thus complete the suit of elastodynamics solutions based on the Helmholtz approach?

4.2 DESCRIPTION OF THE NON-AXISYMMETRIC GUIDED WAVE PROBLEM IN CYLINDRICAL COORDINATES

4.2.1 GOVERNING EQUATIONS

Recall from Chapter 3, the wave equations for the potentials Φ and \vec{H} , i.e.,

$$c_p^2 \nabla^2 \Phi = \ddot{\Phi} \quad (\text{wave equation for } \Phi) \quad (4.3)$$

$$c_s^2 \nabla^2 \vec{H} = \ddot{\vec{H}} \quad (\text{wave equation for } \vec{H}) \quad (4.4)$$

and the gauge condition

$$\Gamma = \vec{\nabla} \cdot \vec{H} = f(\vec{r}, t) \quad (\text{gauge condition}) \quad (4.5)$$

where c_p and c_s are the pressure and shear wavespeeds defined as

$$c_p = \sqrt{\frac{\lambda + 2\mu}{\rho}}, \quad c_s = \sqrt{\frac{\mu}{\rho}} \quad (4.6)$$

It is apparent from Eqs. (4.3), (4.6) that the scalar potential Φ is associated with *pressure waves* whereas the vector potential \vec{H} is associated with *shear waves* [18].

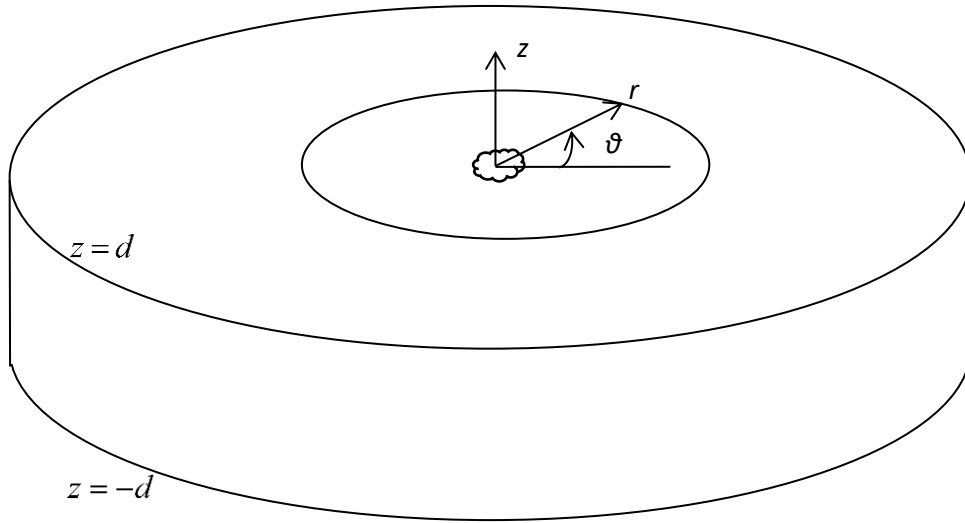


Figure 4.1 Non-axisymmetric guided wave propagation in a plate

For time-harmonic waves of circular frequency ω , Eq. (4.3), (4.4), and (4.5) becomes

$$\nabla^2 \Phi + \frac{\omega^2}{c_p^2} \Phi = 0 \quad (4.7)$$

$$\nabla^2 \vec{H} + \frac{\omega^2}{c_s^2} \vec{H} = 0 \quad (4.8)$$

$$\Gamma = \vec{\nabla} \cdot \vec{H} = f(\vec{r}, \omega) \quad (\text{gauge condition}) \quad (4.9)$$

In cylindrical coordinates, Eq. (4.7), (4.8) expands to

$$\frac{\partial^2 \Phi}{\partial r^2} + \frac{1}{r} \frac{\partial \Phi}{\partial r} + \frac{1}{r^2} \frac{\partial^2 \Phi}{\partial \theta^2} + \frac{\partial^2 \Phi}{\partial z^2} + \frac{\omega^2}{c_p^2} \Phi = 0 \quad (4.10)$$

$$\frac{\partial^2 H_z}{\partial r^2} + \frac{1}{r} \frac{\partial H_z}{\partial r} + \frac{1}{r^2} \frac{\partial^2 H_z}{\partial \theta^2} + \frac{\partial^2 H_z}{\partial z^2} + \frac{\omega^2}{c_s^2} H_z = 0 \quad (4.11)$$

$$\frac{\partial^2 H_r}{\partial r^2} + \frac{1}{r} \frac{\partial H_r}{\partial r} + \frac{1}{r^2} \frac{\partial^2 H_r}{\partial \theta^2} + \frac{\partial^2 H_r}{\partial z^2} - \frac{2}{r^2} \frac{\partial H_\theta}{\partial \theta} - \frac{1}{r^2} H_r + \frac{\omega^2}{c_s^2} H_r = 0 \quad (4.12)$$

$$\frac{\partial^2 H_\theta}{\partial r^2} + \frac{1}{r} \frac{\partial H_\theta}{\partial r} + \frac{1}{r^2} \frac{\partial^2 H_\theta}{\partial \theta^2} + \frac{\partial^2 H_\theta}{\partial z^2} + \frac{2}{r^2} \frac{\partial H_r}{\partial \theta} - \frac{1}{r^2} H_\theta + \frac{\omega^2}{c_s^2} H_\theta = 0 \quad (4.13)$$

On the one hand, examination of Eqs. (4.10) and (4.11) reveals that potentials Φ and H_z are uncoupled and hence these two governing equations can be solved independently. On the other hand, examination of Eqs. (4.12) and (4.13) reveals that potentials H_r and H_θ are tightly coupled and hence, these two governing equations cannot be solved independently which makes the problem challenging and justifies the work presented in the rest of this chapter.

4.2.2 DISPLACEMENT AND STRESS COMPONENTS

Expansion of Eq. (4.1) yields the displacement components in cylindrical coordinates, i.e.,

$$u_r = \frac{\partial \Phi}{\partial r} + \frac{1}{r} \frac{\partial H_z}{\partial \theta} - \frac{\partial H_\theta}{\partial z} \quad (4.14)$$

$$u_\theta = \frac{1}{r} \frac{\partial \Phi}{\partial \theta} + \frac{\partial H_r}{\partial z} - \frac{\partial H_z}{\partial r} \quad (4.15)$$

$$u_z = \frac{\partial \Phi}{\partial z} + \frac{\partial H_\theta}{\partial r} + \frac{H_\theta}{r} - \frac{1}{r} \frac{\partial H_r}{\partial \theta} \quad (4.16)$$

Hence, substitution of Eqs. (4.14)-(4.16) in the strain-displacement equations and then into the stress-strain relations yields the stress components (Figure 4.2).

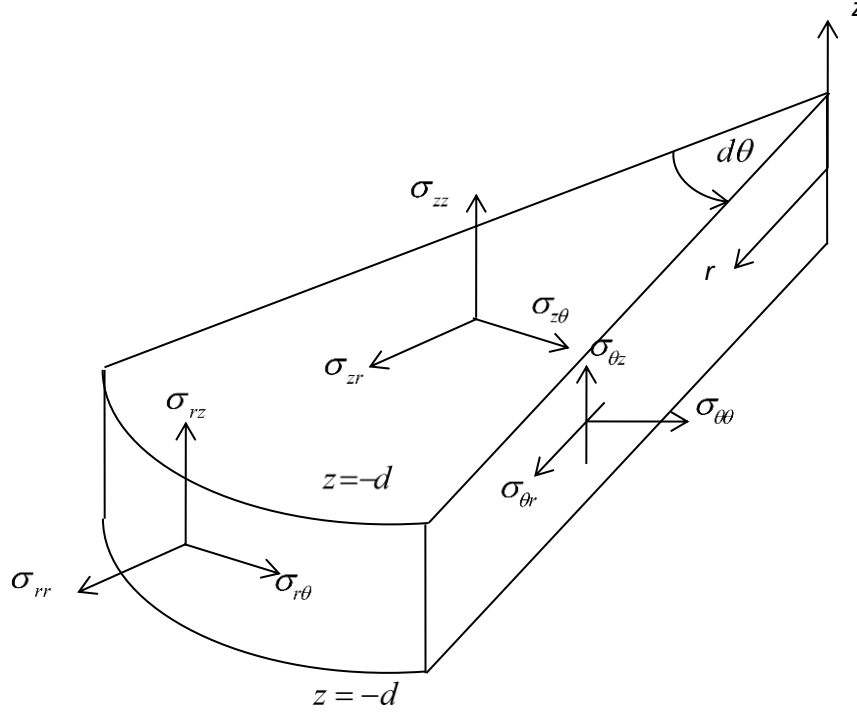


Figure 4.2 Tractions on a differential element of a plate in cylindrical coordinates

Strain-displacement relations:

$$\begin{aligned}
 \varepsilon_{rr} &= \frac{\partial u_r}{\partial r} & \varepsilon_{r\theta} &= \frac{1}{2} \left(\frac{1}{r} \frac{\partial u_r}{\partial \theta} + \frac{\partial u_\theta}{\partial r} - \frac{u_\theta}{r} \right) \\
 \varepsilon_{\theta\theta} &= \frac{1}{r} \frac{\partial u_\theta}{\partial \theta} + \frac{u_r}{r} & \text{and} & \quad \varepsilon_{\theta z} &= \frac{1}{2} \left(\frac{\partial u_\theta}{\partial z} + \frac{1}{r} \frac{\partial u_z}{\partial \theta} \right) \\
 \varepsilon_{zz} &= \frac{\partial u_z}{\partial z} & \varepsilon_{rz} &= \frac{1}{2} \left(\frac{\partial u_z}{\partial r} + \frac{\partial u_r}{\partial z} \right)
 \end{aligned} \tag{4.17}$$

Stress-strain relations:

$$\begin{aligned}
 \sigma_{rr} &= \lambda\Delta + 2\mu\varepsilon_{rr} & \sigma_{r\theta} &= 2\mu\varepsilon_{r\theta} \\
 \sigma_{\theta\theta} &= \lambda\Delta + 2\mu\varepsilon_{\theta\theta} & \text{and} & & \sigma_{\theta z} &= 2\mu\varepsilon_{\theta z} \\
 \sigma_{zz} &= \lambda\Delta + 2\mu\varepsilon_{zz} & & & \sigma_{rz} &= 2\mu\varepsilon_{rz}
 \end{aligned} \tag{4.18}$$

where,

$$\Delta = \varepsilon_{rr} + \varepsilon_{\theta\theta} + \varepsilon_{zz} \tag{4.19}$$

Recall governing equation (4.53)

$$\frac{\partial^2 \Phi}{\partial r^2} + \frac{1}{r} \frac{\partial \Phi}{\partial r} + \frac{1}{r^2} \frac{\partial^2 \Phi}{\partial \theta^2} + \frac{\partial^2 \Phi}{\partial z^2} + \frac{\omega^2}{c_p^2} \Phi = 0 \tag{4.20}$$

Calculate the derivatives

$$\begin{aligned}
 \frac{\partial u_r}{\partial r} &= \frac{\partial^2 \Phi}{\partial r^2} + \frac{1}{r} \frac{\partial^2 H_z}{\partial r \partial \theta} - \frac{1}{r^2} \frac{\partial H_z}{\partial \theta} - \frac{\partial^2 H_\theta}{\partial r \partial z} & \frac{\partial u_\theta}{\partial r} &= \frac{1}{r} \frac{\partial^2 \Phi}{\partial r \partial \theta} - \frac{1}{r^2} \frac{\partial \Phi}{\partial \theta} + \frac{\partial^2 H_r}{\partial r \partial z} - \frac{\partial^2 H_z}{\partial r^2} \\
 \frac{\partial u_r}{\partial \theta} &= \frac{\partial^2 \Phi}{\partial r \partial \theta} + \frac{1}{r} \frac{\partial^2 H_z}{\partial \theta^2} - \frac{\partial^2 H_\theta}{\partial \theta \partial z} & \frac{\partial u_\theta}{\partial \theta} &= \frac{1}{r} \frac{\partial^2 \Phi}{\partial \theta^2} + \frac{\partial^2 H_r}{\partial \theta \partial z} - \frac{\partial^2 H_z}{\partial r \partial \theta} \\
 \frac{\partial u_r}{\partial z} &= \frac{\partial^2 \Phi}{\partial r \partial z} + \frac{1}{r} \frac{\partial^2 H_z}{\partial \theta \partial z} - \frac{\partial^2 H_\theta}{\partial z^2} & \frac{\partial u_\theta}{\partial z} &= \frac{1}{r} \frac{\partial^2 \Phi}{\partial \theta \partial z} + \frac{\partial^2 H_r}{\partial z^2} - \frac{\partial^2 H_z}{\partial r \partial z}
 \end{aligned} \tag{4.21}$$

$$\begin{aligned}
 \frac{\partial u_z}{\partial r} &= \frac{\partial^2 \Phi}{\partial r \partial z} + \frac{\partial^2 H_\theta}{\partial r^2} + \frac{1}{r} \frac{\partial H_\theta}{\partial r} - \frac{H_\theta}{r^2} - \frac{1}{r} \frac{\partial^2 H_r}{\partial r \partial \theta} + \frac{1}{r^2} \frac{\partial H_r}{\partial \theta} \\
 \frac{\partial u_z}{\partial \theta} &= \frac{\partial^2 \Phi}{\partial \theta \partial z} + \frac{\partial^2 H_\theta}{\partial r \partial \theta} + \frac{1}{r} \frac{\partial H_\theta}{\partial \theta} - \frac{1}{r} \frac{\partial^2 H_r}{\partial \theta^2} \\
 \frac{\partial u_z}{\partial z} &= \frac{\partial^2 \Phi}{\partial z^2} + \frac{\partial^2 H_\theta}{\partial r \partial z} + \frac{1}{r} \frac{\partial H_\theta}{\partial z} - \frac{1}{r} \frac{\partial^2 H_r}{\partial \theta \partial z}
 \end{aligned}$$

Substitution of Eq. (4.17) into Eq. (4.19) yields

$$\Delta = \varepsilon_{rr} + \varepsilon_{\theta\theta} + \varepsilon_{zz} = \frac{\partial u_r}{\partial r} + \frac{1}{r} \frac{\partial u_\theta}{\partial \theta} + \frac{u_r}{r} + \frac{\partial u_z}{\partial z} \tag{4.22}$$

Substituting the related derivative in Eq. (4.22) and using Eq. (4.20) one gets

$$\begin{aligned}
\Delta &= \frac{\partial^2 \Phi}{\partial r^2} + \frac{1}{r} \frac{\partial^2 H_z}{\partial r \partial \theta} - \frac{1}{r^2} \frac{\partial H_z}{\partial \theta} - \frac{\partial^2 H_\theta}{\partial r \partial z} + \frac{1}{r} \left(\frac{1}{r} \frac{\partial^2 \Phi}{\partial \theta^2} + \frac{\partial^2 H_r}{\partial \theta \partial z} - \frac{\partial^2 H_z}{\partial r \partial \theta} \right) \\
&+ \frac{1}{r} \left(\frac{\partial \Phi}{\partial r} + \frac{1}{r} \frac{\partial H_z}{\partial \theta} - \frac{\partial H_\theta}{\partial z} \right) + \frac{\partial^2 \Phi}{\partial z^2} + \frac{\partial^2 H_\theta}{\partial r \partial z} + \frac{1}{r} \frac{\partial H_\theta}{\partial z} - \frac{1}{r} \frac{\partial^2 H_r}{\partial \theta \partial z} \\
&= \frac{\partial^2 \Phi}{\partial r^2} + \frac{1}{r^2} \frac{\partial^2 \Phi}{\partial \theta^2} + \frac{1}{r} \frac{\partial \Phi}{\partial r} + \frac{\partial^2 \Phi}{\partial z^2} \\
&= -\frac{\omega^2}{c_p^2} \Phi
\end{aligned} \tag{4.23}$$

Substitution of Eq. (4.17) and (4.23) into Eq.(4.18) gives

$$\begin{aligned}
\sigma_{rr} &= -\lambda \frac{\omega^2}{c_p^2} \Phi + 2\mu \frac{\partial u_r}{\partial r} & \sigma_{r\theta} &= \mu \left(\frac{1}{r} \frac{\partial u_r}{\partial \theta} + \frac{\partial u_\theta}{\partial r} - \frac{u_\theta}{r} \right) \\
\sigma_{\theta\theta} &= -\lambda \frac{\omega^2}{c_p^2} \Phi + 2\mu \left(\frac{1}{r} \frac{\partial u_\theta}{\partial \theta} + \frac{u_r}{r} \right) & \text{and } \sigma_{\theta z} &= \mu \left(\frac{\partial u_\theta}{\partial z} + \frac{1}{r} \frac{\partial u_z}{\partial \theta} \right) \\
\sigma_{zz} &= -\lambda \frac{\omega^2}{c_p^2} \Phi + 2\mu \frac{\partial u_z}{\partial z} & \sigma_{rz} &= \mu \left(\frac{\partial u_z}{\partial r} + \frac{\partial u_r}{\partial z} \right)
\end{aligned} \tag{4.24}$$

Substitution of Eq. (4.21) into Eq. (4.24) yields the stress components as

$$\sigma_{rr} = -\lambda \frac{\omega^2}{c_p^2} \Phi + 2\mu \left(\frac{\partial^2 \Phi}{\partial r^2} + \frac{1}{r} \frac{\partial^2 H_z}{\partial r \partial \theta} - \frac{1}{r^2} \frac{\partial H_z}{\partial \theta} - \frac{\partial^2 H_\theta}{\partial r \partial z} \right) \tag{4.25}$$

$$\sigma_{\theta\theta} = -\lambda \frac{\omega^2}{c_p^2} \Phi + 2\mu \left(\frac{1}{r^2} \frac{\partial^2 \Phi}{\partial \theta^2} + \frac{1}{r} \frac{\partial^2 H_r}{\partial \theta \partial z} - \frac{1}{r} \frac{\partial^2 H_z}{\partial \theta \partial r} + \frac{1}{r} \frac{\partial \Phi}{\partial r} + \frac{1}{r^2} \frac{\partial H_z}{\partial \theta} - \frac{1}{r} \frac{\partial H_\theta}{\partial z} \right) \tag{4.26}$$

$$\sigma_{zz} = -\lambda \frac{\omega^2}{c_p^2} \Phi + 2\mu \left(\frac{\partial^2 \Phi}{\partial z^2} + \frac{\partial^2 H_\theta}{\partial r \partial z} + \frac{1}{r} \frac{\partial H_\theta}{\partial z} - \frac{1}{r} \frac{\partial^2 H_r}{\partial \theta \partial z} \right) \tag{4.27}$$

$$\sigma_{r\theta} = \mu \left(\frac{2}{r} \frac{\partial^2 \Phi}{\partial \theta \partial r} + \frac{1}{r^2} \frac{\partial^2 H_z}{\partial \theta^2} - \frac{1}{r} \frac{\partial^2 H_\theta}{\partial \theta \partial z} + \frac{\partial^2 H_r}{\partial r \partial z} - \frac{\partial^2 H_z}{\partial r^2} + \frac{1}{r^2} \frac{\partial \Phi}{\partial \theta} + \frac{1}{r} \frac{\partial H_r}{\partial z} - \frac{1}{r} \frac{\partial H_z}{\partial r} \right) \tag{4.28}$$

$$\sigma_{\theta z} = \mu \left(\frac{2}{r} \frac{\partial^2 \Phi}{\partial \theta \partial z} + \frac{\partial^2 H_r}{\partial z^2} - \frac{\partial^2 H_z}{\partial r \partial z} + \frac{1}{r} \frac{\partial^2 H_\theta}{\partial \theta \partial r} + \frac{1}{r^2} \frac{\partial H_\theta}{\partial \theta} - \frac{1}{r^2} \frac{\partial^2 H_r}{\partial \theta^2} \right) \tag{4.29}$$

$$\sigma_{rz} = \mu \left(2 \frac{\partial^2 \Phi}{\partial r \partial z} + \frac{1}{r} \frac{\partial^2 H_z}{\partial \theta \partial z} + \frac{\partial^2 H_\theta}{\partial r^2} - \frac{H_\theta}{r^2} + \frac{1}{r} \frac{\partial H_\theta}{\partial r} - \frac{1}{r} \frac{\partial^2 H_r}{\partial \theta \partial r} + \frac{1}{r^2} \frac{\partial H_r}{\partial \theta} - \frac{\partial^2 H_\theta}{\partial z^2} \right) \tag{4.30}$$

4.3 A JUDICIOUS FORM OF THE GAUGE CONDITION

In this section, we showed the derivation of a judicious form of the gauge condition that can be used for the non-axisymmetric problem. The gauge depends on the nature of the problem. However, the proper choices of gauge make the problems easier to solve [34]. A multitude of choices exist [31] as used in elastodynamics [18] [32] and electrodynamics [33] [34] [35]. For example, Gazis [40] [32] used $\vec{\nabla} \cdot \vec{H} = F(\vec{r}, t)$ in order to simplify the shear potentials when developing the solution of wave propagation in a hollow cylinder [32].

We propose to view the gauge condition Eq. (4.9) as a superposition of Lamb wave gauge (f_{LW}) and SH wave gauge (f_{SH}) [26]; hence we write Eq. (4.9) as:

$$\vec{\nabla} \cdot \vec{H} = f(\vec{r}, \omega) = f_{LW}(\vec{r}, \omega) + f_{SH}(\vec{r}, \omega) \quad (\text{"Bhuiyan-Giurgiutiu" gauge condition}) \quad (4.31)$$

Expanding Eq. (4.31) in cylindrical coordinates yields

$$\frac{\partial H_r}{\partial r} + \frac{H_r}{r} + \frac{1}{r} \frac{\partial H_\theta}{\partial \theta} + \frac{\partial H_z}{\partial z} = f_{LW}(\vec{r}, \omega) + f_{SH}(\vec{r}, \omega) \quad (4.32)$$

On the one hand, we observe that the SH waves should not have any out-of-plane displacement component u_z . On the other hand, it can be observed from Eq. (4.14) that the out-of-plane displacement component u_z does not depend on the potential H_z . Hence, it is apparent that the H_z potential is associated with the SH waves and hence we can write the SH gauge part of Eq. (4.32) as

$$\frac{\partial H_z}{\partial z} = f_{SH}(\vec{r}, \omega) \quad (\text{SH gauge}) \quad (4.33)$$

This shear potential allocation also works for the axisymmetric and straight-crested guided waves as discussed in Chapter 3 and ref. [26].

The remainder of Eq. (4.32) is allocated to the Lamb wave gauge, i.e.,

$$\frac{\partial H_r}{\partial r} + \frac{H_r}{r} + \frac{1}{r} \frac{\partial H_\theta}{\partial \theta} = f_{LW}(\vec{r}, \omega) \quad (\text{Lamb wave gauge}) \quad (4.34)$$

We take $f_{LW}(\vec{r}, \omega) = f_{LW}(r, \theta, \omega)$. Hence, Eq. (4.34) becomes

$$\frac{\partial H_r}{\partial r} + \frac{H_r}{r} + \frac{1}{r} \frac{\partial H_\theta}{\partial \theta} = f_{LW}(r, \theta, \omega) \quad (4.35)$$

Differentiation of Eq. (4.35) with respect to z gives

$$\frac{\partial^2 H_r}{\partial r \partial z} + \frac{1}{r} \frac{\partial H_r}{\partial z} + \frac{1}{r} \frac{\partial^2 H_\theta}{\partial \theta \partial z} = 0 \quad (4.36)$$

Upon rearrangement and multiplication by r , Eq. (4.36) yields

$$r \frac{\partial^2 H_r}{\partial r \partial z} + \frac{\partial H_r}{\partial z} = - \frac{\partial^2 H_\theta}{\partial \theta \partial z} \quad (4.37)$$

Using the differential product rule, Eq. (4.37) yields

$$\frac{\partial}{\partial r} \left(r \frac{\partial H_r}{\partial z} \right) = \frac{\partial}{\partial \theta} \left(- \frac{\partial H_\theta}{\partial z} \right) \quad (4.38)$$

We now introduce a new potential H_v such that

$$r \frac{\partial H_r}{\partial z} = \frac{\partial H_v}{\partial \theta} \quad \text{and} \quad - \frac{\partial H_\theta}{\partial z} = \frac{\partial H_v}{\partial r} \quad (\text{alternate LW gauge condition}) \quad (4.39)$$

Substitution of Eq. (4.39) into Eq. (4.38) yields the identity

$$\frac{\partial^2 H_v}{\partial r \partial \theta} = \frac{\partial^2 H_v}{\partial \theta \partial r} \quad (4.40)$$

Thus, the LW gauge condition Eq. (4.35) has been replaced by the new gauge condition Eq. (4.39). It can be noted from Eq. (4.39) that the new potential H_v creates a bridge between H_r and H_θ through the differential relation Eq. (4.39). As it will be shown in Section 4.4.2, the new potential H_v satisfies the wave equation. This new potential H_v

can be used to coalesce the effect of the two potentials H_r, H_θ and thus reduce the number of unknown potentials to only three (Φ, H_v, H_z), instead of the original four (Φ, H_r, H_θ, H_z).

4.4 SIMPLIFICATION OF THE NON-AXISYMMETRIC PROBLEM USING THE GAUGE CONDITION

4.4.1 REDUCTION OF THE NUMBER OF POTENTIALS USING THE GAUGE CONDITION

Recall the modified form of the gauge condition, Eq. (4.39),

$$\begin{aligned} r \frac{\partial H_r}{\partial z} &= \frac{\partial H_v}{\partial \theta} \\ -\frac{\partial H_\theta}{\partial z} &= \frac{\partial H_v}{\partial r} \end{aligned} \quad (4.41)$$

We will use this relation to simplify the governing equations, displacement equations, and stress equations.

4.4.2 SIMPLIFICATION OF THE GOVERNING EQUATIONS FOR NON-AXISYMMETRIC WAVES IN CYLINDRICAL COORDINATES

Recall Eq. (4.12)

$$\frac{\partial^2 H_r}{\partial r^2} + \frac{1}{r} \frac{\partial H_r}{\partial r} + \frac{1}{r^2} \frac{\partial^2 H_r}{\partial \theta^2} + \frac{\partial^2 H_r}{\partial z^2} - \frac{2}{r^2} \frac{\partial H_\theta}{\partial \theta} - \frac{1}{r^2} H_r + \frac{\omega^2}{c_s^2} H_r = 0 \quad (4.42)$$

Differentiation of Eq. (4.42) with respect to z yields

$$\frac{\partial^3 H_r}{\partial r^2 \partial z} + \frac{1}{r} \frac{\partial^2 H_r}{\partial r \partial z} + \frac{1}{r^2} \frac{\partial^3 H_r}{\partial \theta^2 \partial z} + \frac{\partial^3 H_r}{\partial z^3} - \frac{2}{r^2} \frac{\partial^2 H_\theta}{\partial \theta \partial z} - \frac{1}{r^2} \frac{\partial H_r}{\partial z} + \frac{\omega^2}{c_s^2} \frac{\partial H_r}{\partial z} = 0 \quad (4.43)$$

Substitution of Eq. (4.41) into Eq. (4.43) yields, after some manipulation,

$$\frac{\partial^3 H_v}{\partial r^2 \partial \theta} + \frac{1}{r} \frac{\partial^2 H_v}{\partial r \partial \theta} + \frac{1}{r^2} \frac{\partial^3 H_v}{\partial \theta^3} + \frac{\partial^3 H_v}{\partial \theta \partial z^2} + \frac{\omega^2}{c_s^2} \frac{\partial H_v}{\partial \theta} = 0 \quad (4.44)$$

Equation (4.44) can be expressed as

$$\frac{\partial}{\partial \theta} \left(\frac{\partial^2 H_v}{\partial r^2} + \frac{1}{r} \frac{\partial H_v}{\partial r} + \frac{1}{r^2} \frac{\partial^2 H_v}{\partial \theta^2} + \frac{\partial^2 H_v}{\partial z^2} + \frac{\omega^2}{c_s^2} H_v \right) = 0 \quad (4.45)$$

Integration of Eq. (4.45) with respect to θ and selection of the integration constant to be zero yields

$$\frac{\partial^2 H_v}{\partial r^2} + \frac{1}{r} \frac{\partial H_v}{\partial r} + \frac{1}{r^2} \frac{\partial^2 H_v}{\partial \theta^2} + \frac{\partial^2 H_v}{\partial z^2} + \frac{\omega^2}{c_s^2} H_v = 0 \quad (4.46)$$

Equation (4.46) is a wave equation. Thus, the new potential H_v also satisfies the wave equation and propagates with the wavespeed c_s .

Recall Eq. (4.13)

$$\frac{\partial^2 H_\theta}{\partial r^2} + \frac{1}{r} \frac{\partial H_\theta}{\partial r} + \frac{1}{r^2} \frac{\partial^2 H_\theta}{\partial \theta^2} + \frac{\partial^2 H_\theta}{\partial z^2} + \frac{2}{r^2} \frac{\partial H_r}{\partial \theta} - \frac{1}{r^2} H_\theta + \frac{\omega^2}{c_s^2} H_\theta = 0 \quad (4.47)$$

Differentiation of Eq. (4.47) with respect to z gives

$$\frac{\partial^3 H_\theta}{\partial r^2 \partial z} + \frac{1}{r} \frac{\partial^2 H_\theta}{\partial r \partial z} + \frac{1}{r^2} \frac{\partial^3 H_\theta}{\partial \theta^2 \partial z} + \frac{\partial^3 H_\theta}{\partial z^3} + \frac{2}{r^2} \frac{\partial^2 H_r}{\partial \theta \partial z} - \frac{1}{r^2} \frac{\partial H_\theta}{\partial z} + \frac{\omega^2}{c_s^2} \frac{\partial H_\theta}{\partial z} = 0 \quad (4.48)$$

Substitution of the gauge condition Eq. (4.41) into Eq. (4.48) yields, after some manipulation,

$$\frac{\partial^3 H_v}{\partial r^3} + \frac{1}{r} \frac{\partial^2 H_v}{\partial r^2} + \frac{1}{r^2} \frac{\partial^3 H_v}{\partial r \partial \theta^2} + \frac{\partial^2 H_v}{\partial r \partial z^2} - \frac{1}{r^2} \frac{\partial H_v}{\partial r} - \frac{2}{r^3} \frac{\partial^2 H_v}{\partial \theta^2} + \frac{\omega^2}{c_s^2} \frac{\partial H_v}{\partial r} = 0 \quad (4.49)$$

Equation (4.49) can be expressed as

$$\frac{\partial}{\partial r} \left(\frac{\partial^2 H_v}{\partial r^2} + \frac{1}{r} \frac{\partial H_v}{\partial r} + \frac{1}{r^2} \frac{\partial^2 H_v}{\partial \theta^2} + \frac{\partial^2 H_v}{\partial z^2} + \frac{\omega^2}{c_s^2} H_v \right) = 0 \quad (4.50)$$

Integration of Eq. (4.50) with respect to r and selection of the integration constant to be zero yields

$$\frac{\partial^2 H_v}{\partial r^2} + \frac{1}{r} \frac{\partial H_v}{\partial r} + \frac{1}{r^2} \frac{\partial^2 H_v}{\partial \theta^2} + \frac{\partial^2 H_v}{\partial z^2} + \frac{\omega^2}{c_s^2} H_v = 0 \quad (4.51)$$

Equation (4.51) is the same wave equation as Eq. (4.46). Thus, the two coupled governing equations in H_r, H_θ have combined into a single governing equation in the new potential H_v . This new governing equation is a wave equation with wavespeed c_s . The new shear potential H_v replaces the two initial shear potentials H_r and H_θ .

Hence, the use of Eq. (4.41) into Eqs. (4.12), (4.13) yields a single equation, i.e.,

$$\frac{\partial^2 H_v}{\partial r^2} + \frac{1}{r} \frac{\partial H_v}{\partial r} + \frac{1}{r^2} \frac{\partial^2 H_v}{\partial \theta^2} + \frac{\partial^2 H_v}{\partial z^2} + \frac{\omega^2}{c_s^2} H_v = 0 \quad (4.52)$$

Equation (4.52) is the wave equation for the new potential H_v . It can be noted that the new potential H_v propagates with wavespeed c_s , hence it is associated with the shear waves just like the old potentials H_r and H_θ . Thus, the governing equations for non-axisymmetric wave propagation in cylindrical coordinates can now be reduced to three uncoupled equations in the potentials Φ, H_v, H_z , i.e.,

$$\frac{\partial^2 \Phi}{\partial r^2} + \frac{1}{r} \frac{\partial \Phi}{\partial r} + \frac{1}{r^2} \frac{\partial^2 \Phi}{\partial \theta^2} + \frac{\partial^2 \Phi}{\partial z^2} + \frac{\omega^2}{c_p^2} \Phi = 0 \quad (4.53)$$

$$\frac{\partial^2 H_z}{\partial r^2} + \frac{1}{r} \frac{\partial H_z}{\partial r} + \frac{1}{r^2} \frac{\partial^2 H_z}{\partial \theta^2} + \frac{\partial^2 H_z}{\partial z^2} + \frac{\omega^2}{c_s^2} H_z = 0 \quad (4.54)$$

$$\frac{\partial^2 H_v}{\partial r^2} + \frac{1}{r} \frac{\partial H_v}{\partial r} + \frac{1}{r^2} \frac{\partial^2 H_v}{\partial \theta^2} + \frac{\partial^2 H_v}{\partial z^2} + \frac{\omega^2}{c_s^2} H_v = 0 \quad (4.55)$$

4.4.3 SIMPLIFICATION OF THE DISPLACEMENT AND STRESS EXPRESSIONS

Substitution of Eq. (4.41) into the expressions of u_r and u_θ of Eqs. (4.14), (4.15)

gives

$$\begin{aligned}
u_r &= \frac{\partial \Phi}{\partial r} + \frac{\partial H_v}{\partial r} + \frac{1}{r} \frac{\partial H_z}{\partial \theta} \\
u_\theta &= \frac{1}{r} \frac{\partial \Phi}{\partial \theta} + \frac{1}{r} \frac{\partial H_v}{\partial \theta} - \frac{\partial H_z}{\partial r}
\end{aligned} \tag{4.56}$$

The displacement component u_z of Eq. (4.16) should also be represented in terms of Φ and H_v . For the moment, let,

$$u_z = \frac{\partial \Phi}{\partial z} + \kappa \frac{\partial H_v}{\partial z} \tag{4.57}$$

where κ is a wavenumber parameter that can be determined as $\kappa = -\xi^2 / \eta_s^2$. (see Section 4.5.2)

Hence, the application of the new gauge condition Eq. (4.41) into Eqs. (4.14)-(4.16) yield the following simplified displacement expressions:

$$u_r = \frac{\partial \Phi}{\partial r} + \frac{\partial H_v}{\partial r} + \frac{1}{r} \frac{\partial H_z}{\partial \theta} \tag{4.58}$$

$$u_\theta = \frac{1}{r} \frac{\partial \Phi}{\partial \theta} + \frac{1}{r} \frac{\partial H_v}{\partial \theta} - \frac{\partial H_z}{\partial r} \tag{4.59}$$

$$u_z = \frac{\partial \Phi}{\partial z} + \kappa \frac{\partial H_v}{\partial z} \tag{4.60}$$

Recall the strain-displacement relations:

$$\begin{aligned}
\varepsilon_{rr} &= \frac{\partial u_r}{\partial r} & \varepsilon_{r\theta} &= \frac{1}{2} \left(\frac{1}{r} \frac{\partial u_r}{\partial \theta} + \frac{\partial u_\theta}{\partial r} - \frac{u_\theta}{r} \right) \\
\varepsilon_{\theta\theta} &= \frac{1}{r} \frac{\partial u_\theta}{\partial \theta} + \frac{u_r}{r} & \text{and} & \quad \varepsilon_{\theta z} &= \frac{1}{2} \left(\frac{\partial u_\theta}{\partial z} + \frac{1}{r} \frac{\partial u_z}{\partial \theta} \right) \\
\varepsilon_{zz} &= \frac{\partial u_z}{\partial z} & \varepsilon_{rz} &= \frac{1}{2} \left(\frac{\partial u_z}{\partial r} + \frac{\partial u_r}{\partial z} \right)
\end{aligned} \tag{4.61}$$

Recall the stress-strain relations:

$$\begin{aligned}
\sigma_{rr} &= \lambda\Delta + 2\mu\varepsilon_{rr} & \sigma_{r\theta} &= 2\mu\varepsilon_{r\theta} \\
\sigma_{\theta\theta} &= \lambda\Delta + 2\mu\varepsilon_{\theta\theta} & \text{and} & & \sigma_{\theta z} &= 2\mu\varepsilon_{\theta z} \\
\sigma_{zz} &= \lambda\Delta + 2\mu\varepsilon_{zz} & & & \sigma_{rz} &= 2\mu\varepsilon_{rz}
\end{aligned} \tag{4.62}$$

where Δ was calculated in Eq. (4.23) as

$$\Delta = -\frac{\omega^2}{c_p^2} \Phi \tag{4.63}$$

Calculate the derivatives

$$\begin{aligned}
\frac{\partial u_r}{\partial r} &= \frac{\partial^2 \Phi}{\partial r^2} + \frac{\partial^2 H_v}{\partial r^2} + \frac{1}{r} \frac{\partial^2 H_z}{\partial r \partial \theta} - \frac{1}{r^2} \frac{\partial H_z}{\partial \theta} & \frac{\partial u_\theta}{\partial r} &= \frac{1}{r} \frac{\partial^2 \Phi}{\partial r \partial \theta} - \frac{1}{r^2} \frac{\partial \Phi}{\partial \theta} + \frac{1}{r} \frac{\partial^2 H_v}{\partial r \partial \theta} - \frac{1}{r^2} \frac{\partial H_v}{\partial \theta} - \frac{\partial^2 H_z}{\partial r^2} \\
\frac{\partial u_r}{\partial \theta} &= \frac{\partial^2 \Phi}{\partial r \partial \theta} + \frac{\partial^2 H_v}{\partial r \partial \theta} + \frac{1}{r} \frac{\partial^2 H_z}{\partial \theta^2} & \frac{\partial u_\theta}{\partial \theta} &= \frac{1}{r} \frac{\partial^2 \Phi}{\partial \theta^2} + \frac{1}{r} \frac{\partial^2 H_v}{\partial \theta^2} - \frac{\partial^2 H_z}{\partial r \partial \theta} \\
\frac{\partial u_r}{\partial z} &= \frac{\partial^2 \Phi}{\partial r \partial z} + \frac{\partial^2 H_v}{\partial r \partial z} + \frac{1}{r} \frac{\partial^2 H_z}{\partial \theta \partial z} & \frac{\partial u_\theta}{\partial z} &= \frac{1}{r} \frac{\partial^2 \Phi}{\partial \theta \partial z} + \frac{1}{r} \frac{\partial^2 H_v}{\partial \theta \partial z} - \frac{\partial^2 H_z}{\partial r \partial z}
\end{aligned} \tag{4.64}$$

$$\begin{aligned}
\frac{\partial u_z}{\partial r} &= \frac{\partial^2 \Phi}{\partial r \partial z} + \kappa \frac{\partial^2 H_v}{\partial r \partial z} \\
\frac{\partial u_z}{\partial \theta} &= \frac{\partial^2 \Phi}{\partial \theta \partial z} + \kappa \frac{\partial^2 H_v}{\partial \theta \partial z} \\
\frac{\partial u_z}{\partial z} &= \frac{\partial^2 \Phi}{\partial z^2} + \kappa \frac{\partial^2 H_v}{\partial z^2}
\end{aligned}$$

Substituting Eq. (4.63) and Eq. (4.61) into Eq.(4.62), one gets

$$\begin{aligned}
\sigma_{rr} &= -\lambda \frac{\omega^2}{c_p^2} \Phi + 2\mu \frac{\partial u_r}{\partial r} & \sigma_{r\theta} &= \mu \left(\frac{1}{r} \frac{\partial u_r}{\partial \theta} + \frac{\partial u_\theta}{\partial r} - \frac{u_\theta}{r} \right) \\
\sigma_{\theta\theta} &= -\lambda \frac{\omega^2}{c_p^2} \Phi + 2\mu \left(\frac{1}{r} \frac{\partial u_\theta}{\partial \theta} + \frac{u_r}{r} \right) & \text{and} & & \sigma_{\theta z} &= \mu \left(\frac{\partial u_\theta}{\partial z} + \frac{1}{r} \frac{\partial u_z}{\partial \theta} \right) \\
\sigma_{zz} &= -\lambda \frac{\omega^2}{c_p^2} \Phi + 2\mu \frac{\partial u_z}{\partial z} & & & \sigma_{rz} &= \mu \left(\frac{\partial u_z}{\partial r} + \frac{\partial u_r}{\partial z} \right)
\end{aligned} \tag{4.65}$$

Substitution of Eq. (4.64) into Eq. (4.65) yields the simplified stress expressions:

$$\sigma_{rr} = -\lambda \frac{\omega^2}{c_p^2} \Phi + 2\mu \left(\frac{\partial^2 \Phi}{\partial r^2} + \frac{\partial^2 H_v}{\partial r^2} + \frac{1}{r} \frac{\partial^2 H_z}{\partial r \partial \theta} - \frac{1}{r^2} \frac{\partial H_z}{\partial \theta} \right) \tag{4.66}$$

$$\sigma_{\theta\theta} = -\lambda \frac{\omega^2}{c_p^2} \Phi + 2\mu \left(\frac{1}{r^2} \frac{\partial^2 \Phi}{\partial \theta^2} + \frac{1}{r^2} \frac{\partial^2 H_v}{\partial \theta^2} - \frac{1}{r} \frac{\partial^2 H_z}{\partial r \partial \theta} + \frac{1}{r} \frac{\partial \Phi}{\partial r} + \frac{1}{r} \frac{\partial H_v}{\partial r} + \frac{1}{r^2} \frac{\partial H_z}{\partial \theta} \right) \quad (4.67)$$

$$\sigma_{zz} = -\lambda \frac{\omega^2}{c_p^2} \Phi + 2\mu \left(\frac{\partial^2 \Phi}{\partial z^2} + \kappa \frac{\partial^2 H_v}{\partial z^2} \right) \quad (4.68)$$

$$\sigma_{r\theta} = \mu \left(\frac{2}{r} \frac{\partial^2 \Phi}{\partial r \partial \theta} - \frac{2}{r^2} \frac{\partial \Phi}{\partial \theta} + \frac{2}{r} \frac{\partial^2 H_v}{\partial r \partial \theta} - \frac{2}{r^2} \frac{\partial H_v}{\partial \theta} + \frac{1}{r} \frac{\partial H_z}{\partial r} - \frac{\partial^2 H_z}{\partial r^2} + \frac{1}{r^2} \frac{\partial^2 H_z}{\partial \theta^2} \right) \quad (4.69)$$

$$\sigma_{\theta z} = \mu \left(\frac{2}{r} \frac{\partial^2 \Phi}{\partial \theta \partial z} + \frac{\kappa+1}{r} \frac{\partial^2 H_v}{\partial \theta \partial z} - \frac{\partial^2 H_z}{\partial r \partial z} \right) \quad (4.70)$$

$$\sigma_{rz} = \mu \left(2 \frac{\partial^2 \Phi}{\partial r \partial z} + (\kappa+1) \frac{\partial^2 H_v}{\partial r \partial z} + \frac{1}{r} \frac{\partial^2 H_z}{\partial \theta \partial z} \right) \quad (4.71)$$

It is observed from Eqs.(4.58)-(4.71) that the displacements and stress components are expressed in terms of only three potentials Φ , H_v , H_z . Hence only three potentials Φ , H_v , H_z are needed to fully solve the non-axisymmetric guided-wave problem in cylindrical coordinates.

4.5 SOLUTION OF THE NON-AXISYMMETRIC GUIDED WAVE PROBLEM IN CYLINDRICAL COORDINATES

4.5.1 GENERAL SOLUTION FOR THE POTENTIALS

Equations (4.53)-(4.55) may be solved by the method of separation of variables.

Recall the governing equations Eq. (4.53)-(4.55)

$$\frac{\partial^2 \Phi}{\partial r^2} + \frac{1}{r} \frac{\partial \Phi}{\partial r} + \frac{1}{r^2} \frac{\partial^2 \Phi}{\partial \theta^2} + \frac{\partial^2 \Phi}{\partial z^2} + \frac{\omega^2}{c_p^2} \Phi = 0 \quad (4.72)$$

$$\frac{\partial^2 H_v}{\partial r^2} + \frac{1}{r} \frac{\partial H_v}{\partial r} + \frac{1}{r^2} \frac{\partial^2 H_v}{\partial \theta^2} + \frac{\partial^2 H_v}{\partial z^2} + \frac{\omega^2}{c_s^2} H_v = 0 \quad (4.73)$$

$$\frac{\partial^2 H_z}{\partial r^2} + \frac{1}{r} \frac{\partial H_z}{\partial r} + \frac{1}{r^2} \frac{\partial^2 H_z}{\partial \theta^2} + \frac{\partial^2 H_z}{\partial z^2} + \frac{\omega^2}{c_s^2} H_z = 0 \quad (4.74)$$

Let,

$$\Phi = f(r) \cos n\theta F(z) \quad (4.75)$$

Substitution of Eq. (4.75) into Eq. (4.72) yields

$$(f'' + \frac{1}{r} f') \cos n\theta F(z) - \frac{n^2}{r^2} f \cos n\theta F(z) + f \cos n\theta F''(z) + \frac{\omega^2}{c_p^2} f \cos n\theta F(z) = 0 \quad (4.76)$$

Divide Eq. (4.76) by $f(r) \cos n\theta F(z)$ and obtain

$$\frac{f''}{f} + \frac{1}{r} \frac{f'}{f} - \frac{n^2}{r^2} + \frac{F''}{F} + \frac{\omega^2}{c_p^2} = 0 \quad (4.77)$$

Equation (4.77) can be written as

$$\frac{f''}{f} + \frac{1}{r} \frac{f'}{f} - \frac{n^2}{r^2} + \frac{\omega^2}{c_p^2} = -\frac{F''}{F} = \eta_p^2 \quad (\text{separation constant}) \quad (4.78)$$

Equation (4.78) can be separated into two equations

$$r^2 f'' + r f' + (\frac{\omega^2}{c_p^2} - \eta_p^2) r^2 f - n^2 f = 0 \quad (4.79)$$

$$F'' + \eta_p^2 F = 0 \quad (4.80)$$

Define $\xi^2 = \omega^2 / c_p^2 - \eta_p^2$, thus Eq. (4.79) yields

$$r^2 f'' + r f' + (\xi^2 r^2 - n^2) f = 0 \quad (4.81)$$

For an outward propagating wave, Eq. (4.81) accepts the solution

$$f(r) = A_1 H_n^{(1)}(\xi r) \quad (4.82)$$

Equation (4.80) accepts the solution

$$F(z) = A_2 \sin \eta_p z + A_3 \cos \eta_p z \quad (4.83)$$

Substitution of Eqs. (4.82), (4.83) into (4.75) and letting the constants $A_1 A_2 = A$ and $A_1 A_3 = B$ yields

$$\Phi = (A \sin \eta_p z + B \cos \eta_p z) \cos n\theta H_n^{(1)}(\xi r) \quad (4.84)$$

Adding the time-harmonic term $e^{-i\omega t}$, Eq. (4.84) yields

$$\Phi = F_1(z) \cos n\theta H_n^{(1)}(\xi r) e^{-i\omega t} \quad (4.85)$$

where $F_1(z)$ is given by

$$F_1(z) = A \sin \eta_p z + B \cos \eta_p z \quad (4.86)$$

Similarly, taking η_s^2 as separation constant and defining $\xi^2 = \omega^2 / c_s^2 - \eta_s^2$ the solution of Eqs.(4.73), (4.74) can be written as

$$H_v = F_2(z) \cos n\theta H_n^{(1)}(\xi r) e^{-i\omega t} \quad (4.87)$$

$$H_z = F_3(z) \sin n\theta H_n^{(1)}(\xi r) e^{-i\omega t} \quad (4.88)$$

where $F_2(z)$, $F_3(z)$ are given by

$$F_2(z) = C \sin \eta_s z + D \cos \eta_s z \quad (4.89)$$

$$F_3(z) = E \sin \eta_s z + F \cos \eta_s z \quad (4.90)$$

Hence, for outward propagating waves, the solution of Eqs.(4.53)-(4.55) takes the form:

$$\Phi = F_1(z) \cos n\theta H_n^{(1)}(\xi r) e^{-i\omega t} \quad (4.91)$$

$$H_v = F_2(z) \cos n\theta H_n^{(1)}(\xi r) e^{-i\omega t} \quad (4.92)$$

$$H_z = F_3(z) \sin n\theta H_n^{(1)}(\xi r) e^{-i\omega t} \quad (4.93)$$

where ξ is the radial wavenumber, n is the number of azimuthal nodes, and $H_n^{(1)}$ is the Hankel function of the first kind and order n . The number of azimuthal nodes n represents

the number of terms in the Fourier-series azimuthal decomposition of the external loading.

The thickness-wise variation functions $F_1(z)$, $F_2(z)$, $F_3(z)$ are given by

$$F_1(z) = A \sin \eta_p z + B \cos \eta_p z \quad (4.94)$$

$$F_2(z) = C \sin \eta_s z + D \cos \eta_s z \quad (4.95)$$

$$F_3(z) = E \sin \eta_s z + F \cos \eta_s z \quad (4.96)$$

where η_p , η_s are transverse wavenumbers defined as

$$\eta_p^2 = \frac{\omega^2}{c_p^2} - \xi^2, \quad \eta_s^2 = \frac{\omega^2}{c_s^2} - \xi^2 \quad (4.97)$$

and A, B, C, D, E, F are six unknown constants to be determined from the boundary conditions. For convenience, the time-harmonic function $e^{-i\omega t}$ shown in Eqs. (4.91)-(4.93) will be omitted from the sequel.

4.5.2 DETERMINATION OF WAVENUMBER PARAMETER κ

The wavenumber parameter κ is obtained from the governing equation Eq. (4.55), the gauge condition Eq. (4.41), and the displacement equations Eq. (4.16) as follows.

Recall the governing equation for H_v Eq. (4.55), i.e.,

$$\frac{\partial^2 H_v}{\partial r^2} + \frac{1}{r} \frac{\partial H_v}{\partial r} + \frac{1}{r^2} \frac{\partial^2 H_v}{\partial \theta^2} + \frac{\partial^2 H_v}{\partial z^2} + \frac{\omega^2}{c_s^2} H_v = 0 \quad (4.98)$$

Recall the gauge condition Eq. (4.41)

$$\begin{aligned} r \frac{\partial H_r}{\partial z} &= \frac{\partial H_v}{\partial \theta} \\ -\frac{\partial H_\theta}{\partial z} &= \frac{\partial H_v}{\partial r} \end{aligned} \quad (4.99)$$

Recall the u_z part of Eq.(4.16), i.e.,

$$u_z = \frac{\partial \Phi}{\partial z} + \frac{\partial H_\theta}{\partial r} + \frac{H_\theta}{r} - \frac{1}{r} \frac{\partial H_r}{\partial \theta} \quad (4.100)$$

Differentiating Eq. (4.100) with respect to z gives

$$\frac{\partial u_z}{\partial z} = \frac{\partial^2 \Phi}{\partial z^2} + \frac{\partial^2 H_\theta}{\partial r \partial z} + \frac{1}{r} \frac{\partial H_\theta}{\partial z} - \frac{1}{r} \frac{\partial^2 H_r}{\partial \theta \partial z} \quad (4.101)$$

Upon rearrangement and using the gauge condition Eq. (4.99), one obtains

$$\frac{\partial u_z}{\partial z} = \frac{\partial^2 \Phi}{\partial z^2} - \frac{\partial^2 H_v}{\partial r^2} - \frac{1}{r} \frac{\partial H_v}{\partial r} - \frac{1}{r^2} \frac{\partial^2 H_v}{\partial \theta^2} \quad (4.102)$$

Rearrangement of Eq. (4.98) yields

$$\frac{\partial^2 H_v}{\partial r^2} + \frac{1}{r} \frac{\partial H_v}{\partial r} + \frac{1}{r^2} \frac{\partial^2 H_v}{\partial \theta^2} = -\frac{\partial^2 H_v}{\partial z^2} - \frac{\omega^2}{c_s^2} H_v \quad (4.103)$$

Substitution of Eq. (4.103) into Eq. (4.102) gives

$$\frac{\partial u_z}{\partial z} = \frac{\partial^2 \Phi}{\partial z^2} + \frac{\partial^2 H_v}{\partial z^2} + \frac{\omega^2}{c_s^2} H_v \quad (4.104)$$

Differentiation of Eq. (4.60) with respect to z yields

$$\frac{\partial u_z}{\partial z} = \frac{\partial^2 \Phi}{\partial z^2} + \kappa \frac{\partial^2 H_v}{\partial z^2} \quad (4.105)$$

Comparison of Eq. (4.104) and (4.105) gives

$$\kappa \frac{\partial^2 H_v}{\partial z^2} = \frac{\partial^2 H_v}{\partial z^2} + \frac{\omega^2}{c_s^2} H_v \quad (4.106)$$

Recall the expression of H_v given by Eq. (4.92), i.e.,

$$H_v = (C \sin \eta_s z + D \cos \eta_s z) \cos n\theta H_n^{(1)}(\xi r) \quad (4.107)$$

Differentiation of Eq. (4.107) with respect to z twice yields

$$\frac{\partial^2 H_v}{\partial z^2} = -\eta_s^2 H_v \quad (4.108)$$

Substitution of Eq. (4.108) into Eq. (4.106) yields

$$-\eta_s^2 \kappa = -\eta_s^2 + \frac{\omega^2}{c_s^2} \quad (4.109)$$

Recall Eq.(4.97), i.e.,

$$\eta_s^2 = \frac{\omega^2}{c_s^2} - \xi^2 \quad (4.110)$$

Using Eq. (4.110) into Eq. (4.109) gives

$$\kappa = -\frac{\xi^2}{\eta_s^2} \quad (4.111)$$

Equation (4.111) indicates that the wavenumber parameter κ depends on ξ and η_s .

4.5.3 APPLICATION OF FREE-SURFACE BOUNDARY CONDITIONS

The traction-free boundary conditions at the top and bottom faces of a plate of thickness $2d$ are

$$\sigma_{zz} \Big|_{z=\pm d} = 0, \quad \sigma_{\theta z} \Big|_{z=\pm d} = 0, \quad \sigma_{rz} \Big|_{z=\pm d} = 0 \quad (4.112)$$

Equation (4.112) expands to six boundary conditions that are used to determine the six unknowns A, B, C, D, E, F of Eqs. (4.91)-(4.93).

Recall Eqs. (4.68), (4.70), (4.71), (4.91), (4.92), (4.93), (4.94), (4.95), (4.97), i.e.,

$$\sigma_{zz} = -\lambda \frac{\omega^2}{c_p^2} \Phi + 2\mu \left(\frac{\partial^2 \Phi}{\partial z^2} + \kappa \frac{\partial^2 H_v}{\partial z^2} \right) \quad (4.113)$$

$$\sigma_{\theta z} = \mu \left(\frac{2}{r} \frac{\partial^2 \Phi}{\partial \theta \partial z} + \frac{\kappa + 1}{r} \frac{\partial^2 H_v}{\partial \theta \partial z} - \frac{\partial^2 H_z}{\partial r \partial z} \right) \quad (4.114)$$

$$\sigma_{rz} = \mu \left(2 \frac{\partial^2 \Phi}{\partial r \partial z} + (\kappa + 1) \frac{\partial^2 H_v}{\partial r \partial z} + \frac{1}{r} \frac{\partial^2 H_z}{\partial \theta \partial z} \right) \quad (4.115)$$

$$\Phi = F_1(z) \cos n\theta H_n^{(1)}(\xi r) e^{-i\omega t} \quad (4.116)$$

$$H_v = F_2(z) \cos n\theta H_n^{(1)}(\xi r) e^{-i\omega t} \quad (4.117)$$

$$H_z = F_3(z) \sin n\theta H_n^{(1)}(\xi r) e^{-i\omega t} \quad (4.118)$$

$$F_1(z) = A \sin \eta_p z + B \cos \eta_p z \quad (4.119)$$

$$F_2(z) = C \sin \eta_s z + D \cos \eta_s z \quad (4.120)$$

$$\eta_p^2 = \frac{\omega^2}{c_p^2} - \xi^2, \quad \eta_s^2 = \frac{\omega^2}{c_s^2} - \xi^2 \quad (4.121)$$

Differentiation of Eqs. (4.116), (4.117) with respect to z twice gives

$$\frac{\partial^2 \Phi}{\partial z^2} = -\eta_p^2 \Phi, \quad \frac{\partial^2 H_v}{\partial z^2} = -\eta_s^2 H_v \quad (4.122)$$

Substituting Eq. (4.113) into Eq. (4.112) yields

$$\sigma_{zz} \Big|_{z=\pm d} = -\lambda \frac{\omega^2}{c_p^2} \Phi + 2\mu \left(\frac{\partial^2 \Phi}{\partial z^2} + \kappa \frac{\partial^2 H_v}{\partial z^2} \right) \Big|_{z=\pm d} = 0 \quad (4.123)$$

Substitute Eqs. (4.116), (4.117) into Eq. (4.123) and use Eqs. (4.121)-(4.122), the identity relation $-\lambda \omega^2 / c_p^2 - 2\mu \eta_p^2 = \mu(\xi^2 - \eta_s^2)$ [47], and $\kappa = -\xi^2 / \eta_s^2$, to get

$$(\xi^2 - \eta_s^2) F_1(d) + 2\xi^2 F_2(d) = 0 \quad (4.124)$$

$$(\xi^2 - \eta_s^2) F_1(-d) + 2\xi^2 F_2(-d) = 0 \quad (4.125)$$

Substituting Eq. (4.114) into Eq. (4.112) yields

$$\sigma_{\theta z} \Big|_{z=\pm d} = \mu \left(\frac{2}{r} \frac{\partial^2 \Phi}{\partial \theta \partial z} + \frac{\kappa + 1}{r} \frac{\partial^2 H_v}{\partial \theta \partial z} - \frac{\partial^2 H_z}{\partial r \partial z} \right) \Big|_{z=\pm d} = 0 \quad (4.126)$$

For convenience, change $H_n^{(1)}$ into J_n and substitute Eqs. (4.116)-(4.118) into Eq. (4.126)

to get

$$\left[\frac{-2n}{r} J_n(\xi r) \sin n\theta F_1'(z) - \frac{(\kappa+1)n}{r} J_n(\xi r) \sin n\theta F_2'(z) - J_n'(\xi r) \sin n\theta F_3'(z) \right]_{z=\pm d} = 0 \quad (4.127)$$

Assume $\sin n\theta \neq 0$ and divide by $\sin n\theta$ to get, upon rearrangement,

$$\left[\frac{n}{r} J_n(\xi r) \{2F_1'(z) + (\kappa+1)F_2'(z)\} + J_n'(\xi r) F_3'(z) \right]_{z=\pm d} = 0 \quad (4.128)$$

Substituting Eq. (4.115) into Eq. (4.112) yields

$$\sigma_{rz} \Big|_{z=\pm d} = \mu \left(2 \frac{\partial^2 \Phi}{\partial r \partial z} + (\kappa+1) \frac{\partial^2 H_v}{\partial r \partial z} + \frac{1}{r} \frac{\partial^2 H_z}{\partial \theta \partial z} \right) \Big|_{z=\pm d} \quad (4.129)$$

Substitute Eqs. (4.116)-(4.118) into Eq. (4.129) to get

$$\left[2J_n'(\xi r) \cos n\theta F_1'(z) + (\kappa+1)J_n'(\xi r) \cos n\theta F_2'(z) + \frac{n}{r} J_n(\xi r) \cos n\theta F_3'(z) \right]_{z=\pm d} = 0 \quad (4.130)$$

Assume $\cos n\theta \neq 0$ and divide by $\cos n\theta$ to get, upon rearrangement,

$$\left[J_n'(\xi r) \{2F_1'(z) + (\kappa+1)F_2'(z)\} + \frac{n}{r} J_n(\xi r) F_3'(z) \right]_{z=\pm d} = 0 \quad (4.131)$$

Equations (4.128), (4.131) may be combined to yield simpler expressions. Define $P(z)$

and $Q(z)$ as

$$P(z) = 2F_1'(z) + (\kappa+1)F_2'(z) \quad (4.132)$$

$$Q(z) = F_3'(z) \quad (4.133)$$

Hence, Eqs. (4.128), (4.131) can be expressed as

$$\left[\frac{n}{r} J_n(\xi r) P(z) + J_n'(\xi r) Q(z) \right]_{z=\pm d} = 0 \quad (4.134)$$

$$\left[J'_n(\xi r)P(z) + \frac{n}{r} J_n(\xi r)Q(z) \right]_{z=\pm d} = 0 \quad (4.135)$$

Eq. (4.134), (4.135) can be written in matrix form, i.e.,

$$[M] \begin{Bmatrix} P(z) \\ Q(z) \end{Bmatrix}_{z=\pm d} = \begin{Bmatrix} 0 \\ 0 \end{Bmatrix} \quad (4.136)$$

where

$$[M] = \begin{bmatrix} \frac{n}{r} J_n(\xi r) & J'_n(\xi r) \\ J'_n(\xi r) & \frac{n}{r} J_n(\xi r) \end{bmatrix} \quad (4.137)$$

The determinant of Eq. (4.137) is always nonzero since

$$|M| = \frac{n^2}{r^2} J_n^2 - (J'_n)^2 \neq 0 \quad (4.138)$$

Hence, Eq. (4.136) has the null solution as the unique solution, i.e.,

$$\begin{Bmatrix} P(z) \\ Q(z) \end{Bmatrix}_{z=\pm d} = \begin{Bmatrix} 0 \\ 0 \end{Bmatrix} \quad (4.139)$$

Substitution of Eqs. (4.132), (4.133) into Eq. (4.139) yields

$$2F'_1(d) + (\kappa + 1)F'_2(d) = 0 \quad (4.140)$$

$$2F'_1(-d) + (\kappa + 1)F'_2(-d) = 0 \quad (4.141)$$

$$F'_3(d) = 0 \quad (4.142)$$

$$F'_3(-d) = 0 \quad (4.143)$$

Hence, the boundary conditions can be summarized as:

$$(\xi^2 - \eta_s^2)F_1(d) + 2\xi^2 F_2(d) = 0 \quad (4.144)$$

$$(\xi^2 - \eta_s^2)F_1(-d) + 2\xi^2 F_2(-d) = 0 \quad (4.145)$$

$$2F'_1(d) + (\kappa + 1)F'_2(d) = 0 \quad (4.146)$$

$$2F_1'(-d) + (\kappa + 1)F_2'(-d) = 0 \quad (4.147)$$

$$F_3'(d) = 0 \quad (4.148)$$

$$F_3'(-d) = 0 \quad (4.149)$$

where the functions $F_1(z)$, $F_2(z)$, $F_3(z)$ are given by Eqs. (4.94)-(4.96). Expansion of Eqs. (4.144)-(4.149) yields

$$(\xi^2 - \eta_s^2)(A \sin \eta_p d + B \cos \eta_p d) + 2\xi^2(C \sin \eta_s d + D \cos \eta_s d) = 0 \quad (4.150)$$

$$(\xi^2 - \eta_s^2)(-A \sin \eta_p d + B \cos \eta_p d) + 2\xi^2(-C \sin \eta_s d + D \cos \eta_s d) = 0 \quad (4.151)$$

$$2\eta_p(A \cos \eta_p d - B \sin \eta_p d) + (\kappa + 1)\eta_s(C \cos \eta_s d - D \sin \eta_s d) = 0 \quad (4.152)$$

$$2\eta_p(A \cos \eta_p d + B \sin \eta_p d) + (\kappa + 1)\eta_s(C \cos \eta_s d + D \sin \eta_s d) = 0 \quad (4.153)$$

$$E \cos \eta_s d - F \sin \eta_s d = 0 \quad (4.154)$$

$$E \cos \eta_s d + F \sin \eta_s d = 0 \quad (4.155)$$

4.5.3.1 Manipulation of Lamb Wave Equations

The Lamb wave equations Eqs. (4.150)-(4.153) can be rearranged into symmetric and antisymmetric Lamb wave boundary condition equations as follows.

4.5.3.1.1 Symmetric Lamb wave boundary condition equations:

Equation (4.150) plus Eq. (4.151) and Eq. (4.152) minus Eq. (4.153) yield

$$(\xi^2 - \eta_s^2)B \cos \eta_p d + 2\xi^2 D \cos \eta_s d = 0 \quad (4.156)$$

$$2\eta_p B \sin \eta_p d + (\kappa + 1)\eta_s D \sin \eta_s d = 0 \quad (4.157)$$

Equations (4.156), (4.157) can be written in matrix form, i.e.,

$$\begin{bmatrix} (\xi^2 - \eta_s^2) \cos \eta_p d & 2\xi^2 \cos \eta_s d \\ 2\eta_p \sin \eta_p d & (\kappa + 1)\eta_s \sin \eta_s d \end{bmatrix} \begin{Bmatrix} B \\ D \end{Bmatrix} = \begin{Bmatrix} 0 \\ 0 \end{Bmatrix} \quad (4.158)$$

A solution of this homogeneous system of linear equations is only possible if the determinant of the coefficient matrix of Eq. (4.158) is zero, i.e.,

$$\begin{vmatrix} (\xi^2 - \eta_s^2) \cos \eta_p d & 2\xi^2 \cos \eta_s d \\ 2\eta_p \sin \eta_p d & (\kappa + 1)\eta_s \sin \eta_s d \end{vmatrix} = 0 \quad (4.159)$$

Expansion, rearrangement, and using $\kappa = -\xi^2 / \eta_s^2$ in Eq. (4.159) yields

$$(\xi^2 - \eta_s^2)^2 \sin \eta_s d \cos \eta_p d = -4\xi^2 \eta_p \eta_s \sin \eta_p d \cos \eta_s d \quad (4.160)$$

Rearrangement of Eq. (4.160) gives the Rayleigh-Lamb equation for symmetric Lamb waves, i.e.,

$$\frac{\tan \eta_p d}{\tan \eta_s d} = -\frac{(\xi^2 - \eta_s^2)^2}{4\xi^2 \eta_p \eta_s} \quad (\text{Symmetric Lamb waves}) \quad (4.161)$$

Equation (4.161) has an infinite number of irrational solutions ξ^s which are the eigenvalues of Eq. (4.158). For every eigenvalue ξ^s , the homogeneous system (4.158) admits the solution

$$\begin{aligned} B &= -2\xi^2 \cos \eta_s d \\ D &= (\xi^2 - \eta_s^2) \cos \eta_p d \end{aligned} \quad (4.162)$$

The coefficients B, D have one degree of indeterminacy, i.e., can be scaled up or down by an arbitrary constant C^s .

4.5.3.1.2 Antisymmetric Lamb wave boundary condition equations:

Equation (4.150) minus Eq. (4.151) and Eq. (4.152) plus Eq. (4.153) yield

$$(\xi^2 - \eta_s^2)A \sin \eta_p d + 2\xi^2 C \sin \eta_s d = 0 \quad (4.163)$$

$$2\eta_p A \cos \eta_p d + (\kappa + 1)\eta_s C \cos \eta_s d = 0 \quad (4.164)$$

Equations (4.163), (4.164) can be written in matrix form, i.e.,

$$\begin{bmatrix} (\xi^2 - \eta_s^2) \sin \eta_p d & 2\xi^2 \sin \eta_s d \\ 2\eta_p \cos \eta_p d & (\kappa + 1)\eta_s \cos \eta_s d \end{bmatrix} \begin{Bmatrix} A \\ C \end{Bmatrix} = \begin{Bmatrix} 0 \\ 0 \end{Bmatrix} \quad (4.165)$$

A solution of this homogeneous system of linear equations is only possible if the determinant of the coefficient matrix of Eq. (4.165) is zero, i.e.,

$$\begin{vmatrix} (\xi^2 - \eta_s^2) \sin \eta_p d & 2\xi^2 \sin \eta_s d \\ 2\eta_p \cos \eta_p d & (\kappa + 1)\eta_s \cos \eta_s d \end{vmatrix} = 0 \quad (4.166)$$

Expansion and rearrangement of Eq. (4.166) yields

$$(\xi^2 - \eta_s^2)^2 \sin \eta_p d \cos \eta_s d = -4\xi^2 \eta_p \eta_s \sin \eta_s d \cos \eta_p d \quad (4.167)$$

Rearrangement of Eq. (4.167) gives the Rayleigh-Lamb equation for antisymmetric Lamb waves, i.e.,

$$\frac{\tan \eta_p d}{\tan \eta_s d} = -\frac{4\xi^2 \eta_p \eta_s}{(\xi^2 - \eta_s^2)^2} \quad (\text{Antisymmetric Lamb waves}) \quad (4.168)$$

Equation (4.168) has an infinite number of irrational solutions ξ^A which are the eigenvalues of Eq. (4.165). For every eigenvalue ξ^A , the homogeneous system (4.165) admits the solution

$$\begin{aligned} A &= -2\xi^2 \sin \eta_s d \\ C &= (\xi^2 - \eta_s^2) \sin \eta_p d \end{aligned} \quad (4.169)$$

The coefficients A, C have one degree of indeterminacy, i.e., can be scaled up or down by an arbitrary constant C^A .

Equations (4.161), (4.168) can be expressed compactly as

$$\frac{\tan \eta_p d}{\tan \eta_s d} = -\left[\frac{(\xi^2 - \eta_s^2)^2}{4\xi^2 \eta_p \eta_s} \right]^{\pm 1} \quad (\text{Rayleigh-Lamb equation}) \quad (4.170)$$

where +1 corresponds to symmetric Lamb wave modes, -1 corresponds to antisymmetric Lamb wave modes.

4.5.3.2 Manipulation of SH Wave Equations

The SH wave equations Eqs. (4.154), (4.155) can be rearranged into symmetric and antisymmetric SH boundary condition equations as follows.

4.5.3.2.1 Symmetric SH wave boundary condition equations:

Subtraction of (4.154) from Eq. (4.155) yields

$$2F \sin \eta_s d = 0 \quad (4.171)$$

For a non-trivial solution, $F \neq 0$; hence, Eq. (4.171) gives

$$\sin \eta_s d = 0 \quad \text{i.e.,} \quad \eta_s d = m\pi \quad (m = 0, 1, 2, \dots) \quad (4.172)$$

Equation (4.172) has an infinite number of eigenvalue solutions ξ^{SH} . For every eigenvalue ξ^{SH} , the homogeneous equation (4.171) admits the solution $F \neq 0$ with one degree of indeterminacy. We can give F the value unity, i.e.,

$$F = 1 \quad (4.173)$$

The coefficients F can be scaled up or down by an arbitrary constant C^{SH} .

4.5.3.2.2 Antisymmetric SH wave boundary condition equations:

Equation (4.154) plus Eq. (4.155) yields

$$2E \cos \eta_s d = 0 \quad (4.174)$$

For a non-trivial solution, $E \neq 0$; hence, Eq. (4.174) gives

$$\cos \eta_s d = 0 \quad \text{i.e.,} \quad \eta_s d = (2m+1)\pi/2 \quad (m = 0, 1, 2, \dots) \quad (4.175)$$

Equation (4.175) has an infinite number of eigenvalue solutions ξ^{AH} . For every eigenvalue ξ^{AH} , the homogeneous equation (4.174) admits the solution $E \neq 0$ with one degree of indeterminacy. We can give F the value unity, i.e.,

$$E = 1 \quad (4.176)$$

The coefficients E can be scaled up or down by an arbitrary constant C^{AH} .

Equations (4.172), (4.175) can be expressed compactly as

$$\cos \eta_s d \sin \eta_s d = 0 \quad (\text{SH waves}) \quad (4.177)$$

4.5.3.3 Matrix Representation of the Boundary Conditions

Equations (4.156), (4.157), (4.163), (4.164), (4.171), (4.174) can be represented in matrix form as

$$\begin{bmatrix} (\xi^2 - \eta_s^2) \cos \eta_p d & 2\xi^2 \cos \eta_s d & 0 & 0 & 0 & 0 \\ 2\eta_p \sin \eta_p d & (\kappa + 1)\eta_s \sin \eta_s d & 0 & 0 & 0 & 0 \\ 0 & 0 & (\xi^2 - \eta_s^2) \sin \eta_p d & 2\xi^2 \sin \eta_s d & 0 & 0 \\ 0 & 0 & 2\eta_p \cos \eta_p d & (\kappa + 1)\eta_s \cos \eta_s d & 0 & 0 \\ 0 & 0 & 0 & 0 & \sin \eta_s d & 0 \\ 0 & 0 & 0 & 0 & 0 & \cos \eta_s d \end{bmatrix} \begin{Bmatrix} B \\ D \\ A \\ C \\ F \\ E \end{Bmatrix} = \begin{Bmatrix} 0 \\ 0 \\ 0 \\ 0 \\ 0 \\ 0 \end{Bmatrix} \quad (4.178)$$

For constants A, B, C, D, E, F to be nonzero, the determinant of the coefficient matrix must be zero thus yielding the characteristic equations for Lamb and SH waves.

4.5.4 CHARACTERISTIC EQUATIONS

The characteristic equations from Eqs. (4.170) and (4.177) are summarized as

$$\frac{\tan \eta_p d}{\tan \eta_s d} = - \left[\frac{(\xi^2 - \eta_s^2)^2}{4\xi^2 \eta_p \eta_s} \right]^{\pm 1} \quad (\text{Lamb waves}) \quad (4.179)$$

$$\cos \eta_s d \sin \eta_s d = 0 \quad (\text{SH waves}) \quad (4.180)$$

In Eq. (4.179), +1 corresponds to symmetric Lamb wave modes, whereas -1 corresponds to antisymmetric Lamb wave modes. In Eq. (4.180), $\sin \eta_s d = 0$ corresponds

to symmetric SH waves and $\cos \eta_s d = 0$ corresponds to antisymmetric SH waves. Eq. (4.179) is the Rayleigh-Lamb characteristic equation for Lamb waves [8] and Eq. (4.180) is the characteristic equation for SH waves [18]. The solutions of Eq. (4.179) and Eq. (4.180) are the radial wavenumber ξ for Lamb wave modes and SH wave modes, respectively. In Eq.(4.180), symmetric SH wave follows $\sin \eta_s d = 0$ or, $\eta_s d = m\pi$ and antisymmetric SH wave follows $\cos \eta_s d = 0$ or, $\eta_s d = (2m+1)\pi / 2$ ($m = 0, 1, 2, 3, \dots$).

Once the wavenumbers are calculated from the characteristic equations Eqs. (4.179)-(4.180), the unknowns A, B, C, D, E, F can be obtained from Eq. (4.178). Then, the potentials Φ , H_v , H_z can be obtained from Eq. (4.91)-(4.96). The displacements and stresses can be obtained from Eqs. (4.58)-(4.60) and Eqs. (4.66)-(4.71), respectively.

For straight-crested guided wave propagation, the Lamb waves and SH waves were completely decoupled from each other. The Lamb and SH waves are also decoupled for axisymmetric circular-crested guided wave propagation. In contrast, for the non-axisymmetric guided-wave propagation considered here, the Lamb and SH waves are coupled and hence, displacements and stresses will contain both Lamb wave and SH wave components.

4.6 GENERAL HELMHOLTZ SOLUTION FOR NON-AXISYMMETRIC GUIDED WAVES IN CYLINDRICAL COORDINATES

4.6.1 SUMMARY OF THE GENERAL SOLUTION

Equation (4.178) represents a system of six algebraic equations in six unknowns A, B, C, D, E, F . However, this 6×6 system can be expressed as 2×2 , 2×2 , 1×1 , 1×1 systems of which one set of 2×2 and 1×1 systems is for symmetric mode, and the other

2×2 and 1×1 systems is for antisymmetric mode. For every eigenvalue ξ , the homogeneous system Eq. (4.178) admits the solution given in Table 4-1.

The coefficients B, D and A, C which are responsible for the symmetric and antisymmetric Lamb waves, respectively, can be scaled up or down by arbitrary constants C^S and C^A , respectively. The coefficients F and E , which are responsible for symmetric and antisymmetric SH waves, respectively, can be scaled up or down by arbitrary constants C^{SH} and C^{AH} , respectively. The constants A, B, C, D, E, F of Table 4-1 can be substituted into Eqs. (4.91)-(4.93) to get the potentials Φ, H_v, H_z ; then Eqs.(4.58)-(4.60) and Eqs. (4.66)-(4.71) yield the displacements and stresses, respectively ($e^{-i\omega t}$ can be added to explicitly express the harmonic time dependence).

Table 4-1: The constants A, B, C, D, E, F for symmetric and antisymmetric modes

Symmetric Lamb + SH wave modes	Antisymmetric Lamb + SH wave modes
$A = 0, C = 0, E = 0$ $B = -2\xi^2 \cos \eta_s d$ $D = (\xi^2 - \eta_s^2) \cos \eta_p d$ $F = 1$	$B = 0, D = 0, F = 0$ $A = -2\xi^2 \sin \eta_s d$ $C = (\xi^2 - \eta_s^2) \sin \eta_p d$ $E = 1$
Note: $\xi = \xi^S$	$\xi = \xi^A$

The coefficients B, D and A, C which are responsible for the symmetric and antisymmetric Lamb waves, respectively, can be scaled up or down by arbitrary constants C^S and C^A , respectively. The coefficients F and E , which are responsible for symmetric and antisymmetric SH waves, respectively, can be scaled up or down by arbitrary constants

C^{SH} and C^{AH} , respectively. The constants A, B, C, D, E, F of Table 4-1 can be substituted into Eqs. (4.91)-(4.93) to get the potentials Φ , H_v , H_z ; then Eqs.(4.58)-(4.60) and Eqs.(4.66)-(4.71) yield the displacements and stresses, respectively ($e^{-i\omega t}$ can be added to explicitly express the harmonic time dependence).

For an arbitrary non-axisymmetric external loading, the solution will be in the form of a double summation $\sum_{n=0}^{\infty} \sum_{m=0}^{\infty}$, where the subscript m indicates the number of thickness-wise modes ($m=0,1,2,\dots$) whereas n indicates the number of terms in the Fourier series azimuthal decomposition of the external loading. The generic expressions of the solution are given next.

The radial dependence of the outward propagating solution follows the $H_n^{(1)}$ Hankel function and its derivatives. For compactness, we denote

$$\begin{aligned}\varphi_0(\xi r) &= H_0^{(1)}(\xi r) \\ \varphi_0'(\xi r) &= \frac{d}{dr} \{H_0^{(1)}(\xi r)\} = -\xi H_1^{(1)}(\xi r) \quad n=0 \\ \varphi_0''(\xi r) &= \frac{d^2}{dr^2} \{H_0^{(1)}(\xi r)\} = -\xi^2 H_0^{(1)}(\xi r) + \frac{\xi}{r} H_1^{(1)}(\xi r)\end{aligned} \quad (4.181)$$

$$\begin{aligned}\varphi_n(\xi r) &= H_n^{(1)}(\xi r) \\ \varphi_n'(\xi r) &= \frac{d}{dr} \{H_n^{(1)}(\xi r)\} = \xi H_{n-1}^{(1)}(\xi r) - \frac{n}{r} H_n^{(1)}(\xi r) \quad n=1,2,3,\dots \\ \varphi_n''(\xi r) &= \frac{d^2}{dr^2} \{H_n^{(1)}(\xi r)\} = \frac{n^2 + n - \xi^2 r^2}{r^2} H_n^{(1)}(\xi r) - \frac{\xi}{r} H_{n-1}^{(1)}(\xi r)\end{aligned} \quad (4.182)$$

4.6.2 SYMMETRIC LAMB + SH WAVE SOLUTION

For brevity, denote the following functions to represent the thickness-wise variation of the symmetric solution:

$$\begin{aligned}
V_m^S(z) &= -2\xi_m^{S^2} \cos \eta_s d \cos \eta_p z + (\xi_m^{S^2} - \eta_s^2) \cos \eta_p d \cos \eta_s z \\
W_m^S(z) &= 2\xi_m^{S^2} \eta_p \cos \eta_s d \sin \eta_p z + \xi_m^{S^2} (\xi_m^{S^2} - \eta_s^2) (1/\eta_s) \cos \eta_p d \sin \eta_s z ; \quad m = 0, 1, 2, \dots \quad (4.183) \\
U_m^{SH}(z) &= \cos(m\pi z/d)
\end{aligned}$$

Upon differentiation with respect to z , Eq. (4.183) yields

$$\begin{aligned}
V_m'^S(z) &= 2\xi_m^{S^2} \eta_p \cos \eta_s d \sin \eta_p z - \eta_s (\xi_m^{S^2} - \eta_s^2) \cos \eta_p d \sin \eta_s z \\
W_m'^S(z) &= 2\xi_m^{S^2} \eta_p^2 \cos \eta_s d \cos \eta_p z + \xi_m^{S^2} (\xi_m^{S^2} - \eta_s^2) \cos \eta_p d \cos \eta_s z \quad (4.184) \\
U_m'^{SH}(z) &= -(m\pi/d) \sin(m\pi z/d)
\end{aligned}$$

We also denote

$$T_m^S(z) = 2\lambda \xi_m^{S^2} (\xi_m^{S^2} + \eta_p^2) \cos \eta_s d \cos \eta_p z \quad (4.185)$$

where the superscript $_s$ indicates symmetric Lamb waves, ξ_m^S is the wavenumber of the m -th symmetric Lamb wave mode, and $\xi_m^{S^2}$ means $(\xi_m^S)^2$. With these notations, displacements and stresses take the forms given next.

4.6.2.1 Displacements of Symmetric Lamb + SH Wave Solution

$$u_r^S = \sum C_m^S \varphi_n'(\xi_m^S r) \cos n\theta V_m^S(z) e^{-i\omega t} + \sum C_m^{SH} \frac{n}{r} \varphi_n(\xi_m^{SH} r) \cos n\theta U_m^{SH}(z) e^{-i\omega t} \quad (4.186)$$

$$u_\theta^S = -\sum C_m^S \frac{n}{r} \varphi_n(\xi_m^S r) \sin n\theta V_m^S(z) e^{-i\omega t} - \sum C_m^{SH} \varphi_n'(\xi_m^{SH} r) \sin n\theta U_m^{SH}(z) e^{-i\omega t} \quad (4.187)$$

$$u_z^S = \sum C_m^S \varphi_n(\xi_m^S r) \cos n\theta W_m^S(z) e^{-i\omega t} \quad (4.188)$$

where superscript $_{SH}$ indicates symmetric SH waves, ξ_m^{SH} is the wavenumber of the m -th symmetric SH wave mode.

4.6.2.2 Stresses of Symmetric Lamb + SH Wave Solution

$$\begin{aligned}
\sigma_{rr}^S &= \sum C_m^S \left[T_m^S(z) \varphi_n(\xi_m^S r) + 2\mu V_m^S(z) \varphi_n''(\xi_m^S r) \right] \cos n\theta e^{-i\omega t} \\
&+ 2\mu \sum C_m^{SH} \left[-\frac{n}{r^2} \varphi_n(\xi_m^{SH} r) + \frac{n}{r} \varphi_n'(\xi_m^S r) \right] \cos n\theta U_m^{SH}(z) e^{-i\omega t} \quad (4.189)
\end{aligned}$$

$$\begin{aligned}\sigma_{\theta\theta}^S &= \sum C_m^S \left[T_m^S(z) \varphi_n(\xi_m^S r) - 2\mu V_m^S(z) \left\{ \frac{n^2}{r^2} \varphi_n(\xi_m^S r) - \frac{1}{r} \varphi_n'(\xi_m^S r) \right\} \right] \cos n\theta e^{-i\omega t} \\ &+ 2\mu \sum C_m^{SH} \left[\frac{n}{r^2} \varphi_n(\xi_m^{SH} r) - \frac{n}{r} \varphi_n'(\xi_m^{SH} r) \right] \cos n\theta U_m^{SH}(z) e^{-i\omega t}\end{aligned}\quad (4.190)$$

$$\sigma_{zz}^S = \sum C_m^S \varphi_n(\xi_m^S r) \left[T_m^S(z) + 2\mu W_m^S(z) \right] \cos n\theta e^{-i\omega t} \quad (4.191)$$

$$\begin{aligned}\sigma_{r\theta}^S &= \mu \sum C_m^S \left[\frac{2n}{r^2} \varphi_n(\xi_m^S r) - \frac{2n}{r} \varphi_n'(\xi_m^S r) \right] \sin n\theta V_m^S(z) e^{-i\omega t} \\ &+ \mu \sum C_m^{SH} \left[-\frac{n^2}{r^2} \varphi_n(\xi_m^{SH} r) + \frac{1}{r} \varphi_n'(\xi_m^{SH} r) - \varphi_n''(\xi_m^{SH} r) \right] \sin n\theta U_m^{SH}(z) e^{-i\omega t}\end{aligned}\quad (4.192)$$

$$\begin{aligned}\sigma_{\theta z}^S &= -\mu \sum C_m^S \left[V_m^S(z) + W_m^S(z) \right] \frac{n}{r} \varphi_n(\xi_m^S r) \sin n\theta e^{-i\omega t} \\ &- \mu \sum C_m^{SH} \varphi_n'(\xi_m^{SH} r) \sin n\theta U_m^{SH}(z) e^{-i\omega t}\end{aligned}\quad (4.193)$$

$$\begin{aligned}\sigma_{rz}^S &= \mu \sum C_m^S \left[V_m^S(z) + W_m^S(z) \right] \varphi_n'(\xi_m^S r) \cos n\theta e^{-i\omega t} \\ &+ \mu \sum C_m^{SH} \frac{n}{r} \varphi_n(\xi_m^{SH} r) \cos n\theta U_m^{SH}(z) e^{-i\omega t}\end{aligned}\quad (4.194)$$

4.6.3 ANTISYMMETRIC LAMB + SH WAVE SOLUTION

For brevity, denote the following functions to represent the thickness-wise variation of the antisymmetric solution:

$$\begin{aligned}V_m^A(z) &= -2\xi_m^{A^2} \sin \eta_s d \sin \eta_p z + (\xi_m^{A^2} - \eta_s^2) \sin \eta_p d \sin \eta_s z \\ W_m^A(z) &= -2\xi_m^{A^2} \eta_p \sin \eta_s d \cos \eta_p z - \xi_m^{A^2} (\xi_m^{A^2} - \eta_s^2) (1/\eta_s) \sin \eta_p d \cos \eta_s z; m = 0, 1, 2, \dots \\ U_m^{AH}(z) &= \sin((2m+1)\pi z/2d)\end{aligned}\quad (4.195)$$

Upon differentiation with respect to z , Eq. (4.195) becomes

$$\begin{aligned}V_m^{\prime A}(z) &= -2\xi_m^{A^2} \eta_p \sin \eta_s d \cos \eta_p z + \eta_s (\xi_m^{A^2} - \eta_s^2) \sin \eta_p d \cos \eta_s z \\ W_m^{\prime A}(z) &= 2\xi_m^{A^2} \eta_p^2 \sin \eta_s d \sin \eta_p z + \xi_m^{A^2} (\xi_m^{A^2} - \eta_s^2) \sin \eta_p d \sin \eta_s z \\ U_m^{\prime AH}(z) &= ((2m+1)\pi/2d) \cos((2m+1)\pi z/2d)\end{aligned}\quad (4.196)$$

We also denote

$$T_m^A(z) = 2\lambda \xi_m^{A^2} (\xi_m^{A^2} + \eta_p^2) \sin \eta_s d \sin \eta_p z \quad (4.197)$$

where the superscript $_A$ indicates antisymmetric Lamb waves, ξ_m^A is the wavenumber of the m -th antisymmetric Lamb wave mode, and $\xi_m^{A^2}$ means $(\xi_m^A)^2$. With these notations, displacements and stresses take the forms given next.

4.6.3.1 Displacements of the Antisymmetric Lamb + SH Wave Solution

$$u_r^A = \sum C_m^A \varphi_n'(\xi_m^A r) \cos n\theta V_m^A(z) e^{-i\omega t} + \sum C_m^{AH} \frac{n}{r} \varphi_n(\xi_m^{AH} r) \cos n\theta U_m^{AH}(z) e^{-i\omega t} \quad (4.198)$$

$$u_\theta^A = -\sum C_m^A \frac{n}{r} \varphi_n(\xi_m^A r) \sin n\theta V_m^A(z) e^{-i\omega t} - \sum C_m^{AH} \varphi_n'(\xi_m^{AH} r) \sin n\theta U_m^{AH}(z) e^{-i\omega t} \quad (4.199)$$

$$u_z^A = \sum C_m^A \varphi_n(\xi_m^A r) \cos n\theta W_m^A(z) e^{-i\omega t} \quad (4.200)$$

where superscript $_{AH}$ indicates antisymmetric SH waves, ξ_m^{AH} is the wavenumber of the m -th antisymmetric SH wave mode.

4.6.3.2 Stresses of Antisymmetric Lamb + SH Wave Solution

$$\begin{aligned} \sigma_{rr}^A = \sum C_m^A \left[T_m^A(z) \varphi_n(\xi_m^A r) + 2\mu V_m^A(z) \varphi_n''(\xi_m^A r) \right] \cos n\theta e^{-i\omega t} \\ + 2\mu \sum C_m^{AH} \left[-\frac{n}{r^2} \varphi_n(\xi_m^{AH} r) + \frac{n}{r} \varphi_n'(\xi_m^{AH} r) \right] \cos n\theta U_m^{AH}(z) e^{-i\omega t} \end{aligned} \quad (4.201)$$

$$\begin{aligned} \sigma_{\theta\theta}^A = \sum C_m^A \left[T_m^A(z) \varphi_n(\xi_m^A r) - 2\mu V_m^A(z) \left\{ \frac{n^2}{r^2} \varphi_n(\xi_m^A r) - \frac{1}{r} \varphi_n'(\xi_m^A r) \right\} \right] \cos n\theta e^{-i\omega t} \\ + 2\mu \sum C_m^{AH} \left[\frac{n}{r^2} \varphi_n(\xi_m^{AH} r) - \frac{n}{r} \varphi_n'(\xi_m^{AH} r) \right] \cos n\theta U_m^{AH}(z) e^{-i\omega t} \end{aligned} \quad (4.202)$$

$$\sigma_{zz}^A = \sum C_m^A \varphi_n(\xi_m^A r) \left[T_m^A(z) + 2\mu W_m'^A(z) \right] \cos n\theta e^{-i\omega t} \quad (4.203)$$

$$\begin{aligned} \sigma_{r\theta}^A = \mu \sum C_m^A \left[\frac{2n}{r^2} \varphi_n(\xi_m^A r) - \frac{2n}{r} \varphi_n'(\xi_m^A r) \right] \sin n\theta V_m^A(z) e^{-i\omega t} \\ + \mu \sum C_m^{AH} \left[-\frac{n^2}{r^2} \varphi_n(\xi_m^{AH} r) + \frac{1}{r} \varphi_n'(\xi_m^{AH} r) - \varphi_n''(\xi_m^{AH} r) \right] \sin n\theta U_m^{AH}(z) e^{-i\omega t} \end{aligned} \quad (4.204)$$

$$\begin{aligned} \sigma_{\theta z}^A = & -\mu \sum C_m^A \left[V_m'^A(z) + W_m^A(z) \right] \frac{n}{r} \varphi_n(\xi_m^A r) \sin n\theta e^{-i\omega t} \\ & - \mu \sum C_m^{AH} \varphi_n'(\xi_m^{AH} r) \sin n\theta U_m'^{AH}(z) e^{-i\omega t} \end{aligned} \quad (4.205)$$

$$\begin{aligned} \sigma_{rz}^A = & \mu \sum C_m^A \left[V_m'^A(z) + W_m^A(z) \right] \varphi_n'(\xi_m^A r) \cos n\theta e^{-i\omega t} \\ & + \mu \sum C_m^{AH} \frac{n}{r} \varphi_n(\xi_m^{AH} r) \cos n\theta U_m'^{AH}(z) e^{-i\omega t} \end{aligned} \quad (4.206)$$

4.7 SUMMARY AND CONCLUSION

4.7.1 SUMMARY

The Helmholtz vector decomposition theorem was applied to the Navier-Lame equation to obtain the governing equations in terms of potentials and the associated elastodynamic gauge condition. The non-axisymmetric problem in cylindrical coordinates was initially described in terms of four potentials Φ , H_r , H_θ , H_z . This resulted in four coupled governing equations that posed certain mathematical difficulties. Subsequently, the governing equations were decoupled and the number of potentials was reduced from four, Φ , H_r , H_θ , H_z , to three, Φ , H_v , H_z , through a judicious use of the gauge condition. This resulted in a set of only three uncoupled governing equations in Φ , H_v , H_z which were independently solved. The general solution contained six unknowns (two for each of the three potentials). These unknowns were determined from the stress-free boundary conditions at the top and bottom faces of the plate. Manipulation of the boundary conditions yielded the characteristic equations for guided wave propagation (Lamb + SH waves). The general solution for displacements and stresses was finally expressed as a normal-modes expansion that contained both symmetric and antisymmetric Lamb and SH waves.

4.7.2 CONCLUSION

This chapter has shown that it is possible to develop a Helmholtz potential solution for the coupled non-axisymmetric guided wave problem in cylindrical coordinates. The non-axisymmetric guided wave propagation in a plate is a situation where two of the potentials are tightly coupled. The coupling of the governing equations in terms of potentials has prevented so far the development of a complete solution. This chapter has shown how a judicious manipulation of the gauge condition can decouple the governing equations and leads to a straight-forward solution. The manipulation of the gauge condition yielded a new potential, H_v which replaces the effect of H_r , H_θ and thus allowed us to replace two coupled governing equations in H_r , H_θ by a single uncouple equation in H_v . This judicious use of the gauge condition reduced the number of potentials, decoupled the governing equations and facilitated the obtaining of the complete solution for the non-axisymmetric guided-wave propagation in cylindrical coordinates in an elegant straight-forward way.

CHAPTER 5

ANALYTICAL-FEM SIMULATION FOR ENHANCED DAMAGE DETECTION FOR AEROSPACE RIVET HOLE

In this chapter, guided wave propagation and interaction with a generic damage has been formulated using closed-form analytical solution while the local damage interaction, scattering, and mode conversion have been obtained from finite element analysis in the case of a rivet hole with cracks. The rivet hole cracks (damage) in the plate structure gives rise to the non-axisymmetric scattering of Lamb wave, as well as shear horizontal (SH) wave, although the incident Lamb wave source (primary source) is axisymmetric. The damage in the plate acts as a non-axisymmetric secondary source of Lamb wave and SH wave. The scattering of Lamb and SH waves are captured using wave damage interaction coefficient (WDIC). The scatter cubes of complex-valued WDIC are formed that can describe the 3D interaction (frequency, incident direction, and azimuth direction) of Lamb waves with the damage. The scatter cubes are fed into the exact analytical framework to produce the time domain signal. This analysis enables us to obtain the optimum design parameters for better detection of the cracks in a multiple-rivet-hole problem. The optimum parameters provide the guideline for the design of the sensor installation to obtain the most noticeable signals that indicate the presence of cracks in the rivet hole [48].

5.1 INTRODUCTION

The detection of various types of defects in structures, for example, corrosion, cracks, impact, and disbonds is an important research area of structural health monitoring (SHM) and nondestructive evaluation (NDE). Development of fatigue cracks at the rivet holes and fasteners in the aircraft structures is the most frequent problem encountered in aircraft maintenance. The cracks can grow to a critical size and jeopardize the structural integrity if they remain undetected. Ultrasonic guided wave methods can be employed instead of the laborious point-by-point inspection method for fast, accurate, and efficient detection of the crack initiation in rivet holes.

5.1.1 MOTIVATION OF THE RESEARCH WORK

The detection of cracks around the rivet hole has become an important topic of the NDE research field. In 2009, the probability of detection (POD) by a model-assisted approach has been demonstrated for the fatigue crack growth in wing lap joint, wing skin fastener holes, and airframe fastener holes [49]. In 2012, the use of the transfer function approach to model-assisted POD was investigated by Bode et al. [50] through the inspection of a specimen of aircraft lap joint. However, the researchers emphasized the detection of fastener hole cracks mainly based on nondestructive inspection (NDI) technique. In 2015, the SHM-based POD was obtained for the fatigue crack initiation in the lug with a wing attachment which acted as a representative airplane component [51]. The excitation signals of 200–1000 kHz center frequency were used to analyze the guided waves within fundamental Lamb wave modes. In 2014, Fu-Kuo Chang group [52] used ultrasonic SHM techniques to detect the damage and showed the variation of damage index with crack size. They determined the most influencing parameters to the sensitivity of

damage detection and compared the SHM and NDE techniques. A set of transmitter and receiver sensors were used around the cracked rivet hole. However, the study of the proper location of the installed sensors around the damage was not described. The motivation and importance of the present research work have been derived from this research.

5.1.2 STATE OF THE ART

Structural health monitoring techniques are increasingly being used for damage detection and characterization in aerospace structures [53]. The scattering of Lamb waves from various types of damage has been analyzed by many researchers [54]. Norris et al. [55] studied the scattering of flexural waves on thin plates and used ray method to obtain far-field scattering from a circular hole. They showed the azimuthal variation of the scattered flexural wave amplitude. A statistical approach to optimal sensor placement for SHM has been studied by Flynn et al. [56] and their approach in the active sensing methods to three different types of plates have been demonstrated. Bayes risk minimization implemented through the genetic algorithm (GA) has been used to find the optimal arrangement of the transducers [57]. The statistical model parameters were determined experimentally to avoid the difficulty in modeling the mechanical behavior of the individual transducers. However, artificial surface damages were generated at different locations of the plate to implement their statistical approach. Fromme et al. [58] used analytical-finite difference method (FDM) simulation to obtain the scattered field around the cracks at rivet holes, presented results at two different excitation frequencies, and compared these with experimental results. Lamb waves propagating in an infinite plate containing a circular hole, with or without edge cracks, were investigated by Chang and Mal [12] using a hybrid method called the global-local finite element method (FEM).

However, the research work was limited to the symmetric Lamb modes and the incident Lamb wave mode was perpendicular to the crack. Recent research has put emphasis on the simulated results using fast and efficient numerical techniques to understand the Lamb wave behavior prior to implementation of the results in the physical structures [59]. Numerical methods are becoming a popular tool for understanding the complex Lamb wave interaction with complicated boundary conditions [60]. The scatter field of a single rivet hole cracks with a single incident Lamb wave has been described by introducing the wave damage interaction coefficient (WDIC), and the non-reflective boundary (NRB) was implemented to simulate the infinite plate in a successful manner [61].

In the present research, the optimal placement of the transducer, as well as the excitation frequency for the actuator in an active sensing method of SHM, has been obtained based on the wave scattering phenomenon. The wave scattering phenomenon is obtained using FEM while the wave propagation is modeled using exact analytical formulations [62].

5.2 DESCRIPTION OF THE SHM OF MULTIPLE-RIVET-HOLE LAP JOINT

The multiple-rivet-hole lap joint with transmitter and receiver sensors of an active SHM system is illustrated in Figure 5.1. When an electrical voltage is supplied to the piezoelectric transmitter (actuator), it generates mechanical excitation in the structure and produces Lamb waves that propagate in the structure. The Lamb waves interact with the damages, which act as the secondary sources of guided waves. The scattered guided waves propagate in the structures and are received by the piezoelectric sensor. The actuator dispatches Lamb waves to each of the rivet holes at a certain angle that can be calculated from the standoff distance (L) and pitch (P) of each rivet hole (Figure 5.1). The scattering

phenomenon depends on the direction (θ) of incident Lamb waves as well as the azimuth direction (Φ) around the damage (the azimuth direction Φ corresponds to the sensor placement direction).

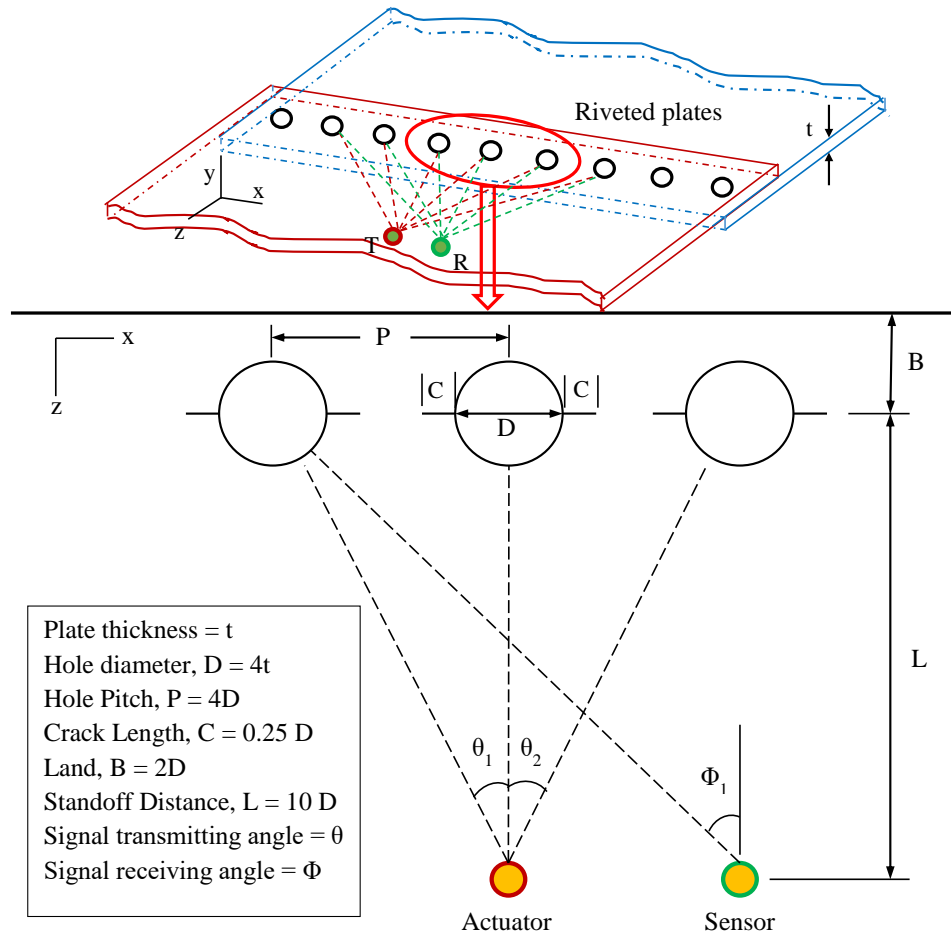


Figure 5.1 Illustration of the multiple-rivet-hole lap joint.

The secondary source (cracked rivet hole) is asymmetric for a certain angle of incident Lamb waves, hence, it acts as a non-axisymmetric secondary source of scattered waves. The scattered waves contain scattered Lamb waves and shear horizontal (SH) waves. Understanding the non-axisymmetric scattered waves around the damage provides the ability to better detect the emanating cracks in the rivet holes. The actuator and sensor installations, as well as the excitation frequency, depend on the non-axisymmetric behavior

of the scattered guided waves. The design of proper transducer installation and selection of the center frequency of excitation enable better capturing of the damage signature originating from the cracks of the rivet holes.

Since no closed form solution exists for the non-axisymmetric scattered waves, a combined analytical and finite element modeling has been introduced in the present chapter. Exact closed-form analytical formulation has been used for the propagation of Lamb waves from the actuator up to the damage in the structure. The interaction of the Lamb waves with the local damage is modeled using finite element analysis and the non-axisymmetric behaviors of the scattered waves are captured through the WDICs and scatter cubes.

5.3 OVERVIEW OF COMBINED ANALYTICAL AND FEM APPROACH

The overview of the combined analytical and FEM approach (CAFA) is illustrated in the schematic diagram as shown in Figure 5.2. It shows that the actuator excites the structure to generate the Lamb waves that propagate into the structure. Then the Lamb waves interact with the damage and undergo scattering and mode conversion.

The scattered wave also propagates into the structure and is finally picked up by a sensor. In CAFA, the Lamb wave generation, propagation, damage interaction, and detection are modeled using the exact analytical expressions, while the wave damage interaction coefficients (WDICs) are extracted as a scatter cube from the small-size local FEM analysis [63], [64]. The findings of the present research have been extended to study the sensitivity and uncertainty analysis of SHM systems [65], [66].

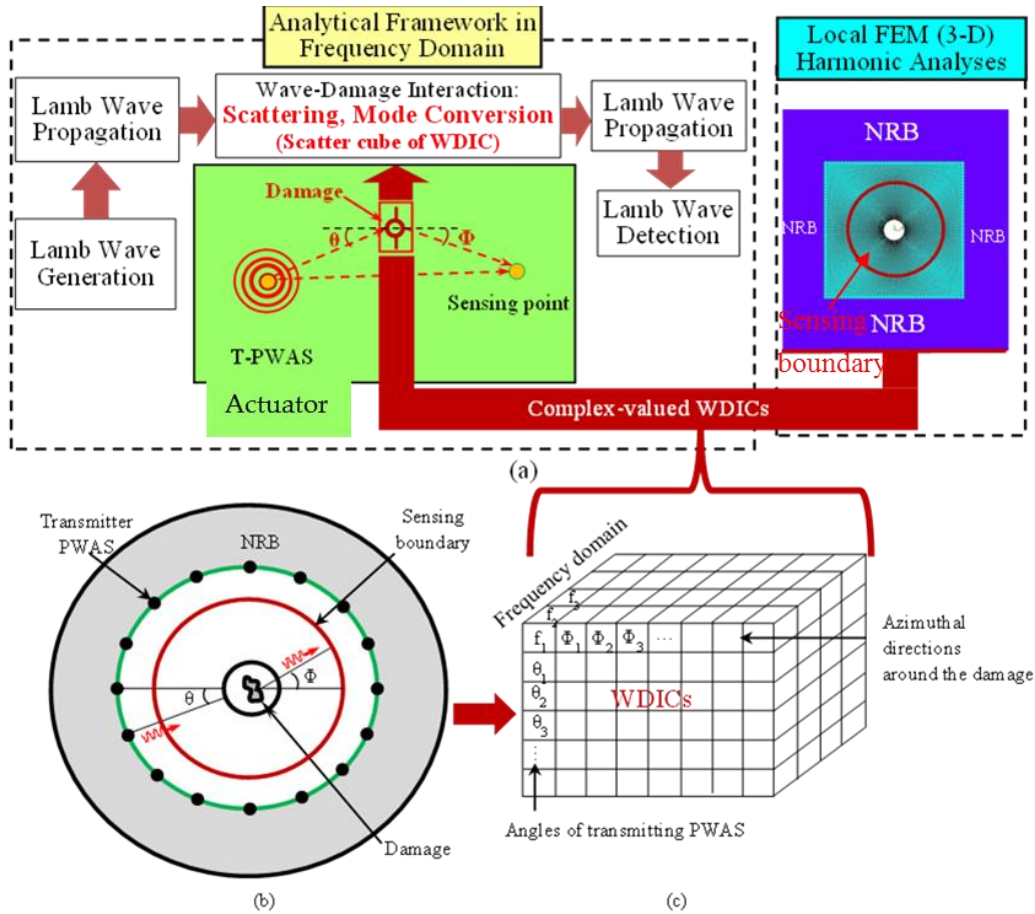


Figure 5.2 Overview of the combined analytical and FEM approach [11]

5.4 DESCRIPTION OF THE ANALYTICAL MODEL

The analytical model consists of several steps. Some steps are reproduced from ref. [11] for the completeness of the study. These steps are described below:

5.4.1 LAMB WAVE GENERATION FROM THE ACTUATOR

Lamb waves are generated from the axisymmetric circular PWAS actuator. Thus, the axisymmetric condition applies to the incident Lamb wave modeling. Lamb waves are generated in the plate and propagate toward the local damage. For outward propagating waves from the actuator, the radial displacement $u_r(r)$ on the top surface of the plate at any distance r from the actuator is given by Giurgiutiu [21], i.e.,

$$u_r(r)|_{z=d} = -\frac{\pi i}{2\mu} \sum_{j=0}^{J_s} \frac{\tilde{\tau}(\xi_j^S) N_S(\xi_j^S)}{D'_S(\xi_j^S)} H_1^{(1)}(\xi_j^S r) e^{-i\omega t} - \frac{\pi i}{2\mu} \sum_{j=0}^{J_A} \frac{\tilde{\tau}(\xi_j^A) N_A(\xi_j^A)}{D'_A(\xi_j^A)} H_1^{(1)}(\xi_j^A r) e^{-i\omega t} \quad (5.1)$$

where $\mu = G$ is the shear modulus of the plate, a is the radius of actuator and the components N_S, N_A, D_S, D_A are defined as

$$\begin{aligned} N_S(\xi) &= \xi \eta_S (\xi^2 + \eta_S^2) \cos \eta_P d \cos \eta_S d ; \quad N_A(\xi) = -\xi \eta_S (\xi^2 + \eta_S^2) \sin \eta_P d \sin \eta_S d \\ D_S &= (\xi^2 - \eta_S^2)^2 \cos \eta_P d \sin \eta_S d + 4\xi^2 \eta_P \eta_S \sin \eta_P d \cos \eta_S d \\ D_A &= (\xi^2 - \eta_S^2)^2 \sin \eta_P d \cos \eta_S d + 4\xi^2 \eta_P \eta_S \cos \eta_P d \sin \eta_S d \end{aligned} \quad (5.2)$$

where $2d$ is the thickness of the plate; η_P, η_S are defined as

$$\eta_P^2 = \frac{\omega^2}{c_P^2} - \xi^2; \quad \eta_S^2 = \frac{\omega^2}{c_S^2} - \xi^2 \quad (5.3)$$

The wavespeeds $c_P = \sqrt{\lambda + 2\mu / \rho}$ and $c_S = \sqrt{\mu / \rho}$ depend on the plate material properties (Lame constants λ, μ and density ρ). The wavenumber ξ depends on the frequency and is the roots of the Rayleigh-Lamb equation [18], i.e.,

$$\frac{\tan \eta_S d}{\tan \eta_P d} = \left[\frac{-4\eta_P \eta_S \xi^2}{(\xi^2 - \eta_S^2)^2} \right]^{\pm 1} \quad (5.4)$$

where +1 and -1 is for symmetric and antisymmetric Lamb wave modes respectively.

Considering the actuator is ideally bonded to the plate of thickness = $2d$, and τ_a is the shear stress between the plate and the transducer, the J_1 Hankel transform of the radial shear stress can be written as

$$\tilde{\tau}(\xi)_{J_1} = \tau_a a^2 J_1(\xi a) \quad (5.5)$$

where J_1 is the first order Bessel function. Substituting Eq.(5.5) into Eq.(5.1) yields

$$\begin{aligned}
u_r(r)|_{z=d} = & -\pi i \frac{a^2 \tau_a}{2\mu} \sum_{\xi^S} \frac{J_1(\xi^S a) N_S(\xi^S)}{D'_S(\xi^S)} H_1^{(1)}(\xi^S r) e^{-i\omega t} \\
& -\pi i \frac{a^2 \tau_a}{2\mu} \sum_{\xi^A} \frac{J_1(\xi^A a) N_A(\xi^A)}{D'_A(\xi^A)} H_1^{(1)}(\xi^A r) e^{-i\omega t}
\end{aligned} \tag{5.6}$$

The Hankel function of the first kind and order one $H_1^{(1)}$ represents an outgoing propagating wave. The wavenumber ξ depends on the frequency and is the roots of the Rayleigh-Lamb equation [18].

5.4.2 ACTUATOR TRANSFER FUNCTION

The PWAS acts as an actuator which is supplied with a voltage input. The PWAS transfer function $g_{PWAS}(\omega)$ relates the applied voltage $\tilde{V}_T(\omega)$ to shear stress τ_a and is defined as

$$F_a = a\tau_a = g_{PWAS}(\omega)\tilde{V}_T(\omega) \tag{5.7}$$

where F_a is the reaction force per unit length from the structure due to the expansion of PWAS mounted on the surface of the structure, a is the radius of actuator, $\tilde{V}_T(\omega)$ can be obtained by the Fourier transform of the time-domain excitation signal $V_T(t)$. The transfer function $g_{PWAS}(\omega)$ of the actuator can be derived as

$$g_{PWAS}(\omega) = \frac{d_{31}}{s_{11}^E} \frac{r(\omega)}{1-r(\omega)} \tag{5.8}$$

where $r(\omega) = k_{str}(\omega) / k_{PWAS}$ is the stiffness ratio between host structure and actuator, d_{31} is piezoelectric strain coefficient, s_{11}^E is the mechanical compliance of the actuator material measured at zero electric field ($E = 0$). The detail derivation of Eq. (5.8). can be found in ref. [67].

5.4.3 STRUCTURE TRANSFER FUNCTION

The roots of the Rayleigh-Lamb equation Eq. (5.4) provide numerous symmetric and antisymmetric wavenumbers ξ^S , ξ^A for a certain excitation frequency ω . These wavenumbers are used in the summation process in Eq. (5.6). In general, the structural transfer function $G(\omega, r)$ may be defined as the conversion of the frequency domain voltage $\tilde{V}_T(\omega)$ and the displacement $u_r(\omega, r)$ induced in the host structure given by Eq. (5.9)

$$u_r(\omega, r) = G(\omega, r)\tilde{V}_T(\omega) \quad (5.9)$$

The structural transfer function $G(\omega, r)$ can be obtained by substituting Eq. (5.7) into Eq.(5.6) and dividing by $e^{-i\omega t}$. For convenience, the symmetric (S) and antisymmetric (A) part of the structure transfer function may be separated as

$$G^S(\omega, r) = -\pi i \frac{ag_{PWAS}(\omega)}{2\mu} \sum_{\xi^S} \frac{J_1(\xi^S a) N_s(\xi^S)}{D'_s(\xi^S)} H_1^{(1)}(\xi^S r) \quad (5.10)$$

$$G^A(\omega, r) = -\pi i \frac{ag_{PWAS}(\omega)}{2\mu} \sum_{\xi^A} \frac{J_1(\xi^A a) N_s(\xi^A)}{D'_s(\xi^A)} H_1^{(1)}(\xi^A r) \quad (5.11)$$

5.4.4 INCIDENT WAVE AT DAMAGE LOCATION

The structure transfer function can be multiplied by the frequency-domain excitation signal $\tilde{V}_T(\omega)$ to obtain the direct incident waves at the sensing location, i.e.,

$$u_{IN}(\omega, R_{IN}) = \tilde{V}_T(\omega) [G^S(\omega, R_{IN}) + G^A(\omega, R_{IN})] \quad (5.12)$$

where the distance R_{IN} from actuator up to sensing location is used.

Similarly, the structure transfer function can be multiplied by $\tilde{V}_T(\omega)$ up to the damage location to obtain the interrogating waves arriving at the damage, i.e.,

$$u_D(\omega, R_D) = \tilde{V}_T(\omega) \left[G^S(\omega, R_D) + G^A(\omega, R_D) \right] \quad (5.13)$$

where the distance R_D from actuator up to the damage location is used

It can be noticed that the Lamb modes propagate independently and the incident wave field is the superposition of symmetric and antisymmetric wave modes.

5.5 EFFECT OF LOCAL DAMAGE THROUGH THE INSERTION OF SCATTER CUBE OF WDIC

The WDIC obtained from the FEM analysis depends on the material properties of host structure while the final signal received depends on both the transducer material properties and host structure properties. The damage effect is contained in the wave damage interaction coefficients (WDIC) that contains the amplitude and phase information of the scattered waves. The concept of WDIC and the steps to calculate the WDICs are discussed below:

5.5.1 CONCEPT OF WDIC AND MATHEMATICAL EXPRESSIONS FOR WDIC CALCULATION

The displacement field of the incident wave (u_{IN}) may be calculated at the center point of the pristine model. The incident displacement field coming towards the center of the damage and the scattered displacement field recorded at the sensing boundary (Figure 5.2b) follows a certain relation [68], i.e.,

$$u_{IN}^A e^{-i\varphi_{IN}^A} C_{AB}(\omega, \theta, \Phi) e^{-i\varphi_{AB}(\omega, \theta, \Phi)} H_m^{(1)}(\xi^B r) = u_{SC}^B(\omega, \theta, \Phi) e^{-i\varphi_{SC}^B(\omega, \theta, \Phi)} \quad (5.14)$$

where $u_{IN}^A e^{-i\varphi_{IN}^A}$ represents any incident mode A at the center of the damage; $C_{AB}(\omega, \theta, \Phi) e^{-i\varphi_{AB}(\omega, \theta, \Phi)}$ represents the amplitude $C_{AB}(\omega, \theta, \Phi)$ and phase $e^{-i\varphi_{AB}(\omega, \theta, \Phi)}$ of WDIC; r is the radius of sensing boundary; $H_m^{(1)}(\xi^B r)$ is the Hankel function of 2-D scattered wave field (B) propagates in outward direction with $m = 1$. C_{AB} stands for the incident A wave mode to the

scattered B wave mode that depends on the direction of incident Lamb wave, azimuthal direction of the damage and the circular frequency. On the right side $u_{SC}^B(\omega, \theta, \Phi) e^{-i\varphi_{SC}^B(\omega, \theta, \Phi)}$ represents the scattered displacement field along the sensing boundary of radius r .

Upon rearrangement, Eq. (5.14) yields

$$C_{AB}(\omega, \theta, \Phi) e^{-i\varphi_{AB}(\omega, \theta, \Phi)} = \frac{u_{SC}^B(\omega, \theta, \Phi)}{u_{IN}^A} \frac{1}{H_m^{(1)}(\xi^B r)} e^{-i\Delta\varphi_{AB}(\omega, \theta, \Phi)} \quad (5.15)$$

where, $\Delta\varphi_{AB}(\omega, \theta, \Phi) = \varphi_{SC}^B(\omega, \theta, \Phi) - \varphi_{IN}^A$. From Eq. (5.15), the amplitude and phase may be separated as

$$C_{AB}(\omega, \theta, \Phi) = \left| \frac{u_{SC}^B(\omega, \theta, \Phi)}{u_{IN}^A} \frac{1}{H_m^{(1)}(\xi^B r)} \right| \quad (5.16)$$

$$\varphi_{AB}(\omega, \theta, \Phi) = \Delta\varphi_{AB}(\omega, \theta, \Phi) - \left[\angle \frac{1}{H_m^{(1)}(\xi^B r)} - \angle \frac{1}{H_m^{(1)}(0^+)} \right] \quad (5.17)$$

For instance, when incident symmetric Lamb wave mode ($S0$ mode) causes scattered $S0$ mode, then both A and B corresponds to the parameters of $S0$ mode. When incident $S0$ mode causes scattered symmetric SH mode, then A corresponds to the parameters of $S0$ mode but B corresponds to the SH wave mode.

WDIC depends on the thickness of the plate. The thickness of the upper and lower plate is considered to be the same for the present analysis. Hence, the result of the top plate will be the same for the bottom plate. That means in order to monitor the damage in the bottom plate, a similar arrangement of transducers is needed as in the top plate. In case of plates with different thickness, the two plates should be considered individually. Each plate should be analyzed using the proposed method to obtain the optimal configuration of the transducers for individual plates. However, there may occur some wave leakages between

the two riveted plates in the region where the two plates are in close contact being virtually bonded. Thus, the thickness of the bonded plate section will come into play and may modify the WDIC profile which can be addressed as well. In this present analysis, the wave leakage is not considered.

5.5.2 SEPARATION OF THE MODES

The displacement wave fields of the local damage can be solved using an FEM model. The scattered wave displacements at the top and bottom surface sensing nodes in both radial (u_r^T and u_r^B) and tangential (u_θ^T and u_θ^B) directions can be used to selectively separate each wave mode, as follows:

$$u_{SC}^{S0} = \frac{u_r^T + u_r^B}{2}; \quad u_{SC}^{A0} = \frac{u_r^T - u_r^B}{2}; \quad u_{SC}^{SH_{S0}} = \frac{u_\theta^T + u_\theta^B}{2}; \quad u_{SC}^{SH_{A0}} = \frac{u_\theta^T - u_\theta^B}{2} \quad (5.18)$$

It should be clearly noted that in this study we focused on the fundamental Lamb wave modes ($S0$ and $A0$) and fundamental shear horizontal mode ($SH0$). The frequency range of our analysis is below the cut-off frequencies of the higher Lamb and SH wave modes. We denote fundamental SH_{S0} mode as SH mode. The extension of our approach to higher modes could be the topic of a future study.

5.5.3 INSERTION OF WDICs IN THE ANALYTICAL MODEL

The scattered displacement fields provide the scattered coefficients for the scattered wave modes ($C_{SS}, C_{AS}, C_{SA}, C_{AA}, C_{SSH}, C_{ASH}$) following Eq. (5.15). Each scattered mode forms a scatter cube considering multiple directions of the incident Lamb wave. The scatter-wave source at the damage location is obtained by multiplying the incident waves at the damage with WDICs, i.e.,

$$u_N^S = C_{SS}(\omega, \theta, \Phi) e^{-i\varphi_{SS}(\omega, \theta, \Phi)} u_D^S + C_{AS}(\omega, \theta, \Phi) e^{-i\varphi_{AS}(\omega, \theta, \Phi)} u_D^A \quad (5.19)$$

$$u_N^A = C_{SA}(\omega, \theta, \Phi) e^{-i\phi_{SA}(\omega, \theta, \Phi)} u_D^S + C_{AA}(\omega, \theta, \Phi) e^{-i\phi_{AA}(\omega, \theta, \Phi)} u_D^A \quad (5.20)$$

$$u_N^{SH} = C_{SSH}(\omega, \theta, \Phi) e^{-i\phi_{SSH}(\omega, \theta, \Phi)} u_D^S + C_{ASH}(\omega, \theta, \Phi) e^{-i\phi_{ASH}(\omega, \theta, \Phi)} u_D^A \quad (5.21)$$

where u_N^S , u_N^A , and u_N^{SH} represent the damage scatter-wave source for modes $S0$, $A0$, and $SH0$, respectively. The scatter-wave source (damage) irradiates the scattered waves that propagate to the sensing location. The 2-D Lamb wave irradiating from a point source accepts the following solution in the cylindrical coordinate system with reference to the new wave source location [21],

$$u_r = \sum_{n=1}^{\infty} a_n^{LW}(z) H_1^{(1)}(\xi_n^{LW} r) e^{-i\omega t} \quad (5.22)$$

$$u_\theta = \sum_{n=1}^{\infty} b_n^{SH}(z) H_1^{(1)}(\xi_n^{SH} r) e^{-i\omega t} \quad (5.23)$$

where $a_n^{LW}(z)$ and $b_n^{SH}(z)$ are the thickness dependent mode shapes for Lamb and SH waves of n^{th} wave mode.

5.5.4 SENSING THE SCATTERED WAVE SIGNALS

Since the amplitude relationship between the interrogating waves and the scattered waves is contained in the WDICs, the transfer function from the damage up to the sensing location is simply $H_1^{(1)}(\xi R_{sc})$, where R_{sc} is the distance from the damage up to the sensing location. Thus, the scattered waves arriving at the sensing point can be calculated as

$$u_{SC}^S = u_N^S H_1^{(1)}(\xi^S R_{sc}); \quad u_{SC}^A = u_N^A H_1^{(1)}(\xi^A R_{sc}); \quad u_{SC}^{SH} = u_N^{SH} H_1^{(1)}(\xi^{SH} R_{sc}) \quad (5.24)$$

Since the frequency domain excitation voltage $\tilde{V}_t(\omega)$ is used to derive the above relations, the inverse Fourier transform is used to obtain the time-domain scattered signal. The out-of-plane displacement wavefield may be obtained through the multiplication of the in-plane

displacements by the mode-shape component ratio, and the out-of-plane velocity would be the time derivative of the out-of-plane displacement [21].

5.6 DESCRIPTION OF THE FEM MODELING

At large distances from the origin, the behavior of circular-crested Lamb waves approaches asymptotically that of straight-crested Lamb waves, but the amplitude is affected by the factor which captures the geometric spreading of the circular wavefront [21]. Considering the standoff distance in the multiple-rivet-hole in Figure 5.1, i.e., the excitation source is far away from the damage, it is a good approximation to use straight-crested Lamb modes as incident waves in the small local damage region during the nodal load calculations of FEM. A 40 mm × 40 mm 3D FE model of a 1.6 mm thick aircraft-grade aluminum-2024-T3 plate is created using commercial ANSYS15 software (ANSYS, Inc., Canonsburg, USA). A non-reflective boundary (NRB) 20 mm wide at each side of the model is used. The crack length ($2a$) to diameter (d) of the hole ratio of 0.5 is used.

5.6.1 IMPOSING THE NODAL POINT LOAD

The 3D view of the local FEM model is shown in Figure 5.3c. Incoming Lamb waves are shown as three red signal signs on one face of the model. Lamb mode excitation is imposed through nodal forces by evaluating integrals of stress mode shape components on the loading nodes. The stress mode shapes are calculated analytically [21] and converted into nodal forces through boundary integration on each element along the loading line.

The element nodal force can be evaluated by using Eq. (5.25) [69] as

$$F_{ix}^e = \int_0^{L_x} \sigma_{xx}^e(s) N_i^e(s) ds; \quad F_{iy}^e = \int_0^{L_x} \sigma_{xy}^e(s) N_i^e(s) ds \quad (5.25)$$

where subscript and superscript e stands for element, L_e represents the element size, F_{ix}^e and F_{iy}^e are nodal forces in x and y direction, i is the element node number, $N_i^e(s)$ is the shape function of selected element type. The nodal forces are updated for each calculation step, imposing Lamb mode excitation for each excitation frequency. The stress mode shapes in the thickness direction at 250 kHz is shown in Figure 5.3d.

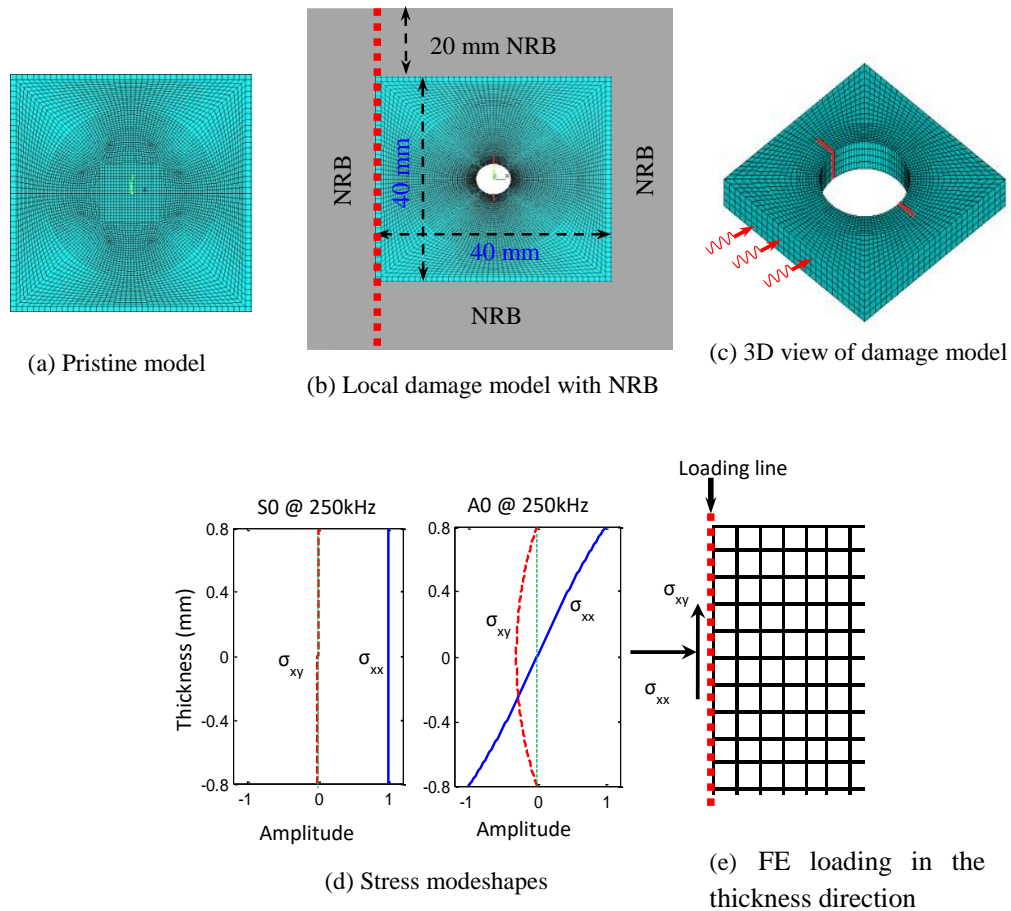


Figure 5.3 Illustration of local finite element method (FEM) modeling (a) Pristine model, (b) Local damage model with NRB, (c) 3D view of damage model (d) Stress modeshapes (e) FE loading in the thickness direction

The stresses are calculated as follows:

For symmetric modes:

$$\begin{aligned}
\sigma_{xx}^S(x, y, t) &= C^S 2\mu\xi\eta_S \left[(\xi^2 + \eta_S^2 - 2\eta_P^2) \cos\eta_S d \cos\eta_P y - (\xi^2 - \eta_S^2) \cos\eta_P d \cos\eta_S y \right] e^{i(\xi x - \omega t)} \\
\sigma_{yy}^S(x, y, t) &= -C^S 2\mu\xi\eta_S (\xi^2 - \eta_S^2) (\cos\eta_S d \cos\eta_P y - \cos\eta_P d \cos\eta_S y) e^{i(\xi x - \omega t)} \\
\sigma_{xy}^S(x, y, t) &= iC^S \mu \left[4\xi^2 \eta_P \eta_S \cos\eta_S d \sin\eta_P y + (\xi^2 - \eta_S^2)^2 \cos\eta_P d \sin\eta_S y \right] e^{i(\xi x - \omega t)}
\end{aligned} \tag{5.26}$$

For antisymmetric modes:

$$\begin{aligned}
\sigma_{xx}^A(x, y, t) &= -C^A 2\mu\xi\eta_S \left[(\xi^2 + \eta_S^2 - 2\eta_P^2) \sin\eta_S d \sin\eta_P y - (\xi^2 - \eta_S^2) \sin\eta_P d \sin\eta_S y \right] e^{i(\xi x - \omega t)} \\
\sigma_{yy}^A(x, y, t) &= C^A 2\mu\xi\eta_S (\xi^2 - \eta_S^2) (\sin\eta_S d \sin\eta_P y - \sin\eta_P d \sin\eta_S y) e^{i(\xi x - \omega t)} \\
\sigma_{xy}^A(x, y, t) &= iC^A \mu \left[4\xi^2 \eta_P \eta_S \sin\eta_S d \cos\eta_P y + (\xi^2 - \eta_S^2)^2 \sin\eta_P d \cos\eta_S y \right] e^{i(\xi x - \omega t)}
\end{aligned} \tag{5.27}$$

5.6.2 MESHING, IMPOSING NRB, AND VERIFICATION OF THE FE MODEL

Non-reflective boundary (NRB) has been employed surrounding the local FEM model (as shown in Figure 5.3b) in order to avoid the reflections from the edges. The adequate non-reflective boundary is implemented following ref. [61] and is not discussed here for the sake of brevity.

Eight-node structure elements (SOLID45) are used to mesh the plate, and spring-damper elements (COMBIN14) are used to construct the NRB. In the thickness direction, 0.4 mm mesh size is used, which is fair enough to capture the thickness mode shapes. Finer meshing is used in the crack region to accommodate the high-stress gradient and coarser meshing is used away from the crack and outside the sensing boundary. The finite element results are validated with the results obtained for Lamb wave incident at 0° degree in reference [68].

The analytical WDIC profiles for the Lamb wave and SH wave for a simple pristine plate was derived by Bhuiyan et al. [63], which showed that WDIC profiles for a pristine plate follow an ideal double-circled shape. The finite element result is compared with the

analytical result as shown in Figure 5.4. The finite element result shows very good agreement with the analytical result.

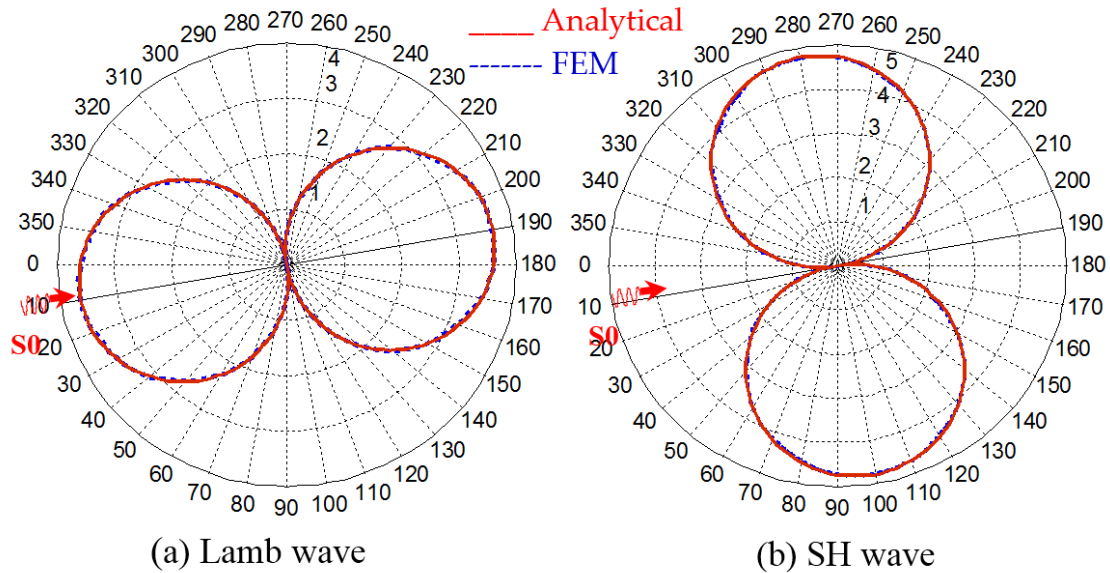


Figure 5.4 Comparison between analytical and FEM results (a) $WDIC_{LW_LW}$ (b) $WDIC_{LW_SH}$ in polar coordinates (pristine plate).

5.6.3 MODELING OF CRACKS IN THE RIVET HOLE

Cracks in the rivet hole are modeled using the discontinuity at the adjacent pair of nodes along the cracks. There are actually two sets of nodes along the crack faces, and each set is representing the nodes on each face (Figure 5.5); the nodes are discontinuous along the crack faces. Two sets of nodes are adjacent to each other unlike the modeling of notch, where there is a small gap between those sets of nodes. Like the nodes, the solid elements are also separated along the crack faces. The modeling of the cracks in finite element using the above approach is good enough to model the actual cracks of rivet holes in the plate-like structure [70].

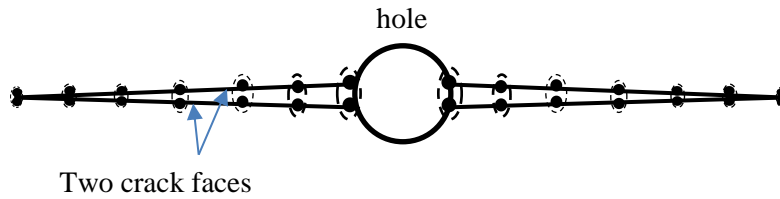


Figure 5.5 Crack modeling schematic. Two nodes along two crack-faces remained unmerged.

5.6.4 SELECTION OF FREQUENCY DOMAIN FOR HARMONIC ANALYSIS

The frequency domain of harmonic analysis was selected based on the dispersion curves shown in Figure 5.6. The frequency range corresponding to the fundamental Lamb and SH wave modes is selected in the present study. It enables us to avoid the complexities associated with higher Lamb and SH wave modes. However, at very low frequencies (<40 kHz), the wavelength of the Lamb modes are very high (Figure 5.7) and requires very wide NRB, hence, requires more FEM computation resources. When incident fundamental Lamb wave modes (S0/A0) interact with the damage there could be non-propagating (evanescent) A1 modes present that die out at a certain distance from the source. It requires a longer distance to die out the non-propagating A1 mode of Lamb wave at very low and very high frequencies as shown in Figure 5.8. At higher frequencies (>900 kHz), the wavelength becomes very small and requires very fine mesh to capture the damage feature, thus, require more computation efforts. At higher frequencies, the higher modes (S1, A1, S2, A2 etc.) of Lamb and SH waves may also appear and make the analysis more complex. Considering these reasons, the frequency domain of 40 to 900 kHz with a frequency step of 2 kHz was selected for the harmonic analysis.

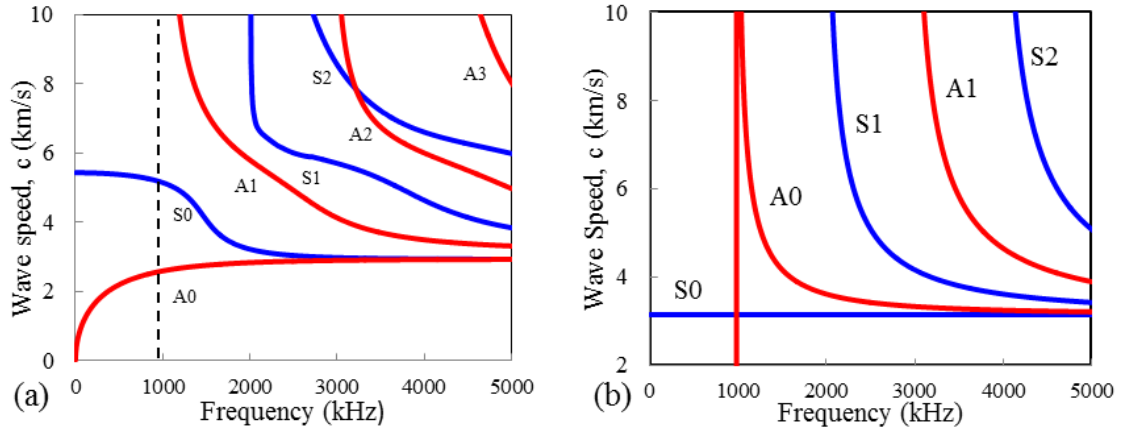


Figure 5.6 Dispersion curves for (a) Lamb wave and (b) SH wave for 1.6 mm thick aluminum plate

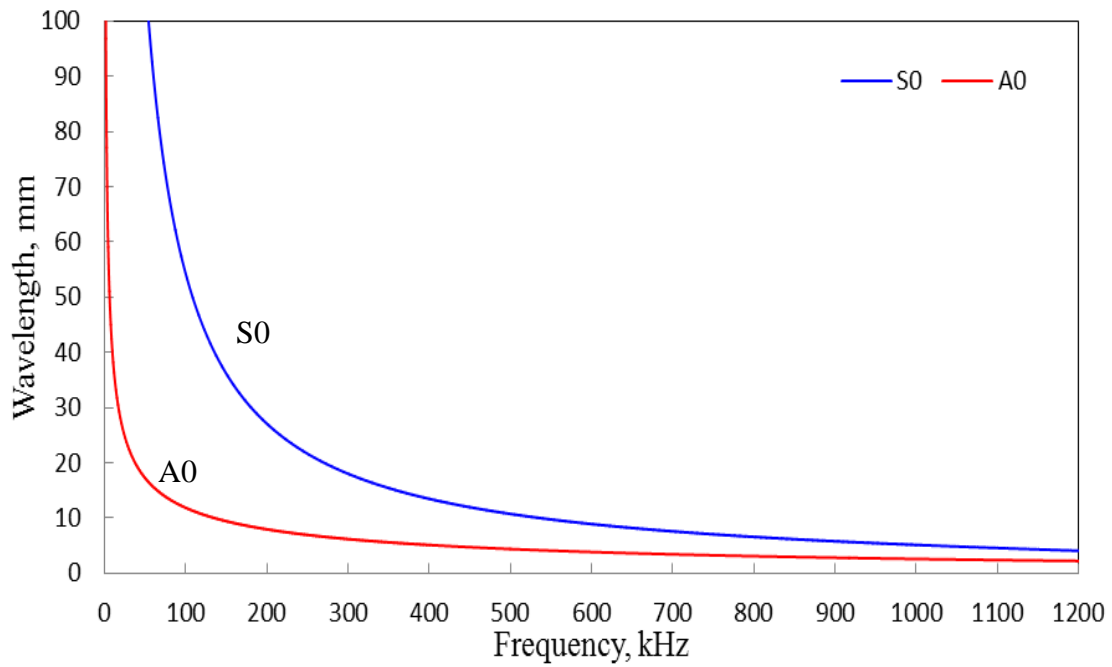


Figure 5.7 S0 and A0 Lamb mode wavelength variation with frequencies for 1.6 mm thick aluminum plate

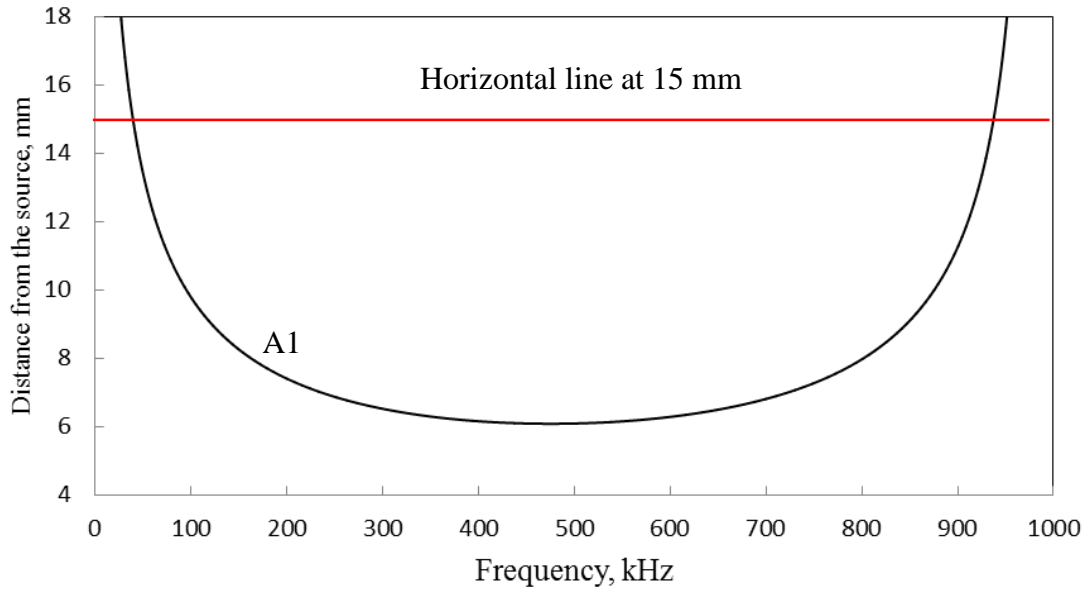


Figure 5.8 Die-out distance required for the non-propagating A1 mode

The sensing boundary is located sufficiently far away from the crack so that all non-propagating Lamb and SH scattered wave modes die out before they reach the sensing locations. Thus, the wave fields at the sensing locations around the rivet hole with cracks are the contributions of propagating Lamb and SH wave modes.

Three sets of FEM simulations were carried out to find the contribution of the butterfly cracks to the WDICs: (a) Lamb wave interaction with rivet hole with butterfly cracks; (b) Lamb wave interaction with rivet hole; and (c) Lamb wave interaction with a pristine plate. In order to get the wavefield at the sensing boundary due to the presence of butterfly cracks in a rivet hole, the wave field of the hole was subtracted from the wave field of rivet hole with butterfly cracks. The wave field of the pristine plate provides the required direct incident wave fields in Eq. (5.16). The WDICs provide the indication of getting strong or weak signals around the damage. In order to readily identify those locations, the WDICs are plotted in polar coordinates.

5.7 DISCUSSION OF THE SIMULATION RESULTS

After performing the FEM simulations, the WDICs are calculated using the mathematical expressions as discussed earlier. In this section, we discuss the WDICs in the form of a scatter cube i.e., their variation with frequency, incidence angle, and sensing angle values. This would give us a preliminary idea of what we should expect in the time domain signals.

5.7.1 FORMATION OF SCATTER CUBE

For each transmitting angle (θ), the WDICs are recorded at azimuth sensing angles (Φ) around the sensing boundary over the selected frequency domain. The results of the harmonic analyses of the 3D FEM model facilitate forming a “scatter cube” of complex-valued WDICs. The three dimensions of the scatter cube contain the WDICs for various frequencies, angles of transmitting PWASs, and angles of sensing PWASs. These WDICs can describe the complicated 3-D interaction between the interrogating waves and damage, i.e., scattering and mode conversion. Since the problem of rivet hole with cracks is symmetric with respect to the midplane of the thickness direction, no antisymmetric wave mode is generated from incident symmetric Lamb wave and vice versa.

5.7.2 DISTORTION OF WDIC PROFILE DUE TO THE PRESENCE OF CRACK

The polar plot of WDIC (WDIC profile) of the scattered S0 Lamb mode and SH mode due to incident S0 Lamb mode at $\theta=9^\circ$ is shown in Figure 5.9. An arbitrary frequency $f = 486$ kHz is selected for illustration purpose only. When there is no damage (pristine) in the plate, there is no scattered wave field and the WDIC profile is an ideal double-circled dipole.

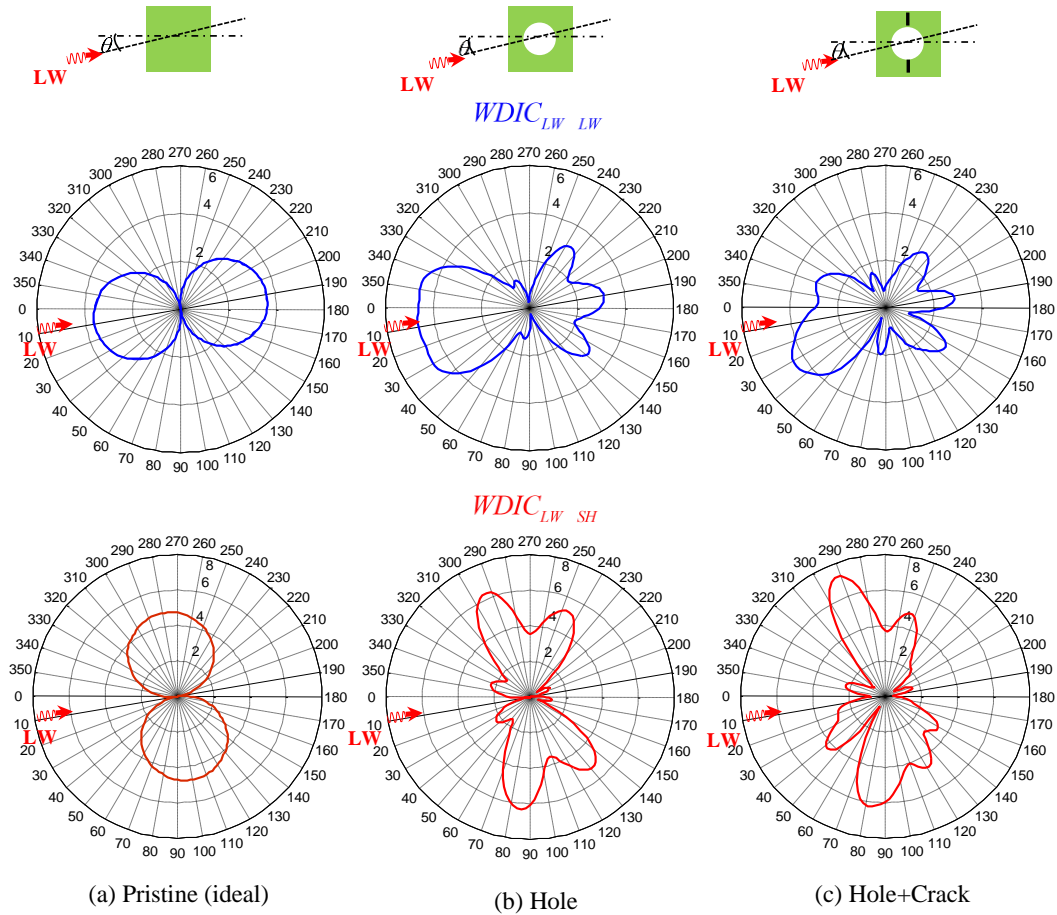


Figure 5.9 Alteration of WDIC profiles of scattered Lamb and SH wave with different damage conditions

When there is a rivet hole in the plate, the presence of scattered field makes distortion of the ideal shape of the WDIC profile as shown in Figure 5.9b. Note that the profile is symmetric about the line of incidence since the rivet hole is symmetric about the line of incidence. When there is damage (butterfly cracks) in the rivet hole, the additional scattered waves due to damage provides an additional distortion of the WDIC profile. The WDIC profile for hole+crack is not symmetric (Figure 5.9c) since the damaged rivet hole (hole+crack) is not symmetric about the line of incidence. In order to clearly identify the effect of damage in the plate, the scattered fields can be separated from the total fields.

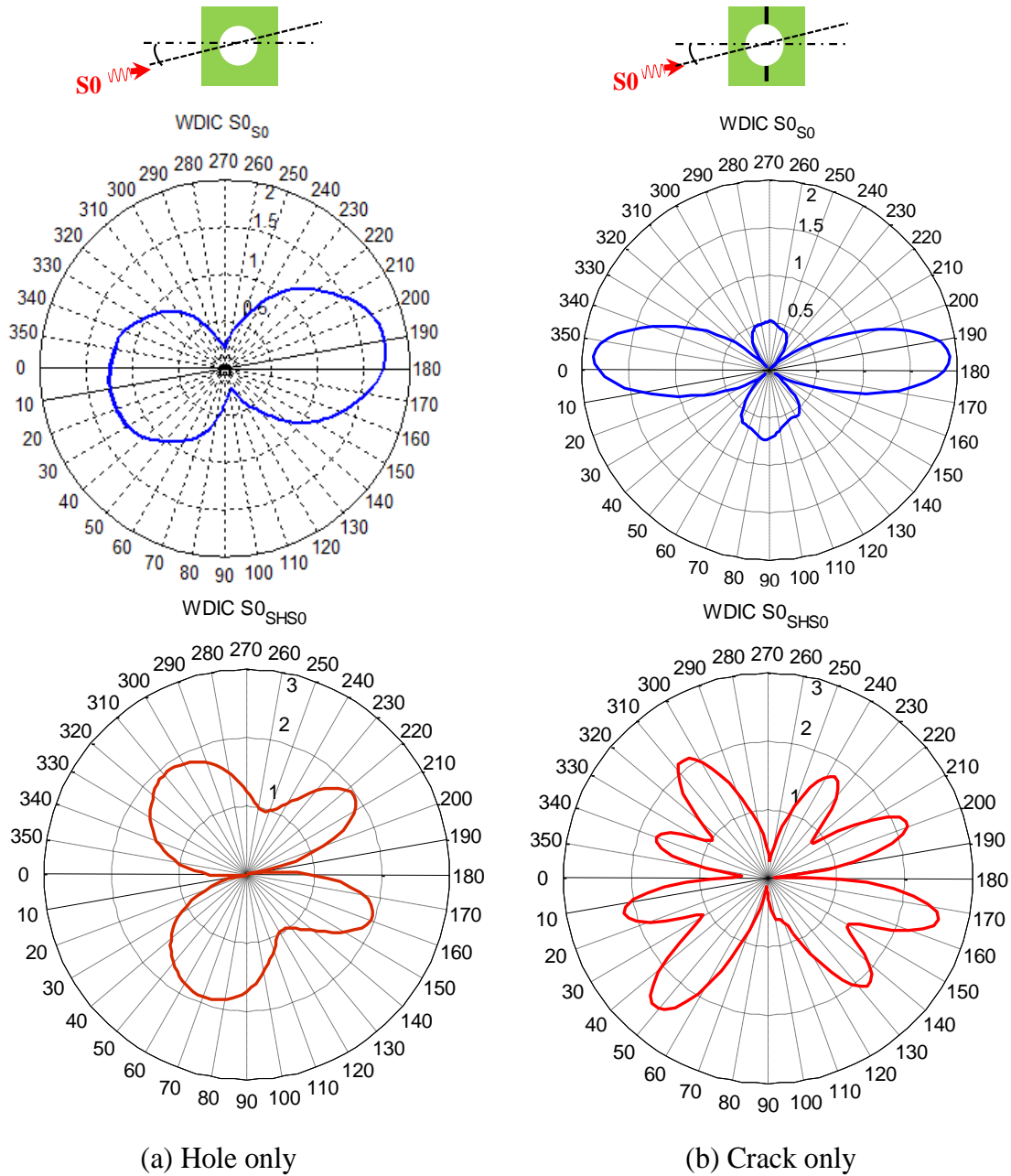


Figure 5.10 Subtracted WDIC profiles of scattered Lamb and SH wave to account the damage effect only

To find out the scattered field due to the presence of hole, incident wave fields (wave fields due to pristine) needs to be subtracted from the total wavefield (incident + scattered) and the corresponding WDIC profile of only the hole is plotted in Figure 5.10a.

Similarly, to find out the scattered field due to the presence of only the crack, the scattered wave field of only the hole and the incident wave fields are subtracted from the total wave field which is due to incident field plus scatter from hole with crack. Figure 5.10b shows the corresponding WDIC profile of scattered S0 Lamb wave and SH wave for only the crack. The WDIC profiles indicate that the magnitude of WDIC reaches to a larger value at certain azimuth angles Φ .

5.7.3 WDIC VARIATION IN FREQUENCY DOMAIN FOR DIFFERENT AZIMUTHAL POSITIONS

WDIC for a certain Lamb wave mode (S0 mode) incident from a particular direction ($\theta=9^\circ$) to the cracked rivet hole is shown in Figure 5.11. Five different azimuthal locations are picked arbitrarily to show the frequency domain variation of the WDICs. Note that at a certain location, a certain frequency of excitation provides the largest magnitude of WDIC. This frequency may be termed as “sensitive frequency” of that location. However, at a certain sensitive frequency, not all the azimuthal locations are necessarily equally sensitive. Thus the selection of the frequency of excitation as well as the location is important to capture the damage signature. By comparing all azimuthal location, it is possible to select a certain frequency that corresponds to the highest magnitude of the WDIC, for example, in this particular case, the star marked frequency ($f = 538$ kHz) can be the most sensitive excitation frequency at location 5 (“most sensitive location”).

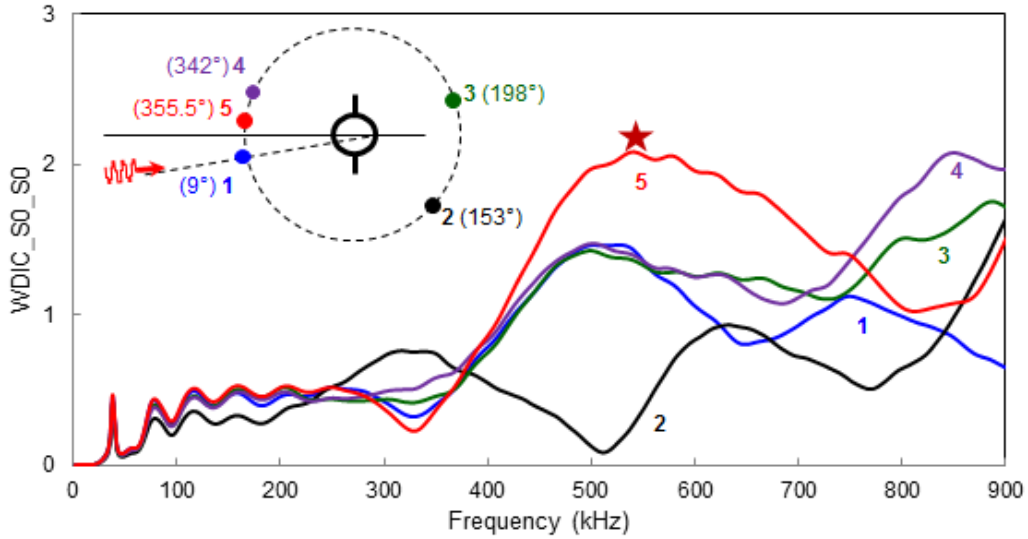


Figure 5.11 Frequency domain variation of $WDIC_{s0_s0}$ at different azimuthal positions ($\theta = 9^\circ$)

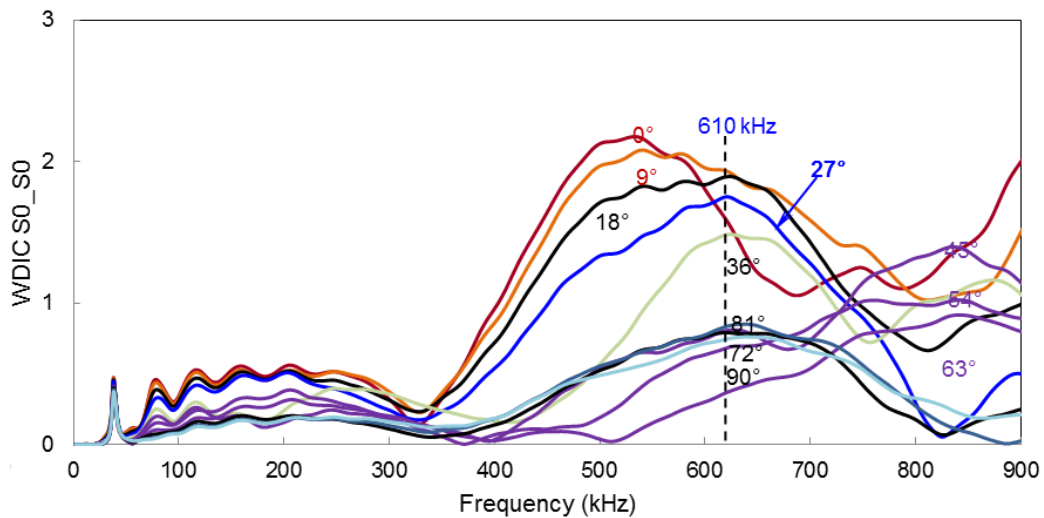


Figure 5.12 Frequency domain variation of $WDIC_{s0_s0}$ for multiple incident directions

5.7.4 WDIC VARIATION IN FREQUENCY DOMAIN FOR MULTIPLE INCIDENT DIRECTIONS

The frequency domain variation of WDIC can be extended at the most sensitive locations for different directions of incident Lamb waves. Figure 5.12 illustrates all possible directions of incident Lamb waves for the multiple-rivet hole lap joint. This plot can be used to find out the optimum excitation frequency for a particular incident direction

of Lamb waves. For example, when S0 Lamb wave hits the cracked rivet hole at $\theta = 27^\circ$, the excitation center frequency $f = 610$ kHz corresponds the highest WDIC.

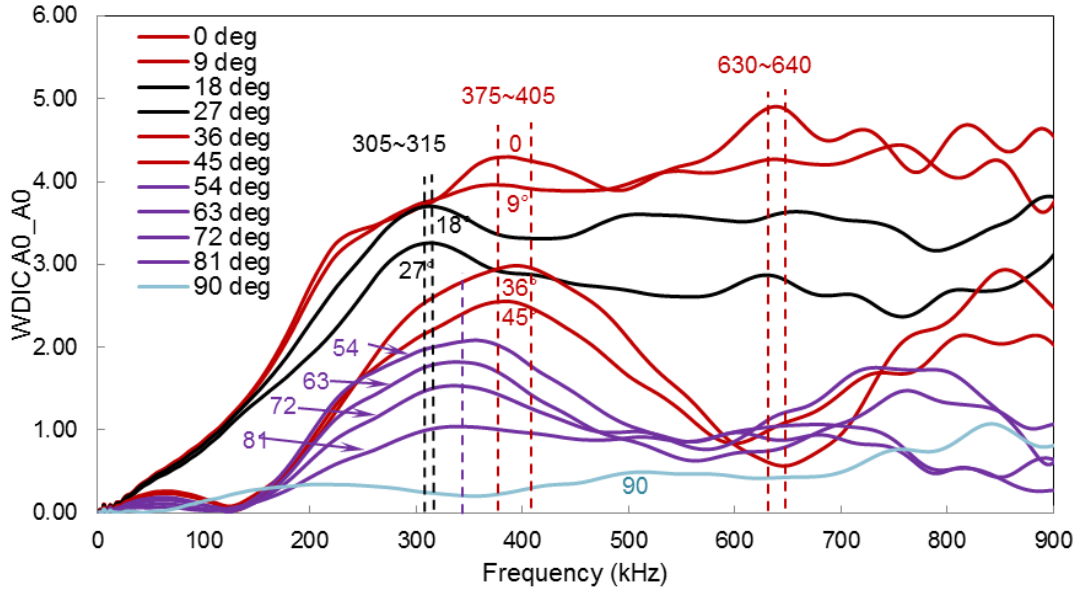


Figure 5.13 Frequency domain variation of $WDIC_{A0_A0}$ for multiple incident directions. The similar frequency domain plots for scattered A0 mode can be produced from the scatter cube of A0 Lamb wave mode incident as shown in Figure 5.13.

5.7.5 AZIMUTHAL VARIATION OF WDIC

The polar plot refers to the azimuthal variation of WDIC and can be used to identify the locations where WDIC reaches a maximum. The azimuthal variation of WDIC for symmetric and antisymmetric Lamb wave incident at 27° to the rivet hole cracks are shown in Figure 5.14. As the frequency changes, the WDIC profile for both symmetric and antisymmetric Lamb wave changes. It is possible to get multiple sensitive locations around the damage for a certain frequency of transmitting signal.

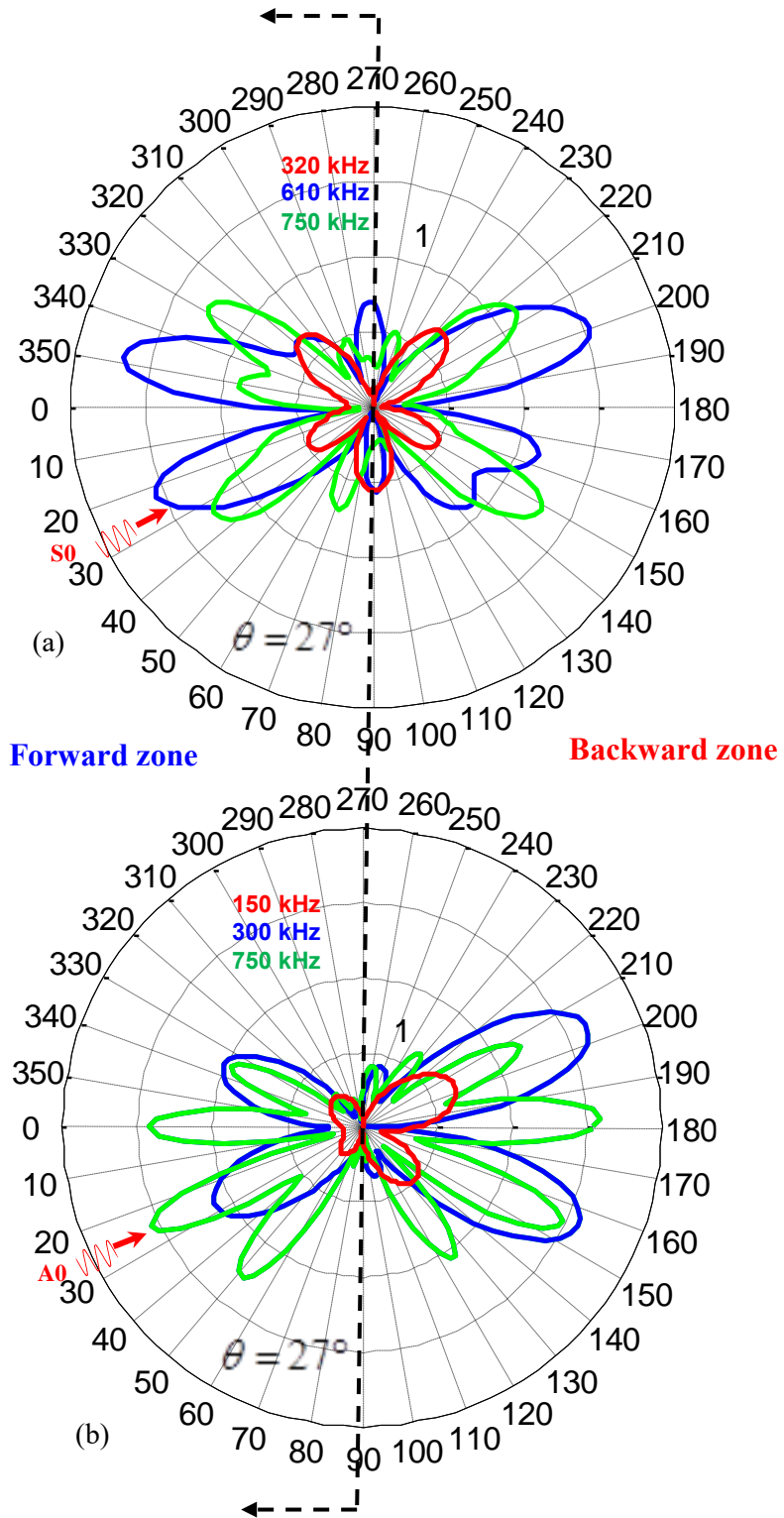


Figure 5.14 Azimuthal variation of (a) $WDIC_{S0_S0}$ (b) $WDIC_{A0_A0}$ at different frequencies

Sometimes, it may be important to classify the sensitive locations into two zones (forward and backward) because, depending on the application, there could be space limitations to install the sensors in a certain zone. In the problem of lap joint in real life structure, it is convenient to install the PWASs in the forward zone only and thus, the most sensitive locations in the forward zone will come into play for optimum design of the sensors.

5.7.6 WDIC POLAR PLOTS FOR MULTIPLE INCIDENT DIRECTIONS

Figure 5.15 shows the variations of WDIC profiles for different angles of incident S0 Lamb wave modes. For each angle of incident, the most sensitive frequency is selected for these polar plots and the most sensitive locations can be obtained based on the highest magnitude of WDIC of scattered S0 modes for each angle of incident. Those sensitive locations can be used to optimize the installation of the sensors around the multiple-rivet-hole lap joints. Figure 5.15 shows the polar plots for incident directions from 0° to 90° . The results for 0° to -90° would be the same because of symmetry with respect to the line of incidence. Thus the all possible location of the actuator with respect to the rivet hole is considered in this analysis. It can be noticed that as the inclination increases, the magnitude of WDIC decreases. When the incident Lamb wave is in line with the cracks ($\theta = 90^\circ$), the damage becomes symmetric with respect to the line of wave incidence. Hence, the WDIC profile for $\theta = 90^\circ$ is symmetric about the line of incidence as shown in Figure 5.15. Though Figure 5.15 shows the WDIC for incident S0 mode only, the similar plots can be generated for A0 mode using the scatter cube of incident A0 mode.

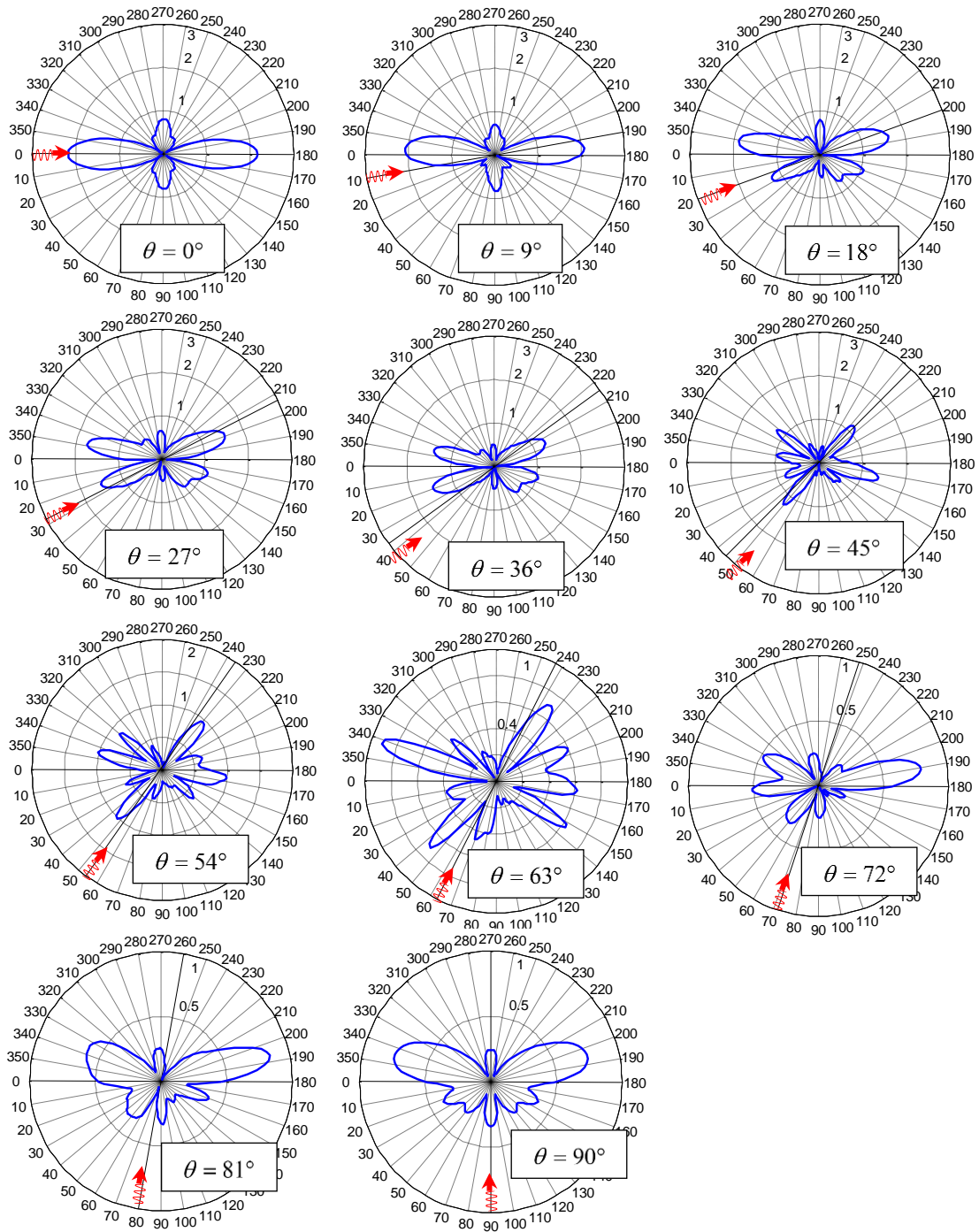


Figure 5.15 $WDIC_{s_0, s_0}$ for various incident angles at most sensitive frequencies

5.8 SIMULATED TIME DOMAIN SIGNALS

The time domain signals vary with the selection of the frequencies and locations of the sensors. Three-count tone-burst excitation signal was applied to a 7-mm diameter

PWAS that was used as an actuator. The actuator was located at 100 mm away from the damage (rivet hole with butterfly cracks). The angular position of the sensor was varied around the damage. The radial distance from the damage to the sensor was kept at 30 mm.

5.8.1 ILLUSTRATION OF SIGNAL EXTRACTION DUE TO CRACK

The signal extraction process is illustrated in Figure 5.16. When there is only the rivet hole in the plate, the signal in the sensor is shown in Figure 5.16a. With the presence of cracks in the rivet hole, the sensor signal changes as shown in Figure 5.16b. By subtracting the two signals, the signals due to only the cracks can be obtained as shown in Figure 5.16c. This illustration is shown for a particular frequency of 538 kHz and when Lamb waves incident perpendicular to the rivet hole crack.

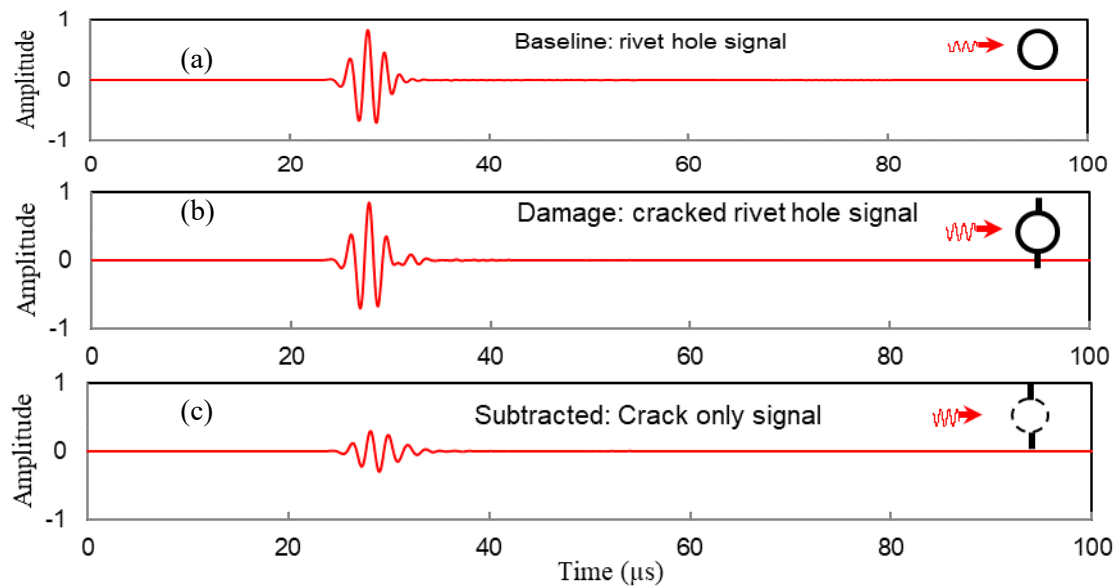


Figure 5.16 (a) The baseline reference signal for the hole. (b) The signal due to Hole + Crack (c) Subtracted signal due to the crack only ($f = 538 \text{ kHz}$, $\theta = 0^\circ$)

5.8.2 DETERMINATION OF OPTIMUM PARAMETER FOR SOME EXAMPLE CASES

In this present research, we considered a simplified case of the multiple-rivet-hole problem as shown in Figure 5.17 where the actuator is located at θ . Later, some specific

values of θ are taken (9° , 18° , 27°) for illustration. A single rivet hole is considered for determining the optimum location of the sensor and the optimum frequency of excitation. Furthermore, the rivet hole is considered located at sufficiently far away from the edge of the plate (the length, B , is large) so that: (1) the reflection from the edge dies out sufficiently before it reaches the sensor (2) the very low amplitude reflected signal, if any, would be seen in the trailing part of the main signal and can be easily discarded.

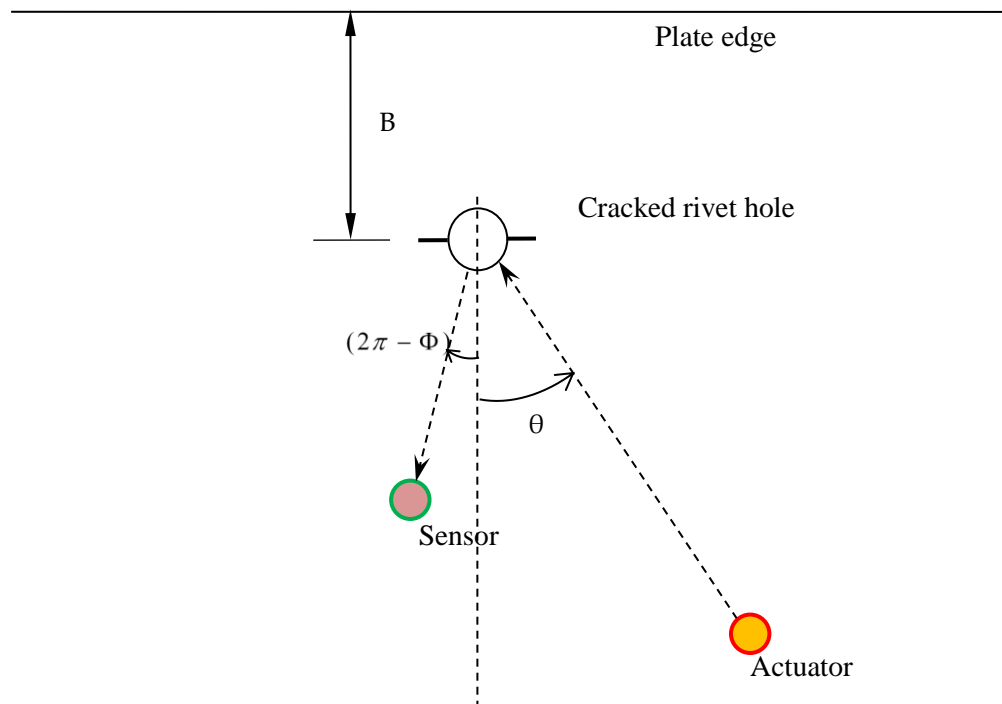


Figure 5.17 A simplified case of the multiple-rivet-hole problem

When there are multiple rivet holes, there will be mutual the interactions of the scattered waves among the rivet holes. When the plate edge is located close to the rivet holes, the plate boundary would act as a secondary source of the scattered waves and distance B would have an effect on the overall result. These complexities have not been included in this present study and will be focused in our future research.

5.8.3 OPTIMUM PARAMETER FOR LAMB WAVE INCIDENT AT $\theta = 9^\circ$

Now we consider a case when the Lamb wave (S0 mode) incident on the damage at $\theta = 9^\circ$. Only the sensing signal from the rivet-hole cracks is illustrated in Figure 5.18. Four different sets of parameters (frequency and location) are considered based on the analysis of scatter cube of complex-valued WDICs.

- (a) Set 1: $f = 328$ kHz, $\Phi = 355.5^\circ$ - corresponds to the low magnitude of WDIC
- (b) Set 2: $f = 538$ kHz, $\Phi = 355.5^\circ$ - corresponds to the highest magnitude of WDIC
- (c) Set 3: $f = 728$ kHz, $\Phi = 355.5^\circ$ - corresponds to a moderate magnitude of WDIC
- (d) Set 4: $f = 538$ kHz, $\Phi = 340^\circ$ - corresponds to a low magnitude of WDIC

For the first three parameter sets, 1, 2, 3, the frequencies are changing while the location of the sensor is same. For set 4, the frequency is corresponding to the highest magnitude of WDIC while the angular location of sensor corresponds to a low magnitude of WDIC. It can be easily noticed from the Figure 5.18 that the parameter set 2 ($f = 538$ kHz, $\Phi = 355.5^\circ$) provides the most noticeable crack signal picked up by the sensor. Thus the right frequency, as well as the right location of the sensor, is important to harness the damage information in the structure. For the Lamb wave incident at $\theta = 9^\circ$, set 2 has the optimum parameters and is the best choice for the NDE/SHM engineers.

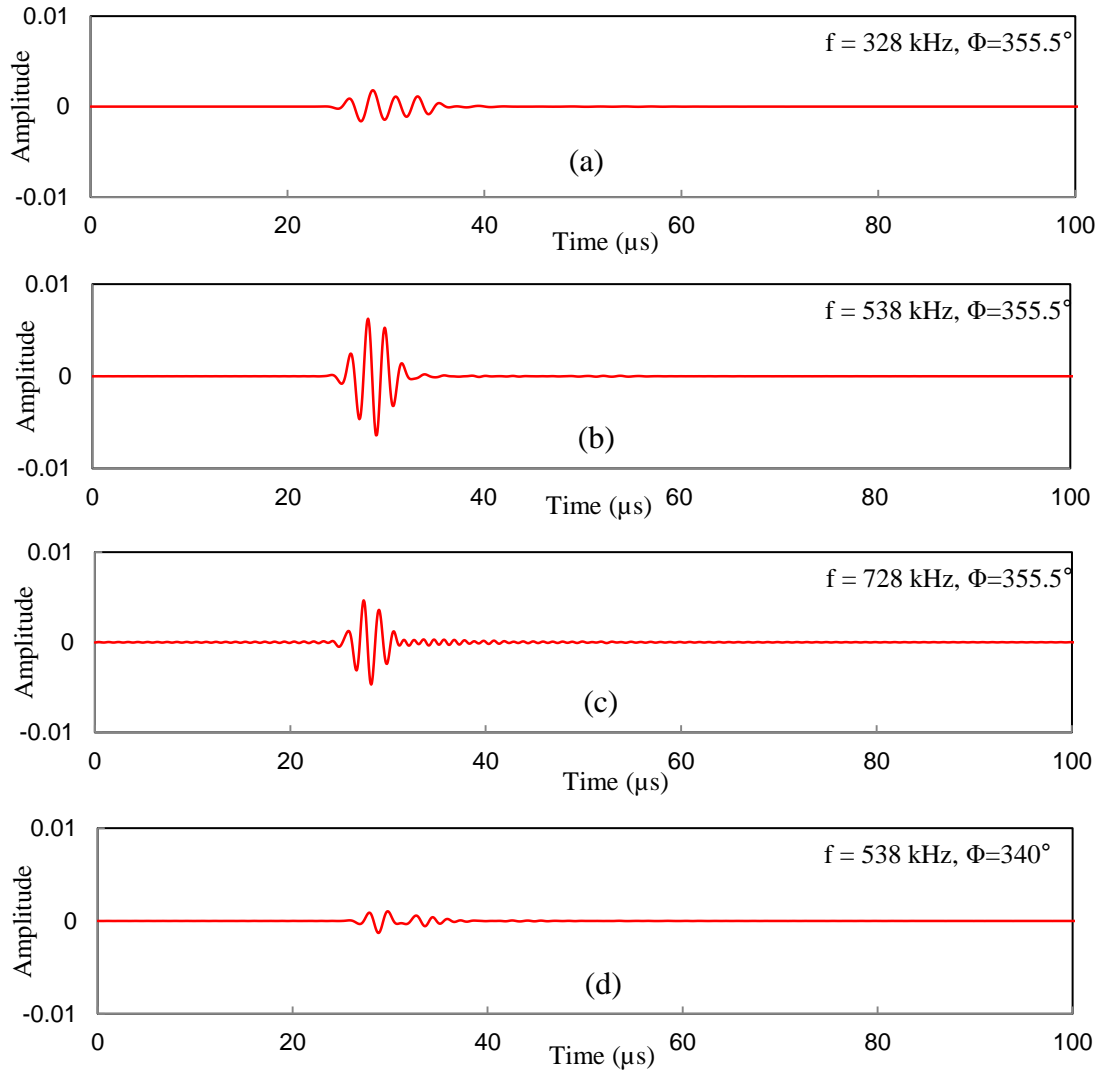


Figure 5.18 Sensing signals for different sets of frequency-location ($\theta = 9^\circ$)

5.8.4 OPTIMUM PARAMETER FOR LAMB WAVE INCIDENT AT $\theta = 18^\circ$

Another case may be illustrated when the Lamb wave (S_0 mode) hits the rivet hole at $\theta = 18^\circ$ which corresponds to one of the situations of the multiple-rivet-hole problem. The real-time domain signals are shown in Figure 5.19 for four different parameter sets. These parameter sets are selected based on the scatter cube analysis that was discussed in Section 5.7.

(a) Set 1: $f = 320 \text{ kHz}, \Phi = 350^\circ$ - corresponds to the low magnitude of WDIC

- (b) Set 2: $f = 486 \text{ kHz}$, $\Phi = 350^\circ$ - corresponds to the highest magnitude of WDIC
- (c) Set 3: $f = 618 \text{ kHz}$, $\Phi = 350^\circ$ - corresponds to a moderate magnitude of WDIC
- (d) Set 4: $f = 618 \text{ kHz}$, $\Phi = 75^\circ$ - corresponds to a low magnitude of WDIC

By observing the time domain signal of Figure 5.19, the obvious selection of the parameter set is either (b) or (c), because both of them correspond to the most sensitive signal. Thus the excitation frequency of 486 or 618 kHz at the transmitter and the receiver sensor at $\Phi = 350^\circ$ is the optimum design parameter set for detecting the cracks in the rivet hole.

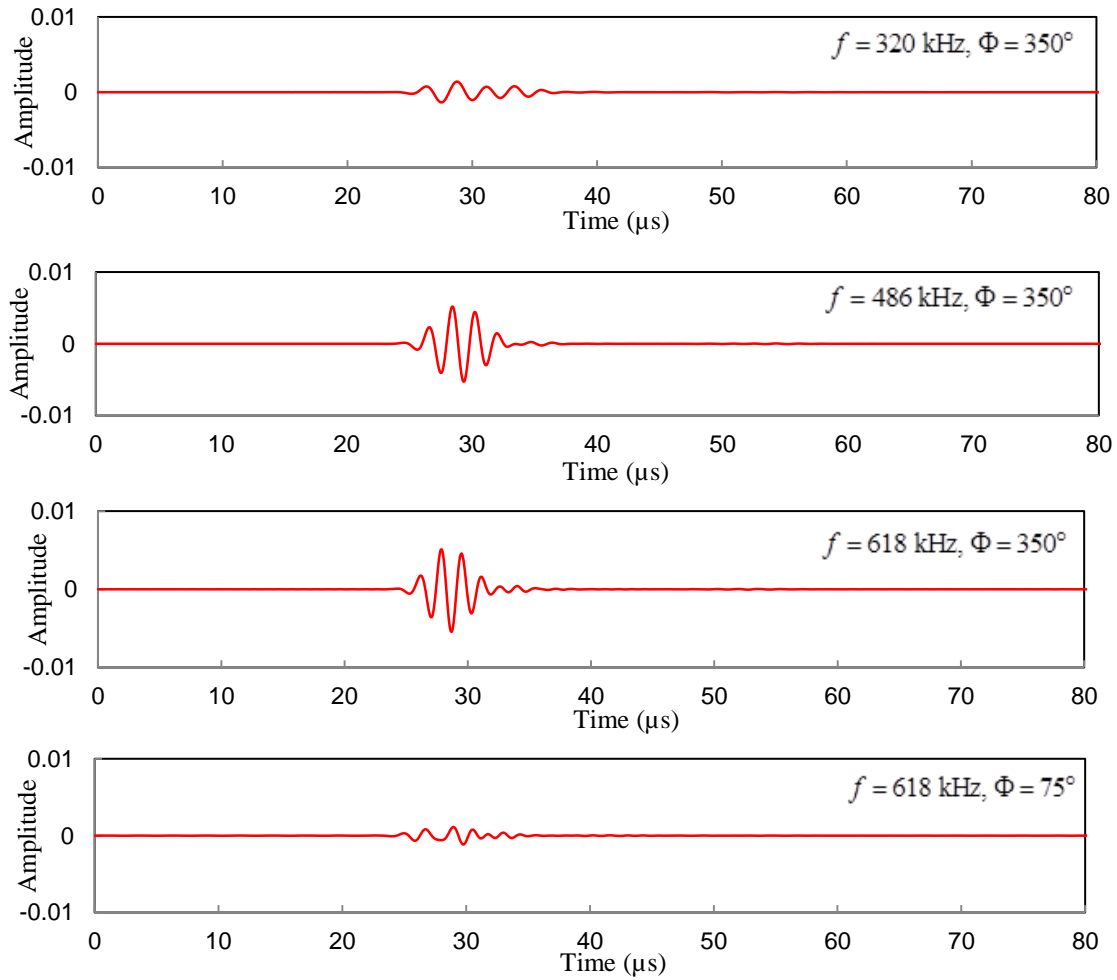


Figure 5.19 Sensing signals for different sets of frequency-location ($\theta = 18^\circ$)

5.8.5 OPTIMUM PARAMETER FOR LAMB WAVE INCIDENT AT $\theta = 27^\circ$

When the Lamb wave (S0 mode) is incident at, we choose four different parameters sets (frequency and location) based on the analysis of scatter cube of complex-valued WDICs.

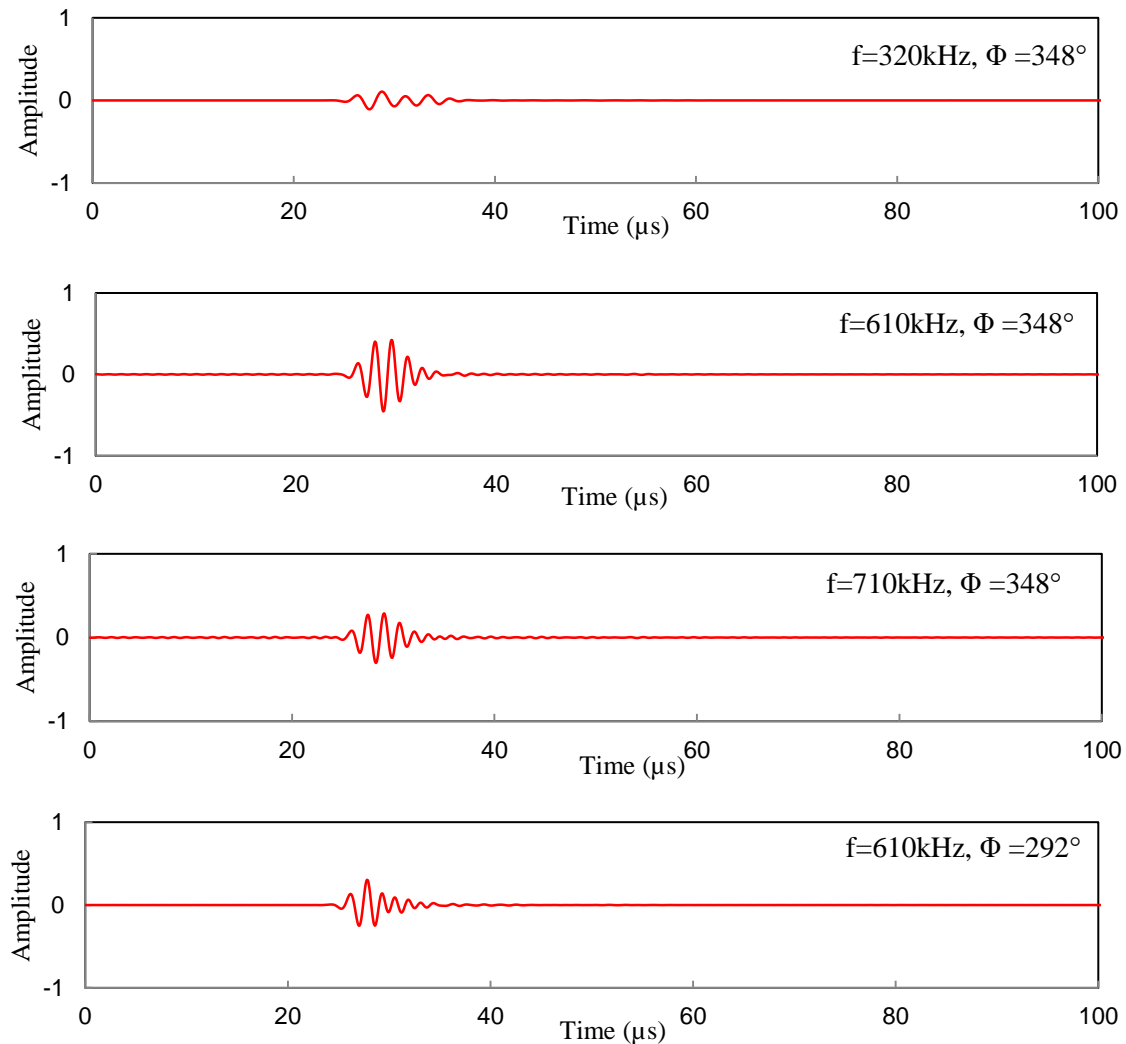


Figure 5.20 Sensing signals for different sets of frequency-location ($\theta = 27^\circ$)

The four sets of parameters are shown below:

- (a) Set 1: $f = 320 \text{ kHz}$, $\Phi = 348^\circ$ - corresponds to the low magnitude of WDIC
- (b) Set 2: $f = 610 \text{ kHz}$, $\Phi = 348^\circ$ - corresponds to the highest magnitude of WDIC

(c) Set 3: $f = 710$ kHz, $\Phi = 348^\circ$ - corresponds to a moderate magnitude of WDIC

(d) Set 4: $f = 610$ kHz, $\Phi = 292^\circ$ - corresponds to a low magnitude of WDIC

In the first three parameter sets, 1, 2, 3, the frequencies are changing while the location of the sensor is same. In set 4, the frequency is corresponding to the highest magnitude of WDIC while the angular location of the sensor corresponds to a low magnitude of WDIC. It can be easily noticed from Figure 5.20 that, the parameter set 2 ($f = 610$ kHz, $\Phi = 348^\circ$) provides the most noticeable crack signal picked up by the sensor. Thus, the right frequency, as well as the right location of the sensor, is important to extract the damage information from the structure. For the Lamb wave incident at $\theta = 27^\circ$, set 2 has the optimum parameters and is the best choice for the NDE/SHM engineers.

In this present study, the generalized procedure was illustrated followed by some specific examples. We may do a similar analysis for each rivet hole of the multiple-rivet-hole problem and determine the optimum positions of the actuator and sensors. We can also optimize the required number of actuators and sensors, but that would require a future study.

5.9 CONCLUSIONS

The exact analytical formulation for wave propagation has been used throughout the structure, except for the local damage area, which was analyzed using the finite element method. In order to detect the crack in a multiple-rivet-hole lap joint, the Lamb waves have been impinging on the damage from all possible directions. Both symmetric and antisymmetric fundamental Lamb wave modes (S_0 and A_0) were used in the analysis. SH waves appeared in the scattered waves besides the Lamb waves. Due to the non-axisymmetric nature of the problem, the wave damage interaction coefficient (WDIC) had

non-axisymmetric behavior around the damage. The scatter cubes were produced for the scattered waves to accommodate the 3D interaction of Lamb waves with the rivet hole cracks: frequency, incident direction, azimuthal sensing direction. From the frequency domain analysis and the azimuthal variation of the WDIC, the proper locations of the sensors and center frequency of excitation have been obtained through the demonstration of some particular cases. The physical time-domain signals were obtained using a piezoelectric transducer for different sets of frequency-location. The optimum selection of the location of the sensor and of the center frequency of excitation gave a strong signal that confirms a better detection of the cracks in the rivet hole. These optimum parameters can be used for making an algorithm of NDE/SHM unit for inspecting the multiple-rivet-hole lap joint.

CHAPTER 6

MULTIPHYSICS FEM SIMULATIONS FOR FATIGUE-CRACK GENERATED ACOUSTIC EMISSIONS VALIDATED BY EXPERIMENTS

This chapter presents the multiphysics FEM simulation of fatigue-crack generated acoustic emissions captured by piezoelectric wafer active sensors (PWAS). PWAS are commonly used for detecting Lamb waves for structural health monitoring (SHM) applications. A new avenue of using the PWAS transducers for detecting the fatigue-crack related acoustic emission (AE) signals. These AE signals have relatively lower amplitudes than the actuator-generated wave signals of an active SHM system. Multiphysics 3D FEM simulations were performed with PWAS transducers under various dipole-loading configurations to simulate fatigue crack-related AE signals. The simulated results were validated by the experimental measurements.

6.1 STATE OF THE ART

The structural health monitoring (SHM) technology is increasingly used for the detection of progressive defects in critical aerospace structures [71]–[74]. SHM has been introduced for both active and passive damage identification for the real-time monitoring of the structures. Monitoring of AE signals from the progressive fatigue damage is categorized as passive online monitoring [48], [75], [76]. The AE signals from the fatigue crack have always been an interest to researchers [77]–[80]. However, the AE signals from

the fatigue crack are usually low-amplitude signals and challenging to detect using conventional AE sensors [81], [82].

Piezoelectric AE sensors such as PICO, S9225, WSA had been used to detect pencil lead break (PLB) simulated AE signals [83], [84]. They were also used for detecting the AE signals from impact damage [85], [86]. However, the AE signals from these sources were generally high-amplitude signals. They had higher-amplitude out-of-plane components and these AE sensors were also well-constructed to sense the out-of-plane wave motion. Thus the AE sensors could effectively sense the high-amplitude AE signals from these sources. However, the AE signals due to a fatigue crack in thin plate-like aerospace structures are much more complex than the simple PLB and impact damage signals [87]–[90].

AE hits from the crack in a notched thick specimen were captured by the piezoelectric AE sensors [81]. However, the surface waves were dominant in these AE signals. AE signals from the fatigue damage in a round steel specimen were analyzed by Ould Amer et.al. [91]. Three clusters of elastic waveforms had been shown, one of which had very low energy content as compared to the other two. However, the fatigue loading cycle in relation to the AE signals was not discussed. Analytical analysis showed that the formation of a penny-shaped crack in the aluminum alloys emits acoustic waves [92]. They simulated different modes of crack formation by a sudden drop of the stress on the crack surface.

The experimental analyses supported by numerical simulations provide deeper insight of the elastic wave propagation phenomena [93]–[95]. Many theoretical works were developed to correlate the AE waveforms to their sources [96]–[98]. In seismology, the

moment tensor approach was used to describe the movement of a fault during an earthquake [99]–[101]. The moment tensor comprises nine generalized couples including three dipoles. Buried monopole and dipole with various step functions and fracture mechanics-based methods were used to model the AE source [102]–[104]. However, the interaction of the AE waveform with the crack boundary in a thin plate is yet to be analyzed. In most cases, researchers rely on the finite element (FE) methods to analyze the near-field interaction [105]. The FE methods are the most effective tool to estimate the near acoustic wave field, however, computationally expensive for far-field estimation [86].

Piezoelectric wafer active sensors (PWAS) were commonly used for active SHM applications [10], [106]. These sensors successfully captured the guided waves in active detection technique [107], [108]. The active detection method required an user-defined excitation signal where the high-amplitude signals can be used to excite the structure. The potential advantage of using the PWAS transducer is that it can measure the in-plane and out-of-plane wave motion through the wafer strain sensing mechanism [10]. However, the use of PWAS transducers in application to fatigue-crack related AE signals are yet to be analyzed. Assessment of the PWAS transducers to capture the AE signals using multiphysics FEM simulation and experiment would be of interest to the SHM and NDE community.

6.2 SCOPE OF THE CHAPTER

This chapter focuses on the multiphysics simulation of fatigue-crack generated AE signals. Dipoles placed at the crack tips were used to simulate the AE event. The resulted elastic waves were captured by simulated PWAS transducers. The acoustic wave interaction with crack geometric feature was studied. The 3D multiphysics modeling,

fatigue crack modeling, and thickness-wise assignment of dipoles are discussed. The effect of rise time, dipole loading orientation, and distance of PWAS transducers are studied.

6.3 DESCRIPTION OF 3D MULTIPHYSICS FEM SIMULATION

Multiphysics simulations were performed on the three-dimensional FE models by combining the physics of piezoelectricity and structural dynamics. The PWAS transducers are modeled simultaneously with the host structure to accomplish the multiphysics simulation. The transient FE analysis was performed to obtain the time-domain signals and the acoustic wave propagation in the structure. Aircraft grade aluminum 2024-T3 material properties were used for the host structure. The modulus of elasticity of the material, $E=73.1$ GPa; Poisson's ratio, $\nu=0.33$; the density, $\rho=2780$ kg/m³; and the shear wave speed, $c_s = 3140$ m/s.

In this research, numerous models were developed to study the effect of different parameters. A comprehensive description is given below for a model that contained all the parameters such as two PWAS transducers, a 20-mm fatigue crack, a dipole perpendicular to the crack, and non-reflective boundaries. This description may serve as a guide to perform AE modeling with fatigue cracks. One can easily generate other models by changing the parameter of interest such as dipole loading characteristic quantity (rise time), dipole loading orientation, number of PWAS transducers, crack length, and model geometry. The step by step description of the comprehensive model is discussed below:

6.3.1 PRACTICAL ASPECTS OF THE MODEL

The geometry of the model is shown in Figure 6.1. A thin (thickness = 1 mm) square plate with 120 mm side was modeled using ANSYS 15.0. Since it has been an interest for the fatigue crack-related AE signal simulation, a fatigue crack was introduced in the plate.

In practice, fatigue crack always initiates from some kind of discontinuities such as holes, notch, joints etc. By keeping this in mind, a small 1-mm diameter hole was modeled at the center of the plate. A 9.5-mm fatigue crack was modeled on each side of the hole. Thus, the total length (2a) of the crack was 20-mm (tip to tip). The host structure was meshed with eight nodes SOLID45 structural element. This geometry was chosen by keeping in mind that we could run an AE-fatigue experiment to validate the simulation results.

6.3.2 MODELING OF THE FATIGUE CRACK

There are numerous ways to model a fatigue crack in FEM [109], [110]. We adopted a popular and simpler method to model the crack. The crack was modeled by using the discontinuity at the adjacent pair of nodes along the two crack surfaces. Two sets of nodes exist along the crack faces and each set represents the nodes on each face. The nodes are discontinuous along the crack faces and there was no interaction between these nodes. Two sets of nodes were adjacent to each other and the solid elements were separated along the crack faces. This type of modeling represents a crack opening situation while crack grows near the peak load of the fatigue loading in practice. The modeling of the cracks using the above approach is fair enough for FE modeling of actual cracks with a small hole in a plate-like structure [70], [109]. The crack was symmetric about the center hole as shown in Figure 6.1a.

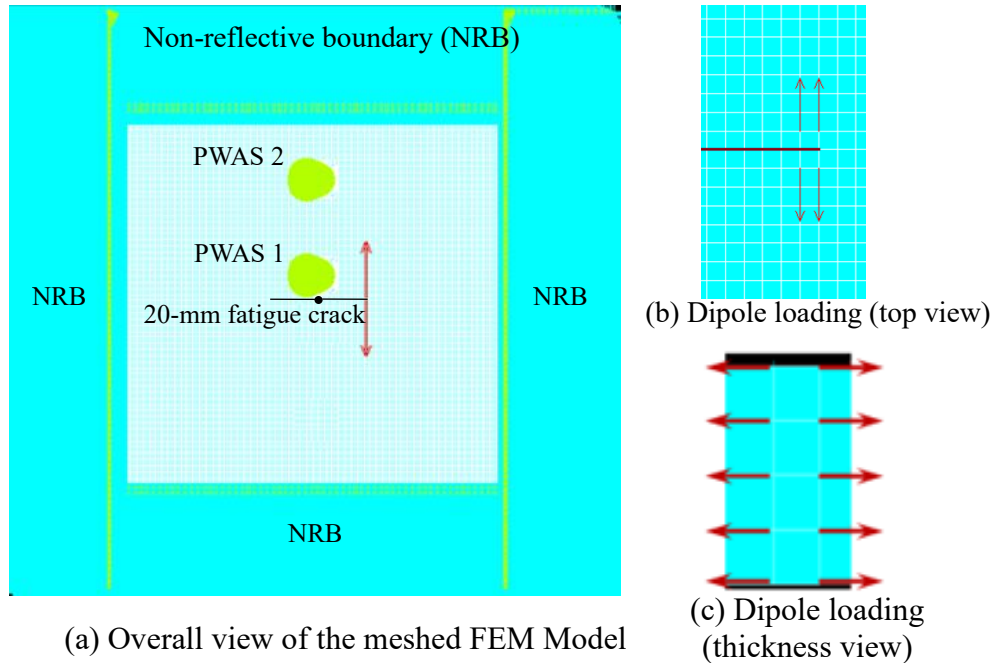


Figure 6.1 The meshed FEM model with in-plane dipole excitation: (a) overall view (obtained directly from ANSYS); (b) zoomed in view of crack tip area showing dipole loading; (c) side view showing the thickness-wise assignment of dipole components

6.3.3 MODELING OF THE PWAS TRANSDUCERS

Two PWAS transducers were modeled on the host aluminum structure. The size of each PWAS was 7-mm. One PWAS was modeled in the near-field of the crack and the center of the PWAS was at 5-mm from the crack. The other PWAS was modeled in the far-field of the crack and the center of the PWAS was at 25-mm from the crack. The PWAS was meshed with eight node SOLID5 coupled field element. This element with properly selected coupled field options can handle the coupling of piezoelectric and structural properties. The thickness-wise polarization was chosen for the modeled PWAS. The following material properties were chosen for PWAS transducers.

$$C = \begin{bmatrix} 97 & 49 & 49 & 0 & 0 & 0 \\ 49 & 49 & 49 & 0 & 0 & 0 \\ 49 & 49 & 84 & 0 & 0 & 0 \\ 0 & 0 & 0 & 24 & 0 & 0 \\ 0 & 0 & 0 & 0 & 22 & 0 \\ 0 & 0 & 0 & 0 & 0 & 22 \end{bmatrix} \text{GPa} \quad (6.1)$$

$$\varepsilon = \begin{bmatrix} 947 & 0 & 0 \\ 0 & 605 & 0 \\ 0 & 0 & 947 \end{bmatrix} \times 10^{-8} \text{ F/m} \quad (6.2)$$

$$e = \begin{bmatrix} 0 & 0 & 0 & 0 & 12.84 & 0 \\ 0 & 0 & 0 & 12.84 & 0 & 0 \\ -8.02 & -8.02 & 18.31 & 0 & 0 & 0 \end{bmatrix} \text{ C/m}^2 \quad (6.3)$$

where C is the elastic stiffness matrix, ε is the dielectric matrix, and e is the piezoelectric stress matrix.

The piezoelectric transduction of the PWAS material gave the voltage signal directly as an output. Any mismatch due to meshing should be avoided for better FEM results. Thus, the PWAS and the underneath host structure was meshed using the same mesh topology. This ensured that each node of the PWAS element coincided with the corresponding node of the host structure element. The nodes between the PWAS element and the structural element are then merged together to simulate a perfect bonding between PWAS and host structure. One can model any additional layer of bonding between PWAS and structure to obtain better accuracy in comparison with experimental measurements. However, one should be careful of the thickness and material properties of the bonding layer. The additional accuracy due to bonding effect may easily be destroyed by improper aspect ratio or mismatch of the bonding layer element size, PWAS element size, and host structure element size. For simplicity, the bonding layer modeling was not included in the

current model. To know more about bonding effect, the readers are suggested to review the work of Santoni-Bottai [111], and Lin et al. [112] in our LAMSS group.

6.3.4 MODELING OF THE ACOUSTIC EMISSION EVENT AT THE CRACK TIP

The acoustic emission source at the crack tip was modeled using the dipole concept suggested by Hamstad et al. [102] and Prosser et al. [94]. The dipoles are basically the components of the moment tensor as discussed by Aki and Richards [99]. The moment tensor components were used to simulate the seismological acoustic events. After gaining knowledge, background, and insight from the previous research, the dipole concept was extended to the current research [113], [114]. Two dipoles were used to simulate the AE event due to fatigue crack growth. The dipoles were applied at the tip of the crack as shown in Figure 6.1b. The dipoles were placed at one element distance from each other to represent a unit growth of the fatigue crack. Since the crack in the thin plate usually happens along the entire thickness, the dipoles were placed along the thickness as a line dipole source (Figure 6.1c).

Each dipole consisted of two self-equilibrating point forces of equal strengths. The magnitude of the point force follows a sharp rising step function. This type of step function represents a wideband AE source. The rise time was the characteristic parameter of the step function. A half-cosine bell rising step function with 1.5 μs rise time was used in the modeling. Following the ref. [102], mathematically, the half-cosine bell step function, $F(t)$ can be expressed as

$$F(t) = \begin{cases} 0.5(1 - \cos(\pi t / \tau)); & 0 \leq t \leq \tau \\ 1; & t > \tau \end{cases} \quad (6.4)$$

where τ is the rise time, t is the time variable.

The time variation and the frequency spectrum of the half-cosine bell step function are shown in Figure 6.2. This type of the smoothing step-up function was used for the modeling since it provided a better simulation of the AE event as mentioned in ref. [102].

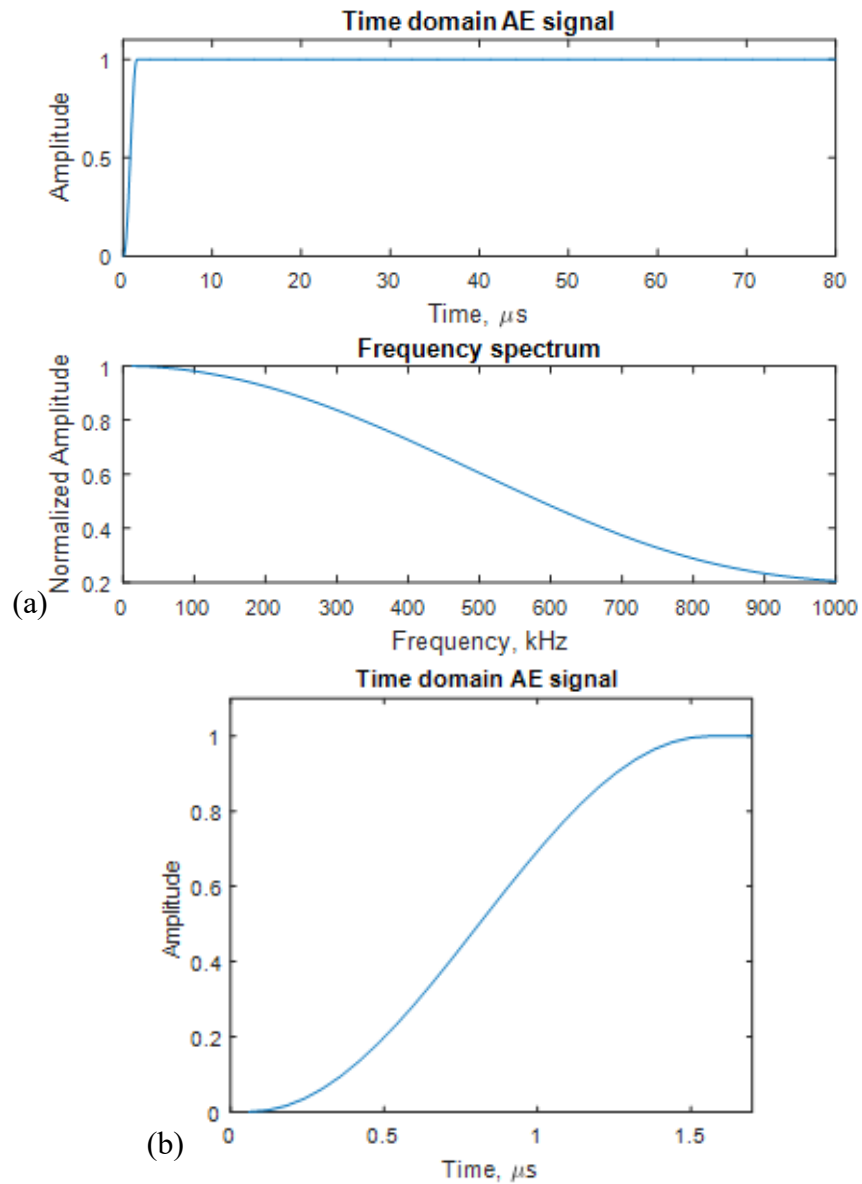


Figure 6.2 The dipole loading used for simulating the AE event at the crack tip. (a) A typical half-cosine bell step function and its frequency response (rise time = $1.5 \mu\text{s}$), (b) the half-cosine bell step-up from 0 to 1 in the amplitude scale.

The meshing followed the criteria mentioned in ref. [102] to achieve better FEM results. The non-reflective boundary (NRB) was used in the FEM model to avoid the reflections from the plate edges. The NRB was modeled using the criteria mentioned in ref. [61].

6.4 MULTIPHYSICS FEM SIMULATION RESULTS

The multiphysics simulation results showed that the acoustic event at the crack tip generated acoustic waves in the structures. These acoustic waves were captured by both PWAS transducers as AE signals. The simulated results can be discussed in two significant aspects as follows:

6.4.1 ACOUSTIC EMISSION PROPAGATION AS GUIDED WAVE

The effect of the AE event at the crack tip propagated as guided waves in the plate. Snapshots at various simulation times are shown in Figure 6.3. The snapshots are illustrating the following: (a) the acoustic wave traveling toward PWAS 1, (b) the waves arriving at PWAS 2 and the second tip of the crack, (c) the secondary AE event generated at the crack-tip, (d) the reflected AE waves traveling backward to the first crack tip, (e) the reflected AE waves hitting again PWAS 1, and (f) the back and forth AE waves along the crack followed by another secondary AE event at the second crack-tip. The AE event occurred at the original crack-tip is referred to as “primary AE event”. The resulting AE waves travel in the plate. The acoustic waves hit the near-field PWAS 1 and then passed it as the time progressed. Subsequently, the guided waves hit the far-field PWAS 2 and the other crack-tip. When the waves hit the second crack-tip, another AE event was generated; this is referred to as “secondary AE event”.

The back and forth motion of the acoustic waves may generate crack resonance as we verified with experimental measurement in a recently published paper [115]. Both primary and secondary AE events may generate the AE signals that were captured by the two PWAS transducers. It was observed that the acoustic waves propagate with Rayleigh surface wavespeed along the crack surface. The near-field PWAS may sense complex guided wave signals as it was placed near the source. The far-field PWAS may sense fully developed AE signals propagated throughout the plate.

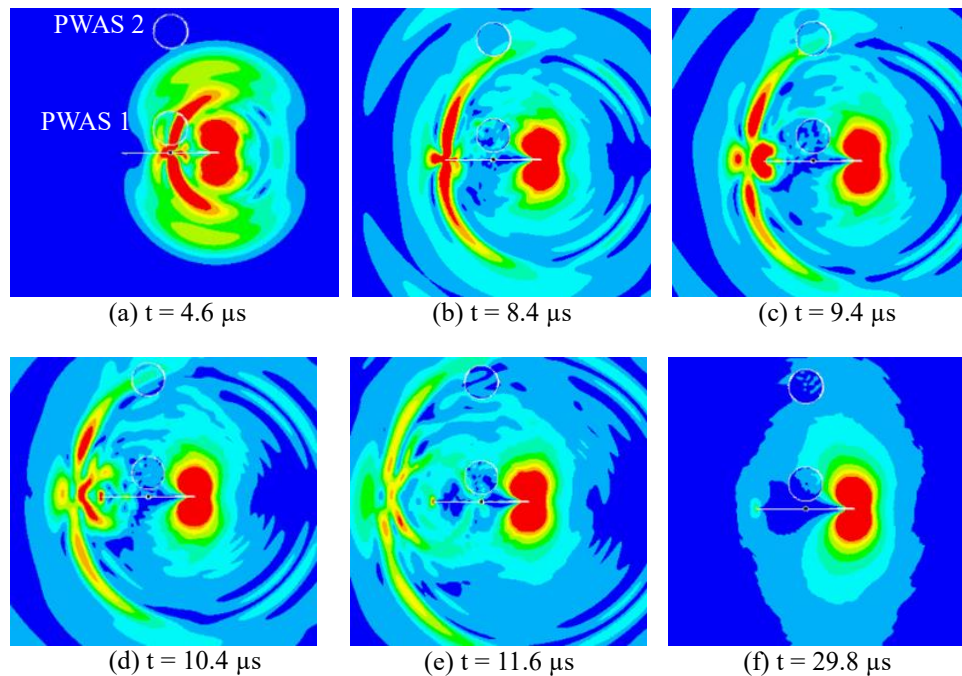


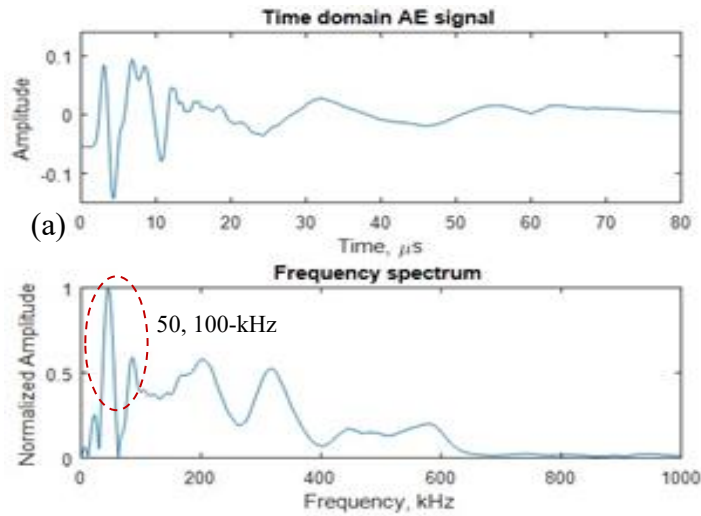
Figure 6.3 The animation snapshots of the acoustic wave propagation at different time of simulation.

6.4.2 SIMULATED AE SIGNALS CAPTURED BY TWO PWAS TRANSDUCERS

From the simulation, it was observed that both PWAS transducers captured the AE signals. The time domain signals of the two PWAS transducers are shown in Figure 6.4a,b. The fast Fourier transform (FFT) was performed to show the frequency spectra of the two

signals. Figure 6.4 shows that the highest peak of the PWAS 1 signal is at 50 kHz. The next consecutive peaks are located at 100, 200, 320 kHz.

Simulated AE signal (PWAS 1)



Simulated AE signal (PWAS 2)

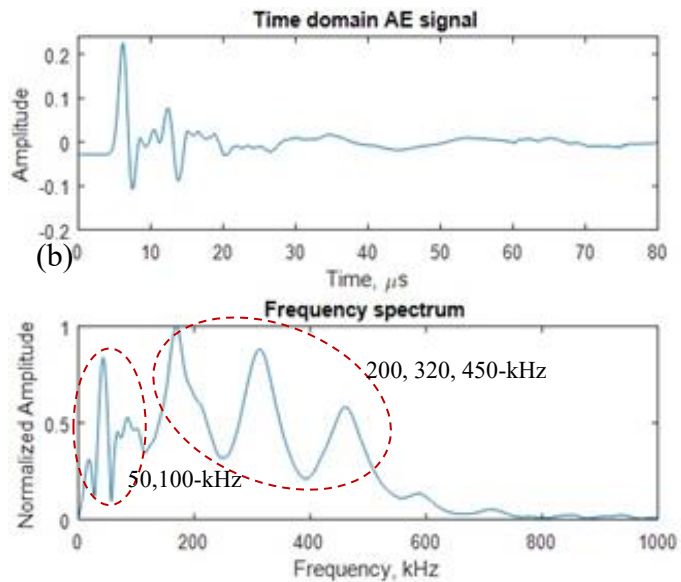


Figure 6.4 Multiphysics simulated AE signals from the two PWAS transducers: (a) near-field PWAS 1 (b) far-field PWAS 2

The highest peak of the PWAS 2 signal is at 200 kHz frequency. The next consecutive peaks are located at 50, 100, 320, 450 kHz. The higher frequency peaks such as 100, 200, 320, 450 kHz seemed to increase in amplitude as compared to the 50-kHz frequency peak. This may be because these high-frequency signals may become fully-developed as they travel away from the source.

6.5 VALIDATION OF MULTIPHYSICS SIMULATION RESULTS WITH EXPERIMENTAL MEASUREMENTS

6.5.1 DESCRIPTION OF EXPERIMENTAL SETUP

To validate the multiphysics simulation results, an in-situ AE-fatigue experiment was designed with two PWAS transducers [116]. The AE signals emanated from the fatigue crack was measured with simultaneous measurement of the fatigue loading. Aircraft grade aluminum Al-2024 T3 material was used in the specimen. The dimension of the specimen was 305 mm length, 100 mm width, and 1 mm thickness. Wave-absorbing modeling clay boundary was used in the experiment as non-reflective boundary. The schematic diagram of the experimental setup is shown Figure 6.5a.

For fatigue crack initiation, a small 1-mm hole was drilled at the center of the specimen and cyclic fatigue loading was applied by the MTS machine. The axial tensile cyclic fatigue loading was varied sinusoidally between 2.3 kN and 23 kN. These load levels gave a stress level of 6.5% and 65% of the yield limit (345 MPa) of the material as commonly used for practical aircraft testing for structural integrity [115]. A 20-mm fatigue crack was grown to mimic the simulation condition. During the initial crack experiment, no AE instrumentation was employed as shown in Figure 6.6a.

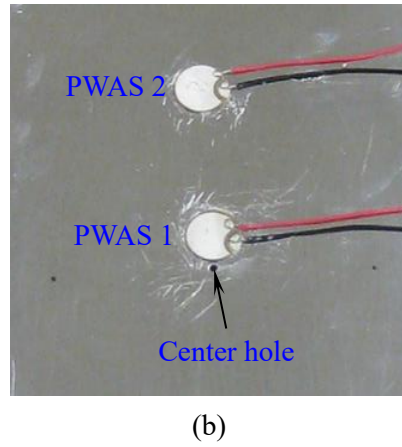
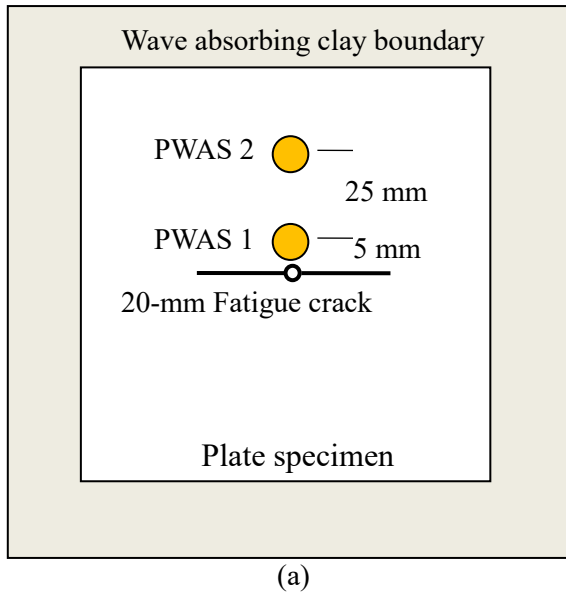


Figure 6.5 (a) Schematic diagram of the specimen with fatigue crack and a PWAS transducer bonded at 5-mm and 25-mm from the crack (b) Actual specimen with two PWAS transducers bonded at 5-mm and 25-mm from the crack.

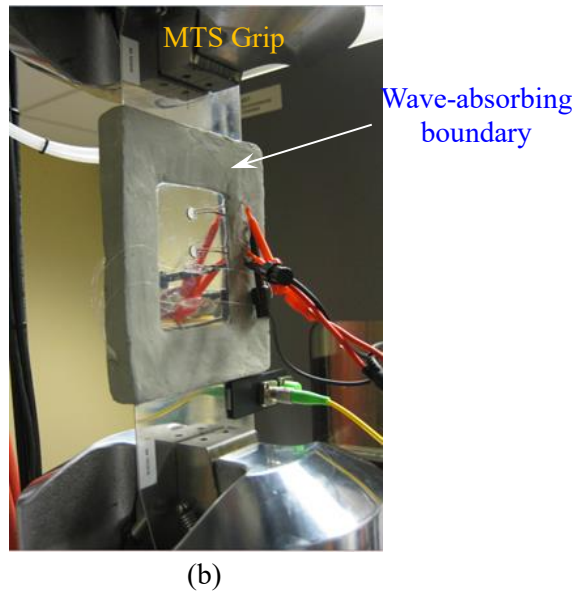


Figure 6.6 (a) Actual test coupon in the MTS grip without any AE instrumentation for the initial 20-mm crack (b) Instrumented Test coupon in the MTS grip for capturing fatigue-crack related AE signals. Two PWAS transducers were used to capture the AE signals.

The specimen with 20-mm fatigue crack was then equipped with two PWAS transducers, wave absorbing clay boundary, and AE instrumentation system. The diameter of each PWAS transducer was 7 mm. Two PWAS transducers were bonded at 5-mm and 25-mm from the crack (Figure 6.5b) thus mimicking the simulation configuration. The instrumented specimen was then continued under fatigue loading as shown in Figure 6.6b. A band-pass filter (30 kHz – 700 kHz) was used to avoid any interference from the low-frequency noises such as hydraulic loading, MTS grips, and mechanical vibrations. A 40dB preamplifier was used in conjunction with the band-pass filter as recommended by the manufacturer of the AE system. Under the axial cyclic loading, the fatigue crack grew from 20-mm to 25-mm. For the triggering of the AE signal measurement, a threshold was chosen at 2 dB above the environmental noise level.

6.5.2 FATIGUE CRACK GENERATED AE SIGNALS CAPTURED BY THE TWO PWAS TRANSDUCERS

The AE signals from the fatigue crack were captured by the two PWAS transducers. Typical AE signals coming from the same AE event captured by the two sensors are shown in Figure 6.7. The time domain waveform and their frequency spectra of the AE signals of a particular AE event are illustrated in Figure 6.7. The same AE event was captured by the two PWAS sensors. The amplitude of the near-field PWAS 1 signal was higher than that of the captured the far-field PWAS 2 signal, as expected. This is because of the geometric spreading of the acoustic wave. The frequency spectra of the two signals (Figure 6.7) show some considerable differences. The highest peak of PWAS 1 signal is located at 50 kHz. There are also other peaks at 100 kHz and 170 kHz. On the PWAS 2 frequency spectrum,

the highest peak is located at 100 kHz. There are also some other peaks at 50, 170, 220, 320 kHz frequencies.

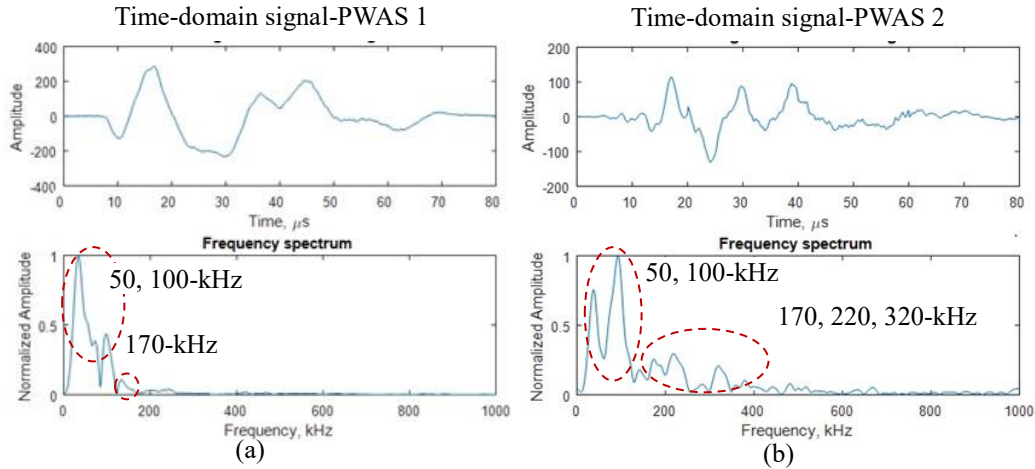


Figure 6.7 Experimentally measured AE signals by the two PWAS transducers: (a) near-field PWAS (b) far-field PWAS.

6.5.3 COMPARISON BETWEEN THE MULTIPHYSICS SIMULATION VS EXPERIMENTAL

RESULTS

The multiphysics simulation and the experimental study suggested that the PWAS transducer were capable of sensing the AE signals. The experimental results show the agreement with the simulation results in the following aspects.

6.5.3.1 The Lower Amplitude Signals as the AE Waves Travel Away from the Crack

The multiphysics simulation showed that the amplitude of the AE signal captured by far-field PWAS 2 was lower than that of the AE signal captured by near-field PWAS 1. The same observation was found true for the experimentally measured AE signals. This is intuitive and expected for any guided wave generated from a point source in 2D geometry. Thus, we may conclude that the AE signals travel as guided waves in the structure. Besides, we may construe that the experimentally measured AE signals were generated from the tip of the fatigue crack.

6.5.3.2 *The Evolution of the Higher Frequency Contents of the AE Signal*

The multiphysics simulation and the experiment both showed the first two peaks of the AE signals as 50 kHz and 100 kHz. Both near-field and far-field PWAS transducers captured these two peaks. In the frequency spectra of the near-field PWAS 1 signals, simulation and experiment both showed the highest peak as 50 kHz.

Multiphysics simulation showed that some higher-frequency contents of the AE signal were developing as the acoustic waves were traveling away from the source. For example, in Figure 6.3, the 100, 200, 320 kHz frequencies gained amplitude as the AE signal traveled to far-field PWAS 2. The experimentally measured AE signals also showed similar trends on the higher frequencies. For example, in Figure 6.7, 100, 170, 220, 320 kHz frequencies gained amplitude as the AE signal traveled to far-field PWAS 2. This was not so intuitive. Thus, to capture all the frequencies of the AE signal, the sensor should be installed in such a way that the AE signals have enough room to become fully developed signals.

6.5.3.3 *Discussion of the Differences in Simulation and Experimental Results*

Besides similarities between the simulation and experimental AE signal, we also observed some differences. The simulated near-field PWAS signal showed some frequency peaks at 200, 320 kHz. These frequency peaks were not so dominant in the experimental near-field PWAS 1 signal. Also, on the far-field AE signal, the 450 kHz peak was observed in the simulation but not in the experimental signal. There could be several reasons for these differences such as the geometry of the actual fatigue crack was not perfectly straight, the crack may not happen entirely throughout the thickness, one component of moment tensor may not be enough to assume in the simulation.

Despite the differences discussed above, the multiphysics simulation results were in very good agreement with the experimental results. The main objective, which was to assess the capability of PWAS transducer to capture the low-amplitude fatigue crack-related AE-signals, was well-supported by both multiphysics simulation and the experimental measurement.

6.6 EFFECT OF RISE TIME ON THE SIMULATED AE SIGNALS

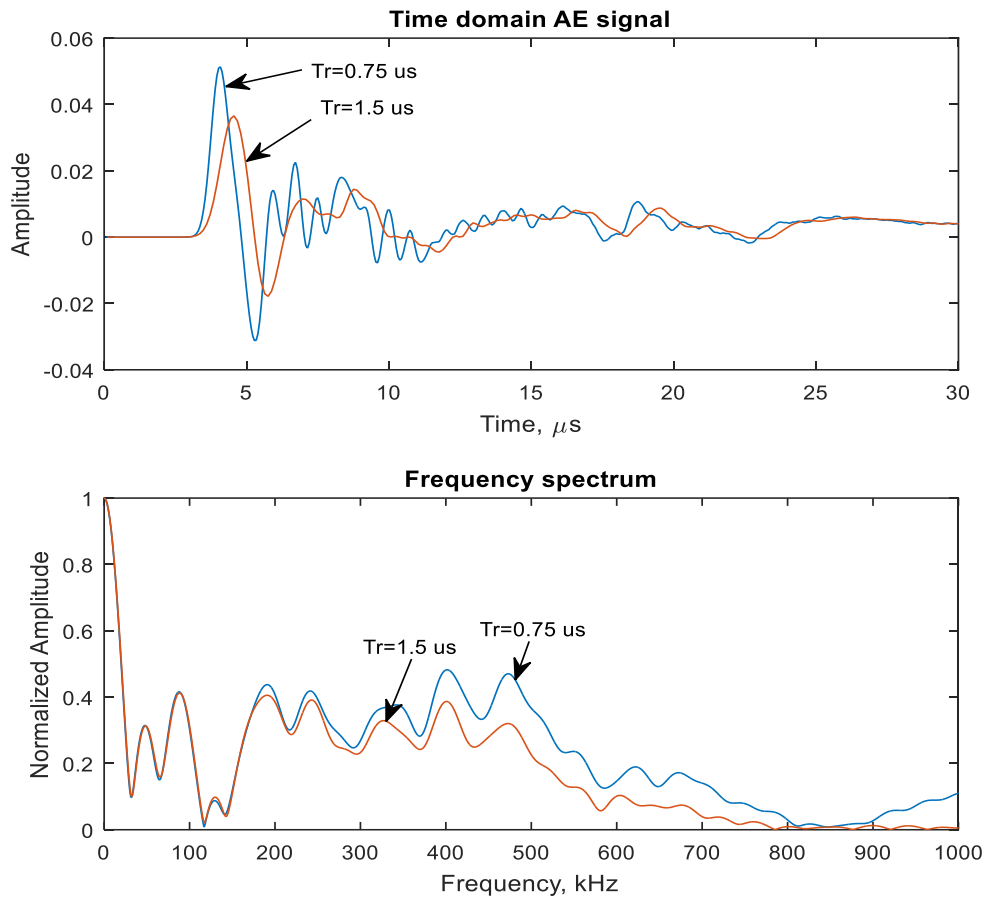
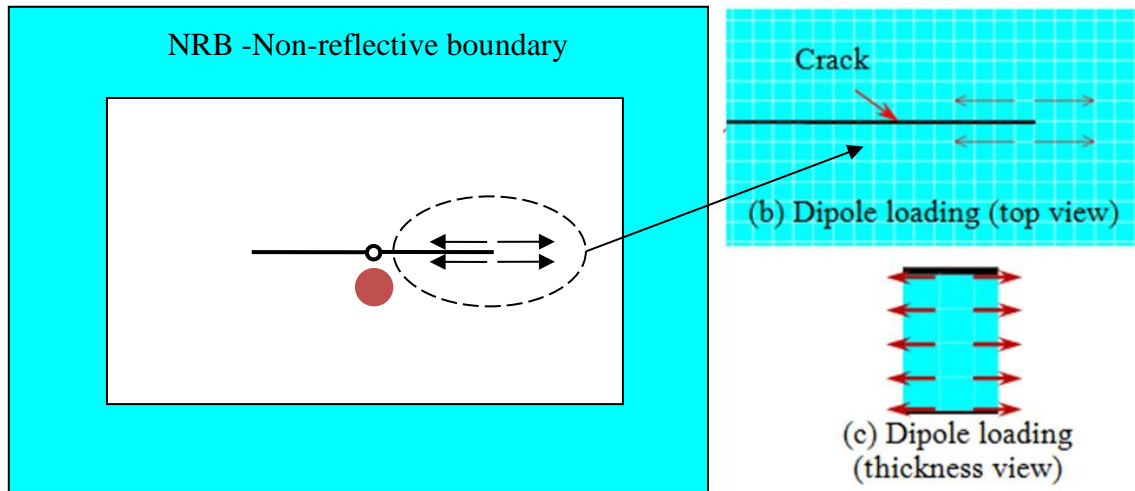


Figure 6.8 Effect of rise time on the simulated AE signals.

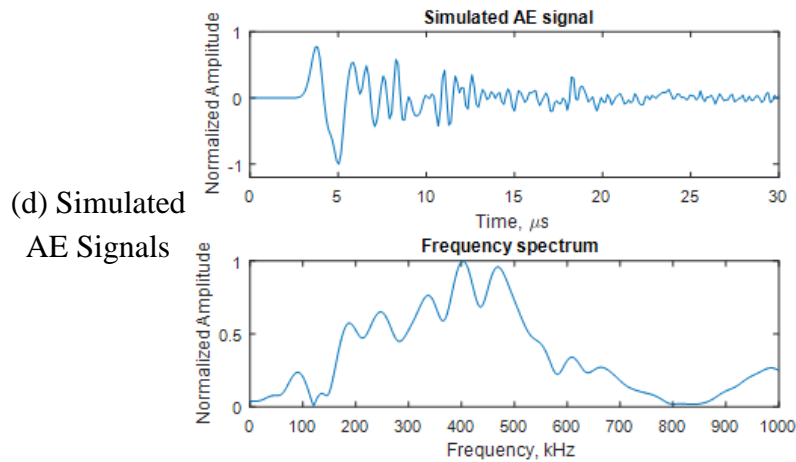
The rise time influences the simulated AE signals. In general, as the rise time decreases the higher frequency contents of the signals increases. It should be noted that shorter rise time needs higher computational time. This study was performed to understand

the behavior of different types of AE signals as we observed during the experiments. This gave us an idea that among many parameters of the simulations, the rise time plays a vital role in simulating various AE signals. The AE signals corresponding to two rise times ($0.75 \mu\text{s}$ and $1.5 \mu\text{s}$) are plotted in Figure 6.8.

6.7 EFFECT OF DIPOLE ORIENTATION IN THE SIMULATED AE SIGNALS



(a) Overview of the FEM model with dipole parallel to the crack



(d) Simulated AE Signals

Figure 6.9 The meshed FEM model with in-plane dipole excitation: (a) overall view; (b) top view zoomed into crack tip area showing dipole loading; (c) side view showing the thickness-wise assignment of dipole components, (d) simulated AE signals

Another major contributing factor to different AE signals is the dipole orientation. Simulated AE signal corresponding to a dipole parallel to the crack is shown in Figure 6.9, which shows that the simulated signals contain higher frequencies than that for the perpendicular dipole discussed earlier. These factors (rise time and dipole orientation) may be considered for simulating various types of AE signals as we may encounter in practice.

6.8 CONCLUSION

Piezoelectric wafer active sensors (PWAS) successfully captured the fatigue crack-related acoustic emission (AE) signals. Both multiphysics simulations and experiments supported this result. The fatigue crack generates low-amplitude AE signals as it grows. The AE signals appear in every cycle of the fatigue loading. This indicates that the AE events happen at every cycle as the fatigue crack grows. The AE hits provide the global information of the physical problem whereas the AE signal analysis provides the detail information of the physical system. The effect of the crack-tip AE event travels as guided acoustic waves throughout the plate. The AE signals show the geometric spreading of the energy and associated reduction of amplitudes as expected in 2D traveling guided waves. The distance of the PWAS transducer has an effect on the sensed AE signals. Near-field PWAS captures higher amplitude AE signals than the far-field PWAS. Higher-frequency content of the AE signals seems to evolve as the AE waves travel away from the crack. The effect of rise time and dipole orientation has been also investigated. We found that these two factors significantly affect the simulated AE signals. Thus, these factors may be used to simulate various types of AE signals depending on applications.

CHAPTER 7

PHYSICS OF MATERIALS BASED ANALYSIS OF AE SIGNALS FROM IN-SITU AE-FATIGUE EXPERIMENTS

This chapter mainly focused on physics of materials based experimental analysis of acoustic emission (AE) waveforms emanating from fatigue cracks. This was accomplished by simultaneous measurement of all possible physical events such as fatigue load, strain, AE, and crack growth. These measurements were synchronized in time to interpret the physics of the AE signals. The design of test plans and procedures are discussed. Proper AE instrumentation was used to capture the AE signals from the growing crack. An in-situ microscope-camera and a high-resolution video camera with extension tubes were installed on the MTS column to optically monitor the fatigue crack growth. The crack growth was observed from centimeter range all the way to micrometer range. Multiple sensor types were used for capturing AE signals; the sensor performances were compared. Many such in-situ experiments were designed and conducted to discover different aspects of the AE signals. In this chapter, three major findings from these in-situ AE-fatigue experiments are discussed:

- (1) Sensor effect on the AE waveforms
- (2) Various AE waveform groups with fatigue load evolution
- (3) Distinguishing crack growth related AE signals from crack rubbing/fretting related AE signals

7.1 INTRODUCTION AND STATE OF THE ART

The study of metal fatigue has always been an interest to the engineering community [117]–[121]. Acoustic emission (AE) technique had been used to monitor progressive defects such as fatigue crack of engineering structures [122]–[124]. Researchers in nondestructive evaluation (NDE) and structural health monitoring (SHM) used AE as a passive method for the detection of structural damage [81], [84], [125]. This method had been tested on metallic, concrete, and composite structures [82], [126], [127]. AE monitoring had also been used for micro-damage evolution in human bones [128]. However, most of them focused on AE-hit analysis to assess the structural damage. One of the major concerns in analyzing the acoustic emissions was that a simple fatigue experiment could generate a huge amount of AE data that inhibited a detailed analysis of the AE waveforms [129].

A statistical Bayesian approach was developed to analyze the huge amount of AE data by Agletdinov et. al. [130]. The AE hit amplitude and cumulative signal strength have been used for capturing damage evolution under static loading in concrete specimens [131]. Nam and Mal [132] emphasized the importance of analyzing the AE waveforms and suggested that the AE waveforms could provide much more information than just hit-based statistical analysis. They identified three types of elastic waves during a fatigue experiment on aluminum alloy specimen. However, no relation between the fatigue loading and the acoustic waves was investigated.

Small fatigue crack growth had been investigated by various methods [133]–[136]. The dynamics of multi-scale deformation mechanism in the materials had been explained by using digital image correlation methods [137]. A dislocation-based crack growth model

was used to investigate crack initiation and growth in aluminum alloys [135]. Theoretically, it had been shown that the crack formation in aluminum alloys emitted acoustic waves [92].

Experiments and simulation were also performed to detect the fatigue crack using acoustic emissions [77]–[79], [85], [90], [138]. The AE signals can be detected by using surface mounted piezoelectric transducers. Both experiment and multiphysics simulation proved that the piezoelectric wafer active sensors (PWAS) successfully captured the AE signals [108], [116]. Acoustic guided wave approaches were used to characterize and localize the defects in thick steel plates, aluminum alloys, and welded joints [139]–[142]. Fatigue crack length estimation by using the AE signals had been attempted [115], [143].

The issue of mechanical joint (bolt connections) related fretting AE noise was considered in the past [144], [145]. These fretting noises were separated from the valid AE signals by comparing the AE events of pre and post lubrication in the mechanical joints. They showed that the load position of the AE event may help interpreting the sources of the AE signals. They used autocorrelation lag and statistical measure (histogram of mean, standard deviation, skewness, and kurtosis) based pattern recognition to address the critical AE signals. They successfully separated the fatigue crack AE signals into three clusters. There are other pattern recognition methods developed for various applications [146]. The AE pattern recognition method had been attempted to use for the crack monitoring in pressure vessels [147], [148] and aircraft structures [149].

Most of the prior work so far primarily focused on the hit-driven statistical methods. In contrast, a few authors, including the current one, prefer the physics-based approach and hence directed their attention to understanding the origin and causation of the wave signals recorded by the AE sensors and developing the computational models to assist this understanding process.

7.2 SCOPE OF THE CURRENT RESEARCH

There are two main phenomena that may be related to AE generation during fatigue crack growth under cyclic fatigue loading: (1) crack initiation and incremental propagation and (2) fretting, rubbing and clapping of the crack faying surfaces. The first one is referred to as “crack growth” events and the second one is referred to as “non-crack growth” events. Both types of events may produce AE waves. The main issue is how can one distinguish the AE signals from the crack events from the non-crack events. The ability to gain understanding of the unique markers in the AE signals to allow us to positively identify crack events and separate them from non-crack events that also produce elastic wave signals that are picked up by the AE sensors.

With our physics-of-materials based approach, we found that a fatigue crack advancing in a thin metallic plate generates AE signals that possess diverse and complex spectral signatures. These spectral signatures are highly related to the physical changes undergoing in the material. The main issue of distinguishing between crack events and non-crack events has been resolved. With the scientific process adopted in this research, several aspects such as sensor effect, several waveform groups identification, and AE source localization were investigated as discussed next.

7.3 SENSOR EFFECT ON THE AE WAVEFORMS

Six sensors were used to study the sensor effect: (1) two miniature AE sensors model - S9225 from PAC MISTRAS Inc., (2) two miniature AE sensors model - PICO from PAC MISTRAS Inc., and (3) two piezoelectric wafer active sensors (PWAS) [150]. First two sensor types are commercially available; they sense mostly out-of-plane wave

motion. The third type is an in-plane strain sensor which was customized in our lab for fatigue AE sensing.

7.3.1 IN-SITU AE-FATIGUE EXPERIMENTAL SETUP

In-situ AE-fatigue experiment was designed to measure the AE signals from the fatigue crack growth under application of cyclic axial fatigue loading. A commonly used material for fatigue-prone aircraft components, aluminum Al-2024 T3, was used to make the test coupons. A thin plate-like specimen geometry was designed and manufactured. The specimen dimensions were 305 mm length, 100 mm width, and 1 mm thickness. This specimen was relatively longer and wider than typical dog-bone shaped narrow specimens (25-mm width) that were tested initially. The main purpose of the bigger specimen was to grow longer fatigue crack before fracture and thus better resemble the actual situation in aerospace structures. The longer fatigue crack growth would generate more AE waves. Practically, it would represent a bigger structure where edge-boundary reflected waves diminish before they reach to the sensors. Furthermore, the bigger specimen would allow using a wave-absorbing clay boundary around the area of interest to minimize the edge reflection from the plate edges. The repeatability of the experimental results was confirmed by testing three identical specimens under the same loading condition. One of such experiments is discussed below.

The overall fatigue experiment was conducted in two main stages: first stage and second stage. In the first stage, a small 1-mm diameter hole was drilled at the center of the test specimen. A hydraulic MTS machine (manufacturer: MTS Systems Corporation) was used to apply the fatigue loading to the test specimen. The specimen was mounted on the MTS grip with appropriate grip pressure and axial tensile cyclic fatigue loading fatigue

loading was applied. The pictorial representation of the experimental setup for initial fatigue crack generation without any AE instrumentation is shown in Figure 7.1. The load level was sinusoidally varied between a maximum and minimum value maintaining an R-ratio ($\sigma_{\min} / \sigma_{\max}$) of 0.1. The minimum and maximum load levels (2.2 kN and 22 kN) were calculated based on the stress level of 6.5% and 65% of the yield strength of the material (345 MPa), respectively. These load levels were selected since they are commonly used load level in practical aircraft testing [151], [152]. The loading rate was 4 Hz. The fatigue crack was initiated from the hole after about 28,000 fatigue cycles. A 20-mm marking was used to track the fatigue crack growth. When the fatigue crack touched the 20-mm marking, the first stage of the experiment was stopped and prepared for the second stage of the experiment.

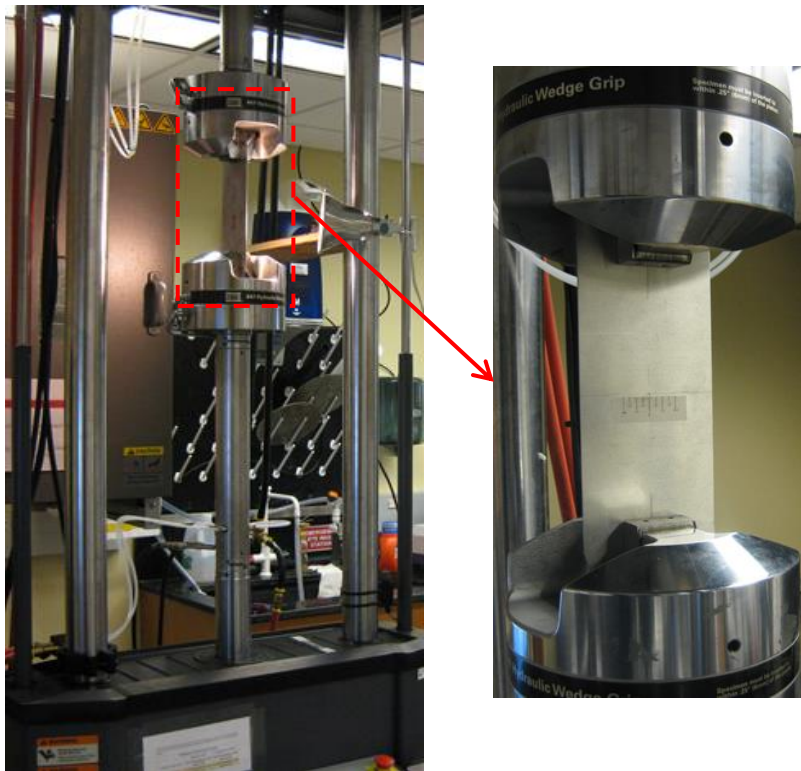


Figure 7.1 Test specimen on the MTS machine for initial 20-mm fatigue crack generation

In the second stage of the experiment, the specimen was equipped with AE instrumentation. The specimen was instrumented with AE sensors and the wave-absorbing clay boundary. Six AE sensors were bonded to the specimen. On one side of the specimen, there were two S9225 sensors and a strain gauge. On the other side of the specimen, there were two PWAS transducers and two PICO transducers. There were only four channels available in the AE system. Thus, we used only four sensors at a time to capture the AE signals. The fatigue loading was continued at a slower rate (0.05 Hz) and the loading level was reduced to 1.23 kN - 12.3 kN. These settings allowed fatigue crack growth in a controlled manner.

The fatigue crack was grown from 20-mm to 30-mm. The strain gauge was used to monitor the strain which was then converted into the load. This allowed monitoring directly the load applied to the specimen. Even though there was a load monitoring from the MTS computer connected to the load cell of the MTS frame, we considered that the load information taken directly from the specimen would give better results for synchronizing AE with fatigue loading. There were two purposes for bonding the strain gauge to the specimen: (1) bonding at 40-mm from the crack would give far-field loading information directly from the specimen and (2) acquiring loading data by AE system by routing the strain output to AE machine.

Three parallel measuring systems were used simultaneously during the AE-fatigue experiment: (a) fatigue loading by the MTS machine, (b) AE and load measurement by the Mistras AE system, and (c) optical fatigue crack growth measurement by a microscope camera and a high-resolution video recorder with extension tubes.

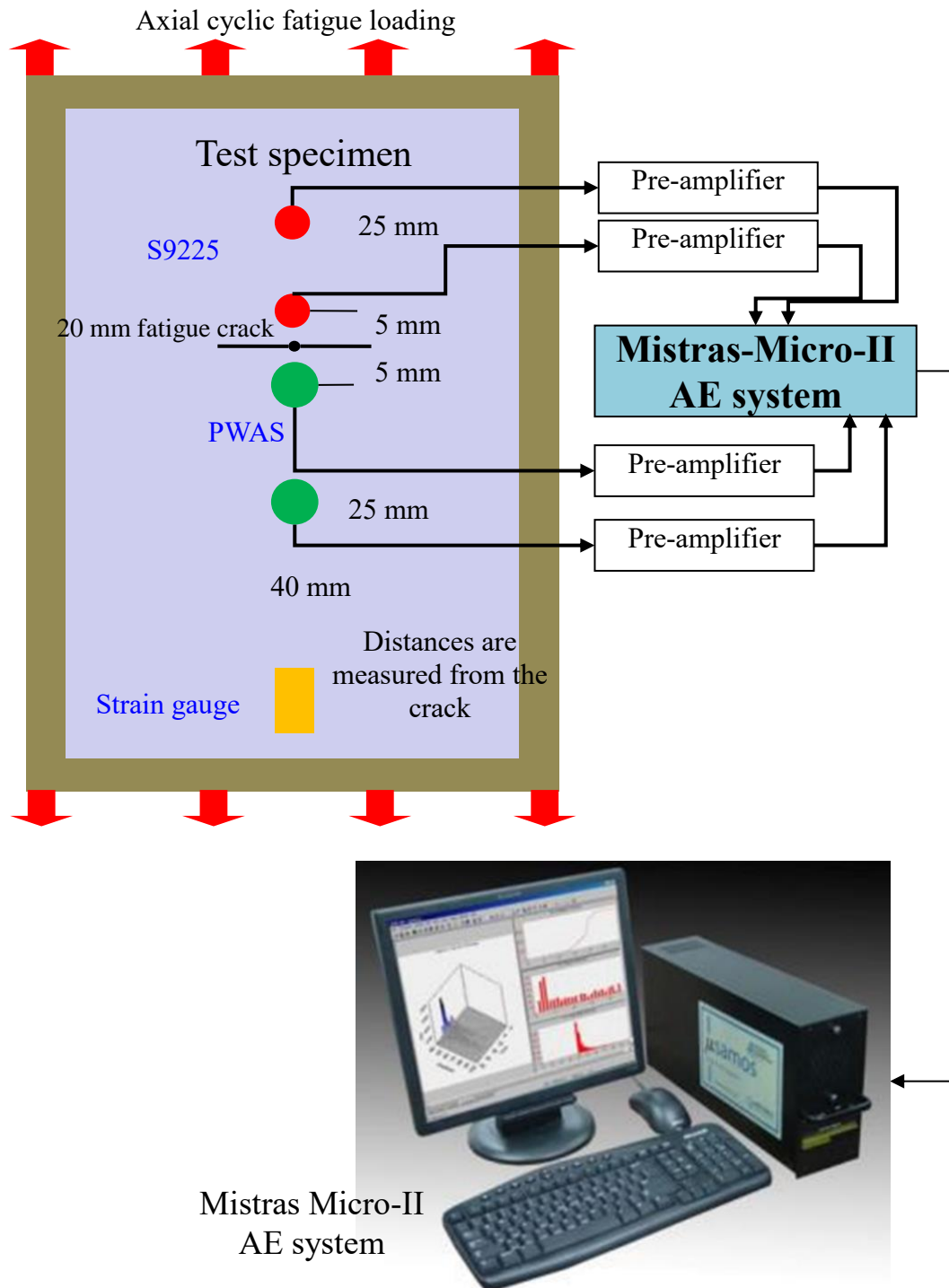


Figure 7.2 Schematic diagram of the experimental setup with two PWAS and two S9225 AE sensors.

Precise synchronization of fatigue load with AE measurement was possible because the AE recording and the load recording was performed by the same AE instrumentation system. A preamplifier with a built-in band-pass filter (30 to 700 kHz) was used with each sensor. A 40-dB gain was selected for the preamplifiers. Thresholds of the sensors were selected just above at 2 dB, the environmental noise level. Higher sampling rate (10 MHz) was chosen to capture the high-frequency AE signals.

7.3.2 AE SPECIMEN INSTRUMENTED WITH PWAS AND S9225 AE SENSORS

First, the experimental schematic and results from PWAS and S9225 are discussed; then, we will discuss that from PWAS and PICO. The schematic diagram of the instrumented specimen with two PWAS and two S9225 is shown in Figure 7.3a. The diameter of the PWAS transducer was 7-mm and the diameter of the S9225 sensor was 3.5-mm. PWAS and S9225 sensors were bonded symmetrically about the crack. The near-field PWAS and S9225 were bonded at 5-mm from the crack and the far-field PWAS and S9225 were bonded at 25-mm from the crack.

The near-field sensors would pick up low-amplitude AE signals which would otherwise diminish as they travel away from the crack due to geometric spreading and material damping. Furthermore, it would capture waveforms from any local interaction of the AE waves and the crack. The instrumented specimen mounted in the MTS grips is shown in Figure 7.3. The close-up views the two sensors are shown in Figure 7.3b,c. The fatigue loading was continued and the corresponding AE signals were captured by all the sensors.

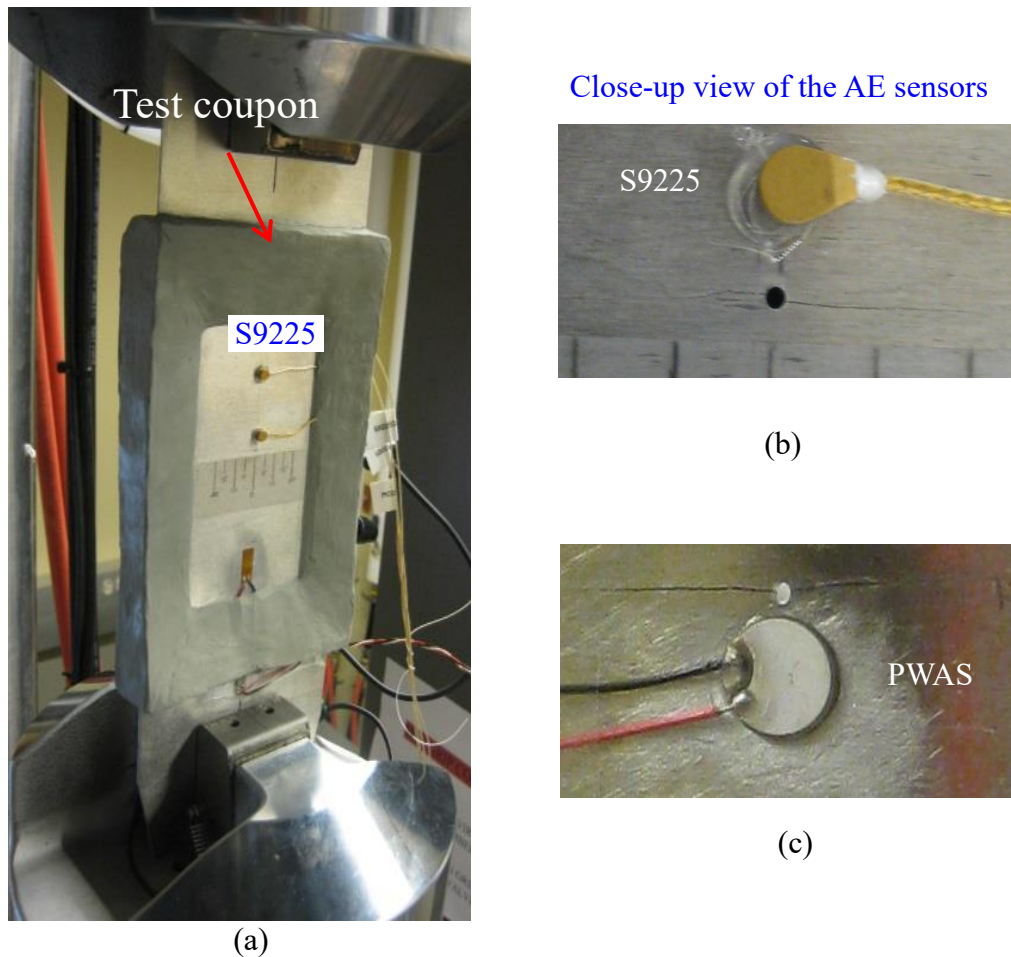


Figure 7.3 (a) Experimented test coupon on MTS load frame subjected to fatigue loading, (b) S9225 AE sensors were bonded to one side of the plate and (c) PWAS transducers were bonded to the other side of the plate.

7.3.3 AE-HIT BASED ANALYSIS: SIMILARITY BETWEEN PWAS AND S9225 AE-HITS

The AE signals from the fatigue crack growth were captured by both near-field and far-field PWAS and S9225 AE sensors. For comparative study, the near-field sensor results are extensively discussed below. One can obtain a similar result from the far-field sensor results except for the amplitude being diminished by geometric spreading. The AE-hit plots of Figure 7.4 show similar patterns for both near-field PWAS and S9225 (60 fatigue cycle results are shown here). The AE-hit amplitude corresponds to the maximum amplitude of an AE waveform converted into a decibel (dB) scale.

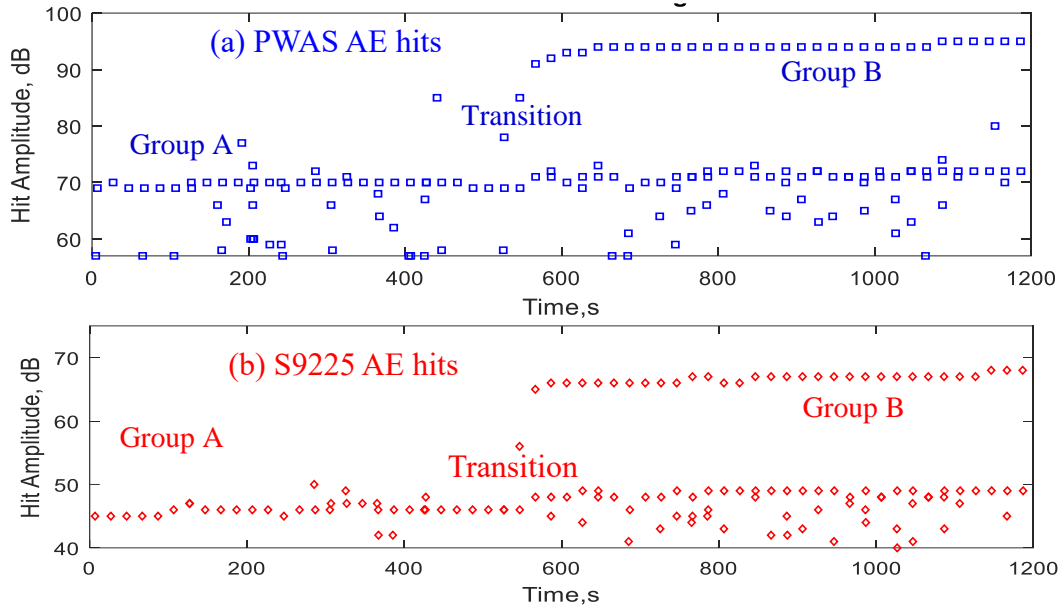


Figure 7.4 AE hits captured by (a) PWAS transducer and (b) S9225 AE sensors, both of them showing the similar trend.

It can be observed from the PWAS AE hit plot that there is a baseline of AE-hits at an almost constant 70 dB amplitude level. Similarly, a baseline of AE-hits can be observed in the S9225 AE-hit plot at about 45 dB amplitude level. These baseline AE hits were named “group A”. The inception of some new AE hits happened after 550 s and it was observed in both plots. The new AE hits were gaining amplitude in the “transition” period and then became almost constant after 600 s. The new AE hits with the highest amplitude after the transition were named as “group B”.

Although the pattern of the two AE-hit plots is similar as shown in Figure 7.4, the AE-hit amplitudes were different. The PWAS captured group B AE-hits have about 96 dB hit-amplitudes and the S9225 captured group B AE-hits have about 68 dB hit-amplitudes. Similar AE-hit amplitude difference can be observed for group A as well. This may be because the size of the PWAS transducer (7-mm diameter) is larger than the size (3.5-mm

diameter) of the S9225 AE sensor. Also, they have different piezoelectric transduction factors and sensing mechanisms.

7.3.4 AE-WAVEFORM BASED ANALYSIS: DIFFERENCES BETWEEN PWAS AND S9225 AE-WAVEFORMS

Based on the AE-hit analysis discussed in Section 7.3.3, we concluded that both AE sensors are in sync in capturing the AE-hits. No apparent difference was observed between the two sensors from the AE-hit based analyses. We further performed a deeper-level analysis, i.e., AE waveform analysis.

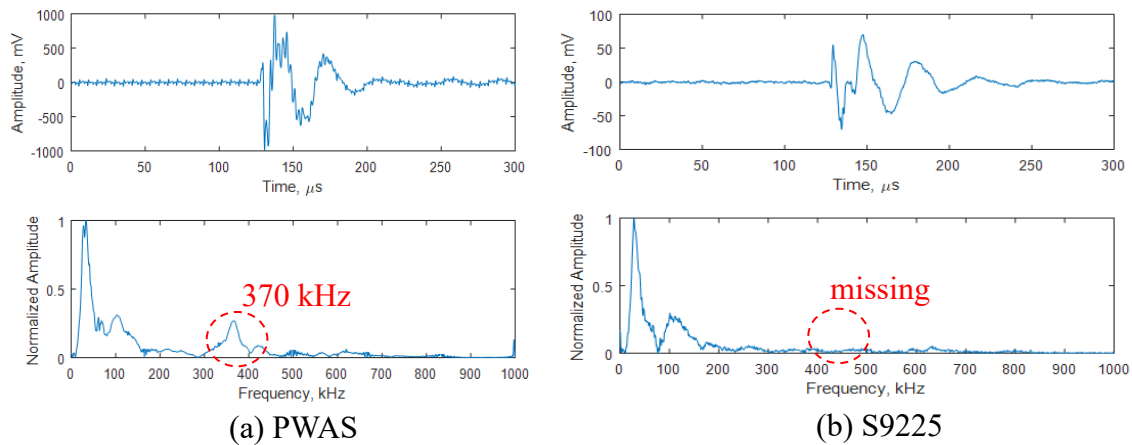


Figure 7.5 “Group A” AE waveform and its frequency spectrum captured by (a) PWAS transducer and (b) S9225 AE sensor at the same time.

Figure 7.5 shows a typical time domain waveform and the frequency spectrum of group A AE signals captured at the same time by PWAS and S9225. The frequency spectra show low-frequency peaks at 40 and 100 kHz successfully captured by both PWAS and S9225 AE sensors. However, PWAS transducer captured an additional 370 kHz frequency peak that is missing in the S9225 frequency spectrum.

Figure 7.6 shows the time domain waveform and the frequency spectrum of the AE signal during the “transition” period captured at the same time by PWAS and S9225. The amplitude of this particular transition AE signal was about five times higher than that of the group A waveform. There was also a difference between the frequency spectrum of group A and of transition AE signals such as the 220 kHz and 450 kHz frequency peaks of the transition AE signals were not observed in group A signals. The low-frequency peaks up to 100 kHz were captured by both PWAS and S9225. However, PWAS transducer captured 220 kHz and 450 kHz frequency peaks that were missing in the frequency spectrum of S9225.

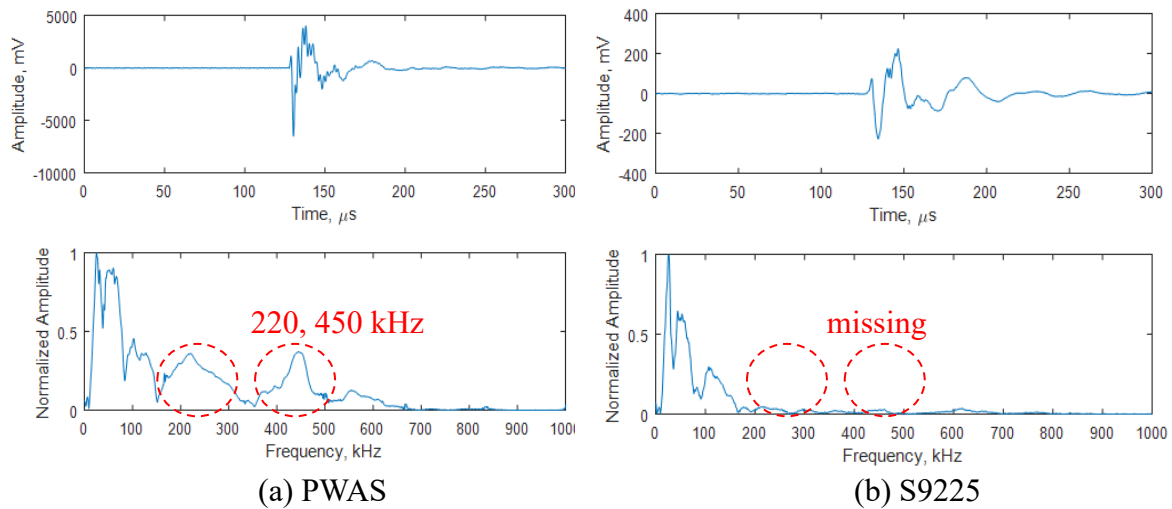


Figure 7.6 “Transition” AE waveform and its frequency spectrum captured up by (a) PWAS transducer and (b) S9225 AE sensor at the same time.

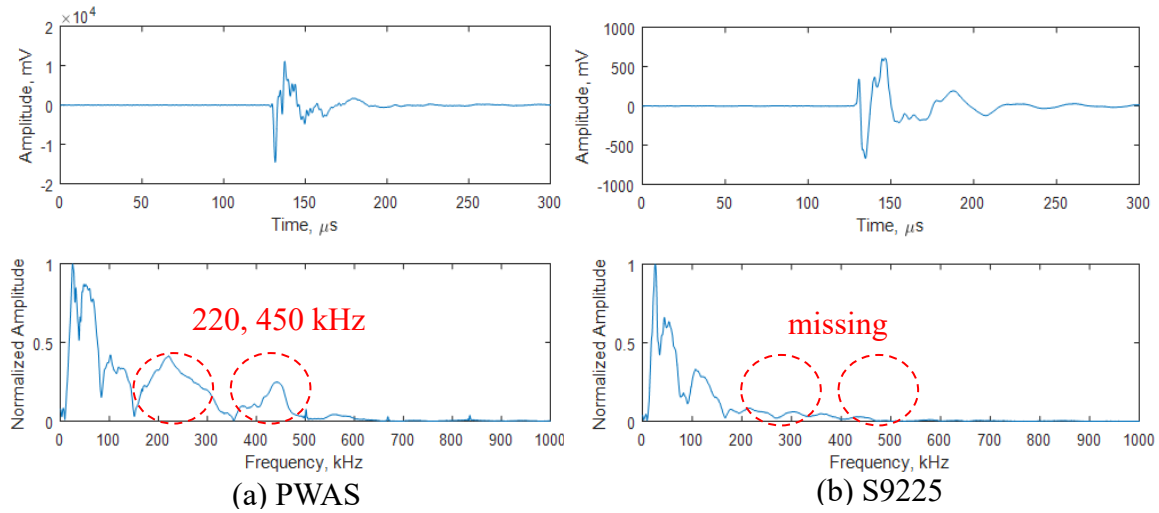


Figure 7.7 “Group B” AE waveform and its frequency spectrum captured by (a) PWAS transducer and (b) S9225 AE sensor at the same time.

Figure 7.7 shows the time domain and frequency spectra of group B AE waveforms captured at the same time by PWAS and S9225. Note that after the transition period (Figure 7.4), there are group A and group B AE hits. The hit-amplitudes of the group B AE waveforms appeared to be constant at a higher level. The frequency spectrum of group B is similar to the transition waveform but different from the group A waveforms. Figure 7.7 shows that the low-frequency peaks up to 100 kHz were successfully captured by both PWAS and S9225. However, PWAS transducer captured 220 kHz and 450 kHz frequency peaks that were missing in the frequency spectrum of S9225 as marked by the dotted ellipses.

7.3.5 EXPLANATION OF WHY S9225 WAS SHOWING WEAK RESPONSES AT SOME HIGHER FREQUENCIES

To find the reason for S9225 AE sensor missing two frequency peaks in the frequency spectrum, we obtained the frequency response curve of S9225 from the manufacturer. Figure 7.8b shows the frequency response of the S9225 sensor for a wide

range of frequencies. It can be observed from Figure 7.8b that there is a weak response in the frequency range of 170-300 kHz. S9225 also showed a weak response in that frequency range as shown in Figure 7.8a. This explains why S9225 was missing 220-kHz frequency peak.

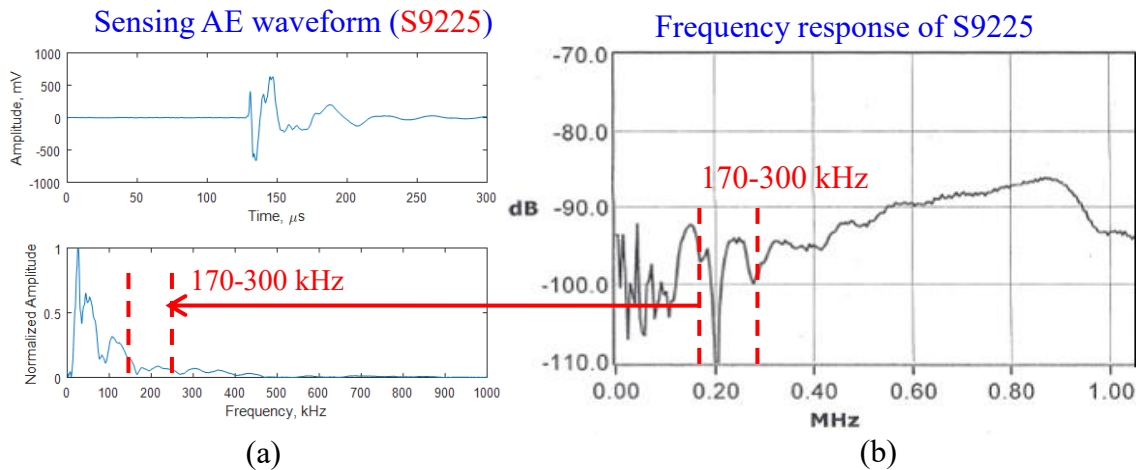


Figure 7.8 (a) Sensing AE signal by the S9225, (b) the frequency response plot of S9225 (from the manufacturer); (b) shows is a weak response in the frequency range of 170-300 kHz and the S9225 also sense a weak signal in this range

S9225 was also missing 370-kHz and 450-kHz frequency peaks as compared to the PWAS transducer. This may indicate that the high-frequency AE signals from the fatigue-crack are related to the in-plane wave motion. Since PWAS transducer measures in-plane and out-of-plane motion through surface strain sensing, it captured the high-frequency in-plane wave motion [153].

7.3.6 AE INSTRUMENTED SPECIMEN WITH PWAS AND PICO AE SENSORS

The experimental schematic and the AE measurement with near-field PWAS and PICO are discussed here. One can obtain a similar result from the far-field sensor results except for the amplitude being diminished by geometric spreading. The schematic of the test specimen with near-field PWAS and PICO sensor is shown in Figure 7.9a. The relative

position of the PWAS and PICO on the actual specimen is shown in Figure 7.9b. Both sensors were bonded at 5-mm from the fatigue crack. The diameter of the PWAS was 7-mm and the diameter of the PICO was 4.75-mm. The thickness of the PWAS was 0.5-mm. The in-situ AE-fatigue experiment on the same specimen with the similar settings was performed as discussed earlier. The results discussed here are obtained from 50-fatigue cycles after the previous 60-fatigue cycles.

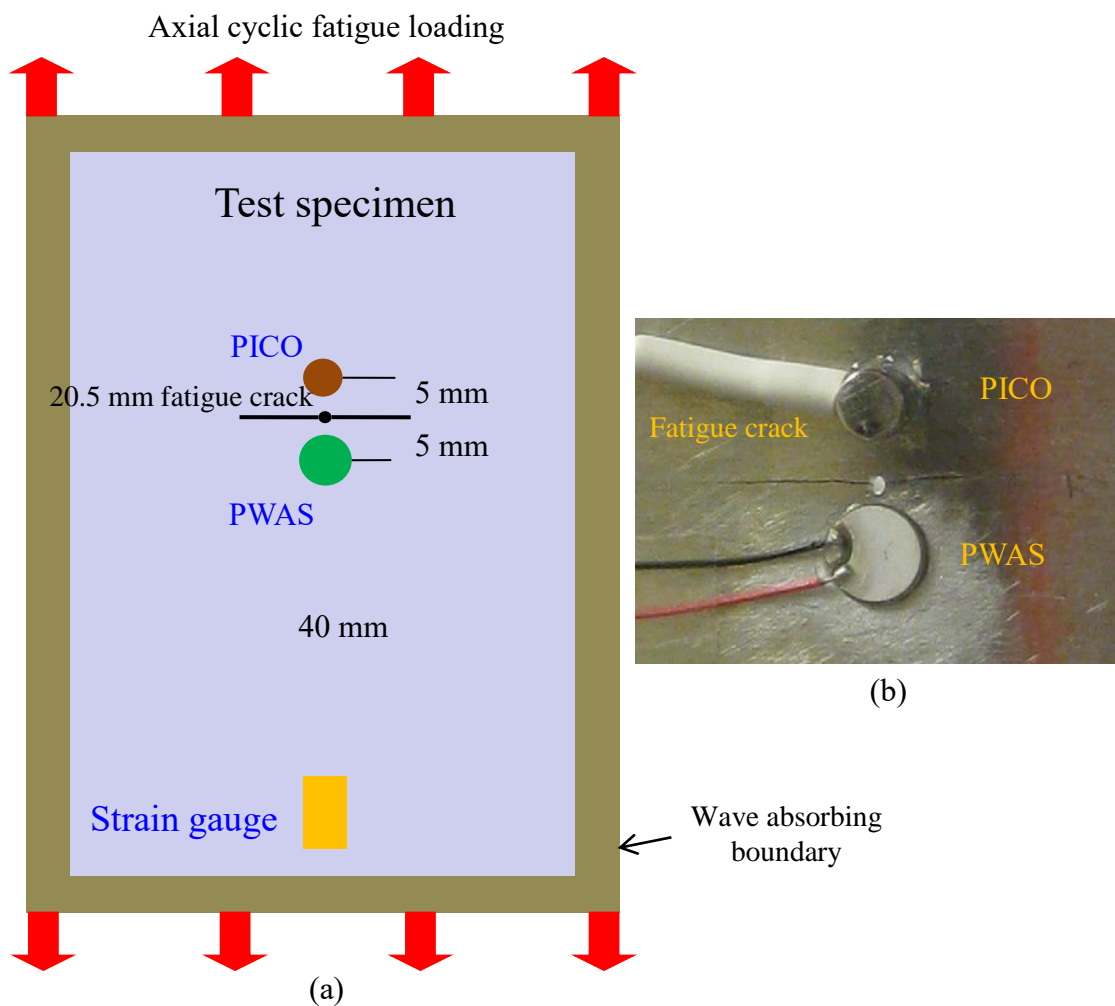


Figure 7.9 (a) Schematic diagram of the experimental setup with PWAS and PICO AE sensors. (b) A zoomed-in view of the PWAS and PICO with respect to the fatigue crack. For scale, please note, the hole has 1-mm diameter.

7.3.7 SIMILARITY BETWEEN PWAS VS PICO FROM AE-HIT BASED ANALYSIS

The AE hits were captured by the PWAS and PICO AE sensors as the fatigue crack grew. The AE hits captured by the PWAS and PICO for 50 fatigue cycles are shown in Figure 7.10. In these particular 50-fatigue cycles, crack growth was optically measured as 300- μm . The average crack growth can be calculated as 6- $\mu\text{m}/\text{cycle}$. In these plots, PWAS has 427 hits and S9225 has 305 hits.

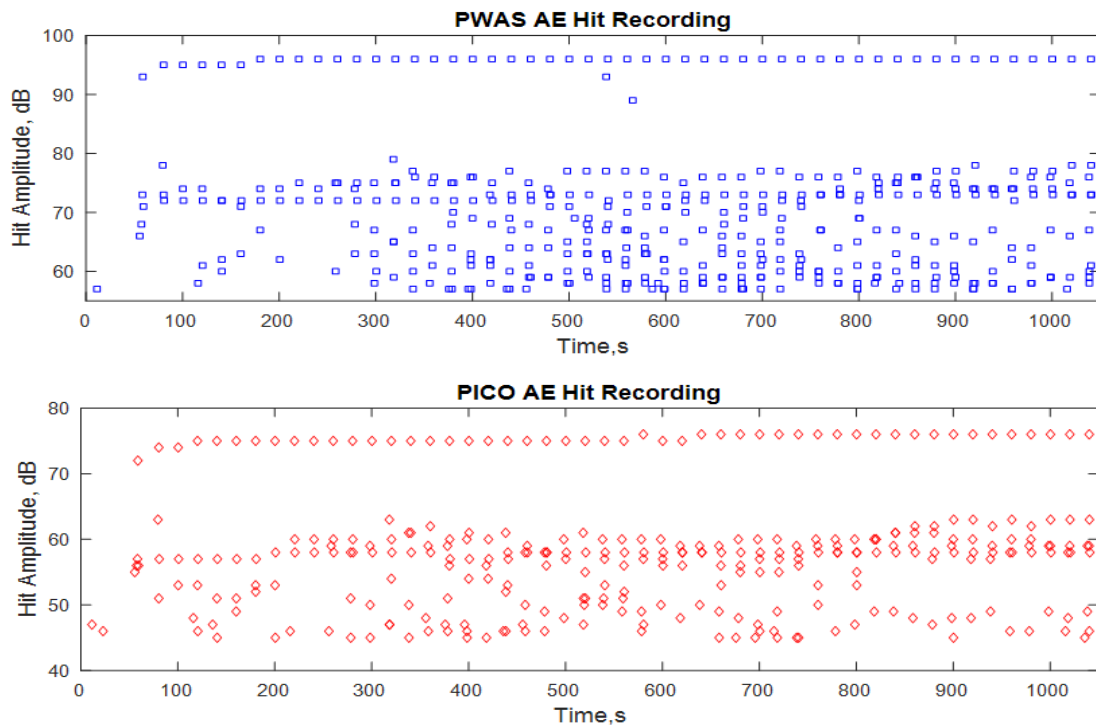


Figure 7.10 The AE hits captured by the PWAS and PICO AE sensors. Both of them are showing a similar trend in the AE-hit plots.

In Figure 7.10, both PWAS and PICO show a similar pattern in the hit-amplitude. In PWAS AE hit plot, there are higher-amplitude AE hits of almost constant amplitude of 96 dB. There are densely populated AE hits of variable amplitudes between 57 to 78 dB. Similarly, in PICO AE hit plot, there are higher-amplitude AE hits of almost constant

amplitude of 78 dB. There are densely populated AE hits of variable amplitudes between 45 to 63 dB.

It can be noted that PICO AE hit amplitudes were higher than that of the S9225. This may be caused by the size of the PICO (4.75 mm diameter) being larger than the size of the S9225 (3.5 mm diameter) AE sensor. The PWAS hit amplitudes were higher than that of the PICO. This may be because the size of PWAS was larger than that of the PICO. Also, they had different piezoelectric transduction factors and sensing mechanisms. In this particular 50 cycles, PWAS captured 427 AE hits while the PICO captured 305 AE hits because some of the low-amplitude AE hits fell below the threshold setting of PICO. Except these very low-amplitude AE hits, both of them successfully captured AE events generated by the fatigue crack.

The PWAS and PICO AE hits and the fatigue loading plotted on a common timeline are shown in Figure 7.11. Only 10-fatigue cycle results are shown in this figure to maintain the clarity of AE hit variation with fatigue loading. It shows that the multiple AE hits happened at every cycle. At a particular instant, a pair of AE hits can be observed: one captured by PWAS (marked by blue “square”), other captured by PICO (marked by red “diamond”). This indicated that they captured the same AE event at almost same time. The AE hits occurred during the cyclic loading period (from minimum load to maximum load) only. In the unloading period (from maximum load to minimum load), no AE hits were observed.

The AE hits started appearing at 53% of the maximum load level and continued until 84% of the maximum load level at some intervals. So far, the PWAS and PICO

showed the very similar pattern from the AE-hit based analysis. Both of them captured the fatigue crack generated AE hits with a very similar level of detail.

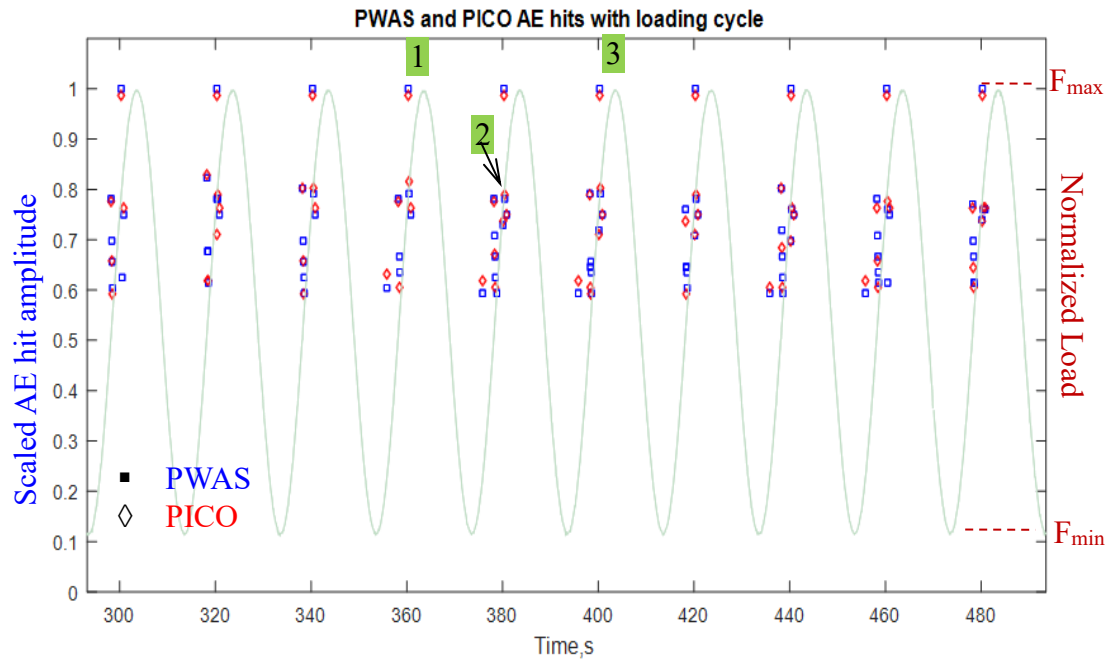


Figure 7.11 PWAS and PICO AE hits synchronized with the fatigue loading cycle.

7.3.8 COMPARISON BETWEEN PWAS AND PICO FROM THE AE-WAVEFORM BASED ANALYSIS

PWAS and PICO AE sensors were compared based on the AE waveforms and their frequency spectra. It was found that all the PWAS and PICO AE waveforms were different even though the AE hits from the same AE event were compared. Three pairs of AE hits as marked by “1”, “2”, “3” on Figure 7.11 were considered for comparison. Pairs “1” and “2” are representatives of all the higher amplitude AE hits. Pair “3” is representative of the lower amplitude AE hits.

The PWAS and PICO AE waveforms for a particular AE event that happened at 360.36 s (“1”) are shown in Figure 7.12a,b. The AE hits corresponding to this AE event

belong to the higher amplitude AE hits (group B) of the previous 60-cycle results discussed in an earlier section. The PWAS-captured AE waveform was consistent with the previous 60 fatigue cycle results. But the PICO waveform (Figure 7.12a) was different from the S9225 waveform (Figure 7.7b) even though they had the same mechanism of sensing. The PICO waveform contained a ringing tone.

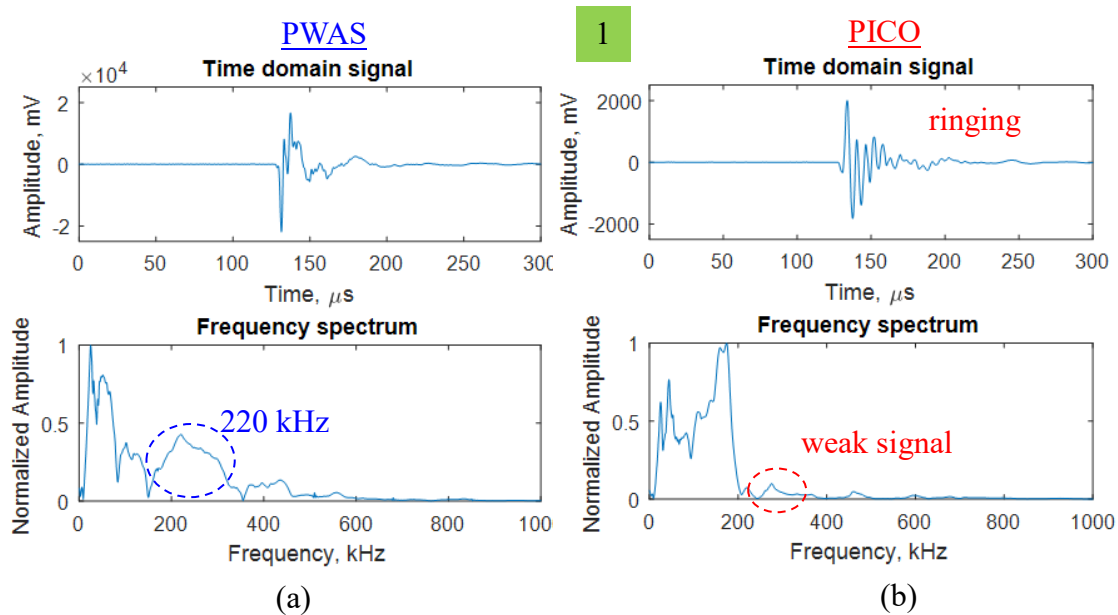


Figure 7.12 The comparison between PWAS and PICO AE waveforms and their frequency spectra for the same AE event at approx. 360.36 s (marked by “1” on Figure 7.11).

The frequency spectra of the PWAS and PICO are also illustrated in Figure 7.12a,b. It shows that the low-frequency peaks such as 30, 60, 110 kHz are captured by both PWAS and PICO AE sensors. But the PICO had the highest peak at 170-kHz and there was a sudden drop in the frequency spectrum after 170-kHz. On the other hand, PWAS captured the 220-kHz and 450-kHz frequency peaks. The PICO showed a very weak response at these frequencies.

The time-domain waveforms and frequency spectra captured by PWAS and PICO are shown in Figure 7.13a,b. These waveforms are corresponding to the pair of AE hits that are captured at 378.79 s (marked by “2” on Figure 7.11). The frequency spectra show that the low-frequency peaks are somewhat similar in both PWAS and PICO AE sensors. But the PICO had the highest peak at 170-kHz and there was a sudden drop in the frequency spectrum after 170-kHz. The PWAS captured a wideband frequency of 110-300 kHz. The PICO showed a very weak response after 200-kHz. The PICO waveform also contained a ringing tone.

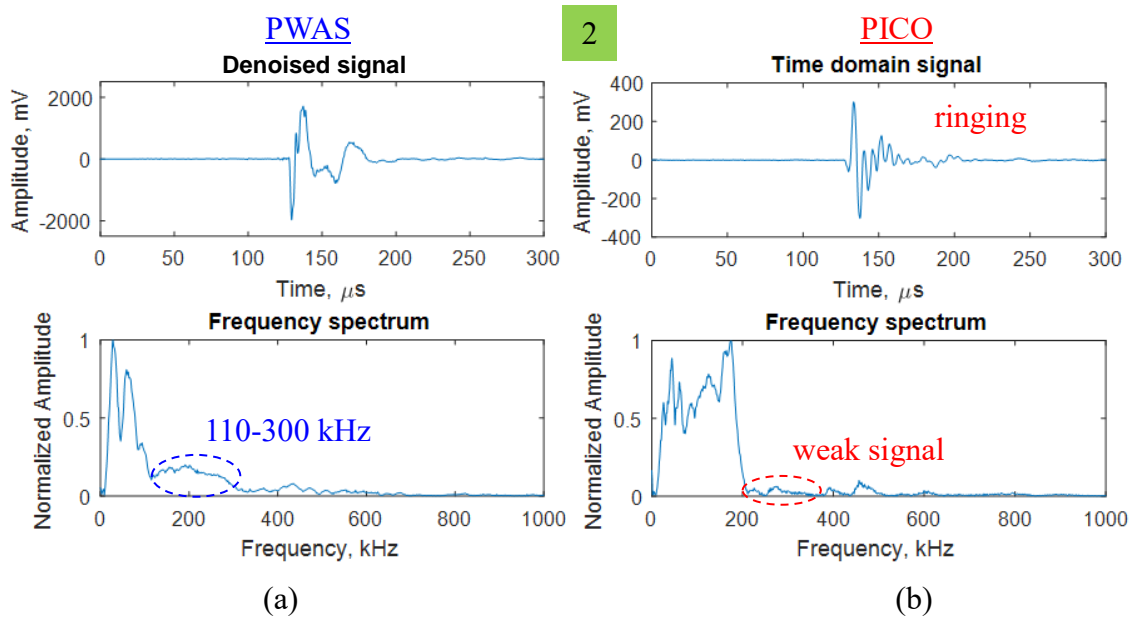


Figure 7.13 The comparison between PWAS and PICO AE waveforms and their frequency spectra for the same AE event at approx. 378.79 s (marked by “2” on Figure 7.11).

The PWAS and PICO AE waveforms corresponding to the AE hits at 400.36 s (“3”) are shown in Figure 7.14a,b. It verifies that the AE waveforms of the 400.36 s (“1”) are same as that of the 360.36 s (“3”). Thus the same observation as Figure 7.12 can be made for Figure 7.14.

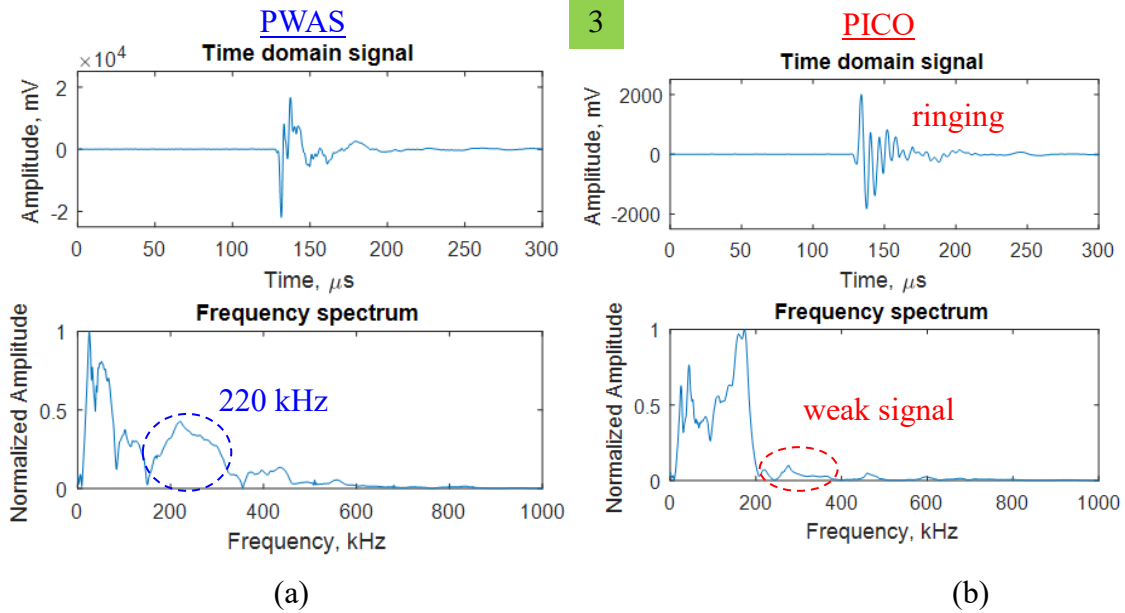


Figure 7.14 The comparison between (a) PWAS and (b) PICO AE waveforms and their frequency spectra for the same AE event at approx. 400.36 s (marked by “3” on Figure 7.11).

Hence, we conclude that the AE signals captured by the PWAS and PICO showed a significant difference based on the AE waveform analysis and frequency spectrum comparison.

7.3.9 EXPLANATION OF WHY PICO WAS SHOWING WEAK RESPONSE AT SOME HIGHER FREQUENCIES

A typical PICO sensing signal and its frequency spectrum are shown Figure 7.15a. The frequency response plot obtained from the sensor manufacturer is shown in Figure 7.15b. The frequency response plot shows a peak at 170 kHz. This explained why the frequency spectrum of the sensed signal showed a peak frequency at 170 kHz. Also, the PICO frequency characteristic plot shows a weak response at 180-270 kHz band. Thus, it showed a weak response at 180-270 kHz band in the sensed signal (Figure 7.15a).

The PICO was also showing a weak response for higher frequencies such as 300, 450 kHz. This may be because the AE waves propagate as symmetric Lamb wave modes which have predominantly in-plane wave motion. But the PICO sensor was sensitive to the out-of-plane wave motion.

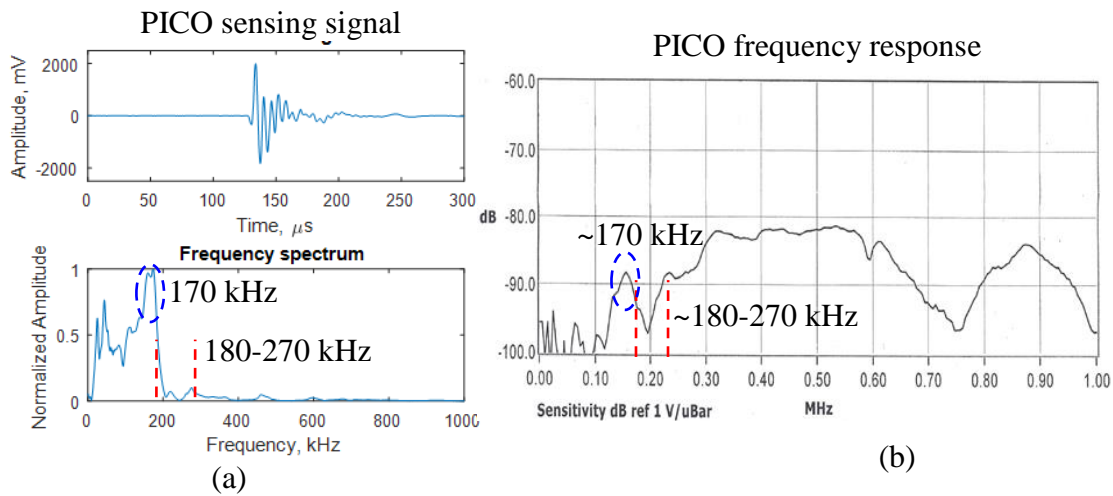


Figure 7.15 (a) A typical AE waveform and its frequency spectrum captured by the PICO AE sensor, (b) frequency response curve of PICO (obtained from the manufacturer).

In both experiments, the PWAS and the commercial AE sensors (S9225 and PICO) showed a very similar pattern from the AE hit based analysis. But they showed significant differences from the AE-waveform based analysis. In both cases, PWAS captured the richer frequency information than that of the S9225 and PICO AE sensors.

7.4 VARIOUS AE WAVEFORM GROUPS WITH FATIGUE LOAD EVOLUTION

The second major finding of the physics-based AE approach is to identify various groups of AE signatures. First, the experimental background of this finding is discussed and then the AE data analysis is illustrated.

7.4.1 IN-SITU AE-FATIGUE EXPERIMENTAL SETUP

The in-situ AE-fatigue experiment was designed and performed to simultaneously measure the AE signals while the fatigue crack grew under fatigue loading. Aircraft grade aluminum Al-2024 T3 material was used to make the test specimen. The dimension of the specimen was 305-mm length, 100-mm width, and 1-mm thickness. The experimental procedures and parameter settings were similar to the previous experiments and are not repeated for the sake of brevity. The only difference was an emphasis on optical crack growth measurement and near-field PWAS AE measurement (schematic is shown in Figure 7.16).

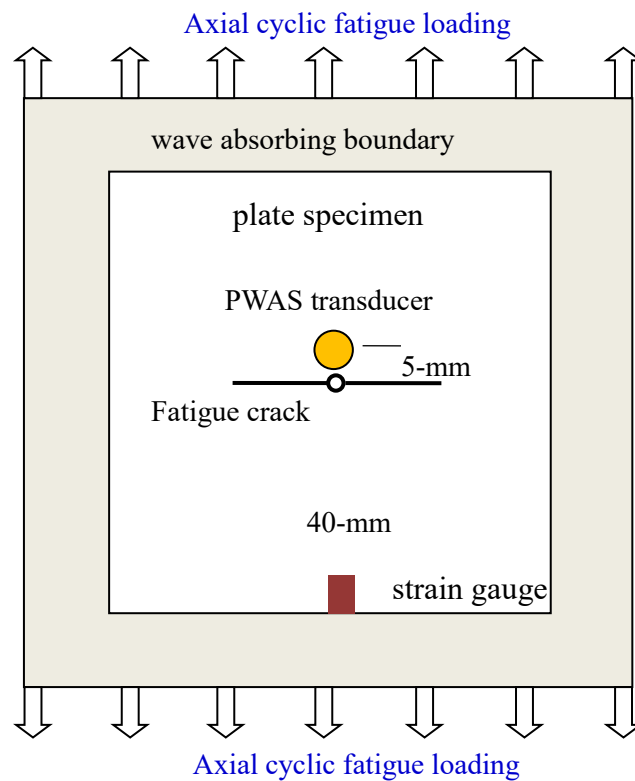


Figure 7.16 Schematic diagram of the fatigue test plate-specimen with a PWAS transducer, 5-mm from the crack.

An in-situ microscope was used to optically monitor the fatigue crack growth as shown in Figure 7.17. A digital camera was attached to the microscope that allowed capturing still images as well as video recordings of the fatigue crack growth. A gooseneck light was used to illuminate the crack zone. It was also used to illuminate the crack from the front and the back of the plate. Various combination of the light adjustment was used for proper image capturing. A high-resolution video recording with extension tube was also attempted to capture crack growth as shown in Figure 7.18.

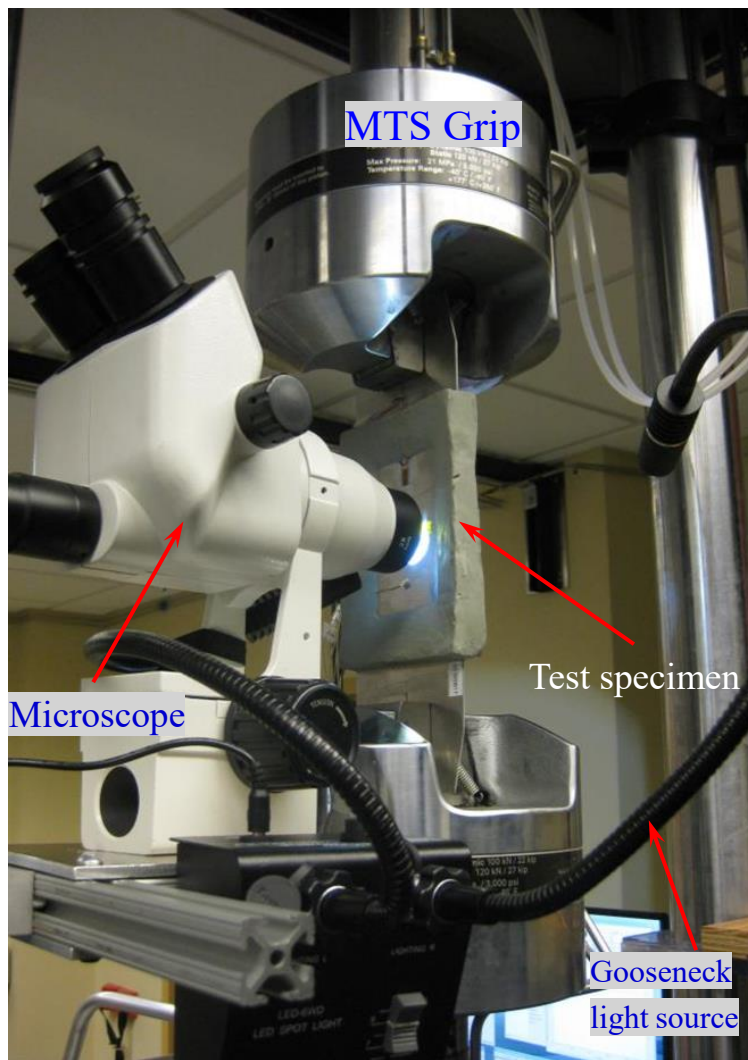


Figure 7.17 The actual fatigue test specimen mounted in the MTS grips with an in-situ microscope

Three parallel measuring systems were used simultaneously during the in-situ AE-fatigue experiment: (a) fatigue loading by the MTS machine, (b) AE and load measurement by the AE system, and (c) fatigue crack growth measurement by an in-situ microscope camera. Since the AE recording and the fatigue load recording was performed in the same AE measuring instrument, it would allow better synchronization between the fatigue load and AE measurement. Thus, the measured AE hit and the fatigue load had a common timeline with respect to the global time of reference.

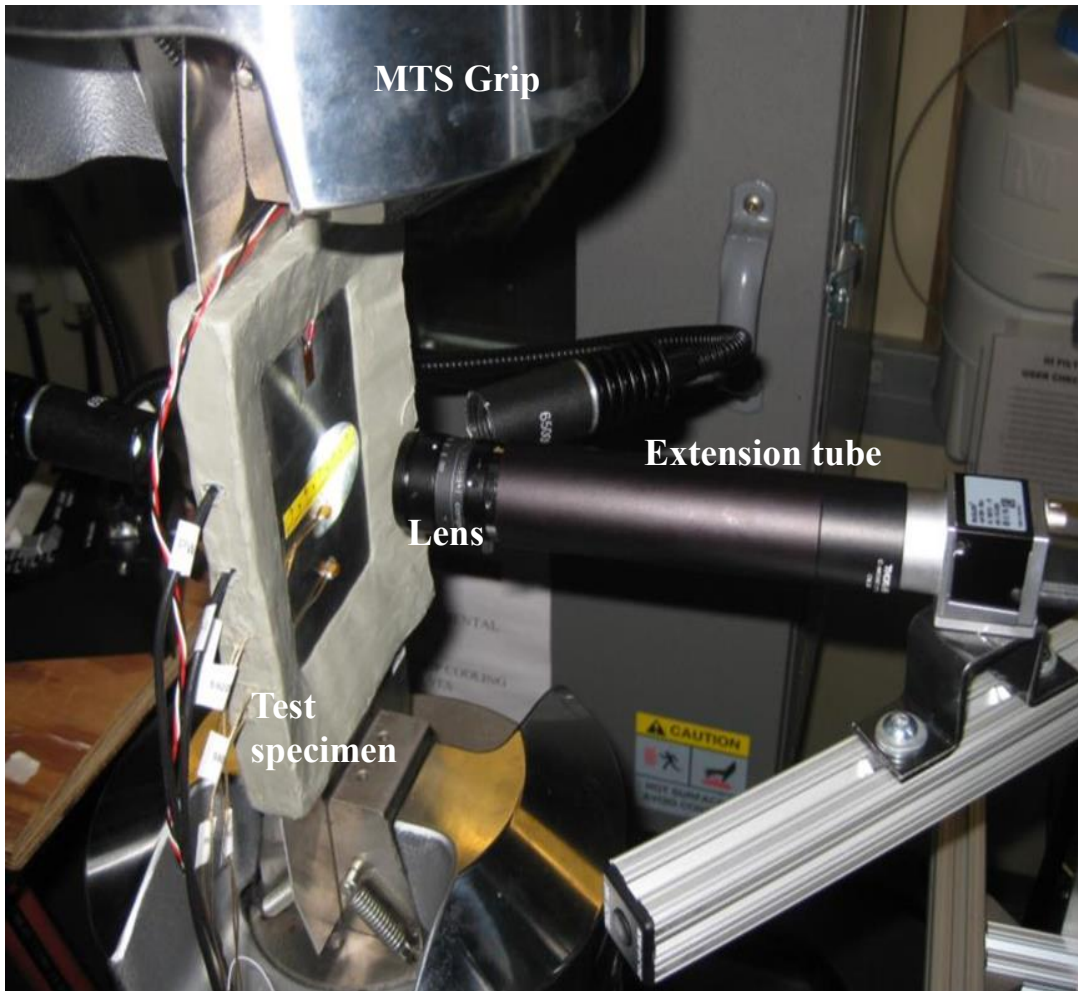


Figure 7.18 The fatigue test specimen mounted in the MTS grips and a high-resolution video camera with an extension tube to measure fatigue crack growth.

7.4.2 AE HITS SYNCHRONIZED WITH THE FATIGUE LOADING

The cyclic fatigue loading and the AE hits were measured in a common timeline. The similar nature of AE hits was also observed in other AE sensors but it is not discussed here for the sake of brevity. The synchronized plot of the fatigue loading and the AE hits captured by the near-field PWAS is shown in Figure 7.19. The AE hit amplitude was measured in dB scale. The fatigue loading was varied sinusoidally between a minimum ($F_{\min}=1.23$ kN) and maximum ($F_{\max}=12.3$ kN) load level with a slow loading rate (0.05 Hz).

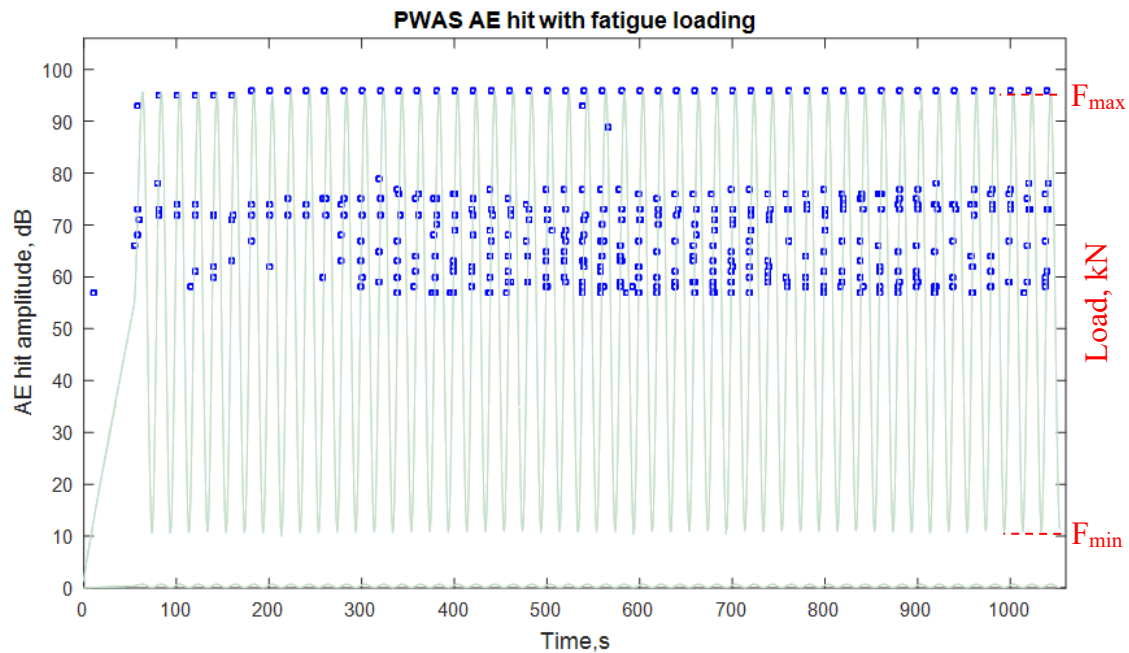


Figure 7.19 AE hits captured by the PWAS transducer are plotted in synchronization with the cyclic fatigue loading.

To preserve the clarity of the load-hit synchronization plot, only 50 fatigue cycles results are shown in Figure 7.19. The near-field PWAS transducer captured 427 AE hits in the 50 fatigue cycles. In this particular 50 cycles, the fatigue crack growth was optically measured as approx. 300- μm . It can be noticed that there are high-amplitude AE hits at about 96 dB. They happened at almost every cycle near the peak load of the fatigue cycle.

There are numerous AE hits in the range of 55-75 dB. At every cycle, there were multiple AE hits.

AE hits were observed during the loading cycle when the fatigue load was going from minimum to the maximum level. On the unloading cycle, when the fatigue load was going from maximum to minimum, no AE hits were observed. Each AE hit corresponded to an AE waveform. Individual waveform analysis of the AE hits was performed to find any possible similarities in the AE signals. That allowed grouping the AE hits as discussed next.

7.4.3 AE WAVEFORMS GROUPS IN RELATION TO THE FATIGUE LOADING

Since PWAS captured richer frequency information than the PICO and S9225 AE sensors, the PWAS AE hits were extensively analyzed. The AE hits were analyzed at individual waveform level. The waveform of each AE hit was analyzed as both time-domain signal and frequency spectrum. Fast Fourier transform (FFT) was used to obtain the frequency spectrum from the time-domain signal. It was found that there were some groups of AE hits that had the same time-domain signal and frequency spectrum. Once the AE waveforms were sorted based on the frequency spectra, the load level similarity was automatically obtained [154].

7.4.3.1 *AE Waveform Groups A, B, C Repetitive at Every Fatigue Cycle*

From Figure 7.19, one can easily distinguish two different zones of AE hits: the higher-amplitude zone at 96 dB and a denser low-amplitude zone at 55-75 dB. In the denser zone, it was identified that there exist a group of AE hits which had the same time-domain signal and frequency spectrum. They were named “group A”. The hit amplitudes of group A were almost constant at 72 dB. Interestingly, all of them happened at approximately 84%

of maximum fatigue load. It indicated that there was a certain AE source due to a change happen in fatigue crack at 84% of maximum load. Group A hits are shown in Figure 7.20a and marked by a dotted ellipse.

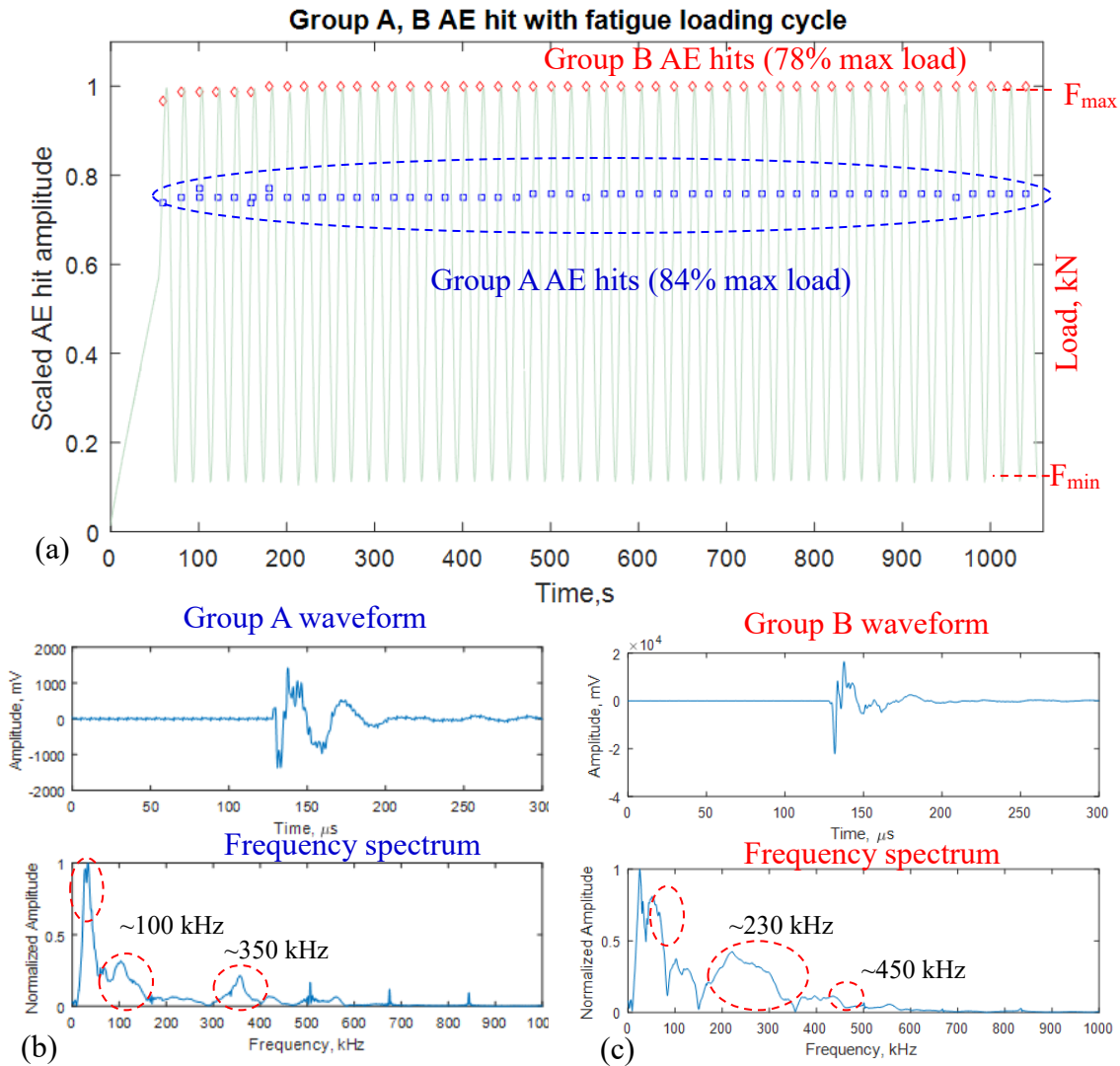


Figure 7.20 (a) Group A, B AE hits are plotted in sync with the cyclic fatigue loading. They happened at every cycle but at different load levels; group A happened at 84% of maximum load level while group B happened at 78% of maximum load level. (b),(c) The waveforms and frequency spectra of group A, B, respectively; the major frequency peaks of each group are marked by dotted ellipses.

All the higher-amplitude (96 dB) AE hits have the same time-domain signal and frequency spectrum. These AE hits were assigned to “group B” and shown in Figure 7.20a. In Figure 7.20a, the AE-hit amplitudes are scaled in such a way that the maximum amplitude of group B has a unit hit amplitude and the other hit-amplitudes were divided by that maximum number. All the AE hits in group B happened at 78% of maximum load level.

7.4.3.2 Load Level Determination for a Certain AE Waveform Group

The load level determination for group A and B waveforms are illustrated in Figure 7.21. First, a vertical line was drawn from each AE hit to the loading cycle which gives the time when the AE hit happened. Then a horizontal line was drawn from that intersection point to the load axis that gave the load level of that particular AE hit. A similar approach has been used for determining the load level of all the AE hit groups.

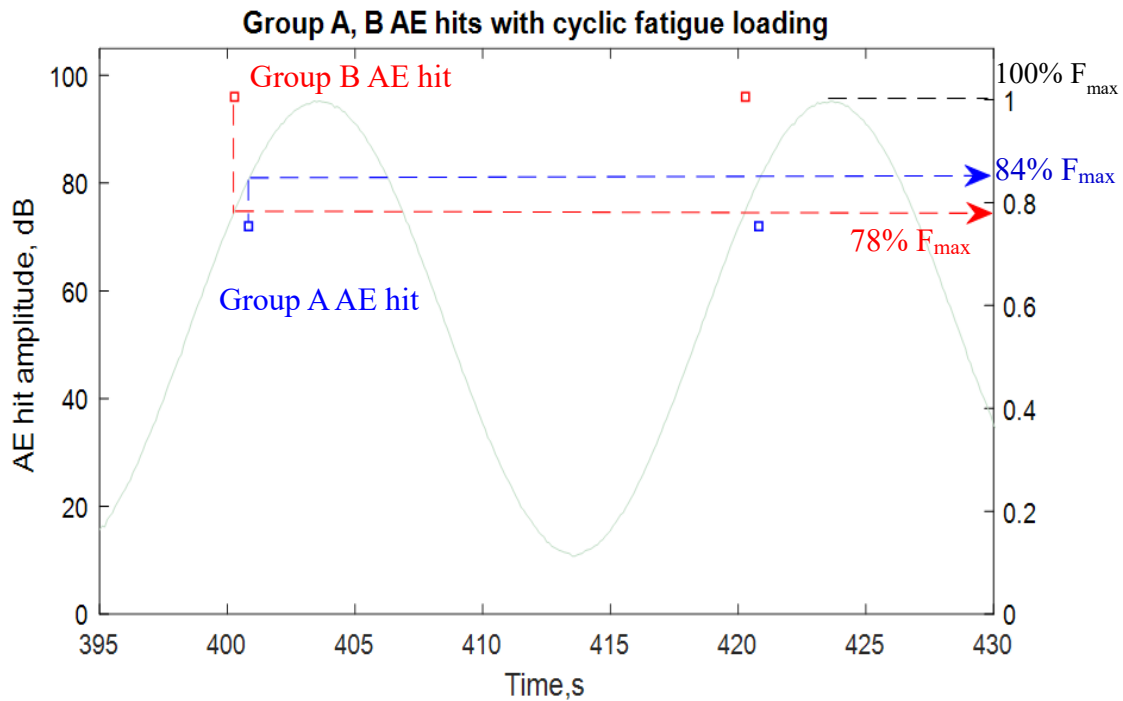


Figure 7.21 Load level determination of group A and group B AE hit.

7.4.3.3 Similarities in the Signals Belonging to One Group

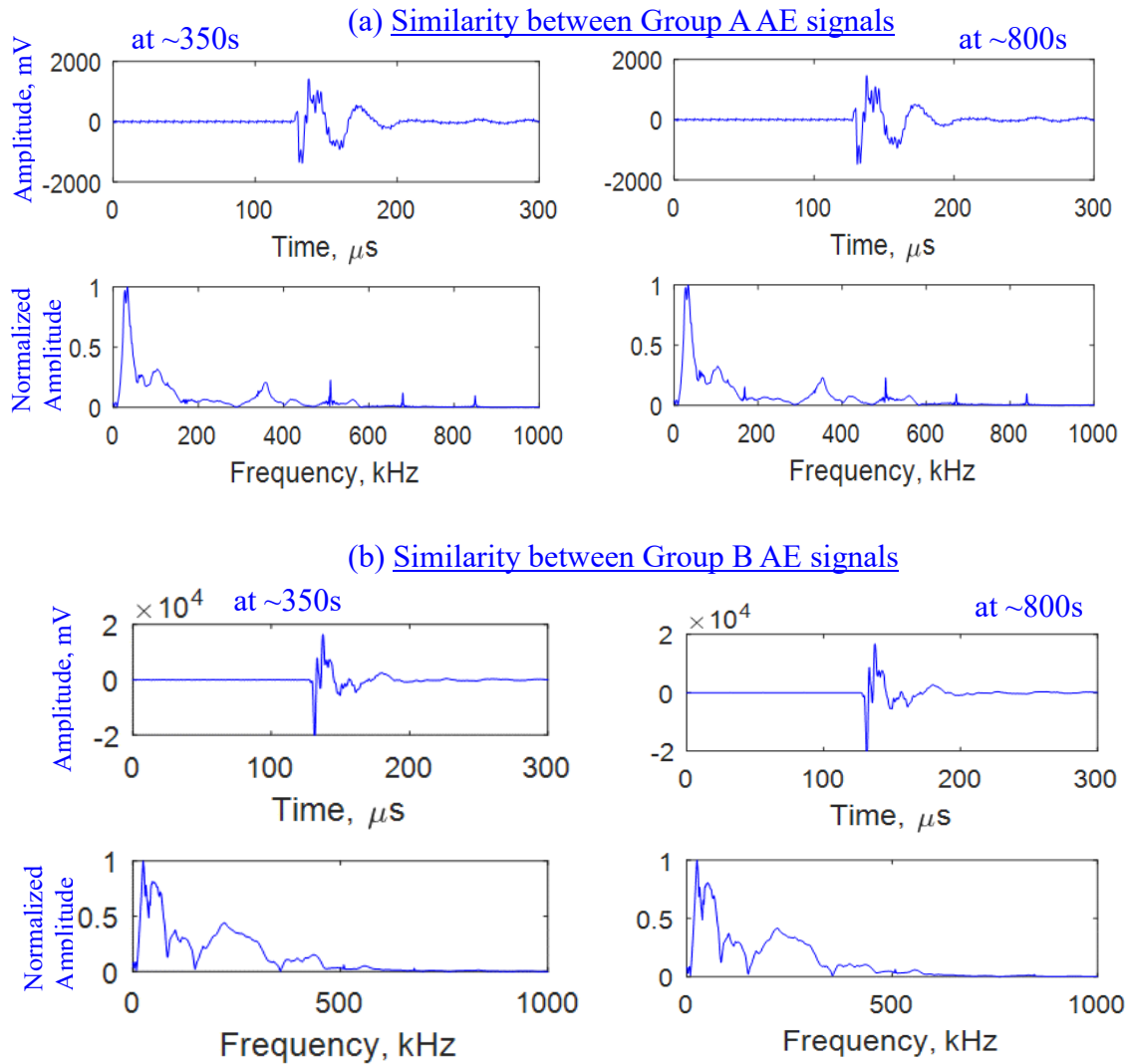


Figure 7.22 Similarity between the AE events happened at two different times (~ 350 s, ~ 800 s) in a particular group. For illustration purpose, only two groups (A, B) are presented here. The time-domain and the frequency spectrum of each signal are plotted.

To illustrate the similarities of the signals belonging to one group, few AE events from group A and group B were picked up. The time-domain signals and frequency spectra of the AE waveforms are plotted in Figure 7.22. The AE events at two different times (~ 350 s, ~ 800 s) are shown here. Figure 7.22a shows that both time-domain signals and frequency spectra of group A are very similar to each other even though they happened at two

different times (~350 s, ~800 s). Figure 7.22b shows that both time-domain signals and frequency spectra of group B are very similar to each other even though they happened at two different times (~350 s, ~800 s). A similar observation was true for AE signals of other groups.

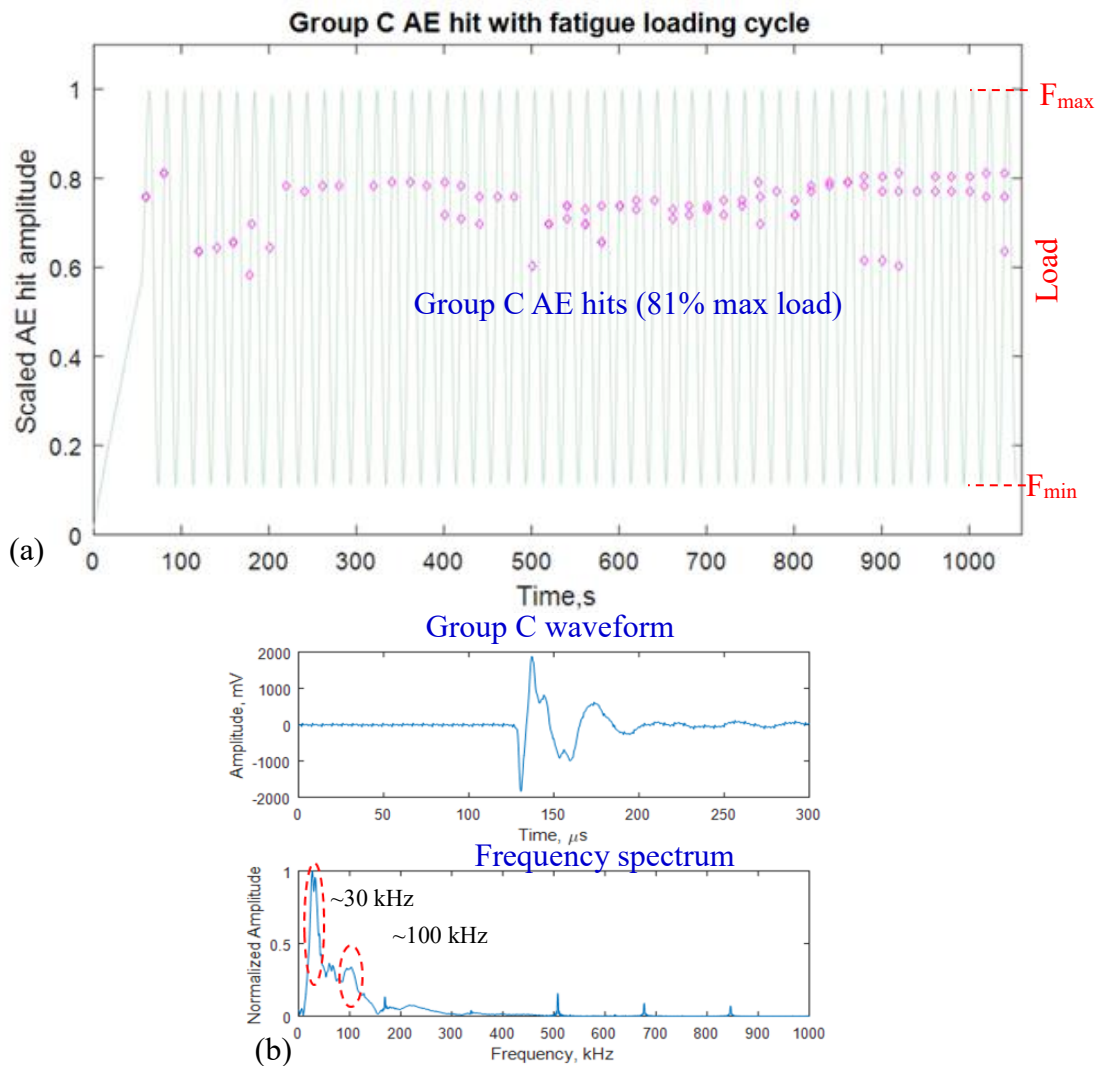


Figure 7.23 (a) Group C AE hits are plotted in sync with the cyclic fatigue loading; the hit amplitude varied over the fatigue cycles, they happened at every cycle approx. 81% of maximum load; (b) the time domain signal and frequency spectrum of a representative group C waveform.

Representative waveforms from groups A, B were plotted in Figure 7.20b and c, respectively. Both time-domain signals and frequency spectra are shown here. It was observed that the AE waveform of group A was different from that of B. Group A has frequency peaks at 40, 100, 350 kHz whereas the group B has frequency peaks at 30, 50, 100, 230, 450 kHz. Group B waveform contained some of the frequency peaks of group A, for example, 100 kHz. The amplitude of the group B waveform was several orders higher than that of the group A. When we compared the time of occurrences of the two waveforms, we found that during the fatigue loading, group B (at 78% F_{max}) happened earlier than the group A (at 84% F_{max}). Both of them happened at every fatigue cycle.

Group C AE hits that happened in between group A and B can be also identified. They happened at 81% of fatigue loading. The AE hit-load plot of group C is shown in Figure 7.23a. It can be shown that until 400s, group C happened once at every fatigue cycle whereas, after 400 s, two group C waveforms happened at every cycle. The amplitudes of the group C hits were not constant unlike group A, B rather they varied. When two group C hits happened as a cluster, one had a higher amplitude than the other. It seemed like the acoustic energy from the fatigue crack had been split into two wave packets.

The time-domain signal and the frequency spectrum of a representative group C waveform are shown Figure 7.23b. They are different from the group A, B. The major frequency peaks of group C waveform are 30, 100 kHz. The low-frequency peaks are dominant in this group.

7.4.3.4 Group D Appeared, Continued, and then Disappeared

Group D AE hits happened at 78% of fatigue loading. The AE hit plot of group D synchronized with the fatigue loading is shown in Figure 7.24a. They appeared for some

time and then discontinued after 320 s. The amplitude of group D was relatively smaller than the group A, B, C. The time-domain signal of a representative group D waveform is shown Figure 7.24b. It can be noticed that there is a regular noise floor before and after the main signal. This can easily be removed to obtain a denoised waveform as plotted in Figure 7.24c.

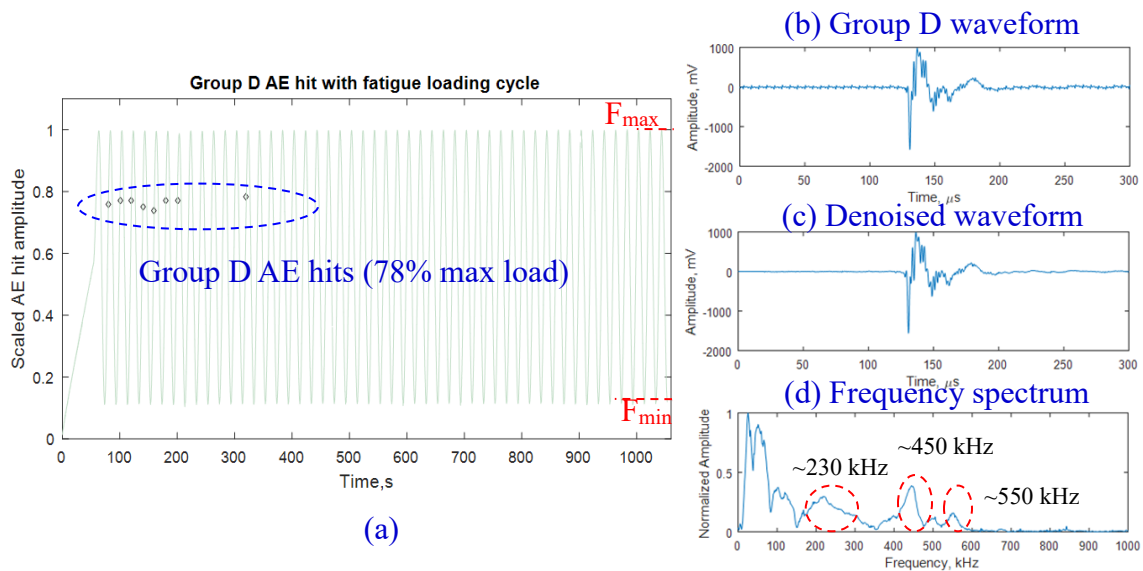


Figure 7.24 (a) Group D AE hits are plotted in sync with the cyclic fatigue loading; they happened at approx. 78% of maximum load, they appeared in the beginning and disappeared after approx. 300s; (b) the raw time domain signal of group D; (c) denoised waveform of (b); (d) frequency spectrum of the denoised group D waveform.

The frequency spectrum of the denoised waveform is shown in Figure 7.24c. They have same frequency content as group B waveforms except for an additional peak at 550 kHz in group D. They also happened at the similar fatigue load level as group B. The group B and D may be related to the same AE event due to a change in the fatigue crack.

7.4.3.5 Group E Appeared as a Cluster at Every Cycle

Group E AE hits in sync with the cyclic fatigue loading are plotted in Figure 7.25a. The main feature of these hits was that they happened as a cluster of two or three hits in

every cycle. They happened between 51-58% of maximum load in the fatigue loading cycle. They appeared after approx. 250 s and then continued in every fatigue cycle. In a cluster, the first hit had a higher amplitude than the second and third hits. The time-domain signals and frequency spectra of these AE hits in a cluster are exactly same except the amplitudes. The waveform of a representative AE hit is shown in Figure 7.25b. The first AE hit of a particular cluster is shown in this figure. The frequency spectrum shows that the dominant frequency peaks are located at 30, 60, 200 kHz.

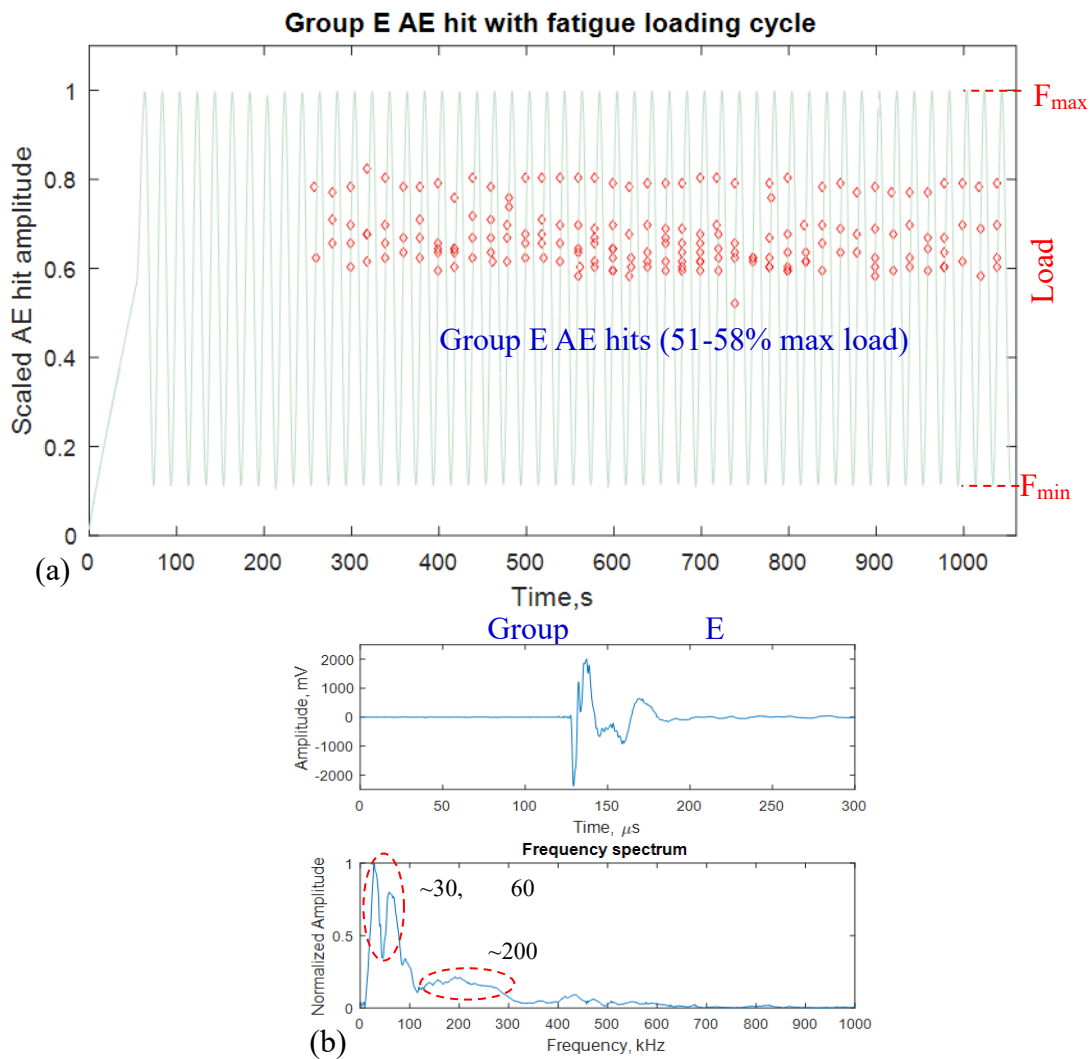


Figure 7.25 (a) Clustered Group E AE hits in sync with the cyclic fatigue loading (b) the time domain signal and frequency spectrum of a representative group E waveform.

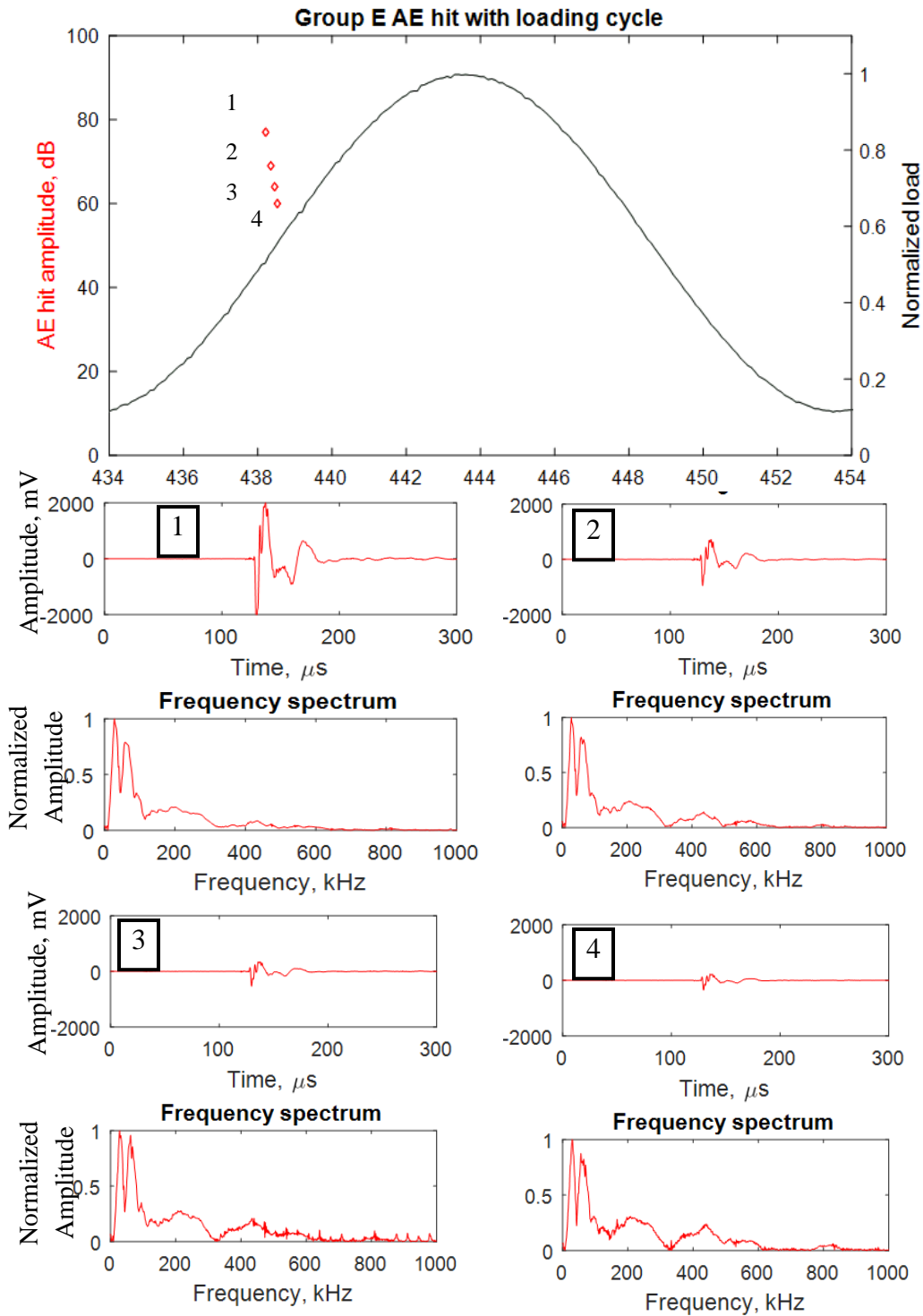


Figure 7.26 Similarity in the frequency spectra of clustered (Group E) AE waveforms

A clustered group E AE hits, their respective waveforms, and frequency spectra in a particular cycle are illustrated in Figure 7.26. It shows that the frequency spectra of all the waveforms are the same, only that the amplitude is getting weaker from first AE hit to last AE hit of a cluster.

7.4.3.6 Possible Explanation for Clustered Group E Waveforms

There may be a sequence of small AE events that were happening in every cycle at relatively low loading levels (51-58% F_{max}). These loading levels were too low to cause crack extension. The possible explanation for the cluster group E AE hits could be:

- a) Crack surfaces have a zigzag saw-tooth thickness-wise pattern because cracks in thin-gauge specimens happen on shear planes. The zigzag nature of the crack was captured by the in-situ microscopic images and is shown in Figure 7.27. The faying surfaces along the thickness can be perceived from Figure 7.27 and its schematic (Figure 7.28). The light was shining directly from behind the fatigue crack.
- b) Because crack propagation has a zigzag path, cracks are not perfectly straight and may “catch” when opening.
- c) Repeated saw-tooth crushing seems to happen, first at 51% load level and then at slightly higher loads, but of progressively smaller AE intensity.
- d) When the first crushing is happening at 51% load, it is releasing higher amplitude AE signals. Subsequent crushings are causing lower amplitude AE signals.

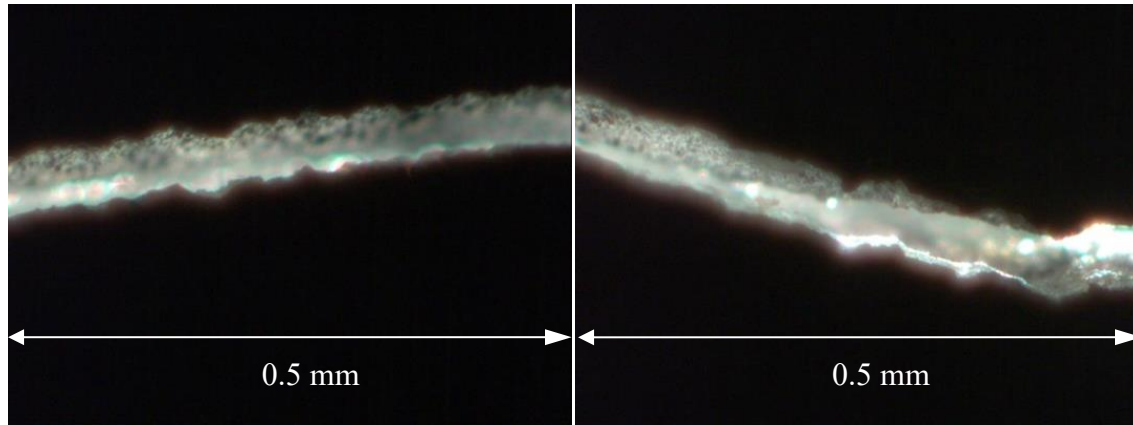


Figure 7.27 The view of the zigzags and the faying surfaces of the fatigue crack. The image was captured at maximum load level; two different locations along the fatigue crack length are shown here; the light was shining behind the crack.

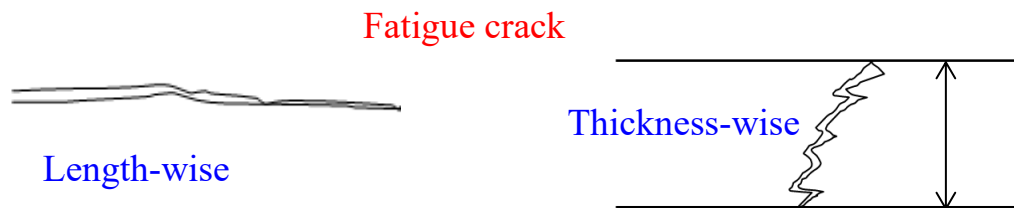


Figure 7.28 Schematic representation of the faying surfaces of the fatigue crack

7.4.3.7 Characteristics of Group F, G, H AE Waveforms

Group F AE hits are shown in Figure 7.29a. These hits happened at the similar time of group E. They also happened at every fatigue cycle. The time-domain signal and the frequency spectrum of a representative group F waveform are shown in Figure 7.29b. The frequency spectrum was same as that of group E except that it had an additional higher frequency at 450 kHz. They happened at 57% of maximum load level. The AE source of group F may be closely related to that of group E.

Group G AE hits happened in between 78% to 81% of maximum load level during fatigue loading period. The AE-hit load synchronization plot is shown in Figure 7.30a. They happened sporadically over the fatigue cycles. The time-domain signal and the

frequency spectrum of a representative group G waveform are shown in Figure 7.30b. They were similar to the group C AE hits based on the frequency spectrum except for the low-frequency peaks at 40 kHz. The other difference is that they happened at a variable load level from 78% to 81% F_{max} .

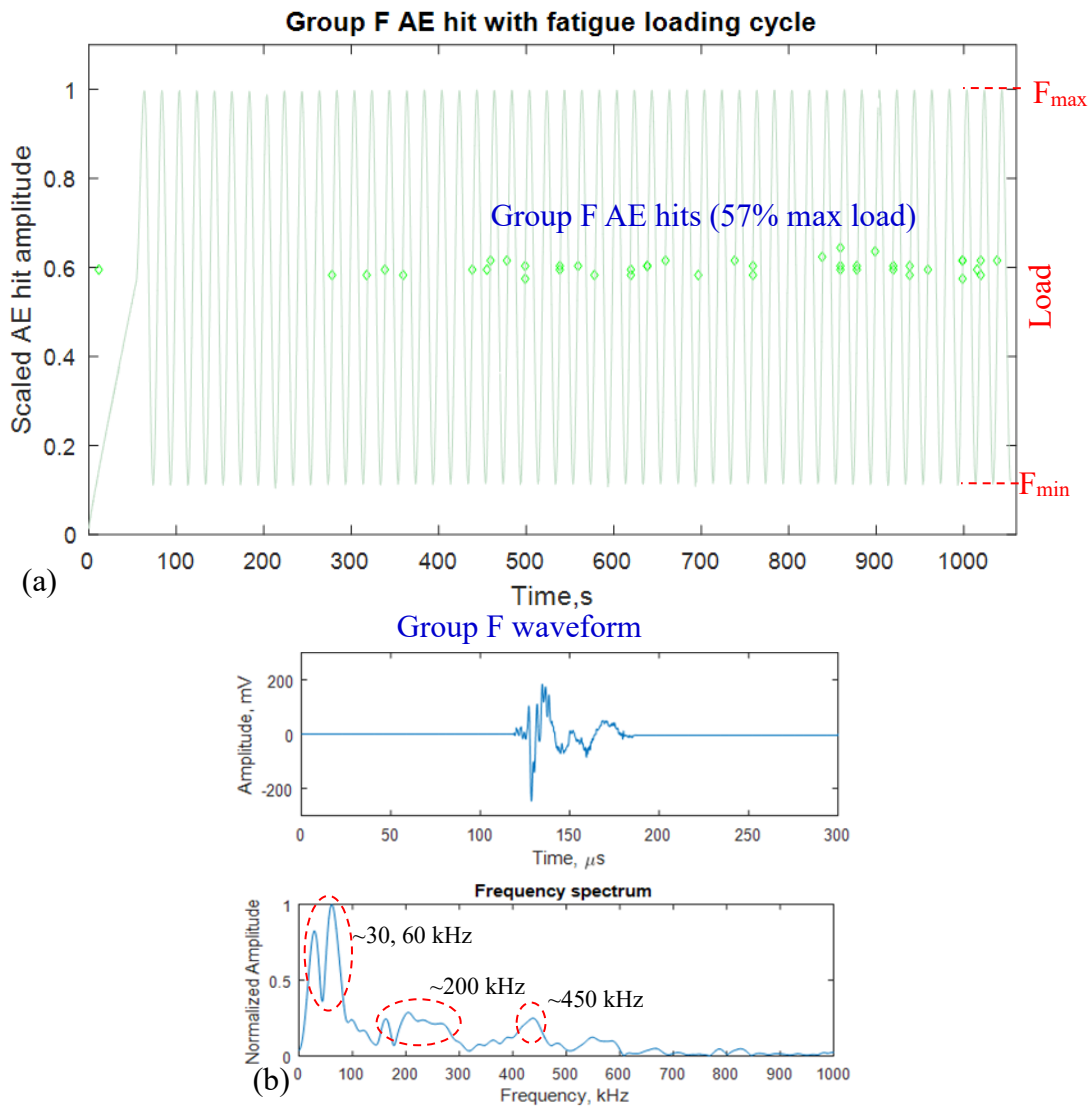


Figure 7.29 (a) Group F AE hits are plotted in sync with the cyclic fatigue loading; they happened at every cycle and at approx. 57% of maximum load, they appeared after approx. 250s and then continued; (b) the time domain denoised signal and frequency spectrum of a representative group F waveform.

A few AE hits were observed near very low load level (e.g., 23% F_{max}). These were assigned as group H. The hits sync with the fatigue load is shown in Figure 7.31a. They appeared for some cycles, then disappeared, and then again appeared. The time-domain signal and the frequency spectrum of a representative group H waveform are shown in Figure 7.31b. The major frequency peaks of the group H waveform were 40, 70, 100, 200 kHz.

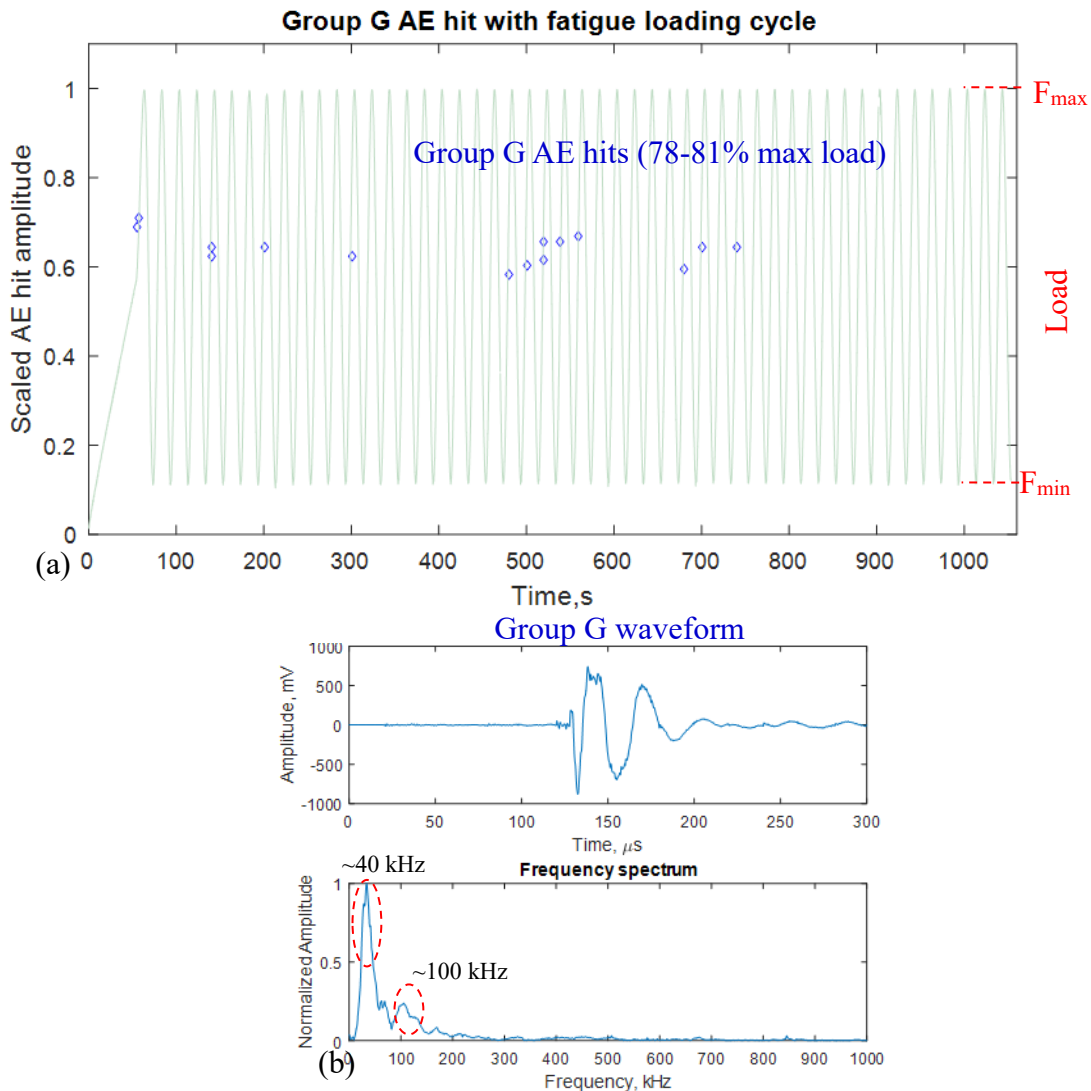


Figure 7.30 (a) Group G AE hits appeared sporadically over the cycles at approx. 78-81% of maximum load; (b) the denoised time domain signal and the frequency spectrum of a representative group G waveform.

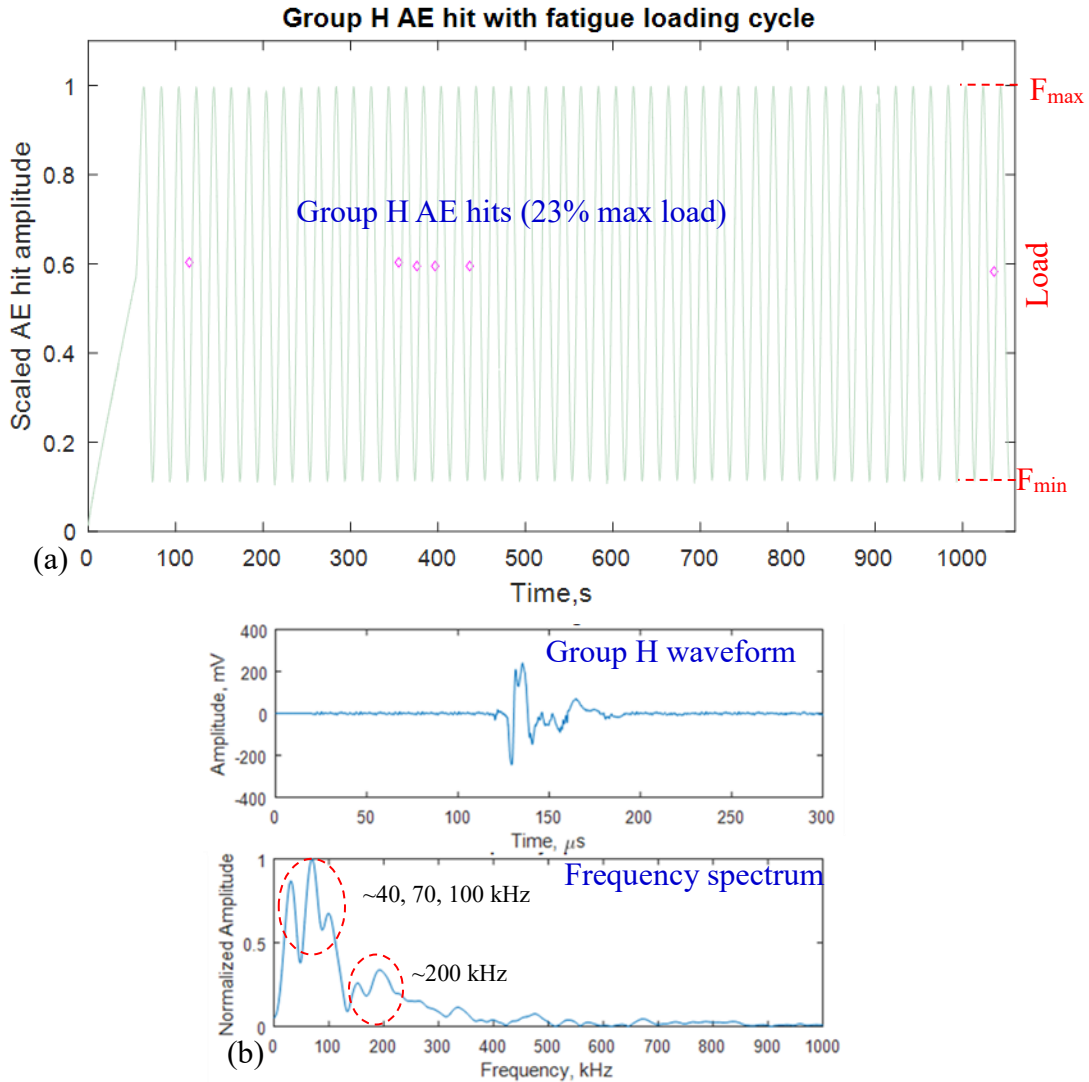


Figure 7.31 (a) Group H AE hits are plotted in sync with the cyclic fatigue loading; they appeared a few times over the cycles at relatively lower load level (23% of max. load); (b) the denoised time domain signal and the frequency spectrum of a representative group H waveform.

We also observed a very few irregular AE hits happened randomly at different load levels (not shown here). Most of them had a sharp peak and we classified them as “rogue”. They had a wideband frequency as mentioned in the summary Table 7.1. They happened somewhere between 23% - 94% F_{max} . They had a very wide range of hit amplitudes that resulted in large standard deviation.

The summary statistics of the 427 AE hits in 50 fatigue cycles is shown in Table 7.1. We had nine different groups of AE hits from A, B, C,...H, Rogue. The number of AE hits, the load level of occurrence, and major frequency peaks for each group are detailed in Table 7.1.

Table 7.1 Summary statistics of the 427 AE hits over the 50 fatigue cycles with 300- μ m crack growth

Waveform type	Number of hits	Load level (%F _{max})	Major freq. bands/peaks (kHz)
A	53	84	40, 100, 350
B	50	78	30, 50, 100, 230, 450
C	89	81	30, 100
D	8	78	30, 70, 100, 230, 450, 550
E	154	51-58	30, 60, 200
F	43	57	30, 60, 200, 450
G	15	78-81	40, 100
H	6	23	40, 70, 100, 200
Rogue	9	23~94	350-1000
Total=	427		

7.5 SOURCE LOCALIZATION OF THE AE SIGNAL GROUPS

A source localization was performed to be certain that fatigue crack generated these various groups of waveforms. This section illustrates a simple methodology for the source localization. A schematic diagram of the fatigue test specimen is shown in Figure 7.32a. It shows the relative positions of the four sensors (two PICO and two PWAS transducers). The actual specimen is shown in Figure 7.32b.

7.5.4 ALL POSSIBLE AE SOURCES

From the close observation of the AE-fatigue test system we could identify three most possible AE sources of the AE signals:

- (1) fatigue crack
- (2) upper grip

(3) lower grip

The possible AE sources are marked by “star” sign in Figure 7.32a. The close-up view of the near-field PWAS and PICO is shown in Figure 7.33. It shows that the edge of the PWAS is closer to the crack than the PICO sensor since the size of the PWAS is larger than the PICO sensor.

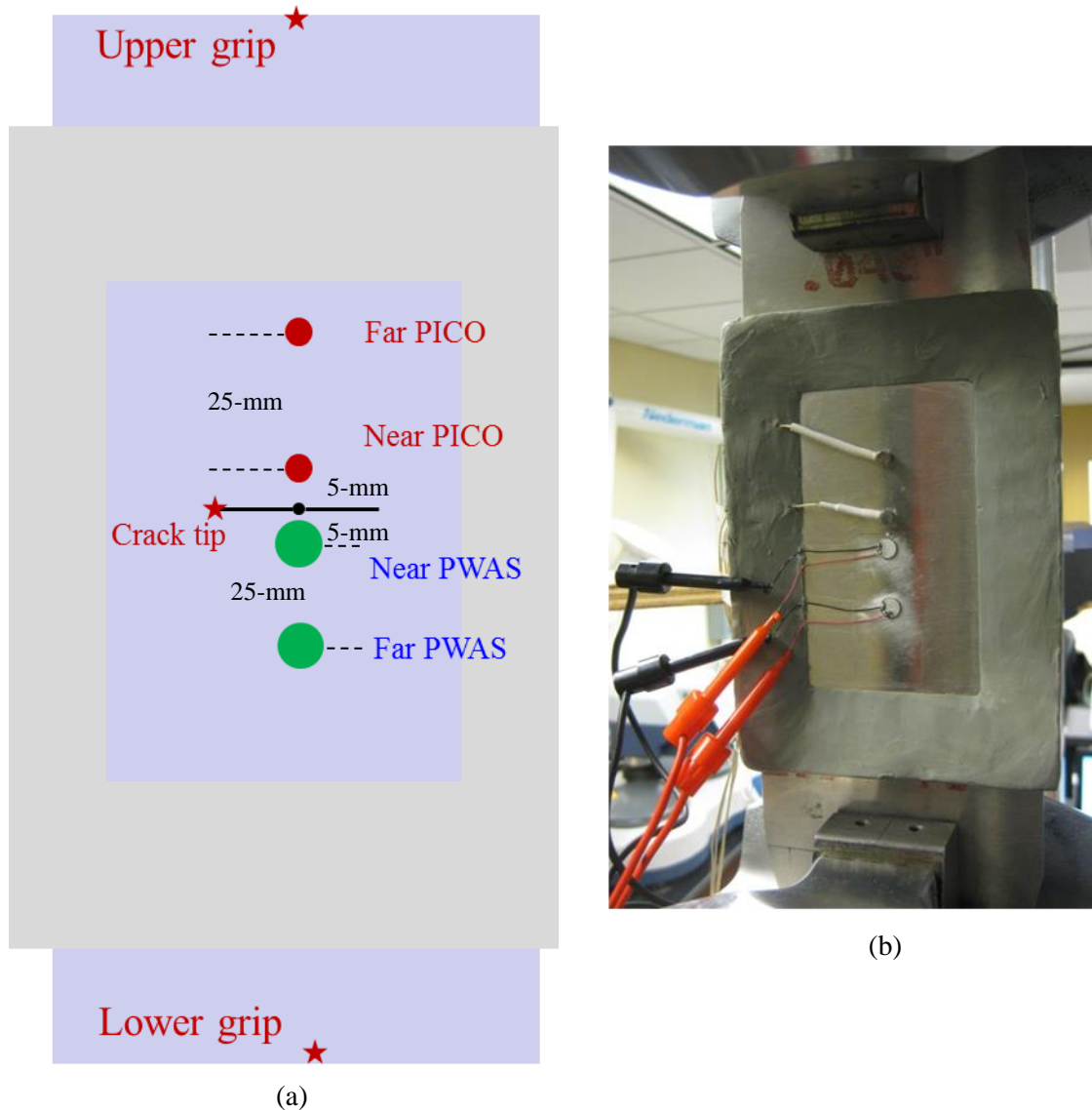


Figure 7.32 (a) Schematic diagram for the source localization of the AE signals; two PWAS transducers and two PICO AE sensors were bonded symmetrically about the fatigue crack and at same distances (5-mm, 25-mm) from the crack; (b) actual fatigue test specimen mounted on the MTS grip showing the positions of the four sensors.

7.5.5 FOUR HYPOTHESES ON THE SEQUENCE-OF-ARRIVALS

The time-of-flights of the AE signals from the four sensors were needed for the illustration. Four hypotheses may be considered based on the sequence-of-arrival (SOA). They are illustrated in Figure 7.34. If the crack is the AE source, the AE waves would hit the near-field PWAS first (1), then the near-field PICO (2), then far-field PWAS (3) and at last far-field PICO (4). The number indicates the sequence of arrival. When we cast these sequence number by the left column of Figure 7.34, one would get $SOA \rightarrow 4-2-1-3$. Similarly, if the upper grip is the AE source then $SOA \rightarrow 1-2-3-4$; if the lower grip is the AE source then $SOA \rightarrow 4-3-2-1$; if upper and lower grips are the AE source then $SOA \rightarrow 2-4-3-1$.

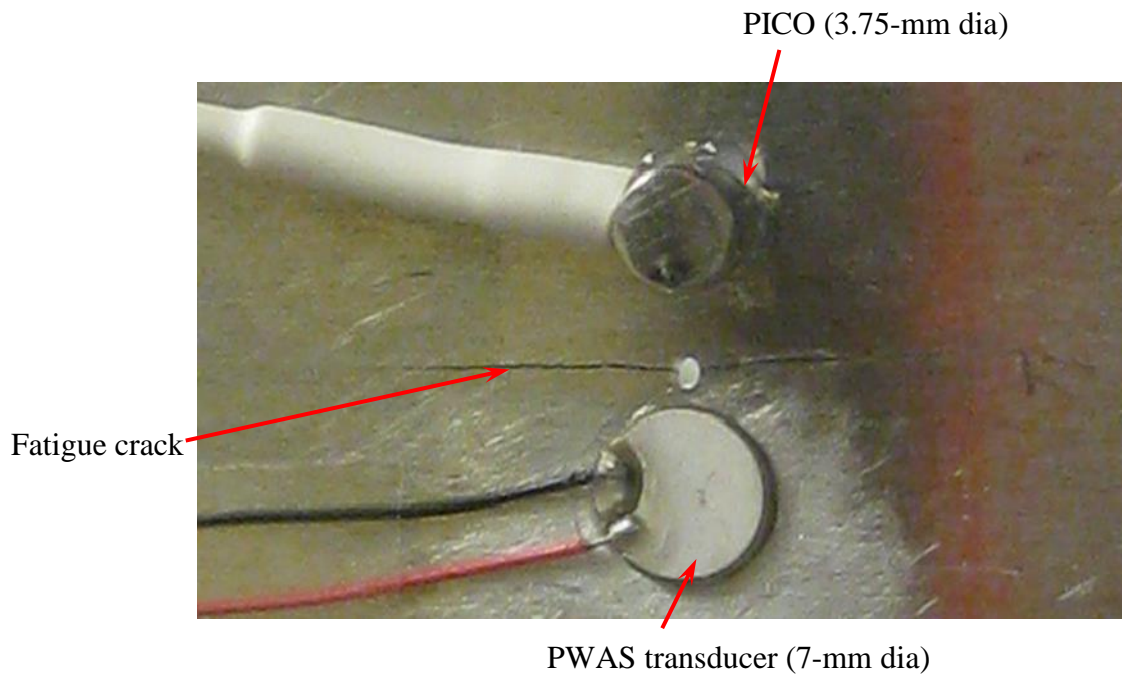


Figure 7.33 Relative position of the near-field PWAS and PICO sensors. The centers of the two sensors were at an equal distance, 5-mm from the crack. [scale: the hole is 1-mm diameter]

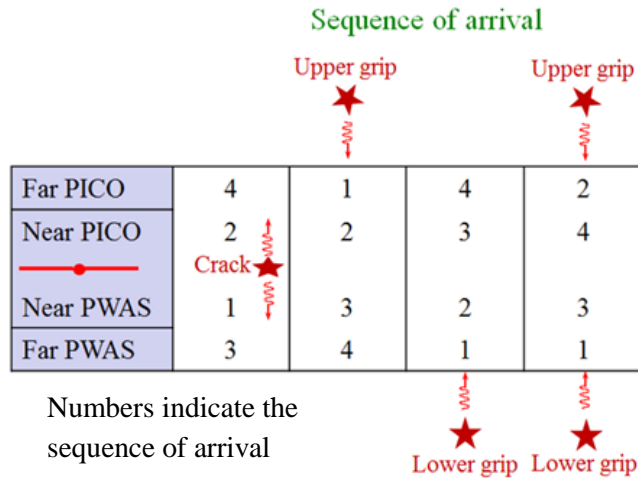


Figure 7.34 Four possible hypotheses on the sequence-of-arrival (SOA) of the AE signals.

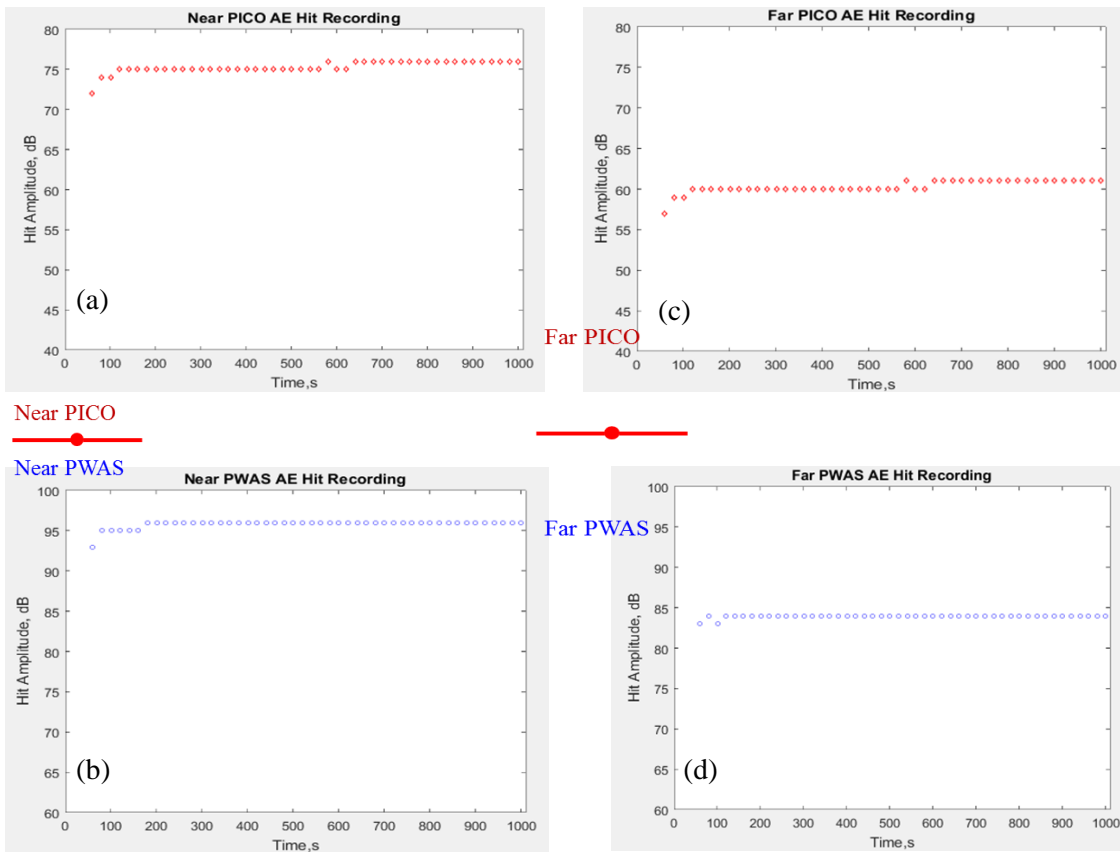


Figure 7.35 Group B AE signals captured by the four sensors: (a) near-field PICO, (b) near-field PWAS, (c) far-field PICO, (d) far-field PWAS.

7.5.6 EXPERIMENTAL RESULTS OF THE SEQUENCE-OF-ARRIVALS

From the experimental AE measurement, the group B AE signals were identified and plotted in Figure 7.35. The near-field PICO and PWAS captured the higher-amplitude AE hits than the far-field PICO and PWAS. The decrease in amplitude in the far-field sensors would give us a preliminary idea that these AE hits may be coming from the crack.

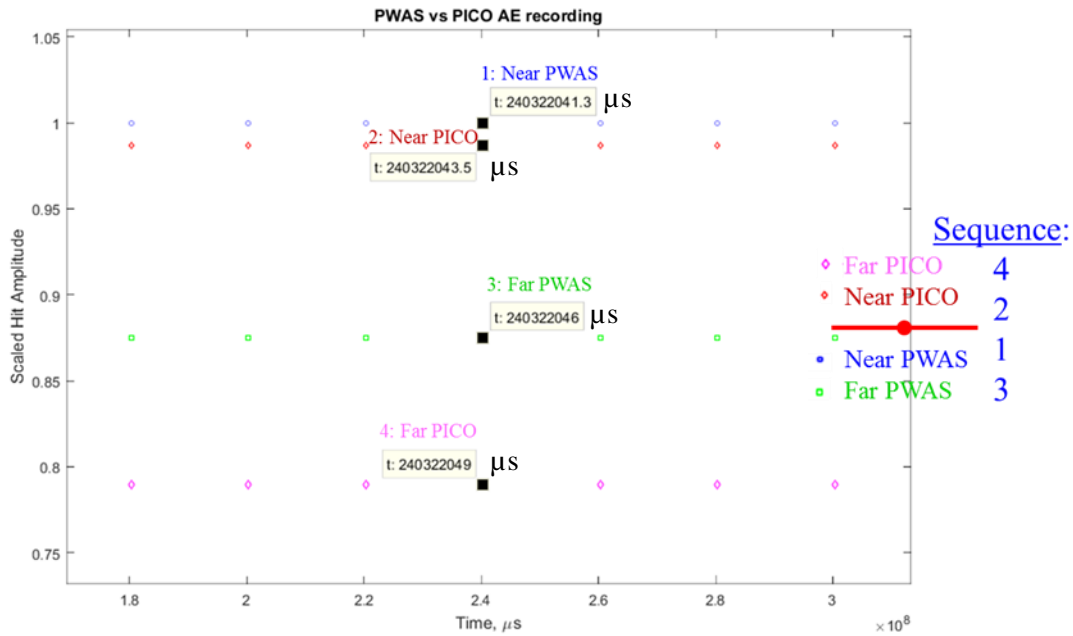


Figure 7.36 The four AE-hit plots of Figure 7.35 are overlapped together in a common timeline and zoomed-in a particular portion around 240 s. A particular AE event occurred around 240 s was captured by the four sensors. The actual time of arrival is stamped by these AE hits.

The four AE-hit plots are overlapped together on a common timeline. A particular portion (170 s to 310 s) of the overlapped plot is zoomed-in as shown in Figure 7.36. It shows that the same AE event at a particular time is captured by the four sensors. The time of arrivals of the AE signals were different since they were at different distances from each other. As an example, an AE event happened near 240 s is picked up and the exact time of arrival is shown in Figure 7.36 by the time stamp near the AE hits. The time of arrival is

shown in micro-second (μs) unit and all of them have the same global time of reference. It shows that the time of arrival for near-field PWAS is 240322041.3 μs , near-field PICO is 240322043.5 μs , far-field PWAS is 240322046 μs , and far-field PICO is 240322049 μs . Thus, experimentally measured SOA is found to be 4-2-1-3.

Hence, we conclude that the AE source is the crack.

Table 7.2 Source localizations for the different groups of AE signals

Group		A	B	C	D	E	F	G	H	Rogue
No. of AE hits (427)		53	50	89	8	154	43	15	6	9
Sequence of Arrival	Far PICO	4	4	4	4	4	4	4	4	-
	Near PICO	2	2	2	2	2	2	2	2	-
	Near PWAS	1	1	1	1	1	1	1	1	2
	Far PWAS	3	3	3	3	3	3	3	3	1
Source location		Crack	MTS Grips							

The same SOA was found to be true for all the AE hits (not shown here). This method was also examined for other groups of AE signals. For all of them except 9 AE hits, the same SOA was obtained from the experimental measurement of the time of flight and not discussed for the sake of brevity. These nine rogue AE hits were picked up by the far PWAS first, then the near PWAS. These were not picked up by the PICO sensors since they were on the other side of the crack. Hence, we conclude that these rogue AE hits were coming from the lower grip of the MTS. The complete summary of the sources of various groups of AE waveforms is shown in Table 7.2.

7.6 DISTINGUISHING CRACK GROWTH AND CRACK-RUBBING/FRETTING AE SIGNALS

The source localization analysis as discussed in the previous section concluded that, out of the 427 AE hits (from 300- μ m crack growth), 418 AE hits were coming from the fatigue crack and the remaining 9 AE hits were coming from the MTS grips (not related to crack). The waveform group analyses discussed earlier revealed that 418 crack-related waveforms can be further sorted into eight distinguishable AE waveform signatures (groups A, B, C, ..., H). The load level synchronization with the AE waveform in a common timeline allowed further separation of the AE signals. Some AE waveform groups occurred at relatively higher load level, such as groups A, B, C, D, G. These five groups occurred above 78% of the maximum load level (please see Table 7.1). These five groups totaled 215 AE waveforms. These groups may be responsible for direct extension (growth) of the fatigue crack.

The remaining three waveform groups (E, F, H) happened at relatively lower load level. For example, group E, F happened within 51-57% of maximum load level and group H happened at 23% of maximum load level. Another important feature of these lower load level AE signals was that they happened in a cluster. A sequence of 3-4 of these AE hits happened in every cycle. These AE hits may represent some kind of crushing, rubbing, fretting of the saw-tooth shaped fatigue crack faying surfaces. It seems that the faying crack surfaces are catching while the crack tends to open under the applied fatigue loading. These three groups totaled 212 AE waveforms which may be responsible micro-fracture events caused by the rubbing and fretting of the crack faying surfaces but may not be related to crack growth.

Several groups of AE waveforms related to crack growth may represent several crack growth mechanisms. The crack growth mechanism in relation to a particular waveform group should be considered in future investigations. Following the physics of materials based approach discussed in this chapter, the AE signals corresponding to longer crack growth (e.g. 10-mm long fatigue crack) may be separated into crack growth and crack-rubbing-fretting related AE signals based on the waveform signatures.

7.7 CONCLUSION

The physics of materials based analysis of AE signals may explain the complex phenomena of metal fatigue and crack growth. The AE-hit analysis currently used in AE practice may not be sufficient to capture detail fatigue crack growth mechanisms. The AE-waveform analysis may give a more comprehensive idea of the metal fatigue. In addition, we found that different types of AE sensors significantly affect the captured AE waveforms. Depending on the application, a certain type of sensor may be more suitable than others. It was found that PWAS transducers may be used to capture the fatigue crack generated AE signals from thin-wall structures. PWAS seems to capture richer frequency spectra than the commercial PICO and S9225 sensors. It is important to distinguish the fatigue crack-related AE signals from the rogue AE signals that may come from non-crack events. AE source localization confirmed the sources of the AE signals.

During fatigue crack growth, various AE waveform groups may be generated. These groups can be sorted based on the spectral signatures. During the fatigue crack growth in a thin metallic specimen, nine different AE waveform groups were observed. A particular waveform group represents a particular source of AE event related to the crack growth. The AE waveforms evolved with fatigue load level.

The fatigue crack extension, as well as the rubbing and fretting of crack faying surfaces, may generate AE signals. The AE waveform group sorting with load level synchronization may be used to distinguish the crack extension related AE signals from the rubbing/fretting AE signals. It was found that certain groups (A, B, C, D, G) were generated from the crack extension while other groups (E, F, H) were generated by crack rubbing and fretting. Micro-fracture events may occur during the crack rubbing and fretting of the crack faying surfaces which may generate AE signals in a clustered form. Some AE waveform groups happened at relatively lower load level (e.g. group E) and appeared as a clustered form. These waveforms may represent the “catching” of the crack faying surfaces.

CHAPTER 8

CAN WE HEAR CRACK LENGTH FROM ACOUSTIC WAVEFORMS?

In this chapter, we focus on analyzing the acoustic waveforms to extract the crack length information. This is an inverse problem and a challenging task. To accomplish the objective, we started with a proof-of-concept development. In this stage, we studied various parameters that could be related to the crack length. We performed 3D multiphysics simulation to visualize the wave propagation in presence of a crack in a plate. An acoustic emission (AE) event was simulated at the tip of the crack. The acoustic waves generated by the AE events and they propagated as guided waves in the plate. The guided waves along the crack faces showed some local vibration modes (crack resonance). A laser Doppler vibrometry experiment was performed to identify the crack resonance phenomenon and the experimental results were used to verify the simulated results [115].

8.1 INTRODUCTION AND STATE OF THE ART

The SHM and NDE researchers are always looking for new the techniques to assess the health of the structure [52], [155]–[157]. The acoustic emission (AE) technique of NDE/SHM has been used for structural defects detection for many years [81], [84], [96], [97], [125], [143], [158], [159]. The AE technique has a wide range of applicability such as the damage monitoring in the isotropic materials, anisotropic composites, and concrete structures [82], [94], [95], [104], [160], [161]. AE has been employed for various purposes such as damage source localization, characterization, crack growth monitoring, etc. [85],

[87], [162], [163]. It was observed that many AE methods just focus on the first few AE wave peaks. These few wave peaks examination gives limited information to extract a few parameters such as the AE wave amplitude, average frequency, time of arrival, and duration, etc. To understand the AE source mechanism, some finite element and analytical work has been reported [104] [164]. In fact, the complex nature of the AE wave generation, propagation, and interaction with the structural features makes the AE waveforms difficult to analyze.

In the past, efforts were made to retrieve the structural feature related information from the AE waveforms [125]. Gagar et al. [143] developed some correlations between AE signals generated during fatigue crack growth and corresponding cyclic loads to determine the crack length. Parametric relationship of AE and fracture mechanics to estimate the crack length in concrete structures was reported by Sagar et al. [165]. However, these methods predominantly rely on experimental data-driven statistical models to understand the AE signatures. To successfully extract more information from the AE events due to fatigue crack growth, it is important to analyze the AE waveforms and to find any clue on estimating the crack length information.

The present study addresses fatigue crack length estimation based on the AE waveform analysis. FEM simulations and experimental results are presented.

8.2 3D FEM SIMULATION OF AE WAVEFORM GENERATION AND CRACK RESONANCE

A 3-D FEM time-domain simulation was performed. The details of the FEM simulation method were described in Chapter 6. Here, the key features of this particular FEM model are briefly reviewed. The illustration of the 3-D FEM modeling is shown in

Figure 8.1. A 10-mm fatigue crack was modeled in a 100 X 100 mm² square plate-like model of thickness 1-mm. The material properties of the aluminum 2024-T3 specimen were chosen to be $E = 73.1\text{GPa}$, $\nu = 0.33$, $\rho = 2780\text{kg/m}^3$ with $c_s = 3140\text{m/s}$. The AE source at the crack tip was modeled using the extended dipole concept as detailed in Chapter 6.

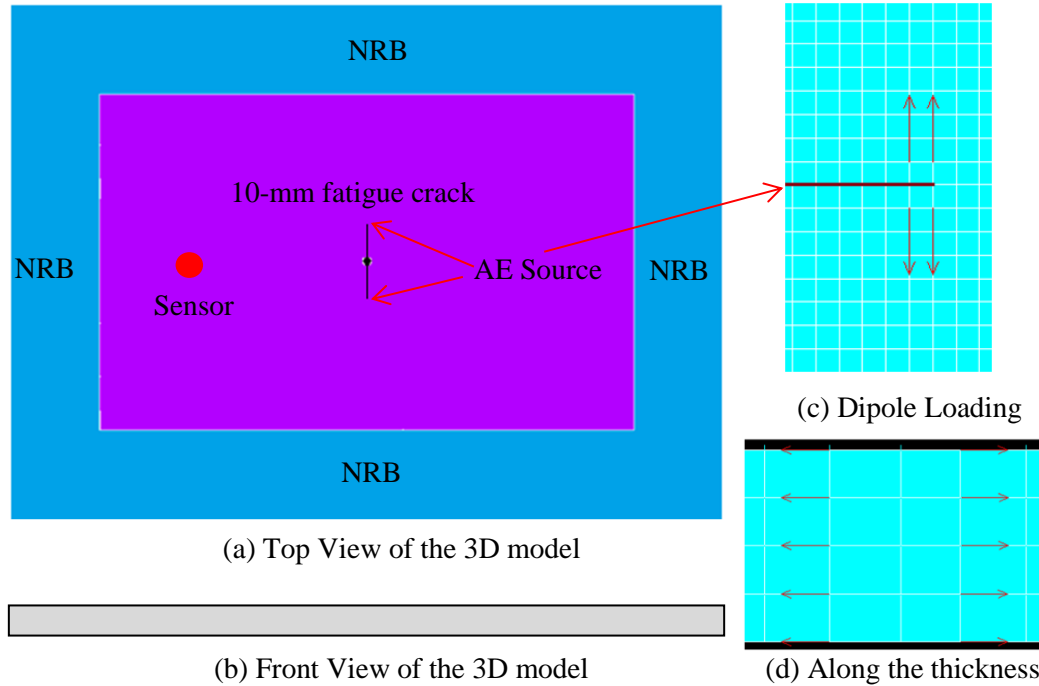


Figure 8.1 3-D FEM model for harmonic analysis (a) top view (b) front view (c) dipole loading at the crack tip (d) line load along the thickness

Non-reflective boundary (NRB) was used in the FEM model to avoid the wave reflections from the model edges. The criteria for accurate FEM results given in ref. [102] were implemented: $\lambda_m / c_s \geq 15$, $D / s \geq 7$, and $\lambda_m / s \geq 5$, where, λ_m be the minimum wavelength, c_s be the cell size in the FEM model, D is the distance between the source and the sensing location, s is the source size. The minimum wavelength λ_m is defined as $\lambda_m = c_s / f$, with c_s being the shear wave speed and f being the maximum frequency. With

these parameters, the FEM simulation can accurately predict the results for the frequency range of up to 840 kHz with $D/s = 100$.

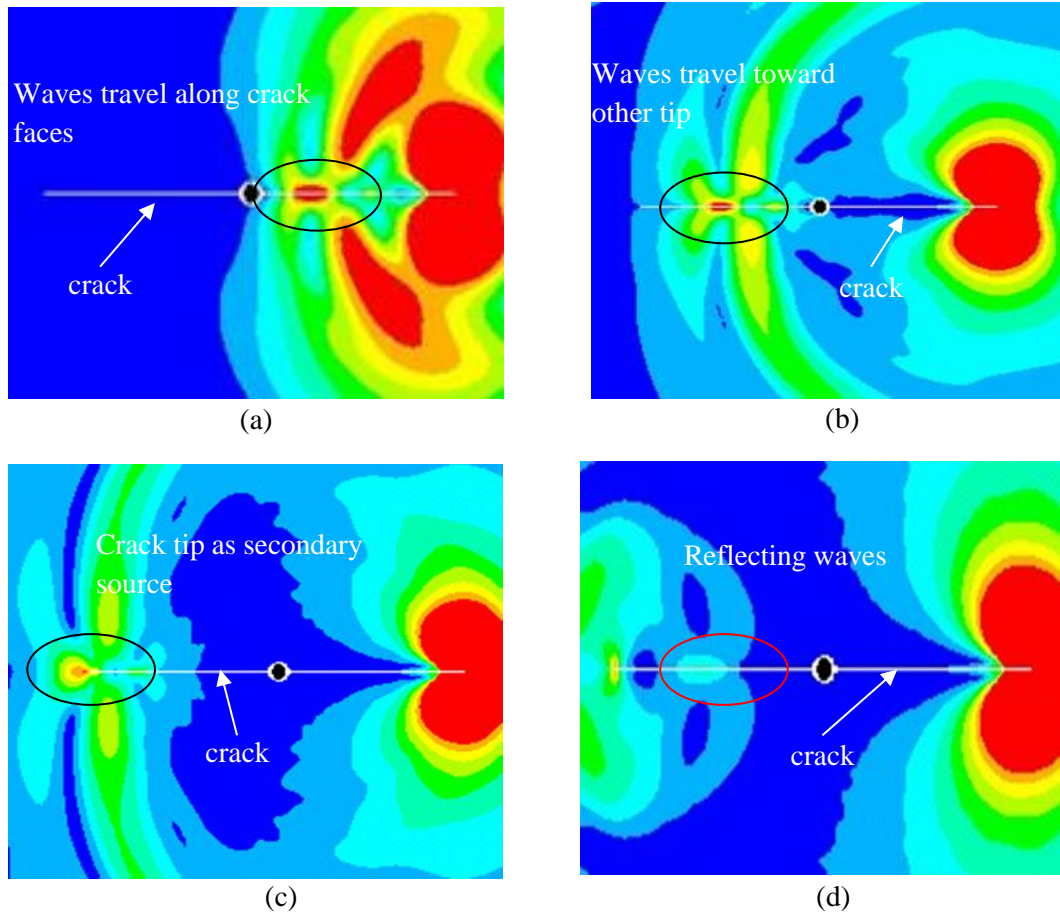


Figure 8.2 Animation snapshots of transient FEM simulation as the time progress (a) $t = 1.5 \mu s$, (b) $t = 3 \mu s$, (c) $t = 3.9 \mu s$, (d) $t = 4.8 \mu s$

Animation snapshots of the transient FEM simulation are presented in Figure 8.2. The acoustic wave emitted at one crack tip travels along the crack faces. When the waves hit the other tip of the crack, it generates secondary waves. The reflected waves travel back along the crack faces. This may cause crack resonances.

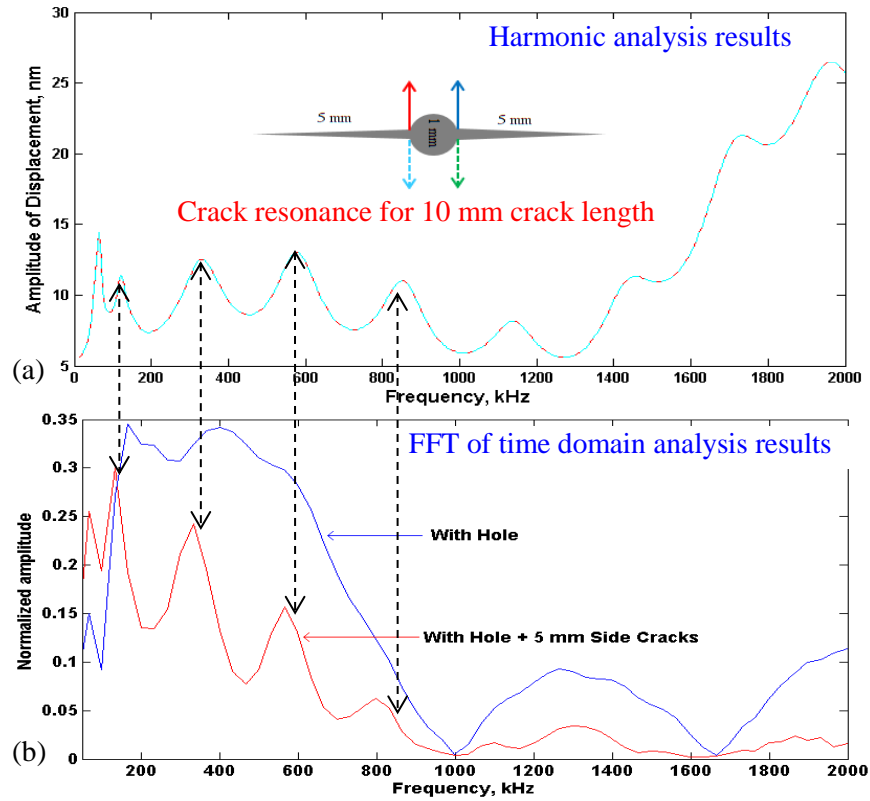


Figure 8.3 FEM simulation results for (a) the crack resonance captured at the mouth of the crack in harmonic analysis, (b) comparison between FFT of AE waveform of the hole and hole+10 mm crack (sensing at 20 mm away from the hole) in transient analysis [166].

Harmonic FEM analysis of the 3-D model was performed by my colleague Dr. Poddar [166]. Harmonic FEM simulation was performed for a plate with a hole + two 5-mm butterfly cracks. The harmonic FEM results are illustrated in Figure 8.3. The crack opening displacement at the mouth of the crack was recorded over the wide frequency band as shown in Figure 8.3a. This also showed that the crack opening resonances occurred at regular frequency intervals. Although the results were shown for a wide range of frequencies, the results of interest were up to 1000 kHz where most of AE signal frequency content was available.

Transient analysis of the same model showed the similar frequency spectra of the displacement responses for the two situations as illustrated in Figure 8.3b. This showed

that the AE signals are modified by the presence of the crack. This gave us an indication that the geometry of the crack may also be estimated from the recorded AE signals. The length of the crack is directly related to the resonance frequencies of the crack. It is also interesting to note that the resonance phenomena captured at the mouth of the crack in harmonic analysis were similar to that captured at 20 mm away from the crack in transient analysis. The comparison between the frequency peaks is illustrated by the dotted lines.

8.3 EXPERIMENTAL VERIFICATION OF CRACK RESONANCES

The finite element simulation results suggest that the fatigue crack resonates during an AE event. A laser Doppler vibrometer (LDV) experiment was performed to verify this hypothesis. The experimental setup is shown in Figure 8.4. A 1 mm thick 2024-T3 aluminum plate with 1.2 m x 1.2 m dimension was used. The large size of the specimen was used to avoid the plate edge reflections. A 16 mm long through thickness slit was made to simulate a fatigue crack. Two 7 mm diameter circular PWAS transducers were mounted as excitation sources at the tip of the slit on opposite faces of the plate.

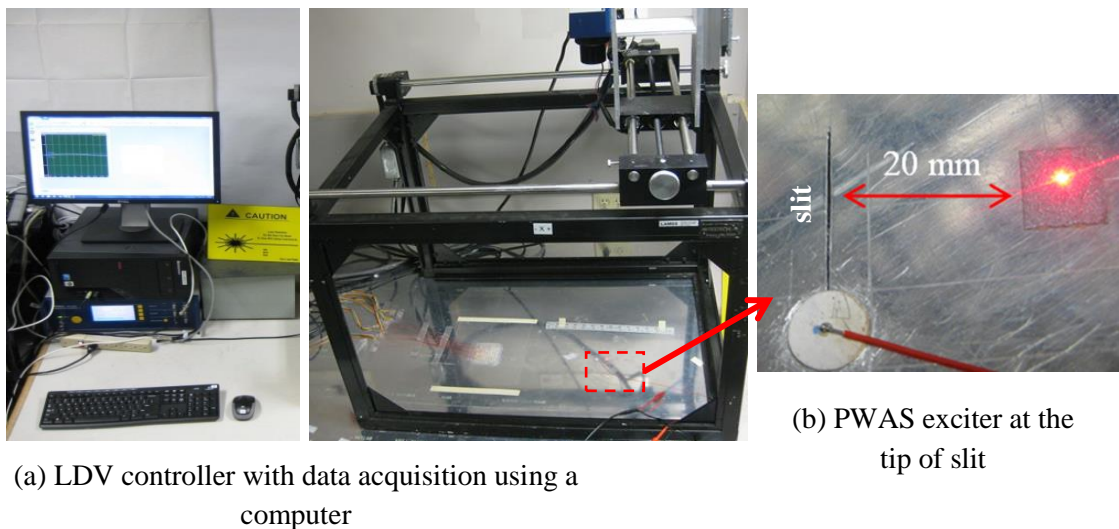


Figure 8.4 Laser Doppler Vibrometer (LDV) experimental setup

A single count tone burst signal of a center frequency of 350 kHz was used to excite the sensors placed at the crack tip. The reason for choosing the single count tone burst signal was to achieve a wider band in the frequency (up to 800 kHz). To correctly simulate an AE signal at the crack tip, the frequency content of the PWAS excitation at the crack tip should cover the entire frequency range of the actual AE waveform. LDV measured the out-of-plane vibration velocity of the plate surface at 20 mm away from the crack.

The out-of-plane velocity of a point at 20 mm away from the center of the crack was measured by LDV. Fourier transform of the time domain signal was used to obtain the frequency spectrum of the signal as shown in Figure 8.5. Several peaks are clearly identified and labeled in the frequency spectrum. Evidently, these peaks represent the frequencies for which the out-of-plane velocity reaches a maximum.

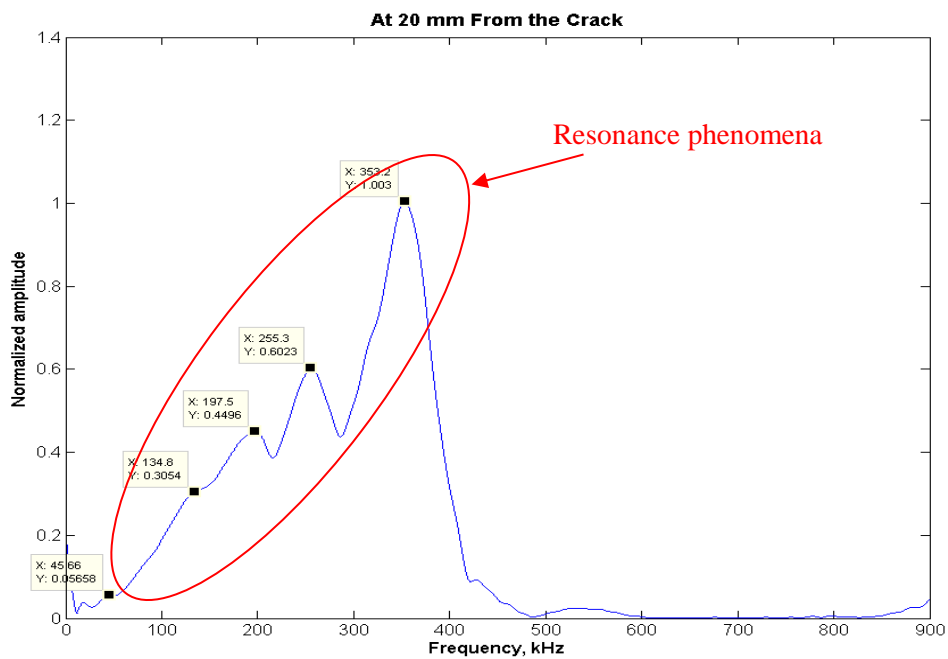


Figure 8.5 LDV experimental results (out-of-plane velocity) measured at 20 mm away from the slit. The resonance frequencies are labeled in the frequency spectrum [167].

Comparing the experimental data with the FEM simulation results, we can see that both results were able to capture several resonances of the crack. However, the amplitude trend is increasing with frequency in the experiment while the opposite happened in the simulation. The reason is the excitation signal in the experiment was tone burst which has a higher amplitude near the center frequency while in the FEM simulation, the excitation was a cosine bell step function which has higher amplitudes in the lower frequencies. This may explain why the trend in the amplitude of the frequency response curve from the two results is not directly comparable. Nonetheless, in both experiment and FEM simulation, some frequency peaks caused by the crack resonance were observed within the AE frequency band.

8.4 SUMMARY AND FINDINGS

The AE waveform generated from the crack tip may interact with the crack itself and cause crack resonance. Transient and harmonic analyses were carried out using a 3-D FEM model to simulate the AE wave generation, propagation, and its interaction with a fatigue crack. Both analyses confirm the local crack resonance phenomena due to the interaction between AE waveform and fatigue crack and showed that they are related to the crack length. LDV experiments were conducted to verify the computational results. Both experimental and simulation results suggested that the AE waveform may be used for determining the fatigue crack length.

CHAPTER 9

TWO CASE STUDIES

This chapter discusses the two case studies that were performed on a metallic stiffened structure and on a carbon fiber composite structure by using a combination of active and passive SHM as well as using commercial ultrasonic NDI equipment. A more realistic scenario was considered in these case studies as discussed next [168], [169].

9.1 CASE STUDIES #1: ACTIVE SHM FOR HORIZONTAL CRACK DETECTION, SIZE, AND SHAPE ESTIMATION IN STIFFENED STRUCTURES

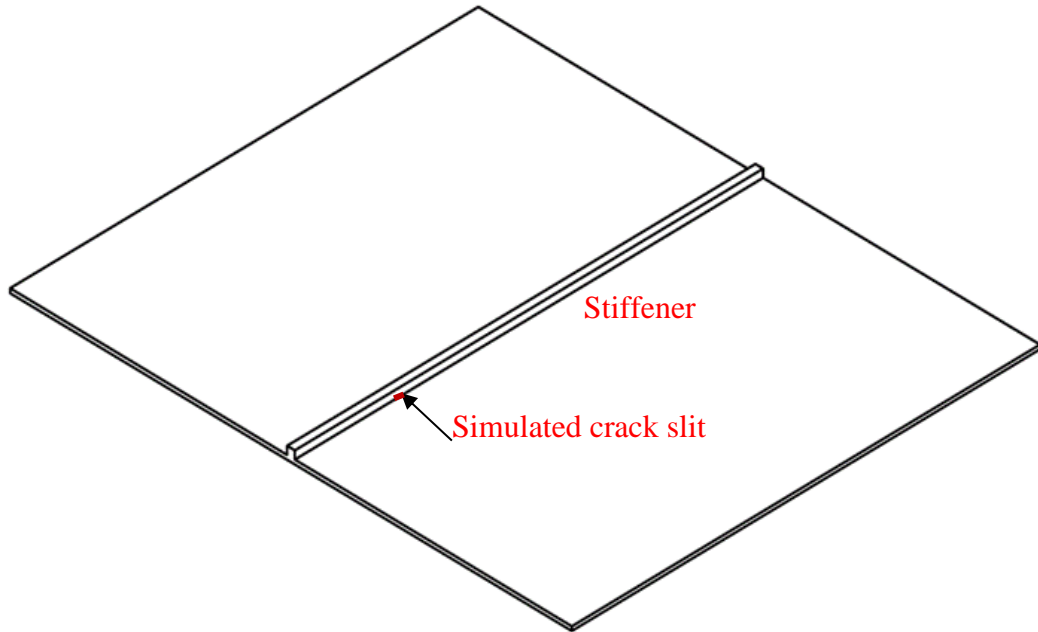
9.1.1 OBJECTIVE

In the past, simplistic structures were often considered for analyzing the guided wave interaction with defects. In this study, we focused on more realistic and relatively complicated structure for detecting defects by using a non-contact sensing approach. A plate with a stiffener was considered for analyzing the guided wave interactions as shown in Figure 9.1. PWAS transducers were used to produce excitation in the structures. The excitation generated multimodal guided waves (aka Lamb waves) that propagate in the plate with stiffener. The presence of stiffener in the plate generated scattered waves. The direct wave and the additional scattered waves from the stiffener were experimentally recorded and studied. These waves were considered as a pristine case in this research. A simulated horizontal semi-circular crack was manufactured in the stiffener using electric discharge machining in the same stiffener. The frequency was chosen to be 200 kHz based on our separate study on the frequency domain [170].

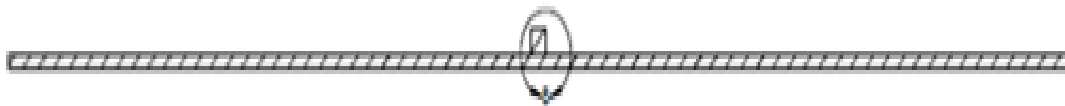
The presence of the crack in the stiffener produces additional scattered waves and trapped wave modes. These scattered waves and trapped wave modes from the cracked stiffener were experimentally measured by using a scanning laser Doppler vibrometer (SLDV). These waves were analyzed and compared with those from a pristine specimen. The analyses suggested that both size and shape of the horizontal crack may be predicted from the pattern of the scattered waves. Different features (reflection, transmission, and mode-conversion) of the scattered wave signals were analyzed. We found that the direct transmission feature for incident A0 wave mode and the mode-conversion feature for incident S0 mode are most suitable for detecting the crack in the stiffener. The reflection feature may give a better idea of sizing the crack.

9.1.2 MANUFACTURING OF THE PLATE WITH STIFFENER

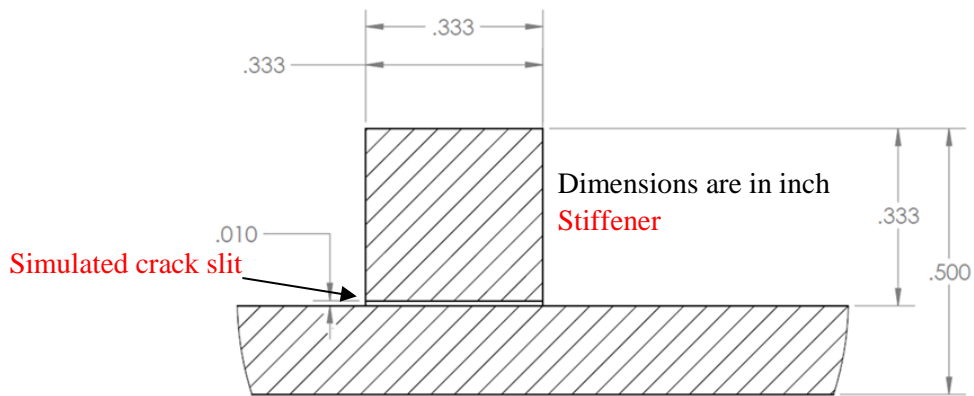
The manufacturing of the plate with stiffener was a little bit tricky and worth discussing with the readers. An aircraft grade aluminum 6061 material was used to manufacture the plate specimen. A 24-in by 24-in square plate with an initial thickness of 0.5 inches was used. In order to make a continuous stiffener in the mid-section of the plate, a milling process was carried out on the entire plate except for a the stiffener portion. The milling process was carried in several iterations to remove one-third of an inch of materials from the plate. This process gave a continuous stiffener on the plate. Thus, the stiffener was an integral continuous part of the plate.



(a) Isometric view of the plate with stiffener



(b) Side view of the plate with stiffener



(c) Zoomed-in view of the stiffener with dimension

Figure 9.1 Geometric dimension of the plate with stiffener used for manufacturing.

The isometric view of the plate with stiffener is shown in Figure 9.1a. The side view of the plate is shown in Figure 9.1b. The dimension of the stiffener was 0.333 inches thick, 0.333 inches wide and 20 inches long. After the milling process, the plate thickness

was 0.167 inches everywhere. A small half-penny-shaped simulated crack was then manufactured at a certain location (6 inches from the plate edge) of the stiffener. Practically, a slit of a finite dimension had been made by using a ram electric discharge machining (EDM). Since the thickness of the slit was very small (0.01 inch, about 3% of the stiffener thickness), it may be referred to as a “crack” for ultrasonic applications. This very thin slit may exhibit similar ultrasonic wave scattering behavior as a crack of similar dimension. The diameter of the penny-shaped crack was 0.333 inches.

9.1.3 EXPERIMENTAL SETUP

A test plan was made for the guided wave crack detection of the plate with stiffener using a non-contact sensing approach. A schematic diagram of the test plan is illustrated in Figure 9.2. The plate was sub-divided into two sections. One section contained the half-penny-shaped crack and the other section had no crack. The section that contains the crack is hereafter referred to as “cracked” and the section without crack is hereafter referred to as “pristine”.

Two PWAS transducers were used as transmitters in each section of the plate. These PWAS transducers were bonded back to back on the opposite surfaces of the plate. This was performed by careful measurement of the transmitter location since both of them have to be bonded at the same location: one at the top and other at the bottom of the plate. These PWAS transducers were used to excite the structure with a selective type of Lamb wave modes (S_0 and A_0).

A wave-absorbing clay boundary was used around the plate to minimize the wave reflections from the plate edges. This wave absorbing boundary was applied very carefully by maintaining a linearly varying thickness profile from inner edge to outer edge of the

boundary. In the past, it was found that a linearly varying profile of the wave absorbing boundary successfully minimized the edge wave reflections. This allowed us to analyze the wave signals that are solely from the stiffener and the crack.

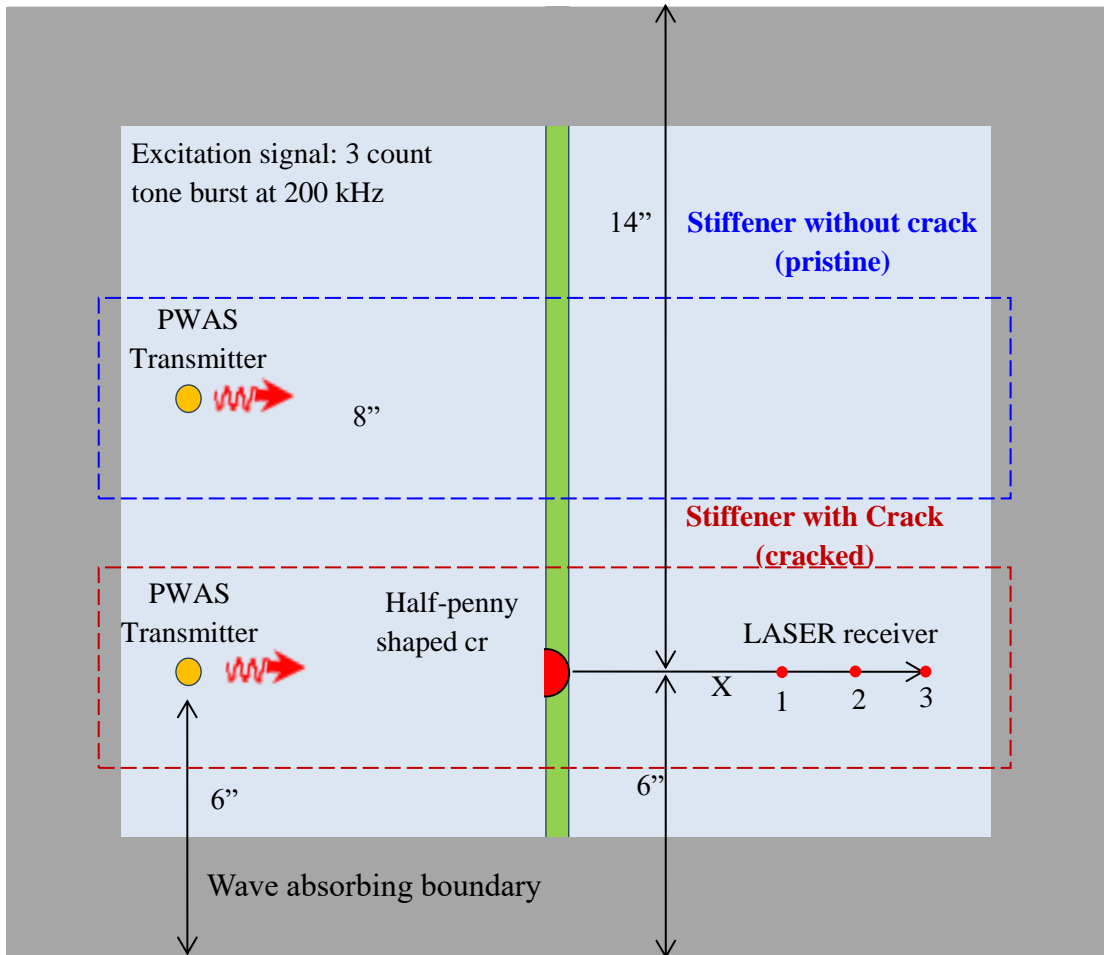
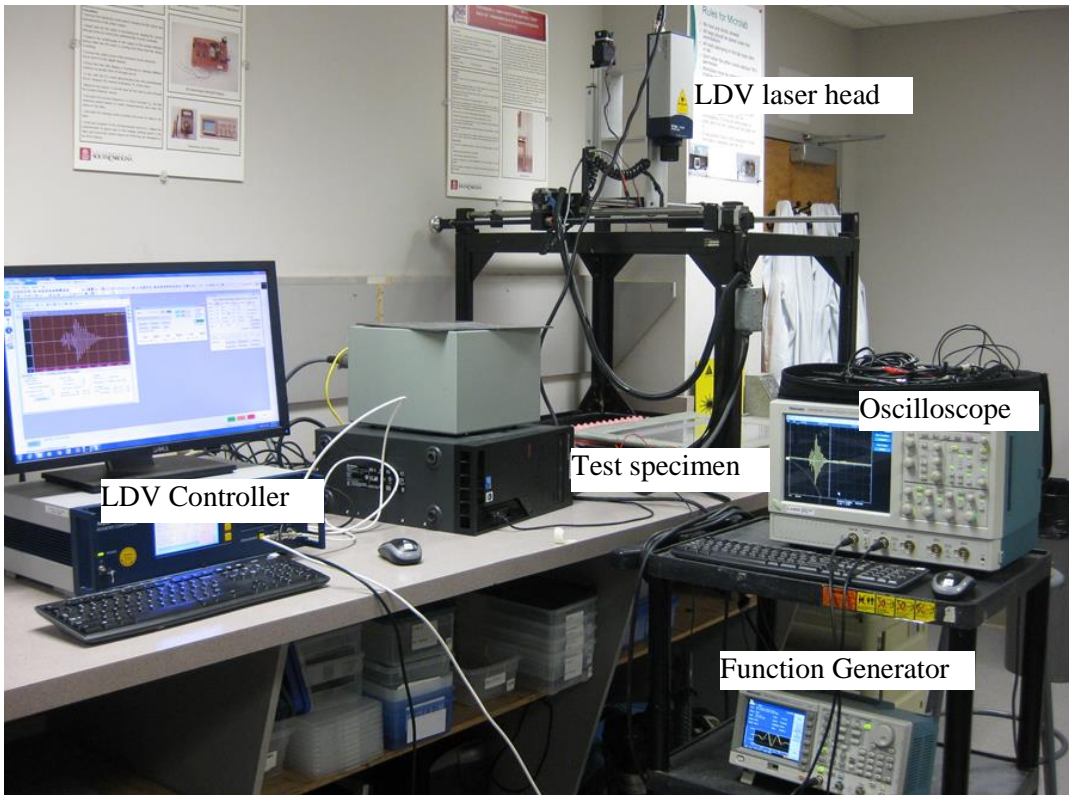
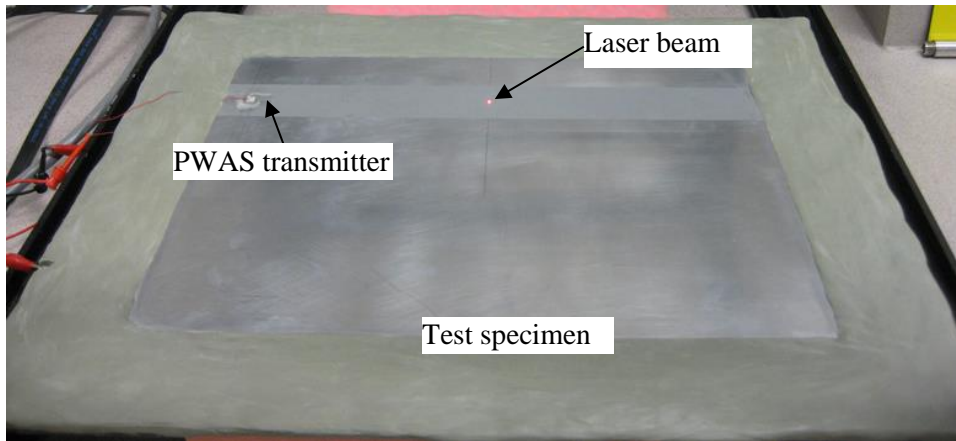


Figure 9.2 Test plan for the ultrasonic inspection of the plate to detect crack in the stiffener using non-contact laser measurement.



(a)



(b)

Figure 9.3 (a) Experimental setup for scanning using laser Doppler vibrometer (LDV), (b) The test specimen with a laser beam at the center of the scanning area.

Laser Doppler vibrometry (LDV) was used in this experiment as a non-contact sensing methodology. A laser receiver had been used to capture the waveforms at different locations. The experimental setup is illustrated in Figure 9.3a. It is worthwhile discussing

the working principle of the LDV briefly. In LDV, a laser beam is directed to a certain location of the plate specimen and the reflected laser beam is compared with an internal reference beam. The out-of-plane motion of the surface changes the frequency and phase of the reflected beam which is measured by an interferometer. The out-of-plane velocity is measured by using the Doppler shift in frequency of the reflected laser beam. This process is internal to the LDV instrument. In our experiments, the laser beam was directed at desired locations by using a motion controller (model: gantry x-y controller). The laser head was kept at a fixed height from the plate (about 32 inches).

The laser measurements were performed over an area by using a suitable discretization. Out-of-plane velocity measurements at certain fixed locations (1, 2, 3 in Figure 9.2) were also performed. The test specimen with a laser beam is shown in Figure 9.3b. A very thin reflective tape was used to improve the signal-to-noise ratio of the laser measurement.

9.1.4 RESULTS AND DISCUSSIONS

The laser scanning was performed over an area of 15 inches by 2 inches. Both S_0 and A_0 Lamb wave modes were excited by the PWAS transducers.

9.1.4.1 *Wavefield Analysis for Crack Detection, Shape and Size Estimation*

The laser measurement results for the pristine and cracked stiffener with S_0 Lamb wave excitation are illustrated in Figure 9.4a and Figure 9.4b, respectively. In case of the pristine stiffener, one sees waves reflected by the stiffener and waves transmitted through the stiffener. Both the reflected and transmitted waves maintain a straight-crested wavefront.

For the cracked stiffener, waves reflected from the stiffener and transmitted through the stiffener also exist. In addition, there are reflected and transmitted waves associated

with the crack in the stiffener. Thus, the straight-crested nature of the reflected and transmitted waves is broken. Interestingly, the straight-crested nature in the reflected waves is broken more than in the transmitted waves as observed from the wavefield shown in Figure 9.4b.

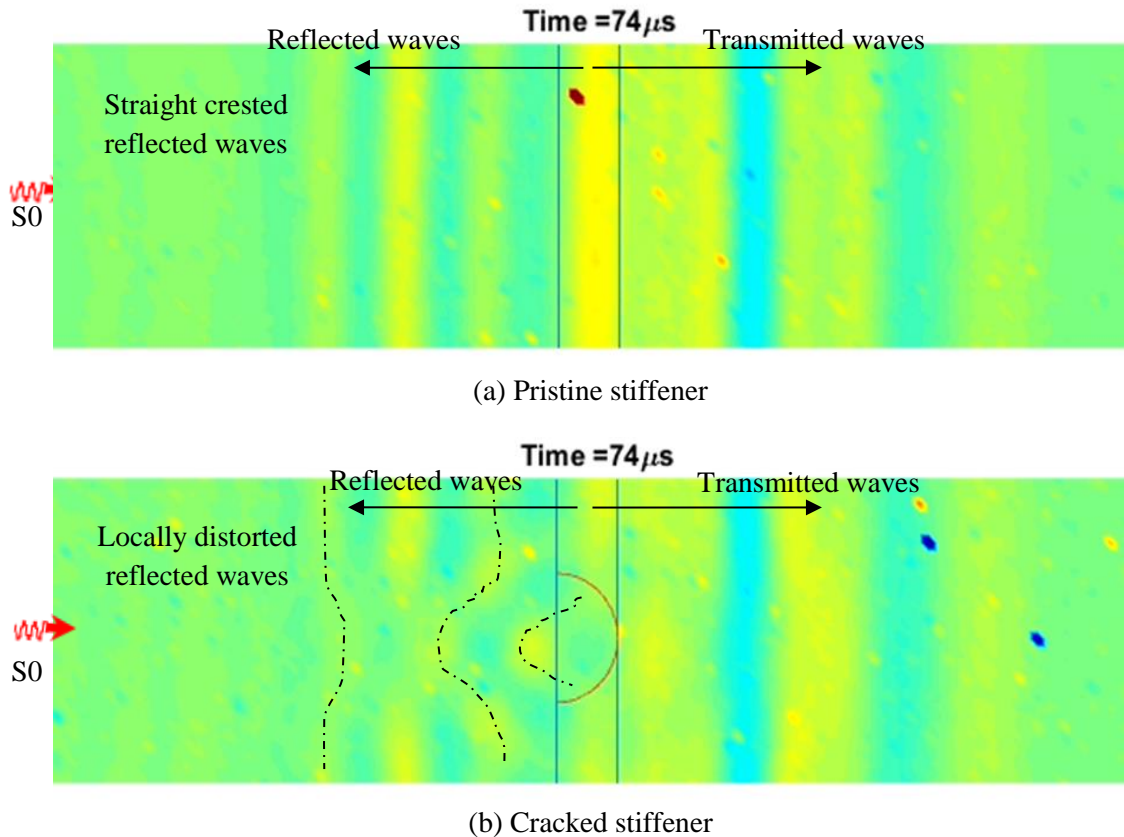


Figure 9.4 LDV scanning results for comparison of the wavefield due to the pristine and cracked stiffener. In both cases, S0 Lamb waves are incident waves. The wavefields are captured at the same time of 74-μs. (a) The wavefield due to the pristine stiffener: reflected and transmitted waves are straight-crested waves, (b) the wavefield due to the cracked stiffener: reflected and transmitted waves are no more straight-crested waves; trapped wavemodes are generated within the half-penny-shaped crack; the effect of crack is carried by the propagating waves in the plate.

In addition, trapped wave modes exist within the half-penny-shaped crack. The trapped waves are originated from multiple reflections within the semi-circle boundary of the crack which is the line of discontinuity. The back and forth motion of the trapped waves

may produce additional waves that can travel on the reflected and transmitted sides of the stiffener.

The shape of the crack can be visualized from the wavefield isolines (isoline - line with equal signal amplitude and phase) of the as shown by the dotted lines in Figure 9.4b. In addition, the size of the deformed isoline is pretty much similar to the size of the crack. It is interesting to note that these isolines deformed more on the reflection side than the transmission side of the stiffener.

9.1.4.2 *Waveform analysis for Incident A0 Lamb Waves*

In SHM, it is important to study the propagating wavemodes that give an idea how far the effect of the crack can be detected. In other words, by studying this effect one can predict how far off one can put sensors to detect the crack in the stiffener.

The transmitted wave packets due to A0 incident Lamb wave are illustrated in Figure 9.5. It shows the comparison between the pristine case and cracked case. Three waveforms are captured at three different locations such as 4.2, 4.6, 4.8 inches from the stiffener. It can be observed that the amplitude of the transmitted A0 wave packet is a distinguishing factor between the pristine and cracked cases. The amplitude of the transmitted A0 packet is increased in each of the signal obtained from cracked stiffener. Since this is a horizontally oriented crack, the A0 waves find an easier path to go directly through the plate with less interruption in the crack area of the stiffener.

At a shorter distance from the stiffener, it would be much stronger signals. As the distance becomes larger, the geometric spreading of the waves causes lower amplitudes. Despite that, we observed that at about 5 inches away from the stiffener, we can clearly see the difference between the pristine and cracked signals.

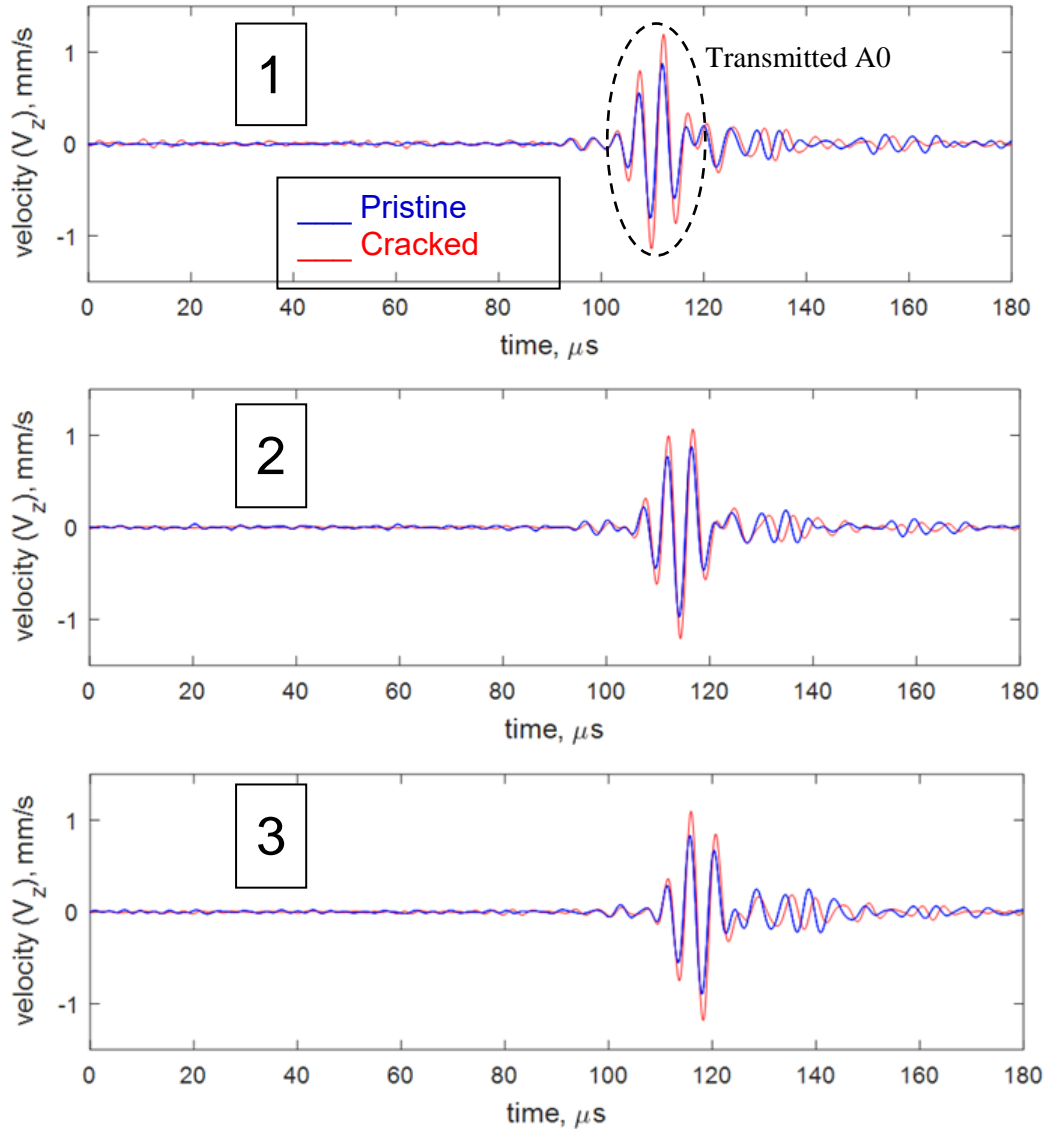


Figure 9.5 Transmitted waveform comparison between pristine and cracked stiffener due to A0 incident Lamb wavemode. The waveforms are captured at three different locations on the transmission side as marked by 1, 2, 3 in Figure 9.2. The points 1, 2, 3 are located at 4.2, 4.6, 4.8 inches from the stiffener. Due to the presence of a horizontally oriented crack, more transmission of A0 mode is observed.

9.1.4.3 Waveform Analysis for Incident S0 Lamb Waves

The transmitted wave packets due to S0 incident Lamb wave are illustrated in Figure 9.6. It shows the comparison between the pristine and cracked cases. Three waveforms are captured at three different locations such as 4.2, 4.6, 4.8 inches from the stiffener. It can be observed that the amplitude of the first S0 packet is more or less same

for pristine and cracked stiffeners which was not the case for incident A0 as discussed earlier.

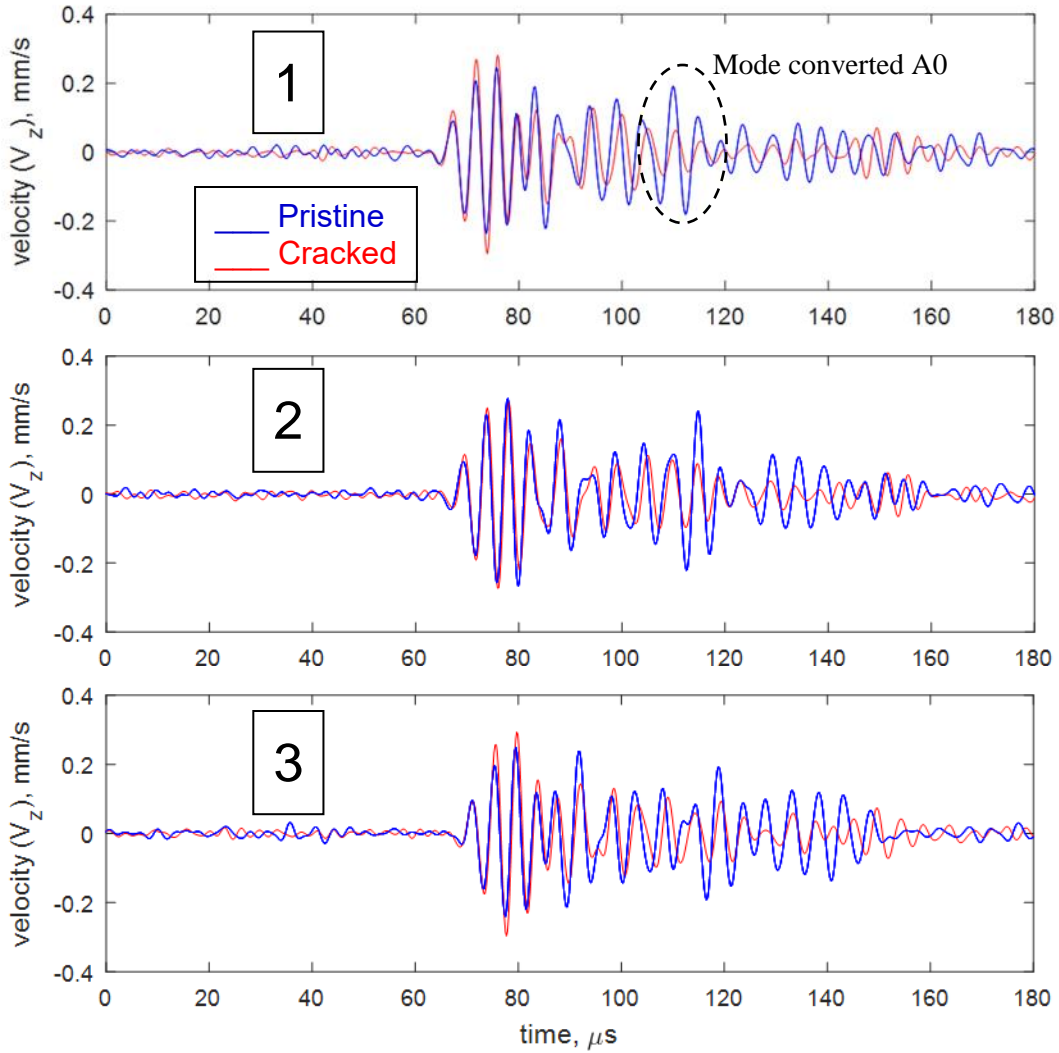


Figure 9.6 Transmitted waveform comparison between pristine and cracked stiffener due to S0 incident Lamb wavemode. The waveforms are captured at three different locations on the transmission side as marked by 1, 2, 3 in Figure 9.2. The points 1, 2, 3 are located at 4.2, 4.6, 4.8 inches from the stiffener. Due to the presence of horizontally oriented crack, less mode-conversion of the S0 model is observed.

For S0 incident wave, it can be observed that mode conversion is the distinguishing factor between the cracked and pristine signal. For cracked stiffener, there is less mode conversion (from S0 to A0) than for the pristine stiffener. The stiffener is the source of

asymmetry in the plate, which causes the mode conversion from S_0 to A_0 . Since the crack is oriented horizontally, producing a semi-circular discontinuity, the S_0 waves experience less mode conversion in this area. The crack area in the stiffener eases the path of S_0 wave propagation without being mode converted from the stiffener.

At a shorter distance from the stiffener and in the reflection side of the stiffener, there would be much stronger distinguishing signals between the pristine and cracked stiffeners. The transmission side is less sensitive than the reflection side. Despite that, we still clearly see the difference between the pristine and cracked signals when we look at the appropriate distinguishing features (mode conversion in this case) at about 5 inches away from the stiffener.

9.1.5 SUMMARY AND FINDINGS

A more complicated, but realistic structure has been used for the experimental study of ultrasonic guided Lamb wave interaction with structural damage. A plate with a pristine stiffener and the same plate with a horizontal half-penny-shaped crack in the stiffener were studied. The presence of crack in the stiffener produces additional scattered waves and trapped waves. These scattered waves and trapped waves were experimentally measured by a scanning laser Doppler vibrometer (SLDV). The scattered waves from the pristine stiffener and cracked stiffener were analyzed and compared. The analyses suggested that both size and shape of the horizontal crack in the stiffener may be predicted from the pattern of the scattered waves. In addition, we found that certain features of the scattered waves may be more suitable than others. Identification of an appropriate feature of the scattered waves may provide better information of the damage. For instance, in this experiment, the direct transmission feature may be used to detect the crack for incident A_0 Lamb wave.

The mode-conversion feature may be used to detect the crack for incident S0 Lamb wave.

The reflection feature may be used to determine the shape and size of the crack.

9.2 CASE STUDIES #2: SHM AND NDE OF A MANUFACTURED COMPOSITE PLATE

9.2.1 OBJECTIVE

In this case study, we focus on composite structures which possess more complexity in the guided wave propagation because of anisotropic behavior of composite materials. Aircraft structures often experience impacts from many different sources, for example, bird-strike, airport debris, flying objects. A composite plate was manufactured by using compression molding process with proper pressure and temperature cycle. Eight layers of woven composite prepreg were used to make the plate. The pristine composite plate is inspected by using a phased array based nondestructive tool (Rollerform). An area scan is performed to monitor any internal manufacturing flaws in the pristine plate. Relatively higher number of elements (64) with high frequency (3.5 MHz) phased array probe is used to detect any smaller defects during the manufacturing. The signatures of the wave signals show a minimal amount of defects in the plate. This NDE scanning process confirmed that there was no additional source of scattered waves inside the composites. The composite plate was then used for more practical application i.e. impact detection and localization. An SHM technique is implemented with PWAS transducers to detect and localize the impact on the plate. The guided acoustic waves generated from the impact travel in the plate and are recorded by two clusters of sensors. The acoustic signals are then analyzed using a wavelet transform based time-frequency analysis. The proposed SHM technique

successfully detects and localizes the impact event on the plate. The experimentally measured impact locations are compared with the actual impact locations.

9.2.2 COMPOSITE PLATE MANUFACTURING USING COMPRESSION MOLDING PROCESS

Polyphenylene Sulfide (PPS) fabric prepreg from TenCate Cetex was used to manufacture a thermoplastic composite (TPC) plate. The PPS prepreg was a pre-consolidated reinforced laminate with continuous woven carbon fibers. The prepreg was first cut from a big roll of fabric according to the desired shape (square in this case) with a dimension of 305 mm by 305 mm (12 inches by 12 inches) as shown in Figure 9.7. Each cutting section served as a layer.



Figure 9.7 Cutting and laying up the PPS prepreg fabrics according to the desired size

Eight layers of woven fabric were stacked up to form a laminate. Proper personal safety equipment such as gloves and safety glasses are always recommended during handling the carbon fibers.

9.2.2.1 Laminate Preparation

The eight-layer laminate was placed between two flat platens of a hot press as shown in Figure 9.8. Two thin protective films of plastics with a very high melting point

were used on top and bottom of the stack up. The protective films should be about 6 inches bigger in all around the fabric laminate to accommodate any extra resin flow during the curing process. These films (1) protected the platens from resin sticking up, (2) maintained a uniform flow of resin during the curing process, (3) helped to remove the plate from the platen after the curing process.

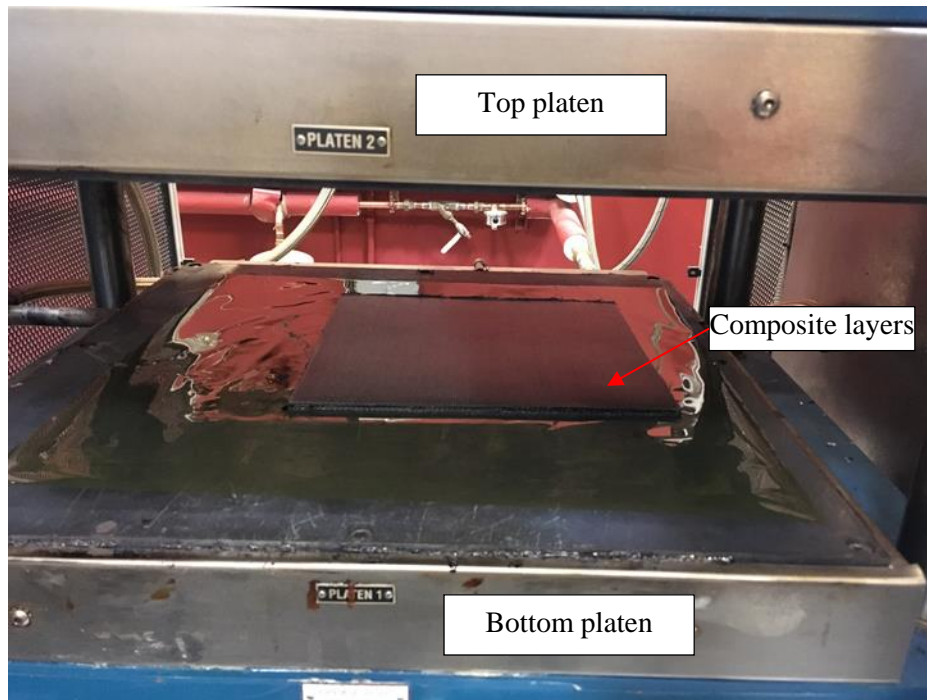


Figure 9.8 Composite layers are placed in the hot-press machine to apply heat and pressure

9.2.2.2 Curing Process in the Hot-Press

The melting temperature of the PPS fabric is 536⁰F. Hence, a cure cycle must contain a temperature higher than the melting point for proper melting and flow of the resin.

Figure 9.9 shows a standard cure cycle used for this laminate. A constant pressure of 150 psi was applied during the cure cycle.

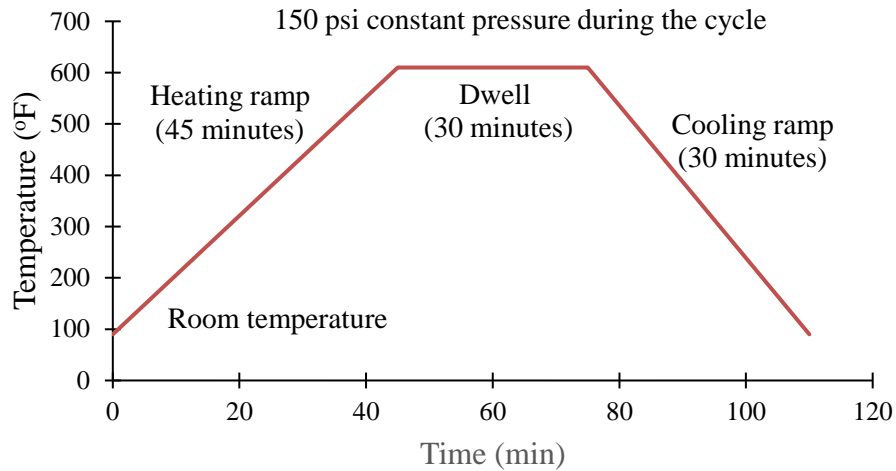


Figure 9.9 Cure cycle for the PPS prepreg



Figure 9.10 Final composite plate after cutting the extra resin flow around the plate

Heating was adjusted in the hot-press machine for raising the laminate temperature to 610⁰F within 45 minutes. Then the temperature of the laminate dwelled at 610⁰F for 30 minutes. At the end of dwell time, the laminate was air cooled from 610⁰F to room temperature in 30 minutes.

After the cure cycle completed in about 2 hours, the laminate was taken out from the platen. The extra resin flow at the edges of the laminate was trimmed. Figure 9.10

shows the final composite laminate after the trimming process. The resulting plate had a thickness of 1.6-mm. The dimension of the final composite plate was 387 mm by 276 mm (11.3 inches by 10.9 inches). The manufactured composite plate was then tested nondestructively as discussed next.

9.2.3 NONDESTRUCTIVE INSPECTION (NDI) OF COMPOSITE PLATE USING PHASED ARRAY ROLLER FORM

An ultrasonic nondestructive inspection (NDI) was performed on the manufactured composite plate. The purpose of this NDI was to verify if there is any major flaws, delamination or defects during the manufacturing process. An ultrasonic scanning was performed on the plate, which can detect defects or delamination across its thickness. The Olympus OmniScan instrument and Rollerform were used to inspect the composite specimen. The Olympus Rollerform is a phased array wheel probe designed for C-scan inspection of the aerospace composite, aluminum panels, and similar components. This device can be used to detect internal porosity, detect and size delaminations and other types of defects.

9.2.3.1 *NDI Experimental Setup*

The Olympus Rollerform sends ultrasonic waves through the plate and then receive the reflected signals through a phased array system. It records the signals from the entire inspection area through a data acquisition system. The Olympus OmniScan instrument processes these signals to generate A-scan, C-scan, and S-scan representations. These plots help visualize, analyze, and measure the results using the OmniScan MXU software.

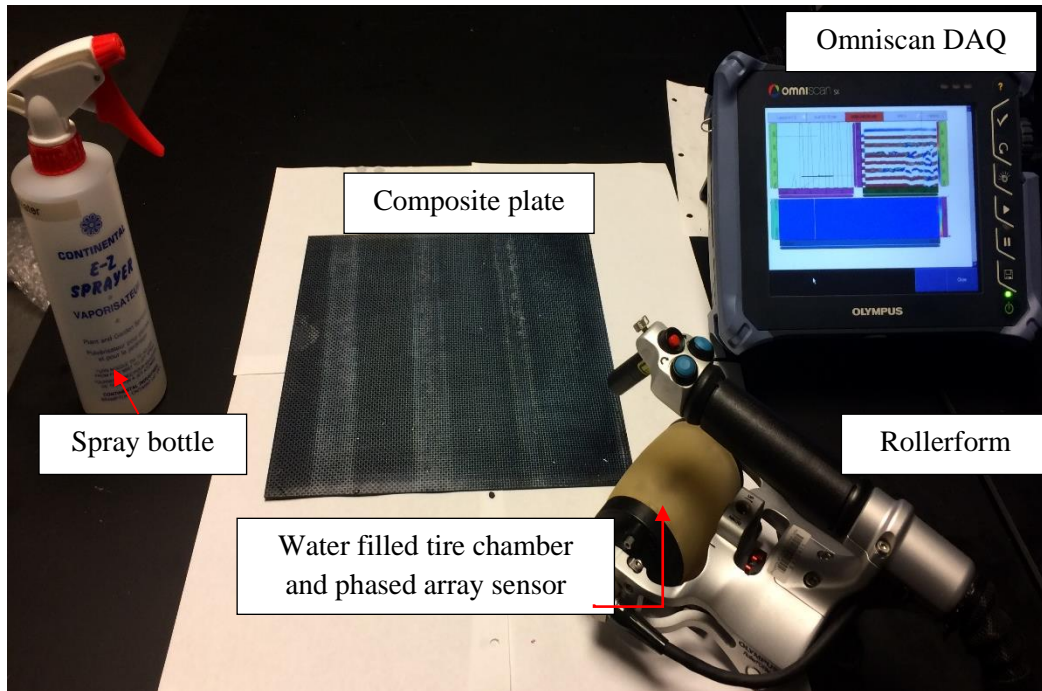


Figure 9.11 NDI experimental setup for damage inspection of the composite plate using phased array based Rollerform from Olympus and Omniscan

The NDI experimental set up is shown in Figure 9.11. There are several necessary components for this inspection such as Omniscan device, Roller form, water spray bottle and the composite test specimen.

9.2.3.2 Phased Array Based Wheel Probe

The acoustic tire contained the phased array probe. It can create a 25 mm delay line in the water for smooth scanning and optimized C-scan inspection of aerospace components. The key feature includes a swappable Olympus 64 element linear phased area probe with frequency 3.5 MHz for scan coverage greater than 50 mm, as shown in Figure 9.12. The effective length of the phased array beam is equal to approximately 49 mm. The tire chamber should be filled with distilled deionized water the night before the experiment to make sure the water is free from bubbles. The second step is to set up the Olympus Omniscan for wheel probe. The properties of the inspected plate can be selected carefully.

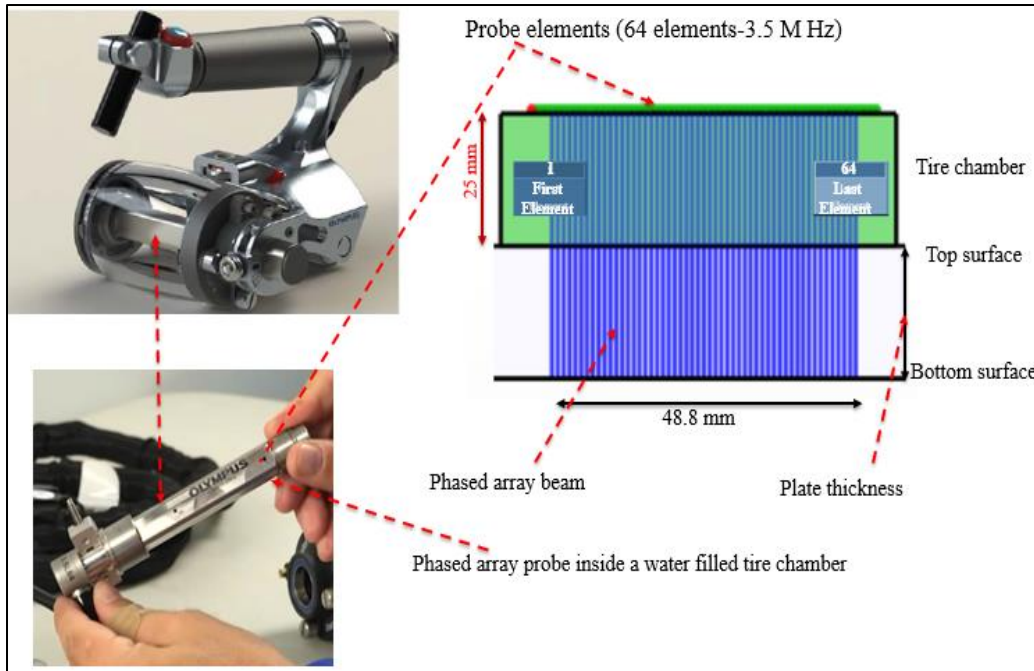


Figure 9.12 The phased array wheel probe element [171]

The internal software parameters have been chosen appropriately following the guideline provided by the Olympus OmniScan. The inspection area should be defined in the scan area menu in each axis.

9.2.3.3 Performing Ultrasonic Scanning

In this experiment, an inner inspection area of 245 mm by 240 mm was chosen since the wheel probe may generate erroneous signals while it is very close to the specimen edge. The inspection area was divided into 5 segments as shown in Figure 9.13. Each segment is 240 mm long and 49 mm wide (the effective beam probe length). The divided area was inspected line after line by the roller form wheel. The scan segments were stitched together to generate a complete ultrasonic image of the composite plate inspection area.

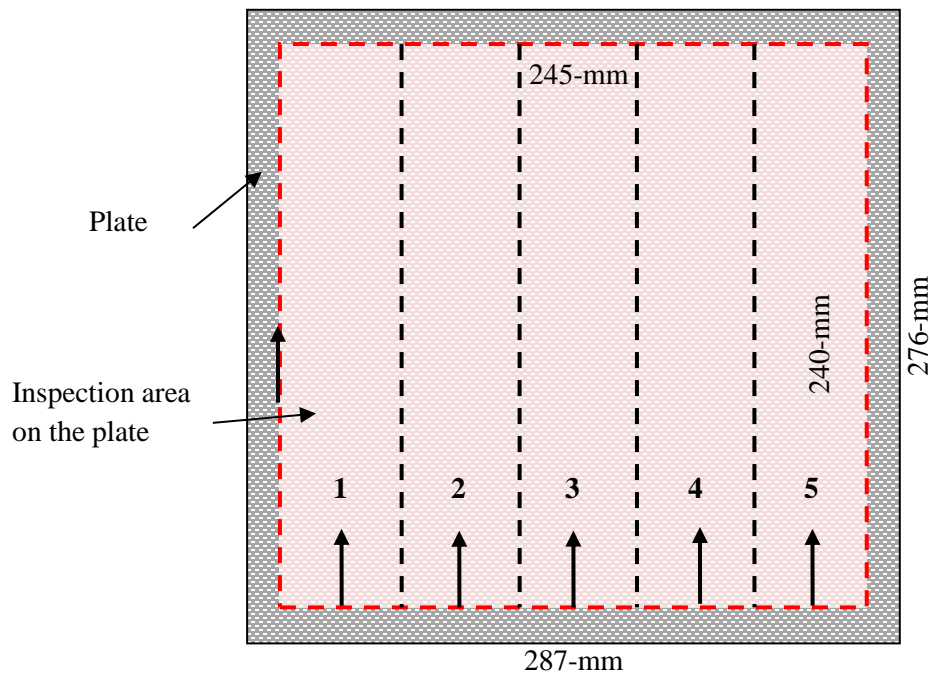
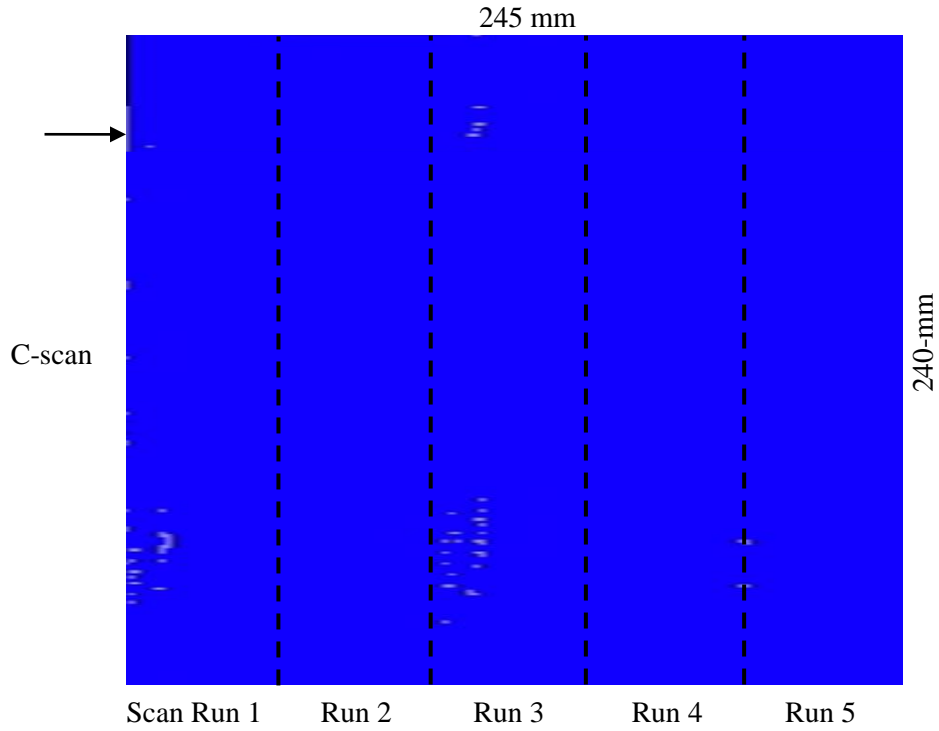


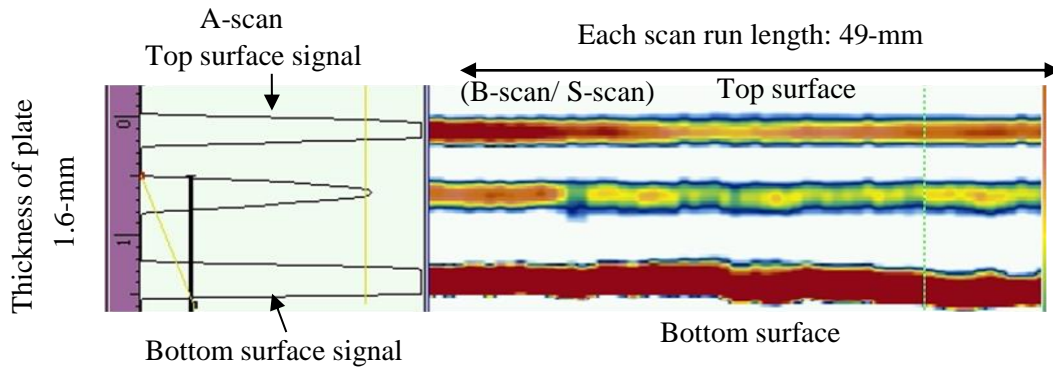
Figure 9.13 The NDI inspection area and the division scheme for ultrasonic scanning

9.2.3.4 3D Ultrasonic Scanning Results

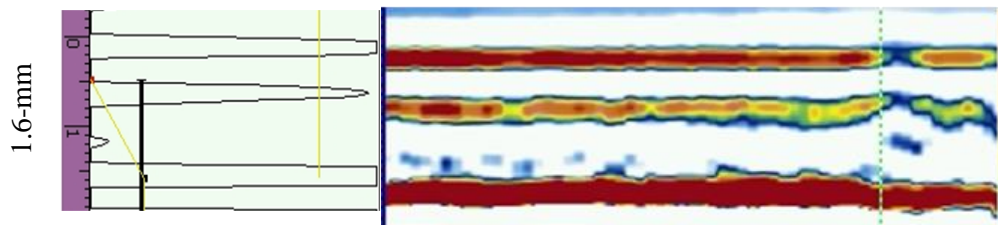
The ultrasonic 3D scanning results are summarized in Figure 9.14. The overall C-scan is represented by a color map as shown in Figure 9.14a. The color map shows an uniformity in color despite few gray spots here and there. This indicates that the composite plate is healthy enough without any defect or delamination. The gray spots might represent some manufacturing flaws or they could be originated from the measurement artifacts, however, they are less than 0.1%. Thus, the manufactured composite plate can be considered as a healthy plate. It also shows that there are no defects across the thickness of the plate.



(a) Ultrasonic scanning image of composite plate



(b) A-scan and S-scan for run 1



(c) A-scan and S-scan for run 5

Figure 9.14 NDI 3D scanning results of the manufactured composite plate

In order to understand more, the signatures of the ultrasonic signals are analyzed in the thickness direction. The A-scan and S-scan of run 1 and 5 are illustrated in Figure 9.14b,c. From the A-scan the top and bottom surface of the plate can be identified by looking at the signature of the signals. The distance between these two signatures represents the plate thickness. The S-scan or sectorial scan represents the two-dimensional representation of signal-amplitude distribution over the length of the scan run and thickness of the plate. The S-scans from two different positions show that there are no defects across the plate thickness.

9.2.4 IMPACT DETECTION AND LOCALIZATION USING SHM TECHNIQUE

After we confirm that the manufactured composite plate contains no significant internal defects from the NDE scanning process, we conducted an impact test on the plate. The impact is a common damage situation that can occur in real-life structures. In this experiment, an SHM technique is implemented to detect and localize the impact. Six PWAS transducers were permanently bonded to the composite plate. Each PWAS transducer was 7-mm in diameter and 0.5-mm in thickness. Experience from previous experiments performed by my colleague Asaad Migot [172], [173] on using PWAS transducer networks for impact localization has been implemented in our study.

9.2.4.1 *SHM Experimental Setup for Impact Detection and Localization*

The experimental setup is shown in Figure 9.15. Two clusters of PWAS sensors were used as named as C1 and C2. In each cluster, there were three PWAS transducers placed at 90 deg. orientation. This configuration of sensors is especially useful when one does not know the exact material properties of the plate. This method can accurately predict the location of the impact by analyzing the signals received by the sensors without knowing the material properties. The theoretical background of this model can be found in ref. [174].

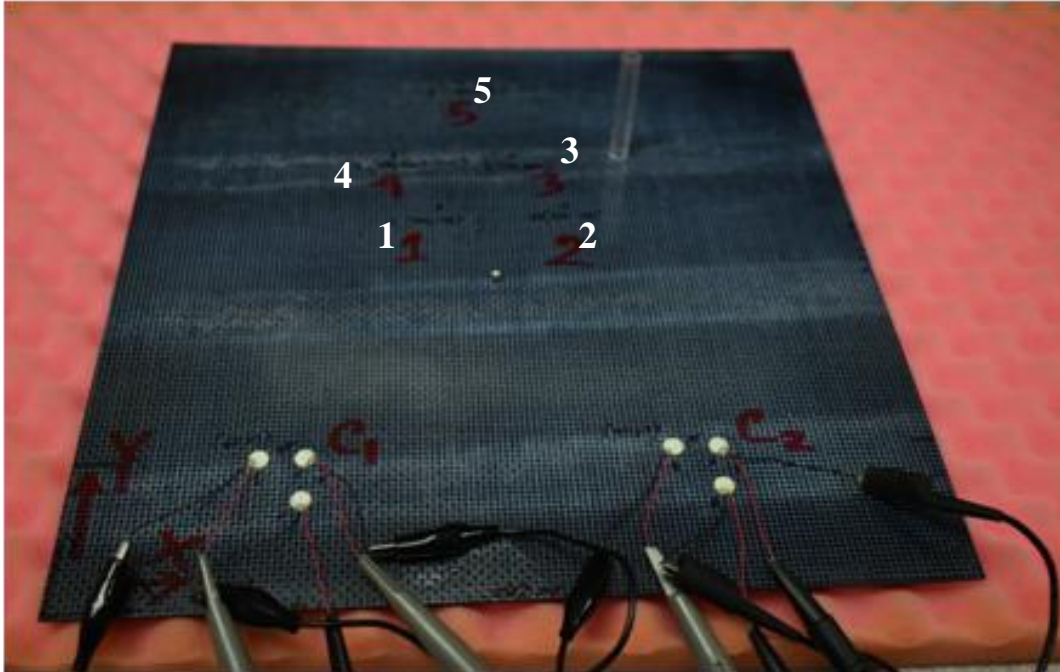


Figure 9.15 SHM scheme for impact detection and localization on the manufactured composite plate

The plate was subjected to impact by a steel ball at five different locations. These locations are marked by 1, 2, 3, 4, 5 in Figure 9.15. At each location, three impact events were created to check the repeatability of the test. The steel ball was freely impact following a special guide fixture from a height of about 2 inches. When the steel ball hits the plate it generates acoustic emissions (AE). The AE energy propagates as guided waves in the plate. The guided waves produce stress and strain waves in plate. The strain waves were captured by the permanently bonded PWAS transducers. Since the six PWAS transducers were located at different distances, the times of flight (TOF) of the received signals were different.

9.2.4.2 *Experimental Signal Analysis and Impact Detection*

The six signals from the six sensors are illustrated in Figure 9.16 and Figure 9.17. Figure 9.16 corresponds to the signals received from impact location #1 and Figure 9.17

corresponds to the signals received from impact location #3. These signals received by the sensors indicate that there was an impact event. In this experiment, low energy impact (height was intentionally kept low) was used to show how sensitive the proposed SHM system is. In case of high energy impact, it would be much easier to detect the impact event since it would produce higher amplitude AE signals.

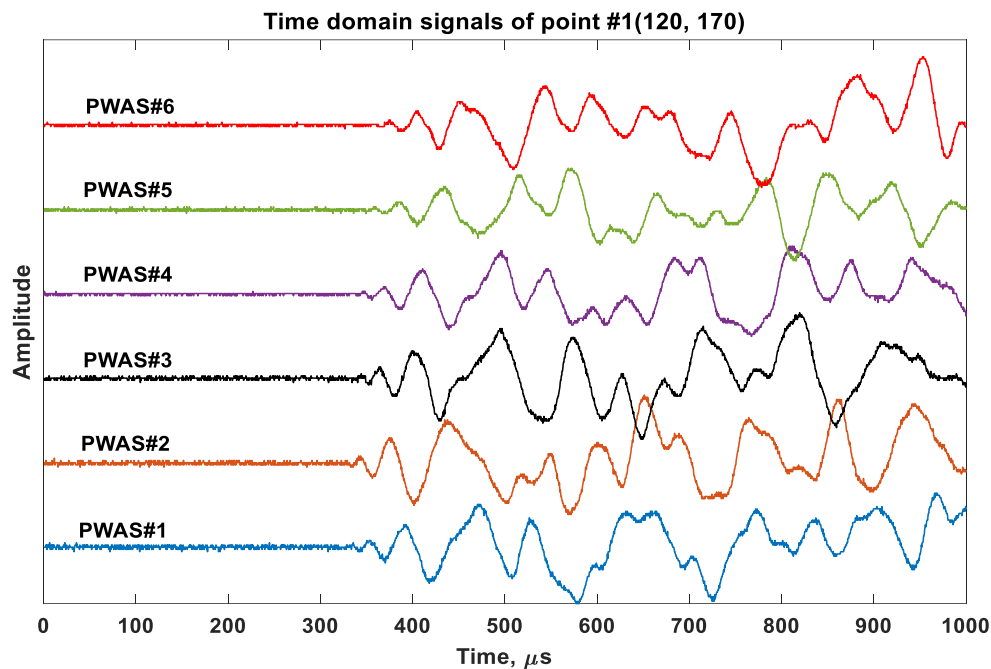


Figure 9.16 PWAS recorded acoustic signals due to impact at location #1

9.2.4.3 Impact Localization

To localize the impact event in the plate, it is important to determine the time-of-flight in a correct manner. Just by looking at the time-domain signals, often it is hard to determine the time of flight. The accurate way is to use a signal processing method to determine TOF. A wavelet transform based method was used in this paper to determine the TOF. The wavelet transform based method is demonstrated in Figure 9.18. As an example, two PWAS signals received from impact event#3 are considered.

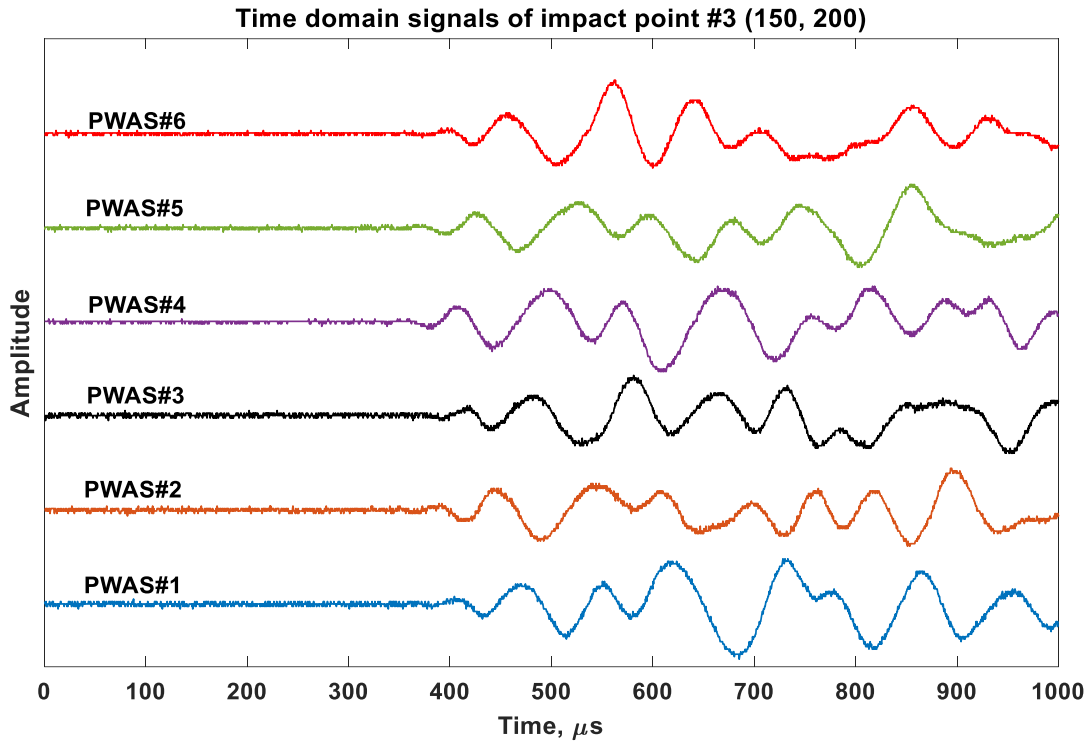


Figure 9.17 PWAS recorded acoustic signals due to impact at location #3

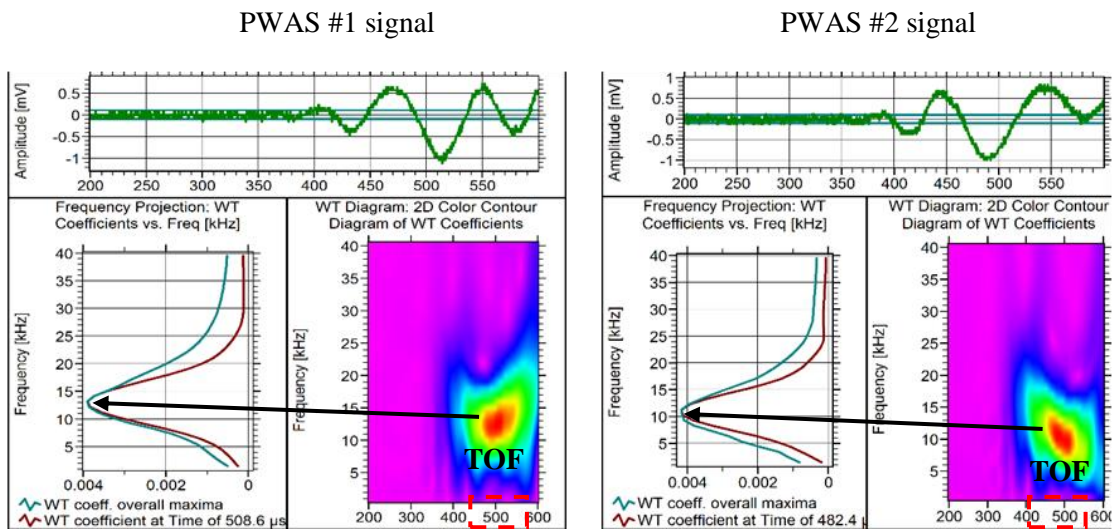


Figure 9.18 Wavelet transform of the PWAS recorded signals to determine time of flight (TOF) (for location #3)

In wavelet transform (WT), adjustable windows can better keep track of time and frequency information as compared to short-time Fourier transform (STFT), another popular method. WT can zoom in on short bursts and zoom out to detect long, slow oscillations by auto adjustment of the windows. Since the nature of the signal is unknown during an impact, WT provides more accurate information from the time-frequency analysis. A freeware Vallen WT software was used to perform the signal WT.

The frequency-time plot using the WT is shown by the color plots in Figure 9.18. It shows the amplitude mapping over various frequencies and time. At each time and frequency, a WT coefficient variation can be plotted as shown on the bottom-left of each box. An overall maximum of the WT coefficient has been plotted. The time at which the WT profile matches the overall WT maxima provide the TOF. This process has been repeated for all PWAS signals to determine the TOFs.

Once the TOFs for all the AE signals were known, a localization algorithm was used to determine the impact location. The localization algorithm was developed based on the theory proposed by Kundu et al. [174] as used in ref. [173]. The experimental measurement and the actual impact location is summarized in Table 9.1. The visual representation of the actual impact location and measured impact location is shown in Figure 9.19. It shows that the experimentally measured impact locations are in good agreement with the actual impact location.

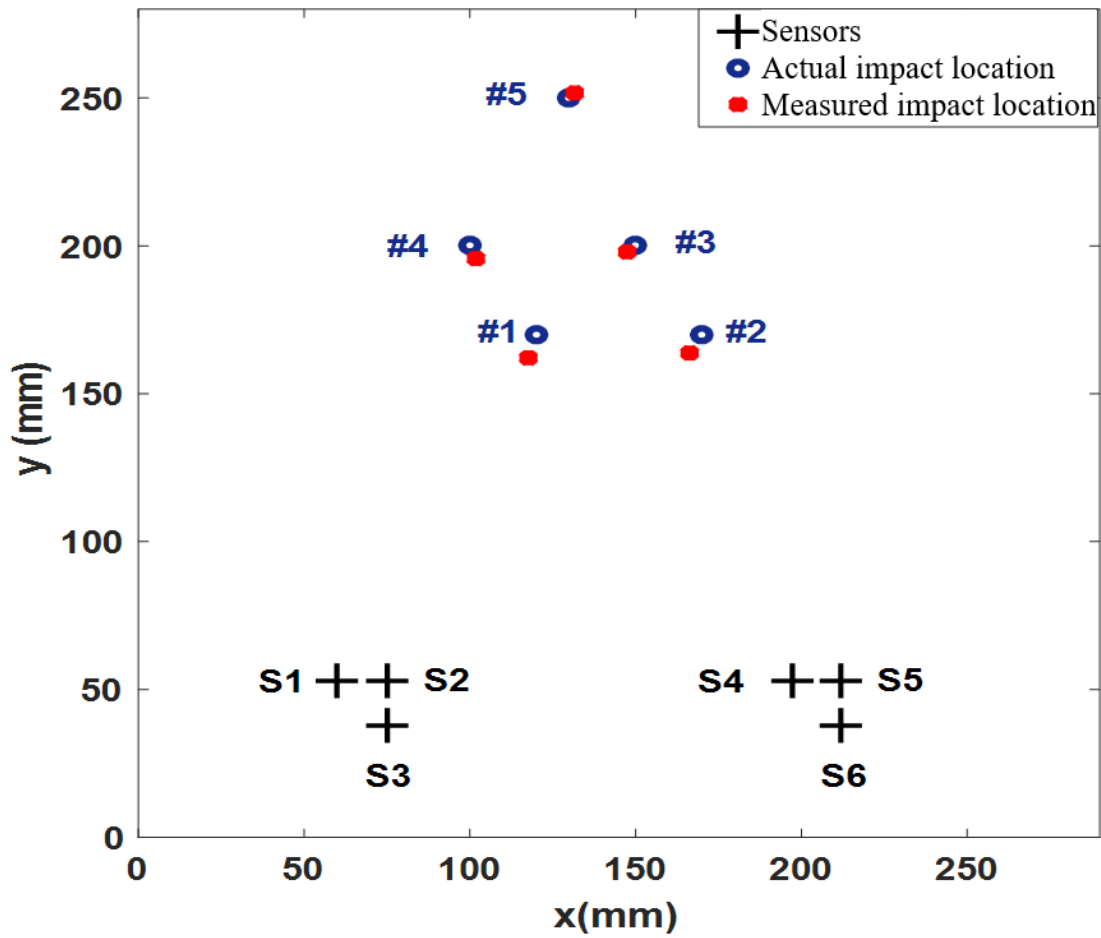


Figure 9.19 Experimentally measured impact location and actual impact location on the manufactured composite plate

Table 9.1 Experimental measurement vs. actual location of the impact

Impact event	Actual location (x, y) mm	Measured location (x, y) mm
#1	(120, 170)	(117.7, 161.9)
#2	(170, 170)	(166, 163.8)
#3	(150, 200)	(147.4, 197.8)
#4	(100, 200)	(101.8, 195.5)
#5	(130, 250)	(131.7, 251.6)

9.2.5 SUMMARY AND FINDINGS

A hot press with proper cure cycle was used for manufacturing a composite plate without any significant internal defects. We found that the manufactured plate had a minimal to no defect that can affect the impact detection and localization. A phased array based 3D ultrasonic scanning was used for fast inspection of internal damage in a manufactured plate. Relatively high number of elements (64) with a high frequency (3.5 MHz) phased array probe was used to detect any manufacturing defects. No significant internal defects were found. PWAS transducers were permanently bonded to the composites to detect and localize impact events. A wavelet transform based signal processing was used to accurately determine the time of flight of the acoustic signals. The proposed SHM technique can successfully be implemented in practice to monitor impact damage. We found that the experimental measurements are in good agreement with actual impact localization.

CHAPTER 10

CONCLUSIONS AND FUTURE WORK

This dissertation has presented physics-based approaches to structural health monitoring and nondestructive evaluation with ultrasonic guided waves. The focus has been on the development of analytical, finite element, and experimental techniques for guided wave-based active and passive sensing procedures.

The dissertation started with a literature review and fundamentals of guided waves, physics-based concepts of SHM and NDE, and different types of sensors. The elastodynamic gauge condition was analytically derived from the equations of motion and the Helmholtz potential representation of the physical vector quantities. A novel concept of the gauge condition was proposed. The application of the new gauge condition was demonstrated on two well-known plate guided wave problems: (a) straight-crested guided waves, (b) axisymmetric circular-crested guided waves. These demonstrations primarily showed how the use of the new gauge condition simplified the elastodynamic analysis of guided wave propagation. Then, our concept of the gauge condition was applied to a complicated problem which was the coupled non-axisymmetric guided wave propagation in a plate. An analytical solution based on Helmholtz potential was developed for the first time for the non-axisymmetric guided wave propagation in a plate. Normal-mode expressions for the displacements and stresses were developed and presented.

The dissertation continued with a hybrid global analytical and local FEM approach to enhanced damage detection in aerospace rivet holes. An aerospace lap joint with

multiple rivet holes was considered. A scatter cube of wave damage interaction coefficient (WDIC) was developed for a rivet hole with butterfly cracks. The scatter cube contained the damage information for all possible directions of wave interactions at all possible frequencies. The analysis of the scatter cube showed the optimum combination between actuator-sensor locations around the damage site and frequencies of transmitting signals. A few examples were demonstrated by showing the simulated time-domain signals in some particular cases.

The dissertation continued with multiphysics FEM simulations of a predictive design for a passive SHM system. For the multiphysics simulations, it considered a practical problem which was the detection of acoustic emissions (AE) generated by a fatigue-crack. Various design parameters were studied. The underpinning of the acoustic emission source modeling, fatigue crack modeling, wave propagation visualization, and crack resonance was developed.

The dissertation continued with the physics of materials-based analysis of in-situ AE signals from AE-fatigue experiments. Multiple experiments were conducted to validate the multiphysics simulation results and interpret the fatigue-crack generated AE signals. Various types of AE sensors were used to capture the AE signals. Hit-based and waveform-based analyses were performed on the AE signals. Various groups of AE waveform signatures and their sources were localized from the waveform-based analysis. A fatigue crack length estimation was proposed based on the AE waveforms. Two case study experiments of practical active and passive SHM usage were demonstrated. A review of the main conclusions of this research is given next.

10.1 RESEARCH CONCLUSIONS

10.1.1 ELASTODYNAMIC GAUGE CONDITION

The gauge condition originated in elastodynamics from the Navier-Lame equations upon application of Helmholtz theorem. The proper choice and manipulation of the gauge condition may simplify the problem and permits straightforward analytical solutions. The gauge condition provides the necessary conditions for the complete solution of the elastic waves in plates by the potential function approach. The gauge condition may be considered as the superposition of separate gauge conditions for Lamb waves and SH waves, respectively. Each gauge condition contains a different combination of the shear vector potential components. The gauge condition established a bridge between Lamb waves and SH waves. The gauge condition may decouple in the case of physical problems in which the Lamb and SH waves are expected to decouple. The decoupling of the gauge condition does not violate the classical Lamb wave and SH wave solutions; rather, it simplifies the problem. The gauge condition plays a vital role in the separation of Lamb waves and SH waves; thus, it transforms a complicated problem into two simpler problems. In Chapter 3 of the dissertation, the manipulation of the gauge condition was illustrated on two well-known problems of guided waves in plates in which the Lamb waves and SH waves can be physically decoupled. The next challenge for this approach, i.e., solving a coupled problem (Lamb waves + SH waves) such as the non-axisymmetric guided wave propagation in a plate, was addressed next.

10.1.2 ANALYTICAL SOLUTION TO THE NON-AXISYMMETRIC PROBLEM

In Chapter 4 of the dissertation, we showed that it is possible to develop a Helmholtz potential solution for the coupled non-axisymmetric guided wave problem in

cylindrical coordinates by manipulating the gauge condition. The non-axisymmetric guided wave propagation in cylindrical coordinates is a situation where two of the potentials are tightly coupled. The coupling of the governing equations in terms of potentials has prevented so far the development of a complete Helmholtz solution for this difficult problem. Chapter 4 showed how a judicious manipulation of the gauge condition can decouple the governing equations and leads to a straight-forward solution. The manipulation of the gauge condition yielded a new potential, H_v , which replaces the effect of H_r , H_θ and thus allowed us to replace two coupled governing equations in H_r , H_θ by a single uncouple equation in H_v . This judicious use of the gauge condition reduced the number of potentials, decoupled the governing equations and facilitated the obtaining of the complete solution for the non-axisymmetric guided-wave propagation in cylindrical coordinates in an elegant straight-forward way.

10.1.3 ANALYTICAL-FEM APPROACH FOR RIVET HOLE CRACK DETECTION

An exact analytical formulation has been used throughout the structure, except for the local damage area, which was analyzed using the finite element method. In order to detect multiple-rivet-hole lap joint cracks, Lamb waves impinging on the damage from all possible directions were considered. Both symmetric and antisymmetric fundamental Lamb wave modes (S_0 and A_0) were used in the analysis. Besides the Lamb waves, SH waves also appeared in the scattered waves. Due to the non-axisymmetric nature of the problem, the wave damage interaction coefficient (WDIC) had non-axisymmetric behavior around the damage. Scatter cubes were produced for the scattered waves to accommodate the three-way interaction (frequency, incident direction, azimuthal direction) of Lamb waves with the rivet hole cracks. From the frequency domain analysis and the azimuthal

variation of the WDIC, the proper locations of the sensors and the appropriate center frequency of excitation were obtained. Some particular example cases were demonstrated. The simulated time-domain signals were obtained for different frequency–location combinations by using a global analytical framework. The optimum selection of sensor location and center frequency of excitation gave a strong signal that confirmed a better crack detection in the rivet hole. The optimum parameters can be used to make an effective NDE/SHM algorithm for inspecting the multiple-rivet-hole lap joint.

10.1.4 MULTIPHYSICS FEM SIMULATIONS OF FATIGUE-CRACK GENERATED AE

PWAS transducers successfully captured the fatigue crack-related AE signals. Both multiphysics simulations and experimental results supported this finding. The fatigue crack generates low-amplitude AE signals as it grows. We recorded AE signals being produced in every fatigue loading cycle. This indicates that the AE events happen at every cycle as the fatigue crack grows. During a low cycle fatigue experiment, the AE hits provide the global information of the physical problem whereas the AE signal analysis provides the detail information of the physical phenomenon. The AE event produced at the crack tip travels as guided acoustic waves throughout the structure. The AE signals show the geometric energy spreading and amplitude reduction. The distance between the PWAS transducer and the AE source has an effect on the sensed AE signals. Near-field PWAS captures higher amplitude AE signals than far-field PWAS. Some higher-frequency contents of the AE signals seem to develop as they travel away from the crack tip AE source. The effect of the rise time and dipole orientation in the FEM simulation was also investigated. We found that these two factors significantly affect the simulated AE signals.

Thus, these factors may be used to simulate various types of AE signals for various applications.

10.1.5 PHYSICS-BASED ANALYSIS OF EXPERIMENTAL AE SIGNALS

The physics of materials based analysis of AE signals may explain the complex phenomena of metal fatigue. The current AE hit based analysis may not be sufficient to capture detailed fatigue crack growth mechanisms. The AE-waveform based analysis may give a comprehensive idea of the fatigue crack growth phenomenon. Different types of sensors significantly affect the recorded AE waveforms. Depending on the application, a certain type of sensor may be more suitable than others. It was found that PWAS transducers may be used to capture the fatigue crack generated AE signals in thin wall structures. PWAS seems to capture richer frequencies than the commercial PICO and S9225 sensors. It is also important to distinguish the fatigue crack-related AE signals from the rogue AE signals that may come from non-crack events. AE source localization confirmed the sources of the AE signals.

During the fatigue crack growth, various AE waveforms may be generated. These AE waveforms can be sorted into groups based on their spectral signatures. During fatigue crack growth in a thin metallic specimen, nine different AE waveform groups were observed. A particular waveform group represents a particular source of AE event related to the crack growth. The AE waveforms evolved with fatigue load level.

Fatigue crack extension, as well as rubbing and fretting of crack faying surfaces, may generate AE signals. AE waveform sorting synchronized with load level was used to distinguish the AE signals related to crack extension from the rubbing and fretting AE signals. It was found that certain groups (A, B, C, D, G) were generated from the crack

extension while certain groups (E, F, H) are generated by the crack rubbing and fretting. Micro-fracture events may occur during the crack rubbing and fretting of the crack faying surfaces which may generate AE signals in a clustered form. Some AE waveform groups happened at relatively lower load level (e.g. group E) and appeared in cluster form. These waveforms may represent the “catching” of the crack faying surfaces.

10.1.6 CAN WE “HEAR” CRACK LENGTH FROM AE WAVEFORMS?

The AE waveform generated from the crack tip may interact with the crack itself and cause crack resonance. Transient and harmonic analyses were carried with a 3-D FEM model to simulate the AE wave generation, propagation, and its interaction with a fatigue crack. Both analyses confirmed the local crack resonance phenomena due to the interaction between an AE waveform and a fatigue crack and showed that they are related to the crack length. LDV experiments were conducted to verify the computational results. Both experimental and simulation results suggested that the AE waveform may be used for determining the fatigue crack length.

10.1.7 FINDINGS OF CASE STUDIES

A plate with a pristine stiffener and a stiffener with a horizontal half-penny-shaped crack were simulated and experimentally tested. The presence of the crack in the stiffener produces additional scattered waves and trapped waves. These scattered waves and trapped waves were experimentally measured by a scanning laser Doppler vibrometer (SLDV). The scattered waves from the pristine stiffener and cracked stiffener were analyzed and compared with each other. The analyses suggested that both the size and the shape of the horizontal crack may be predicted from the scattered wave pattern. In addition, we found that certain feature of the scattered waves may be more suitable for damage detection than

others. Identification of an appropriate feature of the scattered waves may provide better information about the damage. For instance, in this experiment, the direct transmission feature may be used to detect the crack for incident A0 Lamb wave, whereas the mode-conversion feature may be used to detect the crack for incident S0 Lamb wave. The reflection feature may be used to determine the shape and size of the crack.

A hot press process with proper cure cycle was used to manufacture a composite plate without any significant internal defect. A phased array based 3D ultrasonic scanning was used for fast inspection of internal damage in the manufactured plate. Relatively higher number of elements (64) with high frequency (3.5 MHz) phased array probe was used to detect any smaller defects produced during the manufacturing. We found that the manufactured plate had a few small internal defects but these did not affect the impact detection and localization. PWAS transducers were permanently bonded to the composite plate to detect and localize impact events. A wavelet transform based signal processing was used to accurately determine the time of flight of the acoustic signals. The proposed SHM technique can be successfully implemented in practice to monitor impact damage. We found that the experimental measurements are in good agreement with actual impact locations.

10.2 MAJOR CONTRIBUTIONS

This dissertation has contributed to the SHM and NDE research in a variety of ways. The major contributions of this dissertation to the SHM/NDE state of the art are listed below:

1. A novel concept of the elastodynamic gauge condition was proposed. We found that the gauge condition may be considered as the superposition of separate

gauge conditions for Lamb waves and SH waves, respectively. Each gauge condition contains a different combination of the shear vector potential components. The gauge condition established a bridge between Lamb waves and SH waves in plate-guided waves. It was found that the gauge condition played a vital role in developing simplified analytical solutions of several guided-wave propagation problems.

2. An analytical solution to the non-axisymmetric problem was developed for the first time in cylindrical coordinates using the Helmholtz-potential based approach which has not been reported elsewhere. The judicious use of the gauge condition reduced the number of potentials, decoupled the governing equations and facilitated the obtaining of a complete solution for the non-axisymmetric guided-wave propagation in cylindrical coordinates in an elegant straightforward way.
3. An enhanced damage detection technique for aerospace rivet holes has been proposed. The scatter cube of wave-damage interaction coefficients was developed. An analytical framework developed by a previous researcher was used to incorporate the scatter cube and obtain the time domain signals. The optimum combination of frequency and sensor location was obtained for a better design of SHM systems.
4. Multiphysics 3D FEM simulation of the fatigue-crack generated acoustic emission and propagation was performed in ways which have not yet been reported in the literature. The underpinning of the acoustic emission source modeling, fatigue crack modeling, and crack resonance was developed.

5. Piezoelectric wafer active sensors (PWAS) were shown to be effective low-cost AE sensors for capturing the fatigue crack generated AE signals. It has been verified by using both multiphysics simulations and experiments that the PWAS can successfully capture the features of the fatigue crack generated AE.
6. It was found that the AE sensors had a significant effect on the sensing AE signals. A certain sensor may be more suitable than others depending on the application. For fatigue crack generated AE in a thin plate, PWAS captured richer frequency information of the AE waveforms than the commercially available AE sensors (PICO and S9225).
7. A methodology for the AE waveform analysis was developed which would give much more information than the existing AE hit-based approaches. It was found that the AE hit-based analysis may not be sufficient for understanding the fatigue crack-related AE signals.
8. Various waveform signatures were captured from in-situ AE-fatigue experiments. Source localization confirmed that they were generated from the fatigue crack. Aspects of the complex metal fatigue mechanism were explained using the waveform signatures which have not been reported elsewhere.
9. A fatigue crack length estimation method based on the analysis of the fatigue AE waveforms was proposed.
10. Two case studies on realistic problems have been performed based on a combination of active and passive SHM/NDE techniques.

10.3 RECOMMENDATION FOR FUTURE WORK

This dissertation has presented generalized analytical solutions, multiphysics simulation techniques, and an experimental methodology for ultrasonic guided-wave based SHM and NDE. This work has laid the foundation for future investigations to extend the methodologies to more complicated structures. The suggestions for future work are listed below:

1. The general solution of the non-axisymmetric guided-wave problem developed in this dissertation may be used for any plate guided-wave problem with non-axisymmetric excitation. For example, a plate subjected to an arbitrary azimuthal variation of loading. The nature of the azimuthal loading will determine the number and magnitude of the angular modes to be considered in the Fourier expansion.
2. One of the major applications of the general non-axisymmetric solution would be the theoretical analysis of guided wave scattering from a damage of arbitrary shape. This is a problem of continuous interest in ultrasonic nondestructive evaluation (NDE) and structural health monitoring (SHM). The general non-axisymmetric guided wave solution can be used for dealing with the scattering of guided waves from non-axisymmetric damage such as corrosion, fatigue crack, notches, etc. The incident guided waves and the non-axisymmetric guided waves scattered from a damage should satisfy the local boundary conditions at the damage site. These boundary conditions would be used to determine the coefficients of the complex-mode expansion representation of the stresses and displacements. Upon knowing the coefficients of the complex-

mode expansion, one can analytically determine the scatter wavefield. Subsequently, the predicted reflection, transmission, and mode conversion coefficients could be used to achieve a better design of the NDE and SHM systems for specific applications.

3. One can determine the proper gauge condition using the methodology proposed in the dissertation applied to other elastodynamic problem.
4. An experiment may be designed based on the simulated results to detect the rivet-holes crack with Lamb waves incident from multiple directions. The SHM system design may be extended for making an algorithm for the multiple-rivet-hole lap joint and detecting the cracks in any of the rivet holes. The research may be further extended by considering the interactions among the rivet holes and the boundary reflections from the edges. In the overlapped section of the lap joint, some wave leakages may occur, thus, the overlapped thickness of the plate would come into play. The wave leakage effects may be considered while obtaining the optimum parameters.
5. The full history of the AE hits for the fatigue crack growth from beginning to failure may be analyzed at the waveform level. It would be a labor-intensive but worthwhile analysis if we could establish possible relations between the AE signal-groups and the fatigue crack length. The AE waveforms would be further analyzed to capture any possible local interaction between the AE signals and the fatigue crack. A multiphysics simulation could be performed to predict the failure mechanism corresponding to different AE signal groups.

6. The mechanism of crack growth within one fatigue cycle may be established from the captured AE signals. In-situ microscopic measurement of the fatigue crack length would be performed and correlate with the captured AE signals. The AE system, MTS machine, and the optical measurement could be synchronized together for better understanding and interpretation of the AE signals.
7. The crack resonance phenomenon observed in the multiphysics simulation of the AE waveform may be further analyzed to extract the fatigue crack length information. The multiphysics simulation at the intermediate length of the crack may be performed to obtain the AE waveforms at these lengths.

REFERENCES

- [1] Federal Aviation Administration, “Air traffic by the numbers,” 2017.
- [2] Boeing Company, “Statistical summary of commercial jet airplane accidents-worldwide operations 1959-2016,” 2016.
- [3] American Society of Civil Engineers, “ASCE’s 2017 infrastructure report card,” 2017.
- [4] Congressional Budget Office, “Public spending on transportation and water infrastructure - 1956 to 2014,” 2014.
- [5] D. Stargel, “Multi-scale structural mechanics and prognosis,” *Air Force Office of Scientific Research (AFOSR) Spring Review*. Arlington, VA, p. 21, 2014.
- [6] I. Perez, M. Diulio, S. Maley, and N. Phan, “Structural health management in the NAVY,” *Struct. Heal. Monit. Int. J.*, vol. 9, no. 3, pp. 199–207, 2010.
- [7] W. L. Richards, E. Madaras, W. H. Prosser, and G. Studor, “NASA applications of structural health monitoring technology,” in *9th International Workshop on Structural Health Monitoring*, 2013, p. 46.
- [8] H. Lamb, “On Waves in an Elastic Plate,” *Proc. R. Soc. A Math. Phys. Eng. Sci.*, vol. 93, no. 648, pp. 114–128, 1917.
- [9] L. E. Goodman, “Circular-crested vibrations of an elastic solid bounded by two parallel planes,” *Proc. 1st Natl. Congr. Appl. Mech.*, pp. 65–73, 1952.
- [10] V. Giurgiutiu, A. Zagrai, and J. Bao, “Piezoelectric Wafer Embedded Active Sensors for Aging Aircraft Structural Health Monitoring,” *Struct. Heal. Monit.*, vol. 1, no. 1, pp. 41–61, 2002.
- [11] Y. Shen, “Structural health monitoring using linear and nonlinear ultrasonic guided waves,” *PhD Diss.*, p. 224, 2014.
- [12] Z. Chang and A. Mal, “Scattering of Lamb waves from a rivet hole with edge cracks,” *Mech. Mater.*, vol. 31, no. 3, pp. 197–204, 1999.

- [13] V. Giurgiutiu and J. Bao, "Embedded-ultrasonics Structural Radar for In Situ Structural Health Monitoring of Thin-wall Structures," *Struct. Heal. Monit.*, vol. 3, no. 2, pp. 121–140, 2004.
- [14] L. Yu and V. Giurgiutiu, "In-situ optimized PWAS phased arrays for Lamb wave structural health monitoring," *J. Mech. Mater. Struct.*, vol. 2, no. 3, pp. 459–487, 2007.
- [15] C. H. Wang, J. T. Rose and F. Chang, "A Synthetic Time-Reversal Imaging Method for Structural Health Monitoring," *Smart Mater. Struct.*, vol. 13, no. 2, pp. 415–423, 2004.
- [16] V. Giurgiutiu, A. Reynolds, and C. A. Rogers, "Experimental Investigation of E / M Impedance Health Monitoring for Spot-Welded Structural Joints Description of the Specimen," *J. Intell. Mater. Syst. Struct.*, vol. 10, no. 10, pp. 802–812, 1999.
- [17] V. Giurgiutiu and A. Zagari, "Electro-mechanical impedance method for crack detection in thin plates," *J. Intell. Mater. Syst. Struct.*, vol. 12, no. 10, pp. 709–718, 2001.
- [18] K. F. Graff, *Wave Motion in Elastic Solids*, Dover. Oxford University Press, 1975.
- [19] H. Helmholtz, "Über Integrale der Hydrodynamischen Gleichungen, Welche den Wirbelbewegungen Entsprechen," *J. für die reine und Angew. Math.*, vol. 1858, no. 55, pp. 25–55, 1858.
- [20] H. Helmholtz, "On Integrals of the Hydrodynamical Equations, which Express Vortex-Motion," *Philos. Mag. J. Sci.*, vol. 33, no. 226, pp. 485–512, 1867.
- [21] V. Giurgiutiu, *Structural health monitoring with piezoelectric wafer active sensors*, 2nd ed. Elsevier Academic Press, 2014.
- [22] A. Kamal, M. Gresil, and V. Giurgiutiu, "Shear Horizontal Guided Waves in Laminated Composite Plates Using SH-PWAS," in *NDT of Composites*, 2013.
- [23] W. Zhou, H. Li, and F.-G. Yuan, "Guided wave generation, sensing and damage detection using in-plane shear piezoelectric wafers," *Smart Mater. Struct.*, vol. 23, no. 1, pp. 1–10, 2014.
- [24] E. Glushkov, N. Glushkova, R. Lammering, A. Eremin and M. N. Neumann, "Lamb wave excitation and propagation in elastic plates with surface obstacles: proper choice of central frequency," *Smart Mater. Struct.*, vol. 20, no.1 p. 11, 2011.
- [25] V. Giurgiutiu, "Embedded NDE with Piezoelectric Wafer- Active Sensors in Aerospace Applications," *J. Mater.*, vol. January, no. Special, 2003.

- [26] M. Y. Bhuiyan and V. Giurgiutiu, “Using the gauge condition to simplify the elastodynamic analysis of guided wave propagation,” *Incas Bull.*, vol. 8, no. 3, pp. 11–26, 2016.
- [27] L. V. H. Pochhammer, “Ueber die Fortpflanzungsgeschwindigkeiten kleiner Schwingungen in einem unbegrenzten isotropen Kreiscylinder,” *J. für die reine und Angew. Math.*, vol. 81, pp. 324–336, 1876.
- [28] C. Chree, “The equations of an isotropic elastic solid in polar and cylindrical coordinates, their solutions and applications,” *Cambridge Philos. Soc. Math. Phys. Sci. Trans.*, vol. 14, pp. 250–369, 1889.
- [29] L. Rayleigh, “On the Free Vibrations of an Infinite Plate of Homogeneous Isotropic Elastic Matter,” *Proc. London Math. Soc.*, vol. 20, no. 1, pp. 225–234, 1889.
- [30] H. Lamb, “On the flexure of an elastic plate,” *Proc. London Math. Soc.*, vol. 21, no. 1, pp. 70–90, 1889.
- [31] P. M. Morse and H. Feshbach, *Methods of Theoretical Physics*. New York, Toronto, London: McGraw-Hill Book Company, Inc., 1953.
- [32] D. C. Gazis, “Three Dimensional Investigation of the Propagation of Waves in Hollow Circular Cylinders. I. Analytical Foundation,” *J. Acoust. Soc. Am.*, vol. 31, no. 5, pp. 568–578, 1959.
- [33] C. E. Baum, “Vector and scalar potentials away from sources. and gauge invariance in quantum electrodynamics,” *Phys. Notes*, vol. Note 3, pp. 1–31, 1991.
- [34] J. D. Jackson and L. B. Okun, “Historical roots of gauge invariance,” *Rev. Mod. Phys.*, vol. 73, no. 3, pp. 663–680, 2000.
- [35] F. Gronwald and J. Nitsch, “The Physical Origin of Gauge Invariance,” *Electr. Eng.*, vol. 81, pp. 363–367, 1999.
- [36] T. R. Meeker and A. H. Meitzler, “Guided Wave Propagation in Elongated Cylinders and Plates,” *Phys. Acoust. Princ. Methods*, vol. 1, no. 2, pp. 111–167, 1964.
- [37] J. D. Achenbach, “Lamb waves as thickness vibrations superimposed on a membrane carrier wave,” *J. Acoust. Soc. Am.*, vol. 103, no. 5, pp. 2283–2286, 1998.
- [38] J. D. Achenbach and Y. Xu, “Wave motion in an isotropic elastic layer generated by a time-harmonic point load of arbitrary direction,” *J. Acoust. Soc. Am.*, vol. 106, no. 1, pp. 83–90, 1999.

- [39] F. Gronwald and J. Nitsch, “The physical origin of gauge invariance in electrodynamics and some of its consequences,” *Phys. Notes*, vol. Note 3, pp. 1–14, 1998.
- [40] T. Kundu, Ed., *Ultrasonic and Electromagnetic NDE for Structure and Material Characterization*, First. CRC Press, 2016.
- [41] R. A. Scott and J. Miklowitz, “Transient non-axisymmetric wave propagation in an infinite isotropic elastic plate,” *Int. J. Solids Struct.*, vol. 5, no. 1, pp. 65–79, 1969.
- [42] N. Davids and W. Lawhead, “Transient analysis of oblique impact on plates,” *J. Mech. Phys. Solids*, vol. 13, no. 4, pp. 199–212, 1965.
- [43] A. Pytel and N. Davids, “Transient analysis of shear impact,” *J. Appl. Mech.*, vol. 29, no. 1, pp. 33–39, 1962.
- [44] O. Diligent, “Interaction between fundamental Lamb modes and defects in plates,” *Mech. Eng.*, 2003.
- [45] L. Moreau, M. Caleap, A. Velichko, and P. D. Wilcox, “Scattering of guided waves by flat-bottomed cavities with irregular shapes,” *Wave Motion*, vol. 49, no. 2, pp. 375–387, 2012.
- [46] L. Moreau, A. Velichko, and P. D. Wilcox, “Accurate finite element modelling of guided wave scattering from irregular defects,” *NDT E Int.*, vol. 45, no. 1, pp. 46–54, 2012.
- [47] V. Giurgiutiu, *Structural Health Monitoring with Piezoelectric Wafer Active Sensors (Second Edition)*. Oxford: Academic Press, 2014.
- [48] M. Y. Bhuiyan, Y. Shen, and V. Giurgiutiu, “Guided wave based crack detection in the rivet hole using global analytical with local FEM approach,” *Materials (Basel)*, vol. 9, no. 7, p. 602, 2016.
- [49] R. B. Thompson, L. H. Brasche, D. Forsyth, E. Lindgren, P. Swindell, and W. Winfree, “Recent Advances in Model-Assisted Probability of Detection,” in *4th European-American Workshop on Reliability of NDE*, 2009.
- [50] M. D. Bode, J. Newcomer, and S. Fitchett, “Transfer function model-assisted probability of detection for lap joint multi site damage detection,” in *The 31th Review of Progress in Quantitative Nondestructive Evaluation*, 2012, vol. 1430, pp. 1749–1756.
- [51] C. M. Schubert Kabban, B. M. Greenwell, M. P. DeSimio, and M. M. Derriso, “The probability of detection for structural health monitoring systems: Repeated measures data,” *Struct. Heal. Monit.*, vol. 14, no. 3, pp. 252–264, 2015.

- [52] F.-K. Chang, V. Janapati, F. Kopsaftopoulos, S. J. Lee, F. Li, and K. Lonkar, "Quantification of Structural Health Monitoring for Damage Detection," in *The 30th Aircraft Structural Integrity Program (ASIP)*, 2014.
- [53] Z. Sharif-Khodaei and M. H. Aliabadi, "Assessment of delay-and-sum algorithms for damage detection in aluminium and composite plates," *Smart Mater. Struct.*, vol. 23, no. 7, p. 75007, 2014.
- [54] Y. Lu, L. Ye, Z. Su, and C. Yang, "Quantitative assessment of through-thickness crack size based on Lamb wave scattering in aluminium plates," *NDT E Int.*, vol. 41, no. 1, pp. 59–68, 2008.
- [55] A. N. Norris and C. Vemula, "Scattering of Flexural Waves on Thin Plates," *J. Sound Vib.*, vol. 181, no. 1, pp. 115–125, 1995.
- [56] E. B. Flynn and M. D. Todd, "A Bayesian approach to optimal sensor placement for structural health monitoring with application to active sensing," *Mech. Syst. Signal Process.*, vol. 24, no. 4, pp. 891–903, 2010.
- [57] E. B. Flynn and M. D. Todd, "Optimal Placement of Piezoelectric Actuators and Sensors for Detecting Damage in Plate Structures," *J. Intell. Mater. Syst. Struct.*, vol. 21, no. 3, pp. 265–274, 2010.
- [58] P. Fromme and M. B. Sayir, "Detection of cracks at rivet holes using guided waves," *Ultrasonics*, vol. 40, no. 1–8, pp. 199–203, 2002.
- [59] T. Grahm, "Lamb wave scattering from a circular partly through-thickness hole in a plate," *Wave Motion*, vol. 37, no. 1, pp. 63–80, 2003.
- [60] E. Glushkov, N. Glushkova, A. Eremin, and V. Giurgiutiu, "Low-cost simulation of guided wave propagation in notched plate-like structures," *J. Sound Vib.*, vol. 352, pp. 80–91, 2015.
- [61] Y. Shen and V. Giurgiutiu, "Effective non-reflective boundary for Lamb waves: Theory, finite element implementation, and applications," *Wave Motion*, vol. 58, pp. 22–41, 2015.
- [62] M. Y. Bhuiyan, "Guided wave inspection of cracks in the rivet hole of an aerospace lap joint using analytical-FEM approach," MS Thesis, University of South Carolina, 2016.
- [63] M. Y. Bhuiyan, Y. Shen, and V. Giurgiutiu, "Ultrasonic inspection of multiple-rivet-hole lap joint cracks using global analysis with local finite element approach," in *SPIE Proceedings of Health Monitoring of Structural and Biological Systems*, 2016, vol. 9805, p. 98051Z–1–15.

- [64] M. Y. Bhuiyan, Y. Shen, and V. Giurgiutiu, "Interaction of Lamb waves with rivet hole cracks from multiple directions," *Proc. Inst. Mech. Eng. Part C J. Mech. Eng. Sci.*, vol. 231, no. 6, pp. 2974–2987, 2017.
- [65] C. Schubert Kabban, R. Uber, K. Lin, B. Lin, M. Bhuiyan, and V. Giurgiutiu, "Uncertainty Evaluation in the Design of Structural Health Monitoring Systems for Damage Detection†," *Aerospace*, vol. 5, no. 2, pp. 1–19, 2018.
- [66] C. M. Schubert, Kabban, B. Lin, Y. Bhuiyan, C. P. Edelmann, and V. Giurgiutiu, "Sensitivity analysis and uncertainty evaluation in the design of structural health monitoring systems," in *11th International Workshop on Structural Health Monitoring*, 2017, pp. 3069–3076.
- [67] B. Lin, A. Kamal, V. Giurgiutiu, and T. Kamas, "Multimodal Lamb Waves Power and Transfer Function Analysis of Structurally-bounded PWAS," in *ASME SMASIS*, 2012.
- [68] Y. Shen and V. Giurgiutiu, "Combined analytical FEM approach for efficient simulation of Lamb wave damage detection," *Ultrasonics*, vol. 69, pp. 116–128, 2016.
- [69] J. N. Reddy, *An Introduction to the Finite Element Method*, 3rd ed. Newyork, NY: McGraw-Hill, 2006.
- [70] I. Trendafoiloiva, D. G. Gorman, and E. Manoach, "An Investigation on Vibration-based Damage Detection in Circular Plates," *Struct. Heal. Monit.*, vol. 8, no. 4, pp. 291–302, 2009.
- [71] D. Wang, W. Zhang, X. Wang, and B. Sun, "Lamb-wave-based tomographic imaging techniques for hole-edge corrosion monitoring in plate structures," *Materials (Basel)*, vol. 9, no. 11, 2016.
- [72] J. Cai, S. Yuan, and T. Wang, "Signal construction-based dispersion compensation of lamb waves considering signal waveform and amplitude spectrum preservation," *Materials (Basel)*, vol. 10, no. 1, pp. 1–22, 2017.
- [73] J.-B. Ihn and F.-K. Chang, "Pitch-catch Active Sensing Methods in Structural Health Monitoring for Aircraft Structures," *Struct. Heal. Monit. Int. J.*, vol. 7, no. 1, pp. 5–19, 2008.
- [74] S. Yuan *et al.*, "Recent Progress on Distributed Structural Health Monitoring Research at NUAA," *J. Intell. Mater. Syst. Struct.*, vol. 19, no. 3, pp. 373–386, 2008.
- [75] C. Mo *et al.*, "Acoustic emission of deformation twinning in magnesium," *Materials (Basel)*, vol. 9, no. 8, 2016.

- [76] C. S. Rekatsinas, "Time Domain Spectral Finite Element Methods for the Simulation of Wave Propagation in Composite Layered Structures with Active Piezoelectric Sensors," 2016.
- [77] C. K. Lee, P. D. Wilcox, B. W. Drinkwater, J. J. Scholey, M. R. Wisnom, and M. I. Friswell, "Acoustic Emission during Fatigue Crack Growth in Aluminium Plates," *Proc. ECNDT*, vol. Mo.2.1.5, pp. 1–8, 2006.
- [78] T. C. Lindley, I. G. Palmer, and Richards C. E., "Acoustic emission monitoring of fatigue crack growth," *Mater. Sci. Eng.*, vol. 32, pp. 1–15, 1978.
- [79] C. B. Scruby, G. R. Baldwin, and K. A. Stacey, "Characterization of fatigue crack extension by quantitative acoustic emission," *Int. J. Fract.*, vol. 28, pp. 201–222, 1985.
- [80] J. R. Mitchell, D. M. Egle, and F. J. Appl, "Detecting Fatigue Cracks with Acoustic Emission," in *Proceedings of the Oklahoma Academy of Science*, 1973, vol. 53, pp. 121–126.
- [81] H. Chang, E. H. Han, J. Q. Wang, and W. Ke, "Acoustic Emission Study of Fatigue Crack Closure of Physical Short and Long Cracks for Aluminum Alloy LY12CZ," *Int. J. Fatigue*, vol. 31, no. 3, pp. 403–407, 2009.
- [82] M. Abdelrahman, M. K. ElBatanouny, and P. H. Ziehl, "Acoustic emission based damage assessment method for prestressed concrete structures: Modified index of damage," *Eng. Struct.*, vol. 60, pp. 258–264, 2014.
- [83] R. Ernst, F. Zwimpfer, and J. Dual, "One sensor acoustic emission localization in plates," *Ultrasonics*, vol. 64, pp. 139–150, 2016.
- [84] I. M. Perez, H. Cui, and E. Udd, "Acoustic emission detection using fiber Bragg gratings," *SPIE's 8th Annu. Int. Symp. Smart Struct. Mater.*, vol. 4328, pp. 209–215, 2001.
- [85] M. R. Gorman and W. H. Prosser, "Application of Normal Mode Expansion to Acoustic Emission Waves in Finite Plates," *J. Appl. Mech.*, vol. 63, no. 2, pp. 555–557, 1996.
- [86] D. Guo, A. K. Mal, and M. A. Hamstad, "AE Wavefield Calculations in a Plate," in *Proceedings of International AE Conference*, 1998, pp. 19–29.
- [87] D. J. Buttle and C. B. Scruby, "Acoustic Emission Source Location in Fiber Reinforced Plastic Composites," *J. Acoust. Emiss.*, vol. 7, no. 4, pp. 211–223, 1988.

- [88] T. M. Morton, R. M. Harrington, and J. G. Bjeletich, "Acoustic emissions of fatigue crack growth," *Eng. Fract. Mech.*, vol. 5, no. 3, pp. 691–697, Sep. 1973.
- [89] C. B. Scruby, H. N. G. Wadley, and J. E. Sinclair, "The origin of acoustic emission during deformation of aluminum and an aluminum-magnesium alloy," *Philos. Mag. A*, vol. 44, no. 2, pp. 249–274, 1981.
- [90] F. Hamel, J. P. Bailon, and M. N. Bassim, "Acoustic emission mechanisms during high-cycle fatigue," *Eng. Fract. Mech.*, vol. 14, no. 4, pp. 853–860, Jan. 1981.
- [91] A. Ould Amer, A. L. Gloanec, S. Courtin, and C. Touze, "Characterization of fatigue damage in 304L steel by an acoustic emission method," *Procedia Eng.*, vol. 66, pp. 651–660, 2013.
- [92] O. Andreykiv, V. Skalsky, O. Serhiyenko, and D. Rudavskyy, "Acoustic Emission Estimation of Crack Formation in Aluminium Alloys," *Eng. Fract. Mech.*, vol. 77, no. 5, pp. 759–767, 2010.
- [93] A. Castellano, P. Foti, A. Fraddosio, S. Marzano, and M. D. Piccioni, "Mechanical characterization of CFRP composites by ultrasonic immersion tests: Experimental and numerical approaches," *Compos. Part B Eng.*, vol. 66, pp. 299–310, 2014.
- [94] W. H. Prosser, M. A. Hamstad, J. Gary, and A. O’Gallagher, "Finite Element and Plate Theory Modeling of Acoustic Emission Waveforms," *J. Nondestruct. Eval.*, vol. 18, no. 3, pp. 83–90, 1999.
- [95] A. Zelenyak, M. Hamstad, and M. Sause, "Modeling of Acoustic Emission Signal Propagation in Waveguides," *Sensors*, vol. 15, no. 5, pp. 11805–11822, 2015.
- [96] M. Ohtsu and K. Ono, "A generalized theory and source representations of acoustic emission," *J. Acoust. Emiss.*, vol. 5, no. 4, pp. 124–133, 1986.
- [97] A. A. Pollock, "Acoustic emission inspections," 1989.
- [98] W. H. Prosser, "Applications of advanced, waveform based AE techniques for testing composite materials," in *Proc. SPIE*, 1996, vol. 2944, pp. 146–153.
- [99] K. Aki and P. G. Richards, *Quantitative Seismology*. University Science Books, 2002.
- [100] J. A. Hudson, R. G. Pearce, and R. M. Rogers, "Source Type Plot for Inversion of the Moment Tensor," *J. Geophys. Res.*, vol. 94, no. B1, pp. 765–774, 1989.
- [101] C. Frohlich and K. D. Apperson, "Earthquake focal mechanisms, moment tensors, and the consistency of seismic activity near plate boundaries," *Tectonics*, vol. 11, no. 2, pp. 279–296, 1992.

- [102] M. A. Hamstad, A. O’Gallagher, and J. Gary, “Modeling of Buried Monopole and Dipole Sources of Acoustic Emission with a Finite Element Technique,” *J. Acoust. Emiss.*, vol. 17, pp. 97–110, 1999.
- [103] M. V. Lysak, “Development of the Theory of Acoustic Emission by Propagating Cracks in Terms of Fracture Mechanics,” *Eng. Fract. Mech.*, vol. 55, no. 3, pp. 443–452, 1996.
- [104] M. G. R. Sause and S. Richler, “Finite element modelling of cracks as acoustic emission sources,” *J. Nondestruct. Eval.*, vol. 34, no. 1, p. 4, 2015.
- [105] R. Joseph, M. Y. Bhuiyan, and V. Giurgiutiu, “Acoustic emission source modeling in a plate using buried moment tensors,” in *SPIE Proceedings of Health Monitoring of Structural and Biological Systems*, 2017, pp. 1017028-1–8.
- [106] W. Qiang and Y. Shenfang, “Baseline-free Imaging Method based on New PZT Sensor Arrangements,” *J. Intell. Mater. Syst. Struct.*, vol. 20, no. 14, pp. 1663–1673, 2009.
- [107] B. Köhler, T. Gaul, U. Lieske, and F. Schubert, “Shear horizontal piezoelectric fiber patch transducers (SH-PFP) for guided elastic wave applications,” *NDT E Int.*, vol. 82, pp. 1–12, 2016.
- [108] L. Yu, G. Santoni-Bottai, B. Xu, W. Liu, and V. Giurgiutiu, “Piezoelectric wafer active sensors for in situ ultrasonic-guided wave SHM,” *Fatigue Fract. Eng. Mater. Struct.*, vol. 31, no. 8, pp. 611–628, 2008.
- [109] M. I. Friswell and J. E. T. Penny, “Crack Modeling for Structural Health Monitoring,” *Struct. Heal. Monit.*, vol. 1, no. 2, pp. 139–148, 2002.
- [110] Y. Jiang and M. Feng, “Modeling of Fatigue Crack Propagation,” *J. Eng. Mater. Technol.*, vol. 126, no. 1, pp. 77–86, 2004.
- [111] G. Santoni-Bottai, “Fundamental Studies In The Lamb-Wave Interaction Between Piezoelectric Wafer Active Sensor And Host Structure During Structural Health Monitoring,” University of South Carolina, 2010.
- [112] B. Lin, M. Gresil, A. Cuc, and V. Giurgiutiu, “Predictive Modeling of Piezoelectric Wafer Active Sensors for Structural Health Monitoring,” *Ferroelectrics*, vol. 470, no. 1, pp. 168–182, Oct. 2014.
- [113] M. Y. Bhuiyan and V. Giurgiutiu, “Experimental and computational analysis of acoustic emission waveforms for SHM applications,” in *11th International Workshop on Structural Health Monitoring*, 2017, pp. 1–7.

- [114] R. Joseph, M. Y. Bhuiyan, and V. Giurgiutiu, "Influence of fracture modes on acoustic emission source modeling by using buried moment tensors," *J. Nondestruct. Eval. Diagnostics Progn. Eng. Syst.*, no. Under review, pp. 1–21, 2018.
- [115] M. Y. Bhuiyan, J. Bao, B. Poddar, and V. Giurgiutiu, "Toward identifying crack-length-related resonances in acoustic emission waveforms for structural health monitoring applications," *Struct. Heal. Monit. Int. J.*, vol. Online, pp. 1–9, 2017.
- [116] M. Y. Bhuiyan and V. Giurgiutiu, "Multiphysics simulation of low-amplitude acoustic wave detection by piezoelectric wafer active sensors validated by in-situ AE-fatigue experiment," *Materials (Basel)*, vol. 10, no. 8, pp. 1–19, 2017.
- [117] V. Mortezaei, A. Haghshenas, M. M. Khonsari, and B. Bollen, "Fatigue analysis of metals using damping parameter," *Int. J. Fatigue*, vol. 91, Part 1, pp. 124–135, 2016.
- [118] R. O. Ritchie, B. L. Boyce, J. P. Campbell, O. Roder, A. W. Thompson, and W. W. Milligan, "Thresholds for high-cycle fatigue in a turbine engine Ti–6Al–4V alloy," *Int. J. Fatigue*, vol. 21, no. 7, pp. 653–662, 1999.
- [119] M. H. Hafezi, N. N. Abdullah, J. F. O. Correia, and A. M. P. De Jesus, "An assessment of a strain-life approach for fatigue crack growth," *Int. J. Struct. Integr.*, vol. 3, no. 4, pp. 344–376, 2012.
- [120] J. Schijve, "Fatigue of aircraft materials and structures," *Int. J. Fatigue*, vol. 16, no. 1, pp. 21–32, 1994.
- [121] A. Shyam, J. E. Allison, C. J. Szczepanski, T. M. Pollock, and J. W. Jones, "Small fatigue crack growth in metallic materials: A model and its application to engineering alloys," *Acta Mater.*, vol. 55, no. 19, pp. 6606–6616, 2007.
- [122] L. Li, Z. Zhang, and G. Shen, "Influence of grain size on fatigue crack propagation and acoustic emission features in commercial-purity zirconium," *Mater. Sci. Eng. A*, vol. 636, pp. 35–42, 2015.
- [123] A. Maslouhi, "Fatigue crack growth monitoring in aluminum using acoustic emission and acousto-ultrasonic methods," *Struct. Control Heal. Monit.*, vol. 18, no. 7, pp. 790–806, 2011.
- [124] J. Fan, J. Chen, D. Jiang, A. Chemenda, J. Chen, and J. Ambre, "Discontinuous cyclic loading tests of salt with acoustic emission monitoring," *Int. J. Fatigue*, vol. 94, pp. 140–144, 2017.
- [125] T. M. Roberts and M. Talebzadeh, "Acoustic emission monitoring of fatigue crack propagation," *J. Constr. Steel Res.*, vol. 59, no. 6, pp. 695–712, 2003.

- [126] Z. Y. Piao, B. S. Xu, H. D. Wang, and D. H. Wen, "Investigation of acoustic emission source of Fe-based sprayed coating under rolling contact," *Int. J. Fatigue*, vol. 47, pp. 184–188, 2013.
- [127] T. Kamas, V. Giurgiutiu, and B. Lin, "Quasi-Rayleigh waves in butt-welded thick steel plate," in *AIP Conference Proceedings*, 2015.
- [128] S. Agcaoglu and O. Akkus, "Acoustic Emission Based Monitoring of the Microdamage Evolution During Fatigue of Human Cortical Bone," *J. Biomech. Eng.*, vol. 135, no. 8, pp. 1–8, 2013.
- [129] M. Y. Bhuiyan, J. Bao, B. Poddar, and V. Giurgiutiu, "Analysis of acoustic emission waveforms from fatigue cracks," in *SPIE Proceedings of Health Monitoring of Structural and Biological Systems*, 2017, vol. 10170, p. 101702A–1–8.
- [130] E. Agletdinov, E. Pomponi, D. Merson, and A. Vinogradov, "A novel Bayesian approach to acoustic emission data analysis," *Ultrasonics*, vol. 72, pp. 89–94, 2016.
- [131] R. Anay, V. Soltangharaei, L. Assi, T. DeVol, and P. Ziehl, "Identification of damage mechanisms in cement paste based on acoustic emission," *Constr. Build. Mater.*, vol. 164, pp. 286–296, 2018.
- [132] K. Nam and A. Mal, "Characteristics of elastic waves generated by crack initiation in aluminum alloys under fatigue loading," *J. Mater. Res.*, vol. 16, no. 6, pp. 1745–51, 2001.
- [133] R. K. Nalla, J. P. Campbell, and R. O. Ritchie, "Mixed-mode, high-cycle fatigue-crack growth thresholds in Ti–6Al–4V: Role of small cracks," *Int. J. Fatigue*, vol. 24, no. 10, pp. 1047–1062, 2002.
- [134] G. M. Castelluccio and D. L. McDowell, "Assessment of small fatigue crack growth driving forces in single crystals with and without slip bands," *Int. J. Fract.*, vol. 176, no. 1, pp. 49–64, 2012.
- [135] L. W. Wei, E. R. de los Rios, and M. N. James, "Experimental study and modelling of short fatigue crack growth in aluminium alloy Al7010-T7451 under random loading," *Int. J. Fatigue*, vol. 24, no. 9, pp. 963–975, 2002.
- [136] L. Wang, S. R. Daniewicz, M. F. Horstemeyer, S. Sintay, and A. D. Rollett, "Three-dimensional finite element analysis using crystal plasticity for a parameter study of microstructurally small fatigue crack growth in a Al 7075 aluminum alloy," *Int. J. Fatigue*, vol. 31, no. 4, pp. 651–658, 2009.

- [137] S. Ravindran, A. Tessema, and A. Kidane, "Local Deformation and Failure Mechanisms of Polymer Bonded Energetic Materials Subjected to High Strain Rate Loading," *J. Dyn. Behav. Mater.*, vol. 2, no. 1, pp. 146–156, 2016.
- [138] A. Berkovits and D. Fang, "Study of fatigue crack characteristics by acoustic emission," *Eng. Fract. Mech.*, vol. 51, no. 3, pp. 401–416, 1995.
- [139] M. Rabiei and M. Modarres, "Quantitative methods for structural health management using in situ acoustic emission monitoring," *Int. J. Fatigue*, vol. 49, pp. 81–89, 2013.
- [140] J. C. Duke and R. E. Green, "Simultaneous monitoring of acoustic emission and ultrasonic attenuation during fatigue of 7075 aluminium," *Int. J. Fatigue*, vol. 1, no. 3, pp. 125–132, 1979.
- [141] L. Yu, C. A. C. Leckey, and Z. Tian, "Study on crack scattering in aluminum plates with Lamb wave frequency–wavenumber analysis," *Smart Mater. Struct.*, vol. 22, no. 6, p. 65019, 2013.
- [142] J. Yu, P. Ziehl, F. Matta, and A. Pollock, "Acoustic emission detection of fatigue damage in cruciform welded joints," *J. Constr. Steel Res.*, vol. 86, 2013.
- [143] D. Gagar, P. Foote, and P. Irving, "A Novel Closure Based Approach for Fatigue Crack Length Estimation Using the Acoustic Emission Technique in Structural Health Monitoring Applications," *Smart Mater. Struct.*, vol. 23, no. 10, p. 105033, 2014.
- [144] P. G. Doctor, T. P. Harrington, and P. H. Hutton, "Pattern recognition methods for acoustic emission analysis," Battelle Pacific Northwest Labs., Richland, WA, 1979.
- [145] R. B. Melton, P. G. Doctor, and D. S. Daly, "Pattern recognition analysis of acoustic emission data from 7075-T651 aluminum simulated joint specimens," in *Review of Progress in Quantitative Nondestructive Evaluation*, 1983, pp. 489–501.
- [146] K. Ono and Q. Huang, "Pattern recognition analysis of acoustic emission signals," *NDT E Int.*, vol. 30, no. 2, pp. 69–78, 1997.
- [147] P. H. Hutton, R. J. Kurtz, and R. A. Pappas, "Acoustic emission monitoring of ZB-1 intermediate scale vessel test," *Nucl. Eng. Des.*, vol. 84, no. 2, pp. 171–178, 1985.
- [148] P. H. Hutton, R. J. Kurtz, and M. A. Friesel, "Progress for on-line acoustic emission monitoring of cracks in reactor systems," *Nucl. Eng. Des.*, vol. 98, no. 2, pp. 135–140, 1987.

- [149] K. M. Holford, R. Pullin, S. L. Evans, M. J. Eaton, J. Hensman, and K. Worden, “Acoustic emission for monitoring aircraft structures,” *Proc. Inst. Mech. Eng. Part G J. Aerosp. Eng.*, vol. 223, no. 5, pp. 525–532, Jan. 2009.
- [150] M. Y. Bhuiyan, B. Lin, and V. Giurgiutiu, “Acoustic emission sensor effect and waveform evolution during fatigue crack growth in thin metallic plate,” *J. Intell. Mater. Syst. Struct.*, vol. 29, no. 7, pp. 1275–1284, 2017.
- [151] T. John and W. Seneviratne, “Determining the Fatigue Life of Composite Aircraft Structures Using Life and Load-Enhancement Factors,” Federal Aviation Administration, 2011.
- [152] H. J. Grover, “Fatigue of Aircraft Structures,” Naval air systems command, Department of the NAVY, 1966.
- [153] M. Y. Bhuiyan, B. Lin, and V. Giurgiutiu, “Piezoelectric wafer active sensor as a novel acoustic emission transducer,” *Ultrasonics*, no. Under review, pp. 1–32, 2018.
- [154] M. Y. Bhuiyan and V. Giurgiutiu, “The signatures of acoustic emission waveforms from fatigue crack advancing in thin metallic plates,” *Smart Mater. Struct.*, vol. 27, no. 1, pp. 1–15, 2017.
- [155] Q. Wu, F. Yu, Y. Okabe, K. Saito, and S. Kobayashi, “Acoustic emission detection and position identification of transverse cracks in carbon fiber-reinforced plastic laminates by using a novel optical fiber ultrasonic sensing system,” *Struct. Heal. Monit.*, vol. 14, no. 3, pp. 205–213, 2015.
- [156] V. Janapati, F. Kopsaftopoulos, F. Li, S. J. Lee, and F.-K. Chang, “Damage detection sensitivity characterization of acousto-ultrasound-based structural health monitoring techniques,” *Struct. Heal. Monit.*, vol. 15, no. 2, pp. 143–161, Mar. 2016.
- [157] J. Cuadra, P. A. Vanniamparambil, D. Servansky, I. Bartoli, and A. Kontsos, “Acoustic Emission Source Modeling using a Data-Driven Approach,” *J. Sound Vib.*, vol. 341, pp. 222–236, 2015.
- [158] E. D. Niri, a Farhidzadeh, and S. Salamone, “Adaptive multisensor data fusion for acoustic emission source localization in noisy environment,” *Struct. Heal. Monit. Int. J.*, vol. 12, no. 1, pp. 59–77, 2013.
- [159] A. Farhidzadeh, S. Salamone, B. Luna, and A. Whittaker, “Acoustic emission monitoring of a reinforced concrete shear wall by b-value-based outlier analysis,” *Struct. Heal. Monit.*, vol. 12, no. 1, pp. 3–13, 2013.

- [160] G. C. McLaskey and S. D. Glaser, “Acoustic emission sensor calibration for absolute source measurements,” *J. Nondestruct. Eval.*, vol. 31, no. 2, pp. 157–168, 2012.
- [161] A. A. Abouhussien and A. A. A. Hassan, “Detection of bond failure in the anchorage zone of reinforced concrete beams via acoustic emission monitoring,” *Smart Mater. Struct.*, vol. 25, no. 7, p. 75034, 2016.
- [162] J. Jingpin, W. Bin, and H. Cunfu, “Acoustic emission source location methods using mode and frequency analysis,” *Struct. Control Heal. Monit.*, vol. 15, no. 4, pp. 642–651, 2008.
- [163] K. Y. Kim and W. Sache, “Characteristics of an acoustic emission source from a thermal crack in glass,” *Int. J. Fract.*, vol. 31, no. 3, pp. 211–231, 1986.
- [164] O. Andreykiv, V. Skalsky, O. Serhiyenko, and D. Rudavskyy, “Acoustic emission estimation of crack formation in aluminium alloys,” *Eng. Fract. Mech.*, vol. 77, no. 5, pp. 759–767, 2010.
- [165] R. V. Sagar and B. K. R. Prasad, “A Review of Recent Developments in Parametric Based Acoustic Emission Techniques Applied to Concrete Structures,” *Nondestruct. Test. Eval.*, vol. 27, no. 1, pp. 47–68, 2012.
- [166] B. Poddar, “Physics Based Modeling Of Guided Waves For Detection And Characterization Of Structural Damage In NDE and SHM,” 2016.
- [167] B. Poddar, “Physics Based Modeling of Guided Waves for Detection and Characterization of Structural Damage in NDE and SHM,” *PhD Diss.*, p. 182, 2016.
- [168] M. Y. Bhuiyan, M. F. Haider, B. Poddar, and V. Giurgiutiu, “Guided wave crack detection and size estimation in stiffened structures,” in *SPIE Proceedings of Nondestructive Characterization and Monitoring of Advanced Materials, Aerospace, Civil Infrastructure, and Transportation XII*, 2018, vol. 10599, p. 105991Y–1–11.
- [169] M. Y. Bhuiyan, M. F. Haider, A. Migot, and V. Giurgiutiu, “Ultrasonic nondestructive evaluation and health monitoring of a composite plate,” in *Society for the Advancement of Material and Process Engineering- SAMPE Long Beach*, 2018, pp. 1–15.
- [170] M. F. Haider, M. Y. Bhuiyan, B. Poddar, B. Lin, and V. Giurgiutiu, “Combined global-local analysis to determine scattering of Lamb waves for detecting crack in a complex structure: An analytical approach with experimental validation,” *J. Sound Vib.*, no. Under review, 2018.

- [171] “Fast Immersion-free CFRP Inspection using the new Olympus phased array wheel probe,” www.olympus-ims.com, 2016.
- [172] A. Migot and V. Giurgiutiu, “Impact Localization on a Composite Plate With Unknown Material Properties Using PWAS Transducers and Wavelet Transform,” in *ASME Conference on Smart materials, adaptive structures and intelligent systems*, 2017, pp. 1–8.
- [173] A. Migot and V. Giurgiutiu, “Impact localization using sparse PWAS networks and wavelet transform,” in *11th International Workshop on Structural Health Monitoring*, 2017, pp. 391–398.
- [174] T. Kundu, “A new technique for acoustic source localization in an anisotropic plate without knowing its material properties,” in *6th European Workshop on Structural Health Monitoring*, 2012.